



UNIVERSITAT DE
BARCELONA

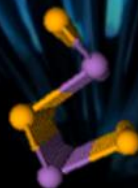
Quasi One Dimensional Antimony Selenide Thin Film Solar Cells for Next Generation Photovoltaics

Pedro Vidal Fuentes

ADVERTIMENT. La consulta d'aquesta tesi queda condicionada a l'acceptació de les següents condicions d'ús: La difusió d'aquesta tesi per mitjà del servei TDX (www.tdx.cat) i a través del Dipòsit Digital de la UB (diposit.ub.edu) ha estat autoritzada pels titulars dels drets de propietat intel·lectual únicament per a usos privats emmarcats en activitats d'investigació i docència. No s'autoritza la seva reproducció amb finalitats de lucre ni la seva difusió i posada a disposició des d'un lloc aliè al servei TDX ni al Dipòsit Digital de la UB. No s'autoritza la presentació del seu contingut en una finestra o marc aliè a TDX o al Dipòsit Digital de la UB (framing). Aquesta reserva de drets afecta tant al resum de presentació de la tesi com als seus continguts. En la utilització o cita de parts de la tesi és obligat indicar el nom de la persona autora.

ADVERTENCIA. La consulta de esta tesis queda condicionada a la aceptación de las siguientes condiciones de uso: La difusión de esta tesis por medio del servicio TDR (www.tdx.cat) y a través del Repositorio Digital de la UB (diposit.ub.edu) ha sido autorizada por los titulares de los derechos de propiedad intelectual únicamente para usos privados enmarcados en actividades de investigación y docencia. No se autoriza su reproducción con finalidades de lucro ni su difusión y puesta a disposición desde un sitio ajeno al servicio TDR o al Repositorio Digital de la UB. No se autoriza la presentación de su contenido en una ventana o marco ajeno a TDR o al Repositorio Digital de la UB (framing). Esta reserva de derechos afecta tanto al resumen de presentación de la tesis como a sus contenidos. En la utilización o cita de partes de la tesis es obligado indicar el nombre de la persona autora.

WARNING. On having consulted this thesis you're accepting the following use conditions: Spreading this thesis by the TDX (www.tdx.cat) service and by the UB Digital Repository (diposit.ub.edu) has been authorized by the titular of the intellectual property rights only for private uses placed in investigation and teaching activities. Reproduction with lucrative aims is not authorized nor its spreading and availability from a site foreign to the TDX service or to the UB Digital Repository. Introducing its content in a window or frame foreign to the TDX service or to the UB Digital Repository is not authorized (framing). Those rights affect to the presentation summary of the thesis as well as to its contents. In the using or citation of parts of the thesis it's obliged to indicate the name of the author.



PhD Thesis

Quasi One Dimensional Antimony Selenide Thin Film Solar Cells for Next Generation Photovoltaics

Pedro Vidal Fuentes



UNIVERSITAT DE
BARCELONA

Quasi One Dimensional Antimony Selenide Thin Film Solar Cells for Next Generation Photovoltaics

Memòria presentada per optar al grau de doctor per la
Universitat de Barcelona

Programa de doctorat en
Enginyeria i Ciències Aplicades

Autor: Pedro Vidal Fuentes

Directors: Dr. Edgardo Saucedo Silva, Dr. Víctor Izquierdo Roca

Tutor: Prof. Dr. Alejandro Pérez Rodríguez



UNIVERSITAT DE
BARCELONA

*Science, without political
and social awareness, is
nothing more than the
cruellest tool that humanity
has ever developed.*

Table of Contents

I - Acknowledgments	7
II - List of acronyms and abbreviations	11
III - Table of Figures	15
IVa - Preface: Publications and summary of the thesis	21
IVb - Prefacio: Publicaciones y resumen de la tesis	27
V - Contribution of the author to publications in the thesis	35
1 - Chapter 1: Introduction	37
1.1 - Socio-economical context.....	37
1.2 - PV state of the art.....	43
1.3 - New emerging photovoltaics: the case of Sb_2Se_3	55
1.3.1 - <i>Evolution and state of the art of Sb_2Se_3</i>	55
1.3.2 - <i>But why Sb_2Se_3 is so interesting?</i>	57
1.3.3 - <i>Defect properties and limitations</i>	62
1.3.4 - <i>Device strategies</i>	65
1.4 - Fundamentals of solar cells	69
1.4.1 - <i>What is a solar cell?</i>	69
1.4.2 - <i>Opto-electronic parameters of a solar cell</i>	77
1.4.3 - <i>Fundamental limits and recombination paths</i>	80
1.5 - Fundamentals of Raman spectroscopy	87
1.6 - Objectives of the thesis	93
2 - Chapter 2: Methodology	95
2.1 - Layer synthesis and device fabrication	95
2.2 - Layers and device characterization	99
3 - Chapter 3: Publications	103
3.1 - Introduction to publications and side experiments.....	105
3.2 - Article 1	125

3.3 - Article 2	141
3.4 - Article 3	159
4 - Conclusions and Outlook	181
5 - Bibliography	185
Appendix.....	211

I - Acknowledgments

These 4 yearlong period, wonderful time, in which I have grown up as a scientist, and more important as a person, would have been impossible without the support I have continuously received. This will be as multilingual as I feel my life.

First of all, I would like to thank Edgardo and Alejandro for giving me the opportunity to fulfil this PhD under your supervision, you have shown me the passion for a relentless career in a never ending learning process.

To Victor, needless to say is that I have found in you a mentor, and a friend. With you it was possible to argue in a deep and passionate manner, always with time (even if it seemed impossible) and patience to explain everything in detail, combined with the ability to listen and trust. You have taught me how to be enthusiastic for every new research possible and to make of the laboratory the funniest playground.

A Alex, Pablo, Cristina, Claudia, Teresa, María e tantos outros case incontables paisanos. Non é doado describir a morriña que sofre unha persoa estando tan lonxe da casa, porén é doada de aturar e faise liviá a espera excusivamente pola vosa presenza nesta dura cidade. A sorte de ter ao meu carón os meus mellores amigos non ten nome nin prezo, aínda que se xunte coa tristura de ter que procurar un futuro tan lonxe, agardo que voltemos todos, e se non, tocará seguir viaxando. Dende logo ter alguén para procurar o mellor licor café, a mellor caña de estrela ou facer un churrasquiño fan da viaxe un paseo. Nesta dedicatoria quero incluír tamén a todos aqueles que agardan por nós e nos reciben como se endexamais marcháramos.

A Ana, tu amor, tu cariño y tu forma de ver la vida me han hecho ser la persona que soy ahora. Siempre has estado incondicionalmente a mi lado durante estos cuatro años, en todos los momentos de estrés dándome tu apoyo y haciendo tuyos mis problemas. Nunca cambies, si todos viéramos la vida como tú todo más bonito y, desde luego, más divertido.

A mi madre, gracias por tu amor y tu confianza ciega, espero no decepcionarte (demasiado) nunca, si he llegado aquí ha sido gracias a ti.

Al resto de mi(s) familia(s), a mi padre, a mis abuelos a Carmina y a Guillermo, por el apoyo y el interés infinito hacia un trabajo difícilmente explicable.

To Nacho and Jacob, you have been my closest friends in the lab and outside it. If I count how many times have you helped me out, in the first page it will be three names.

To Marcel and Diouldé, you have taught me so much, things that may not be present in the thesis as a specific knowledge but that become part of the necessary baggage to become a researcher, always with a smile, always available and always with an answer.

To Yudania, I will not be able to repay you all the kindness and care that you have provided me in these years.

To Max, the knowledge that you have transmitted to me is invaluable, this thesis is indeed half yours. I will count on you for the next session of *push-ups*.

To Robert, even if you started after me, you were always an inspiration, thank you for being so kind all the time, and sorry to ask you the same doubts once and again.

To Sergio, I think I have never meet such a joyful and good person, always with a smile even in the bad days. You were and are a clear example to follow.

To Mohamed, even if the communication sometimes was difficult a smile always says enough.

To Fabien, Enric, Angélica, Viktoriia and Andreina you have become more than co-workers, for me you are really good friends and I harvest all the time and fun we had, I hope it will last for a long time.

To the newcomers, Maykel, Alex J., Alex N., Axel and Ivan, enjoy your research period, and do not stress too much, at least not as much as I was trying to explain everything to you.

To the rest of The IREC workers in the SEMS group, all the people that have come in an internship and in the IREC facilities as a whole, there is

an infinite number of people that I have met during this period, in a working or pleasure environment, you are also part of this manuscript.

II - List of acronyms and abbreviations

1D - one dimensional	CZTSe - $\text{Cu}_2\text{ZnSnSe}_4$
2D - Two dimensional	CRM - Critical raw material
AM 1.5 - Reference global spectrum at air mass 1.5	CSS - Close space sublimation
APV - Agrophotovoltaic	C-V - Capacitance – voltage
ARC - Anti-reflective coating	E_A - Activation energy
AZO - Al-doped ZnO	E_g - Band gap energy
a-Si - Amorphous silicon	E_c - Conduction band energy
BIPV - Building integrated photovoltaics	E_{EA} - Electron affinity energy
c - speed of light	E_F - Fermi level energy
C - capacitance	E_{ph} - Photon energy
CBD - Chemical bath deposition	E_u - Urbach energy
CBM - Conduction band minimum	EU - European Union
CCD - Charged coupled device	E_v - Valence band energy
CdTe - Cadmium Telluride	E_{vac} - Vacuum level energy
CIS - CuInS_2	EDX - Energy dispersive X-ray spectroscopy
CISE - CuInSe_2	EQE - External quantum efficiency
CIGS - CuInGaS_2	eV - Electron Volt
CIGSe - $\text{Cu}(\text{In}_{1-x}\text{Ga}_x)\text{Se}_2$	FE-SEM - Field emission scanning electron microscopy
CIGSe - $\text{Cu}(\text{In}_{1-x}\text{Ga}_x)(\text{S}_{1-y}\text{Se}_y)_2$	FF - Fill factor
CZTS - $\text{Cu}_2\text{ZnSnSe}_4$	G - generation rate

h - Planks's constant	J_{rec} - Recombination current density
HJ-IBC - heterojunction interdigitated back contact	J-V - Current density voltage
HRTEM - High resolution transmission electron microscopy	JV-T - Temperature dependent current density voltage
I - Current	k_B - Boltzman's constant
ICP - Inductively coupled plasma spectroscopy	n - Diode quality factor
IoT - Internet of things	nc-Si - Nano-crystalline silicon
IQE - Internal quantum efficiency	N_A - Concentration of acceptor defects
ITO - Tin-doped indium oxide ($\text{In}_2\text{O}_3:\text{SnO}_2$)	N_D - Concentration of donor defects
i-ZnO - Intrinsic zinc oxide	n_i - intrinsic concentration
J - Current density	NIR - Near infrared
J_0 - Saturation/dark current density	mpp - Maximum power point
J_0 - Reference current density	m-TiO ₂ - mesoporous TiO ₂
J_{gen} - Generation current density	m^* - Effective mass
J_{mpp} - Maximum power point current density	l_n - Width of N-side depletion region
J_{opt} - Current density at optimal bandgap	l_p - Width of P-side depletion region
J_{ph} - Photogenerated current density	L_N - electron diffusion length
J_{sc} - Short circuit current density	L_P - hole diffusion length
	PCE - Power conversion efficiency
	PDA - Post deposition annealing
	PDT - Post deposition treatment

PID - Proportional–integral–derivative	V_a - Applied voltage
PL - Photoluminescence	V_{bi} - Built-in voltage
P - Power	V_{mpp} - Maximum power point voltage
p-Si - polycrystalline silicon	V_{oc} - Open circuit voltage
PV - Photovoltaic	V_{opt} - Voltage at optimal bandgap
PVD - Physical vapour deposition	VBM - Valence band maximum
q - Elemental charge	ViPV - Vehicle integrated photovoltaics
Q1D - Quasi one dimensional	VTD - Vapour transport deposition
R_s - Series resistance	XRD - X-ray diffraction
R_p/R_{sh} - Parallel/shunt resistance	XRF - X-ray fluorescence
RT - Room temperature	α - Absorption coefficient
SCR - Space charge region	λ_{ex} - excitation wavelength
SLG - Soda lime glass	ϵ_0 - Vacuum permittivity
SQ - Shockley-Queisser	ϵ_r - Relative permittivity
SRH - Shockley-Read-Hall	k - Wavevector
T - Temperature	μ_e - Electron mobility
\bar{t} - average scattering time	μ_h - hole mobility
T-Se - trigonal selenium	σ_e - Electron conductivity
TCO - Transparent conductive oxide	σ_h - Hole conductivity
TEM - Transmission electron microscopy	τ - Lifetime
UV - Ultraviolet	χ - susceptibility
V - Voltage/volts	ω - frequency

Ω - solid angle

Ω_{abs} - solid angle of absorption

Ω_{emit} - solid angle of emission

\hbar - Reduced Plank's constant

III - Table of Figures

Figure 1: Electricity generation by source in the OECD, extracted from IEA database.²37

Figure 2: Global coal demand in the present, and future prospect conditional to the policies applied in the future. Data from IEA.⁶38

Figure 3: Cumulative photovoltaic installations from 2010 to 2019 plus conservative and optimistic scenarios for 2020. Extracted from ref.²⁷40

Figure 4: Distributed PV capacity growth by segment, 2007-2024, source IEA.²⁸41

Figure 5: Percentage of global annual production per silicon PV technology. Extracted from ref.³³44

Figure 6: Schematics of a high efficiency silicon HJ-IBC cell Reprinted by permission from Springer Nature: Publisher Nature, Nature Energy: Yoshikawa, K. et al., Silicon Heterojunction Solar Cell with Interdigitated Back Contacts for a Photoconversion Efficiency over 26%. Nat. Energy 2017, 2 (5), 17032. <https://doi.org/10.1038/nenergy.2017.32>., ©(2017).³⁹45

Figure 7: Example of an a-Si flexible module.....47

Figure 8: Schematics of a close space sublimation (CSS) technique employed for the fabrication of superstrate CdTe thin film solar cells. ..48

Figure 9: Schematics of a CIGS basic device substrate configuration. ...51

Figure 10: Crystal structures of some semiconductor materials employed in photovoltaics. Extracted from <https://www.pveducation.org/es/fotovoltaica/czts> (Courtesy of Dr. Bryce Walker).51

Figure 11: Defect densities of: a) CdTe,Te-rich, b) CIGS Cu-poor, and c) CZTS Cu-poor. ©[2016] IEEE. Reprinted, with permission, from [Ingrid Repins, Wild band edges: The role of bandgap grading and band-edge fluctuations in high-efficiency chalcogenide devices, 2016 IEEE 43rd Photovoltaic Specialists Conference (PVSC)].⁸⁰52

Figure 12: Number of publications under the search "Sb₂Se₃ thin film" extracted from Web of science.55

Figure 13: PCE evolution of Sb₂Se₃ devices. CZTSSe data is calculated from data in ref ⁸⁹, Sb₂Se₃ data is extracted from ref ¹⁰⁰56

Figure 14: Phase diagram Sb_2Se_3 . Reprinted with permission of ASM international from Sb (Antimony) Binary Alloy Phase Diagrams, Ghosh, G.; Olesinski, R. W.; Abbaschian, G. J.; Diagrams, A. P, Vol. 6, pp 585–590, 2016; permission conveyed through Copyright Clearance Center, Inc.¹⁰⁵58

Figure 15: Detail of the Energy band diagram of Sb_2Se_3 calculated by DFT by generalized gradient approximation (GGA). Reprinted with permission of John Wiley & Sons.¹⁰⁹59

Figure 16: Left) Crystal structure of Sb_2Se_3 along different crystallographic axes. Right) Non-equivalent atom positions. Right figure reproduced from Ref. ¹²² with permission from the Royal Society of Chemistry.....62

Figure 17: Top) Formation energies and equilibrium concentrations of different defects as a function of the Fermi level under (a) Se and (b) Sb rich conditions. Bottom) Transition energy levels of intrinsic defects on different atomic sites in the bandgap of Sb_2Se_3 . Reprinted (adapted) with permission from Huang, M.; Xu, P.; Han, D.; Tang, J.; Chen, S. Complicated and Unconventional Defect Properties of the Quasi-One-Dimensional Photovoltaic Semiconductor Sb_2Se_3 . ACS Appl. Mater. Interfaces **2019**, 11 (17), 15564–15572. <https://doi.org/10.1021/acsami.9b01220>.¹²³ Copyright 2019 American Chemical Society.64

Figure 18: Schematic of the basic solar cell device substrate structure implemented in this thesis.....67

Figure 19: Solar radiation spectrum. (author: CC BY-SA 3.0, <https://commons.wikimedia.org/w/index.php?curid=2623187>).....69

Figure 20: Schematics of the energy band diagram of a semiconductor material with Fermi energy level identified.71

Figure 21: Simplified band diagram of a PN (left) and P-i-N (right) structures.72

Figure 22: Schematics of formation of the space charge region (SCR) when a N and P semiconductors are brought together.....74

Figure 23: Realistic schematic of the formation of the band structure of an heterojunction solar cell with its main constituents, back contact (bc), absorber, buffer, window and front contact (fc). a) energy band as they will be calculated theoretically or measured experimentally. b) Band diagram once the materials are in contact and the Fermi energy levels

aligned. Image reproduced and adapted with permission of John Wiley and Sons from ref. ¹⁵⁷	76
Figure 24: current-voltage characteristics of a solar cell.....	77
Figure 25: Solar cell equivalent circuit. Left) one diode ideal solar cell. Right) two diode closer to a real solar cell.	79
Figure 26: Maximum efficiency based in the SQ limit in function of the bandgap energy of the absorber material (figure extracted from Wikipedia article Shockley-Queisser limit, credits to Steve Byrnes).....	80
Figure 27: Deviation from ideality of a solar cell due to unavoidable losses. Left) Intrinsic losses of a device with optimal Eg. Right) Translation of the loss process to final power output depending on the bandgap of the device. Reproduced and adapted with permission of John Wiley and Sons. ¹⁶⁵	83
Figure 28: Specific loss mechanisms from a perfect EQE spectra. Reprinted from Publication title, SITES, J., Quantification of Losses in Thin-Film Polycrystalline Solar Cells, 75 (1–2), 243–251, Copyright (2003), with permission from Elsevier. ¹⁶⁷	84
Figure 29: Diagram of the Raman measurement system composed of a top view of the spectrometer and side view of the optical probe.....	91
Figure 30: Basic synthesis protocol and structure of a substrate Sb ₂ Se ₃ device.	96
Figure 31: Examples of Sb ₂ Se ₃ decomposition under laser power. Left) Sb ₂ Se ₃ phase plus α -Se (254.4 cm ⁻¹). Right) decomposed Sb ₂ Se ₃ in α -Sb ₂ O ₃ and β -Sb ₂ O ₃	106
Figure 32: Sb metallic layers evaporated at different rates. Bottom right) Raman scattering of Sb metallic layers with different deposition rates.	108
Figure 33: Optoelectronic parameters in function of the deposition rate.	108
Figure 34: a) Cross-section image of a complete device with the Sb ₂ Se ₃ layer identified. b) Top view of a pristine Sb ₂ Se ₃ layer. c) EDS measurement on the surface of a Sb ₂ Se ₃ layer.....	109
Figure 35: a) Thickness dependence of the optoelectronic properties. b) Average compositional ratio extracted from XRF measurements vs final Sb ₂ Se ₃ thickness.....	111
Figure 36: a) Area normalized IQE of different thickness Sb ₂ Se ₃ devices. b) IQE and IQE(-1V) of best performing device with ~1.5 μ m absorber thickness.....	111

Figure 37: Optoelectronic parameters of different HTL materials with 2 nm thickness.....	113
Figure 38: a) MoSe ₂ pre-synthesis temperature and impact on optoelectronic properties. b) Raman measurements with excitation wavelength $\lambda_{ex} = 633$ nm performed on the as-synthesized MoSe ₂ layer. c) Relation of the areas marked in figure b with the FF factor and PCE of the final devices.	114
Figure 39: Effects of the inclusion of a Ge layer on top of pre-synthesized MoSe ₂ : a) On the optoelectronic parameters, b) on the ribbon alignment, c) on the density charge carrier density (N_{cv}), the space charge region width (SCR _w) and built in voltage (V_{bi}).	115
Figure 40: FE-SEM micrographs of the back contact of Sb ₂ Se ₃ samples with different deposited Ge thickness.....	116
Figure 41: Optoelectronic parameter of the different electron transport layers studied.	116
Figure 42: Schematics of the alkaline PDT process.	117
Figure 43: Effect of the alkali PDT treatment in the: a) median values of the optoelectronic parameters. b) in the internal quantum efficiency....	118
Figure 44: GDOES analysis of the alkaline PDT treatments. Left) normalized ratio between Sb and Se and its distribution through the thickness of the Sb ₂ Se ₃ layer for each alkaline and thickness. Right) distribution of alkaline trough the thickness of the Sb ₂ Se ₃ layer for each different thickness.....	120
Figure 45: Low magnification HAADF image of the X-section of a standard SLG/Mo/Sb ₂ Se ₃ /CdS/i-ZnO/ITO device. Several areas are marked in green, red and blue, where several X-EDS spectrum images were acquired. Right: Processed atomic resolution HAADF image. It corresponds to a single grain in the Sb ₂ Se ₂ layer, marked in the low magnification image in the left with a purple box.	121
Figure 46: Elemental mappings extracted from the X-EDS signals for the SI area marked in green in Figure 45.....	121
Figure 47: (a) Low resolution image of the whole sample cross-section, (b) magnified image of the front interfaces Sb ₂ Se ₃ /CdS/i-ZnO/ITO and (c) high resolution image of the CdS/Sb ₂ Se ₃ interface. (d) HRTEM image of the blue square in figure (c) with two analysis regions in the CdS/Sb ₂ Se ₃ interface. (e) magnification of area 1 (f) fast Fourier transforms (FFT) of the selected area. (g) Inverse FFT filtered by the	

diffraction pattern of the Sb_2Se_3 . (h) magnification of area 2. (i) fast Fourier transforms (FFT) of the selected area. (j) Inverse FFT filtered by the diffraction pattern of the Sb_2Se_3122

Figure 48: Elemental mappings extracted from the X-EDS signals for the SI 2 red area marked in Figure 45.....123

IVa - Preface: Publications and summary of the thesis

The work presented in this thesis has been carried out at the Catalonia Institute for Energy Research (IREC) in the Solar Energy Materials and Systems (SEMS) research group, located in Barcelona (Spain), during the period 2018-2021 in the framework of the research line focused on the identification of new inorganic materials based on chalcogenides for thin film photovoltaic applications. The objective of this thesis was the creation of a photovoltaic technology with potential for mass deployment in society, focused on the study and development of antimony selenide (Sb_2Se_3) absorber layer as an absorber based on non-toxic and abundant materials for thin film solar cells.

For the understanding and development of the Sb_2Se_3 technology, the work carried out was focused, firstly, on characterizing and developing specific analysis methodologies for the evaluation of the physical-chemical properties of the material, relying mainly on Raman spectroscopy. Then, a second stage focused on the development of synthesis studies of Sb_2Se_3 thin films, by means of a sequential process based on the reactive annealing under selenium atmosphere of antimony metal layers deposited by physical deposition techniques. The development of the two previous stages has allowed to finalize the study by evaluating the limitations found in the devices through the analysis of the interfaces, detected as the main source of the suboptimal performance of the devices.

During the course of the doctoral thesis, the work performed and the results obtained have allowed the publication of 7 scientific articles in high impact factor journals, relevant to the photovoltaic community. Of these 7 articles, 3 are a direct result of the work carried out and have been published in first quartile journals (Q1), and 4 are the result of collaborations.

Publications resulting from the research carried out:

P. Vidal-Fuentes, M. Guc, X. Alcobe, T. Jawhari, M. Placidi, A. Pérez-Rodríguez, E. Saucedo, V. Izquierdo-Roca, “Multiwavelength excitation Raman scattering study of Sb_2Se_3 compound: fundamental vibrational properties and secondary phases detection,” *2D Mater.*, vol. 6, no. 4, p. 045054, Sep. 2019, doi: 10.1088/2053-1583/ab4029.

Preface

IMPACT FACTOR (IF): 7.14

P. Vidal-Fuentes, M. Placidi, Y. Sánchez, I. Becerril-Romero, J. Andrade-Arvizu, Z. Jehl, A. Pérez-Rodríguez, V. Izquierdo-Roca, E. Saucedo “Efficient Se-Rich $\text{Sb}_2\text{Se}_3/\text{CdS}$ Planar Heterojunction Solar Cells by Sequential Processing: Control and Influence of Se Content,” *Sol. RRL*, p. 2000141, May 2020, doi: 10.1002/solr.202000141.

IMPACT FACTOR (IF): 8.582

P. Vidal-Fuentes, M. Guc, I. Becerril-Romero, D. Sylla, X. Alcobé, Y. Sánchez, A. Pérez-Rodríguez, E. Saucedo, V. Izquierdo-Roca, “Insights on the Thermal Stability of the Sb_2Se_3 Quasi-1D Photovoltaic Technology” *Sol. RRL*, p. 2100517, 2021, doi: 10.1002/solr.202100517.

IMPACT FACTOR (IF): 8.582

Publications resulted from collaborations:

J. Andrade-Arvizu, V. Izquierdo-Roca, I. Becerril-Romero, **P. Vidal-Fuentes**, R. Fonoll-Rubio, Y. Sánchez, M. Placidi, L. Calvo-Barrio, O. Vigil-Galán, E. Saucedo, “Is It Possible to Develop Complex S-Se Graded Band Gap Profiles in Kesterite-Based Solar Cells?,” *ACS Appl. Mater. Interfaces*, vol. 11, no. 36, 2019, doi: 10.1021/acsami.9b09813.

IMPACT FACTOR (IF): 8.758

K. J. Tiwari, M. Neuschitzer, M. Espíndola-Rodríguez, Y. Sánchez, Z. Jehl, **P. Vidal-Fuentes**, E. Saucedo, P. Malar “Efficient $\text{Sb}_2\text{Se}_3/\text{CdS}$ planar heterojunction solar cells in substrate configuration with (hk0) oriented Sb_2Se_3 thin films,” *Sol. Energy Mater. Sol. Cells*, vol. 215, no. December 2019, p. 110603, Sep. 2020, doi: 10.1016/j.solmat.2020.110603.

IMPACT FACTOR (IF): 6.984

V. Hernández-Calderón, O. Vigil-Galán, M. Guc, A. Carrillo-Osuna, S. Ramírez-Velasco, F.J. Sánchez-Rodríguez, **P. Vidal-Fuentes**, S. Giraldo, E. Saucedo, Y. Sánchez “CdS/ZnS bilayer thin films used as buffer layer in 10%-efficient $\text{Cu}_2\text{ZnSnSe}_4$ solar cells,” *ACS Appl. Energy Mater.*, p. acsaem.0c00937, Jun. 2020, doi: 10.1021/acsaem.0c00937.

IMPACT FACTOR (IF): 4.473

I. Anefnaf, S. Aazou, Y. Sánchez, **P. Vidal-Fuentes**, R. Fonoll-Rubio, K. J. Tiwari, S. Giraldo, Z. J. Li-Kao, J. Andrade-Arvizu, M. Guc, E. Saucedo, Z. Sekkat. “Insights on the Limiting Factors of Cu₂ZnGeSe₄ Based Solar Cells”. *Sol. Energy Mater. Sol. Cells*, 227, January 2021, 111106. <https://doi.org/10.1016/j.solmat.2021.111106>.

IMPACT FACTOR (IF): 6.984

The memory of the doctoral thesis has been structured by means of the three scientific articles of direct production published by Pedro Vidal Fuentes. They present the main results and conclusions of the doctoral thesis carried out and reflect the research work done in the period 2017-2021. More specifically, the report is divided into 4 chapters which are summarized in:

- Chapter 1 - Introduction: This chapter provides an introduction and brief summary of the state of the energy sector today, the role of PV technologies in this context, a review of existing technologies, their degree of maturity, advantages and disadvantages, emerging technologies and finally a description of Sb₂Se₃-based technology and its fit in the context of the energy de-carbonization roadmap.

In more detail, this chapter discusses the latest global data on the use of coal and oil, the main sources of greenhouse gas emissions, along with the growing interest and deployment of renewable energy sources. A small approximation of what the energy infrastructure should look like and what types of energy production will or should dominate the energy sector in the future. In this context the weight of photovoltaics is studied and an overview of the main relevant properties of the different materials used is given. Following the development of photovoltaic technology, including a description detailing the advantages and limitations of the current commercial and pre-industrial technological solutions, and finally, justifying the search for new emerging materials where the Sb₂Se₃ based technology is introduced. In this last part, the evolution of the technology in terms of its photovoltaic performance and its progress and relevance today will be presented. Then, the main physical properties of the Sb₂Se₃-

Preface

based technology will be summarized and compared with those of the most relevant and industrialized photovoltaic technologies. Where the most relevant are the low temperature synthesis, which allows a low cost production, in contrast to silicon technology; an optimal bandgap energy and absorption coefficient allow to further reduce the thickness and, therefore, the material usage. As for its constituent elements, it is composed of non-toxic and abundant materials, in contrast to CdTe and CIGS-based technologies. Its particular quasi one dimensional (Q-1D) strip structure gives the material benign grain boundaries, a key factor that drew attention to the photovoltaic application of the material. In the following subsection, an approach to the literature related to defects and boundaries of Sb_2Se_3 is made. While for a binary semiconductor the expected defects are low, some studies report the opposite, mainly related to anisotropy in the crystal structure. The high V_{oc} deficit is also discussed. To conclude the discussion on the Sb_2Se_3 , a short approach to different device strategies is presented. To conclude the introduction, a subsection dedicated to the fundamentals of solar cells and device operation is included, together with a summary of the basics of Raman spectroscopy. Finally, the objectives of the doctoral thesis are included.

- Chapter 2 - Methodology: this chapter presents the techniques and methodologies used during the doctoral thesis both for the synthesis of the materials and the characterization. In this chapter there is a detailed description of the equipment used, together with a brief discussion of the critical nuances for its use taking into account the peculiarities of the material. Additionally, due to the intensive use of Raman spectroscopy, a special emphasis is made in this section describing in more detail this technique and its application for the characterization of thin films.

- Chapter 3 - Summary of results through publications: in this third chapter, the main results obtained during the course of the work carried out in the development of photovoltaic technology based on Sb_2Se_3 are grouped together. The chapter is structured in a general introduction where the work carried out is contextualized, giving it cohesion and continuity, followed by the presentation of the three scientific articles published in first quartile journals:

The first article, *Multiwavelength excitation Raman scattering study of Sb_2Se_3 compound: fundamental vibrational properties and secondary phases detection*, establishes the basis of the characterization performed by XRD and Raman spectroscopy, presenting the methodologies developed for its correct evaluation and providing compression of the material by comparing the structural and chemical properties between single-crystalline Sb_2Se_3 samples and polycrystalline thin films grown on glass/molybdenum substrates. The development of this work has an important value for the community, because it allows clarifying the Raman signature of the Sb-Se system including the Sb_2Se_3 phase and the main secondary phases, and presents non-invasive and easy to implement methodologies to characterize the thin films.

For this work, a complete characterization of a single-crystal sample was performed, including all excitation wavelengths available at the time, low temperature (10 K) measurements and polarization measurements, in order to fully understand and define the vibrational modes predicted by the theoretical calculations. The results allow us to deconvolute 28 of the 30 expected Raman peaks in the system, which opens the door to using the technique as a non-destructive form of in situ structural evaluation of the devices. Direct comparison with a photovoltaic grade sample allowed us to propose a suitable wavelength for the detection of each secondary phase and, at the same time, how to characterize the Sb_2Se_3/CdS interface of a complete device without damaging it.

The second article, *Efficient Se-Rich Sb_2Se_3/CdS Planar Heterojunction Solar Cells by Sequential Processing: Control and influence of Se content*, is based on the optimization of the reactive annealing under selenium atmosphere of an antimony metal layer to obtain functional photovoltaic devices based on the SLG/Mo/ $Sb_2Se_3/CdS/ITO$ structure. In this work, the impact of the annealing temperature with the selenium/antimony ratio of the synthesized layer is identified. Through this result it is proposed as a suitable method to control the composition of the material opening the possibility of easily modifying the composition of the Sb_2Se_3 absorber layer, being this, in the current state of the art, one of the key factors for the optimization of the conductivity and control of the p-type doping of the Sb_2Se_3 system.

Preface

The work demonstrates how the increase of selenium pressure during the absorber synthesis has beneficial effects on the electrical properties of the material, reflected in an increase of the parallel resistance of the devices. The analysis of these results suggests that this beneficial effect for the device is related to a passivation effect between the 1D structures of the material or at the grain boundaries. Finally, it is shown how the optimization of the processes, realized through the conclusions of the work, allows to implement an optimized photovoltaic device which yields a PCE = 5.7 %.

The third article, *Insights on the Thermal Stability of the Sb₂Se₃ Q1D Photovoltaic Technology*, presents detailed work on the thermal stability of devices based on the Sb₂Se₃/CdS structure with efficiencies >5% synthesized using the optimized conditions identified in the second paper. The Raman and XRD methodologies developed in the first article are used for this work.

The results obtained show a strong impact at low temperatures (< 150 °C) on the devices with P/N structure based on Sb₂Se₃/CdS heterojunctions. The detailed study allows to observe how the devices present a degradation of the junction due to the Se diffusion which promotes the formation of a CdS_{1-x}Se_x solid solution at the CdS/Sb₂Se₃ interface reaching selenium amounts of the order of 40 % with increasing temperature, the selenium impoverishment of Sb₂Se₃ and the final decomposition of the material into secondary phases (α -Sb₂O₃ and Se). The obtained results have led to the elaboration of a hypothesis of the migration of the selenium constituent out of the Sb₂Se₃ crystal structure, first generating defect compensation (V_{Se} and $2Se_{Sb}$) and thus reducing the crystal lattice parameters, followed by diffusion inside the CdS for the formation of the Cd(S,Se) solid solution and the promotion of Se and Sb-O secondary phases.

To sum up the Thesis, the conclusions of the work carried out are gathered in a final section, analyzing the degree of completeness of the objectives obtained and placing them in the context of the bibliography.

IVb - Prefacio: Publicaciones y resumen de la tesis

El trabajo presentado en esta tesis se ha realizado en el Instituto de Investigación en Energía de Cataluña (IREC) en el grupo de investigación de Materiales y Sistemas de Energía Solar (SEMS), ubicado en Barcelona (España), durante el periodo 2018-2021 en el marco de la línea de investigación centrada en la identificación de nuevos materiales inorgánicos basados en calcogenuros para aplicaciones fotovoltaicas de capa delgada. El objetivo de esta tesis fue la creación una tecnología fotovoltaica con potencial de implantación masiva en la sociedad, centrada en el estudio y desarrollo de la capa absorbente de seleniuro de antimonio (Sb_2Se_3) como absorbedor basado en materiales no tóxicos y abundantes para células solares de capa fina.

Para la comprensión y desarrollo de la tecnología de Sb_2Se_3 el trabajo realizado se centró, en primer lugar, en caracterizar y desarrollar metodologías de análisis específicas para la evaluación de las propiedades físico químicas del material, apoyándose principalmente en la espectroscopia Raman. A continuación, se llevó a cabo una segunda etapa centrada en el desarrollo de estudios de síntesis de capas delgadas de Sb_2Se_3 , mediante un proceso secuencial basado en el recocido reactivo bajo atmósfera de selenio de capas metálicas de antimonio depositadas por técnicas de depósito físicas. El desarrollo de las dos etapas anteriores ha permitido finalizar el estudio evaluando las limitaciones encontradas en los dispositivos mediante el análisis de las interfaces, detectadas como principal fuente del funcionamiento sub óptimo de los dispositivos.

Durante el trascurso de la tesis doctoral, el trabajo realizado y los resultados obtenidos han permitido la publicación de 7 artículos científicos en revistas de alto índice de impacto y relevantes para la comunidad fotovoltaica. De estos 7 artículos 3 son producto directo del trabajo realizado y se han publicado en revista del primer cuartil (Q1), y 4 son resultado de colaboraciones.

Publicaciones resultado de la investigación realizada:

P. Vidal-Fuentes, M. Guc, X. Alcobé, T. Jawhari, M. Placidi, A. Pérez-Rodríguez, E. Saucedo, V. Izquierdo-Roca, “Multiwavelength excitation Raman scattering study of Sb_2Se_3 compound: fundamental vibrational properties and secondary phases detection,” *2D Mater.*, vol. 6, no. 4, p. 045054, Sep. 2019, doi: 10.1088/2053-1583/ab4029.

IMPACT FACTOR (IF): 7.14

P. Vidal-Fuentes, M. Placidi, Y. Sánchez, I. Becerril-Romero, J. Andrade-Arvizu, Z. Jehl, A. Pérez-Rodríguez, V. Izquierdo-Roca, E. Saucedo, “Efficient Se-Rich $\text{Sb}_2\text{Se}_3/\text{CdS}$ Planar Heterojunction Solar Cells by Sequential Processing: Control and Influence of Se Content,” *Sol. RRL*, p. 2000141, May 2020, doi: 10.1002/solr.202000141.

IMPACT FACTOR (IF): 8.582

P. Vidal-Fuentes, M. Guc, I. Becerril-Romero, D. Sylla, X. Alcobé, Y. Sánchez, A. Pérez-Rodríguez, E. Saucedo, V. Izquierdo-Roca, “Insights on the Thermal Stability of the Sb_2Se_3 Quasi-1D Photovoltaic Technology” *Sol. RRL*, p. 2100517, 2021, doi: 10.1002/solr.202100517.

IMPACT FACTOR (IF): 8.582

Publicaciones como resultado de colaboraciones:

J. Andrade-Arvizu, V. Izquierdo-Roca, I. Becerril-Romero, **P. Vidal-Fuentes**, R. Fonoll-Rubio, Y. Sánchez, M. Placidi, L. Calvo-Barrio, O. Vigil-Galán, E. Saucedo, “Is It Possible to Develop Complex S-Se Graded Band Gap Profiles in Kesterite-Based Solar Cells?,” *ACS Appl. Mater. Interfaces*, vol. 11, no. 36, 2019, doi: 10.1021/acsami.9b09813.

IMPACT FACTOR (IF): 8.758

K. J. Tiwari, M. Neuschitzer, M. Espíndola-Rodríguez, Y. Sánchez, Z. Jehl, **P. Vidal-Fuentes**, E. Saucedo, P. Malar, “Efficient $\text{Sb}_2\text{Se}_3/\text{CdS}$ planar heterojunction solar cells in substrate configuration with (hk0) oriented Sb_2Se_3 thin films,” *Sol. Energy Mater. Sol. Cells*, vol. 215, no. December 2019, p. 110603, Sep. 2020, doi: 10.1016/j.solmat.2020.110603.

IMPACT FACTOR (IF): 6.984

V. Hernández-Calderón, O. Vigil-Galán, M. Guc, A. Carrillo-Osuna, S. Ramírez-Velasco, F.J. Sánchez-Rodríguez, **P. Vidal-Fuentes**, S. Giraldo, E. Saucedo, Y. Sánchez, “CdS/ZnS bilayer thin films used as buffer layer in 10%-efficient Cu₂ZnSnSe₄ solar cells,” *ACS Appl. Energy Mater.*, p. acsaem.0c00937, Jun. 2020, doi: 10.1021/acsaem.0c00937.

IMPACT FACTOR (IF): 4.473

I. Anefnaf, S. Aazou, Y. Sánchez, **P. Vidal-Fuentes**, R. Fonoll-Rubio, K. J. Tiwari, S. Giraldo, Z. J. Li-Kao, J. Andrade-Arvizu, M. Guc, E. Saucedo, Z. Sekkat, “Insights on the Limiting Factors of Cu₂ZnGeSe₄ Based Solar Cells”. *Sol. Energy Mater. Sol. Cells*, 227, January 2021, 111106. <https://doi.org/10.1016/j.solmat.2021.111106>.

IMPACT FACTOR (IF): 6.984

La memoria de la tesis doctoral se ha estructurado mediante los tres artículos científicos de producción directa publicados por Pedro Vidal Fuentes. En ellos se presentan los principales resultados y conclusiones de la tesis doctoral realizada y reflejan el trabajo de investigación realizado en el periodo 2017-2021. Más concretamente la memoria se divide en 4 capítulos los cuales se resumen en:

- Capítulo 1 - Introducción: En este capítulo se presenta una introducción y breve resumen del estado del sector energético en la actualidad, el papel de las tecnologías fotovoltaicas en este contexto, una revisión de las tecnologías existentes, su grado de madurez, ventajas y desventajas, las tecnologías emergentes y finalmente una descripción de la tecnología basadas en Sb₂Se₃ y su encaje en el contexto de la hoja de ruta de la des-carbonización de la energía.

Más detalladamente, en este capítulo se analizan los últimos datos globales sobre el uso del carbón y el petróleo, principales fuentes de emisión de gases de efecto invernadero, junto con el creciente interés y despliegue de las fuentes de energía renovables. Una pequeña aproximación a cómo debería ser la infraestructura energética y qué

tipos de producción energética dominarán o deberían dominar el sector energético en el futuro. En este contexto se estudia el peso de la energía fotovoltaica y se ofrece una visión general de las principales propiedades relevantes de los diferentes materiales empleados. Siguiendo el desarrollo de la tecnología fotovoltaica, incluyendo una descripción detallando las ventajas y limitaciones de las actuales soluciones tecnológicas comerciales y pre-industriales, y finalmente, justificando la búsqueda de nuevos materiales emergentes donde se introduce la tecnología basada en Sb_2Se_3 . En esta última parte se presentará la evolución de la tecnología en cuanto a su rendimiento fotovoltaico y su progreso y relevancia en la actualidad. A continuación, se resumen las principales propiedades físicas de la tecnología basada en Sb_2Se_3 y se compararan con las de las tecnologías fotovoltaicas más relevantes e industrializadas. Donde las más relevantes son la síntesis a baja temperatura, que permite una producción de bajo coste, en contraste con la tecnología del silicio; una energía de banda prohibida y coeficiente de absorción óptimos permiten reducir aún más el espesor y, por tanto, el uso de material. En cuanto a sus elementos constitutivos, está compuesto por materiales no tóxicos y abundantes, en contraste con las tecnologías basadas en CdTe y CIGS. Su particular estructura cuasi-unidimensional (Q-1D) en tiras, confiere al material unas fronteras de grano benignas, factor clave que hizo llamar la atención sobre la aplicación fotovoltaica del material. En la siguiente subsección se realiza una aproximación a la bibliografía relacionada con los defectos y límites del Sb_2Se_3 . Mientras que para un semiconductor binario los defectos esperados son bajos, algunos estudios informan de lo contrario, principalmente relacionado con la anisotropía en la estructura cristalina. Se analiza además el elevado déficit de V_{oc} . Para finalizar la discusión sobre el Sb_2Se_3 , se presenta una pequeña aproximación a diferentes estrategias de dispositivos. Para terminar la introducción, se incluye una subsección dedicada a los fundamentos de las células solares y el funcionamiento de los dispositivos, junto con un resumen de las bases de la espectroscopia Raman. Finalmente se incluyen los objetivos de la tesis doctoral.

- Capítulo 2 - Metodología: en este capítulo se presentan las técnicas y metodologías utilizadas durante la tesis doctoral tanto para la síntesis de los materiales como en la caracterización. En este capítulo

se realiza una descripción detallada de los equipos utilizados junto una breve discusión de los matices críticos para su utilización teniendo en cuenta las peculiaridades del material. Adicionalmente debido a al uso intensivo de la espectroscopia Raman, en esta sección se hace un especial énfasis describiendo con más detalle esta técnica y su aplicación para la caracterización de capas delgadas.

- Capítulo 3 – Compendio de los resultados mediante publicaciones: en este tercer capítulo, se agrupan los principales resultados obtenidos durante el transcurso del trabajo realizado en el desarrollo de la tecnología fotovoltaica basada en Sb_2Se_3 . El capítulo se estructura en una introducción general donde se contextualiza el conjunto del trabajo realizado dándole cohesión y continuidad, seguido de la presentación de los tres artículos científicos publicados en revistas de primer cuartil:

El primer artículo, *Multiwavelength excitation Raman scattering study of Sb_2Se_3 compound: fundamental vibrational properties and secondary phases detection*, establece las bases de la caracterización realizada mediante XRD y espectroscopia Raman, presentando las metodologías desarrolladas para su correcta evaluación y aportando comprensión del material mediante la comparación de las propiedades estructurales y químicas entre muestras monocristalinas de Sb_2Se_3 y capas delgadas poli-cristalinas crecidas sobre sustratos de vidrio/molibdeno. El desarrollo de este trabajo tiene un valor importante para la comunidad, debido a que permite clarificar la firma Raman del sistema Sb-Se incluyendo la fase Sb_2Se_3 y las principales fases secundarias, y presenta metodologías no invasivas y de fácil implementación para caracterizar las capas delgadas.

Para la realización de este trabajo se realizó una caracterización completa de una muestra monocristalina, incluyendo todas las longitudes de onda de excitación disponibles en ese momento, mediciones a baja temperatura (10 K) y mediciones con polarización, con el fin de comprender y definir completamente los modos vibracionales predichos por los cálculos teóricos. Los resultados nos permiten deconvolucionar 28 de los 30 picos Raman esperados en el sistema, lo que abre la puerta a utilizar la técnica como una forma no destructiva de evaluación estructural in situ de los dispositivos. La

comparación directa con una muestra de grado fotovoltaico permitió proponer una longitud de onda adecuada para la detección de cada fase secundaria y, al mismo tiempo, la forma de caracterizar la interfaz $\text{Sb}_2\text{Se}_3/\text{CdS}$ de un dispositivo completo sin dañarlo.

El segundo artículo, *Efficient Se-Rich $\text{Sb}_2\text{Se}_3/\text{CdS}$ Planar Heterojunction Solar Cells by Sequential Processing: Control and influence of Se content*, se basa en la optimización del recocido reactivo bajo atmósfera de selenio de una capa metálica de antimonio para la obtención de dispositivos fotovoltaicos funcionales basados en la estructura SLG/Mo/ $\text{Sb}_2\text{Se}_3/\text{CdS}/\text{ITO}$. En este trabajo se identifica el impacto de la temperatura de recocido con la relación selenio/antimonio de la capa sintetizada. Mediante este resultado se propone como un método adecuado para controlar la composición del material abriendo la posibilidad de modificar fácilmente la composición de la capa absorbente de Sb_2Se_3 , siendo este, en el estado actual de la tecnología, uno de los factores clave para la optimización de la conductividad, y control del dopado tipo p del sistema Sb_2Se_3 .

El trabajo permite demostrar como el aumento de la presión de selenio durante la síntesis del absorbedor presenta unos efectos beneficiosos en las propiedades eléctricas del material, reflejadas en un aumento de la resistencia en paralelo de los dispositivos. El análisis de estos resultados apunta a que este efecto beneficioso para el dispositivo está relacionado con un efecto de pasivación entre las estructuras 1D del material o en las fronteras de grano. Finalmente se muestra como la optimización de los procesos, realizada mediante las conclusiones del trabajo, permite implementar un dispositivo fotovoltaico optimizado con un rendimiento de $PCE = 5.7\%$.

En el tercer artículo, *Insights on the Thermal Stability of the Sb_2Se_3 Q1D Photovoltaic Technology*, se presenta un detallado trabajo sobre la estabilidad térmica de los dispositivos basados en la estructura $\text{Sb}_2\text{Se}_3/\text{CdS}$ con eficiencias del $> 5\%$ sintetizados mediante las condiciones optimizadas identificadas en el segundo artículo. Para este trabajo se utilizan las metodologías Raman y XRD desarrolladas en el primer artículo.

Los resultados obtenidos muestran un fuerte impacto a bajas temperaturas ($< 150\text{ }^{\circ}\text{C}$) en los dispositivos con estructura P/N basadas en heterouniones $\text{Sb}_2\text{Se}_3/\text{CdS}$. El estudio detallado permite observar como los dispositivos presentan una degradación de la unión debido a la difusión del Se, la cual promueve la formación de una solución sólida $\text{CdS}_{1-x}\text{Se}_x$ en la interfaz $\text{CdS}/\text{Sb}_2\text{Se}_3$ alcanzando cantidades de selenio del orden del 40 % con el aumento de la temperatura, el empobrecimiento en selenio del Sb_2Se_3 y la final la descomposición del material en fases secundarias ($\alpha\text{-Sb}_2\text{O}_3$ y Se). Los resultados obtenidos han dado lugar a la elaboración de una hipótesis de la migración del selenio constituyente fuera de la estructura cristalina del Sb_2Se_3 , primero generando la compensación de defectos (V_{Se} y 2Se_{Sb}) y reduciendo así los parámetros de la red cristalina, seguida de la difusión dentro del CdS para la formación de la solución sólida $\text{Cd}(\text{S},\text{Se})$ y la promoción de fases secundarias Se y Sb-O.

Para finalizar la Tesis se añan en una sección final las conclusiones del trabajo realizado, analizando el grado de completitud de los objetivos obtenidos y poniéndolos en el contexto de la bibliografía.

V - Contribution of the author to publications in the thesis

P. Vidal-Fuentes, M. Guc, X. Alcobe, T. Jawhari, M. Placidi, A. Pérez-Rodríguez, E. Saucedo, V. Izquierdo-Roca, “Multiwavelength excitation Raman scattering study of Sb₂Se₃ compound: fundamental vibrational properties and secondary phases detection” *2D Mater.*, vol. 6, no. 4, p. 045054, Sep. 2019, doi: 10.1088/2053-1583/ab4029. IMPACT FACTOR (IF): 7.14

In this work Pedro Vidal Fuentes performed the synthesis of the layers present in the samples object of the study (with exception of the CdS layer), including the molybdenum metallic back contact, the Sb₂Se₃ absorber, and the front contact layer of i-ZnO/ITO. Raman measurements were performed by him with the available systems at IREC facilities, including the measurements with $\lambda_{ex} = 325, 442, 532, 632$ and 785 nm, while measurements under $\lambda_{ex} = 1064$ nm were performed by him at the University of Barcelona. He also performed the low temperature (10 K) measurements under $\lambda_{ex} = 532$ nm. Pedro Vidal-Fuentes also performed the analysis of the experimental data, participate in the results discussion, and the redaction of the manuscript.

P. Vidal-Fuentes, M. Placidi, Y. Sánchez, I. Becerril-Romero, J. Andrade-Arvizu, Z. Jehl, A. Pérez-Rodríguez, V. Izquierdo-Roca, E. Saucedo “Efficient Se-Rich Sb₂Se₃ /CdS Planar Heterojunction Solar Cells by Sequential Processing: Control and Influence of Se Content,” *Sol. RRL*, p. 2000141, May 2020, doi: 10.1002/solr.202000141. IMPACT FACTOR (IF): 8.582

In this work Pedro Vidal Fuentes was responsible for the synthesis of all the layers present in the samples object of the study (with exception of the CdS layer), including the molybdenum metallic back contact, the Sb₂Se₃ absorber layer and the modifications presented in the article, and the front contact layer of i-ZnO/ITO. He was also responsible for the characterization and analysis of the devices including structural (XRF, FE-SEM, XRD and Raman spectroscopy) and electrical

Contribution of the author to publications in the thesis

characterization of J - V and C - V characteristics, EQE (with and without bias voltage), reflectance and V_{oc} - T measurements. He performed the analysis of the experimental data, discussion of the results, and manuscript redaction.

P. Vidal-Fuentes, M. Guc, I. Becerril-Romero, D. Sylla, X. Alcobé, Y. Sánchez, A. Pérez-Rodríguez, E. Saucedo, V. Izquierdo-Roca, “Insights on the Thermal Stability of the Sb_2Se_3 Quasi-1D Photovoltaic Technology *Sol. RRL*, p. 2100517, 2021, doi: 10.1002/solr.202100517. IMPACT FACTOR (IF): 8.582

In this work Pedro Vidal Fuentes was responsible for the synthesis of all the layers present in the samples object of the study (with exception of the CdS layer), including the molybdenum metallic back contact, the Sb_2Se_3 absorber layer and the modifications presented in the article, and the front contact layer of i-ZnO/ITO. He was also responsible for the characterization and analysis of the devices including structural (XRF, Raman spectroscopy) and electrical characterization of J - V and C - V characteristics. He performed the analysis of the experimental data, discussion of the results, and manuscript redaction.

1 - Chapter 1: Introduction

1.1 – Socio-economical context

Energy production and consumption are defining and decisive factors of the society, aside from the social contract and labour relations. The civilization itself evolves dramatically with the discovery of new energy source or way to exploit it (flow, storage, conversion). Interestingly enough, some environmental historians divide energy harvesting in two big epochs. First solar era (origins - 1800 AD) era were humans use mainly solar energy to cultivate and harvest, including early farming communities to late agrarian ages. A Second era of Industrial revolution, that includes from the begins of coal usage, deriving in petroleum-oil and natural gas to Nuclear power and renewable energy.¹ Thermodynamically speaking, all complex life forms on earth are a consequence to the temperature differential between the Sun and the Earth, and we are just exploring the best ways to harvest and employ this energy. At the end, we are just pursuing our catharsis with the Sun.

Electricity generation by source, OECD, 1990-2019

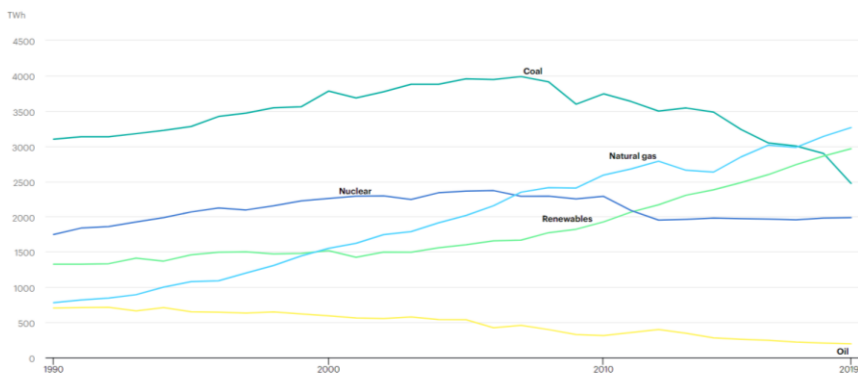


Figure 1: Electricity generation by source in the OECD, extracted from IEA database.²

We are currently living what it seems to be the end of fossil-fuel era (Figure 1),² but not because a lack of production or supply, instead the

1 - Introduction

extraction (or refining) cost are being the main limiting factors.³ Letting aside the point of a finite resource of energy, which will someday expire, not being a clever strategy for the prolongation of the Human society. This forms of dependences with limited fuel sources should and must be eliminated. The amount of available total proved Oil reserves went from $1735.9 \cdot 10^9$ barrels at 2018 to a stagnation at $1733.9 \cdot 10^9$ barrels at the end of 2019, this values are registers of available oil that could be extracted with current engineering level and actual operating costs.⁴ Regarding coal, with a share of 38.3 % was the primary source of power generation in the world in 2019, with total reserves of 1069 Gt.⁵ This represents a problem as it is the primary source of CO₂ emissions, and the current worldwide policies seem not to be handling its substitution, with expectations of remaining at the same levels of demand for the next decades (Figure 2).⁶

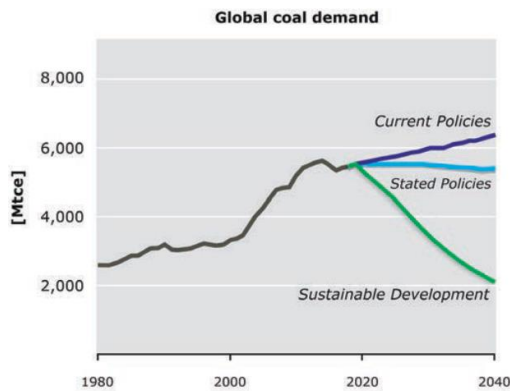


Figure 2: Global coal demand in the present, and future prospect conditional to the policies applied in the future. Data from IEA.⁶

Aside from fossil-fuels, the same kind of limitation stands for fission energy production. The Uranium reservoirs are estimated at 12.5 Mt.⁷ Nevertheless it is still highly recognized as an stable energy source to couple with a mix of renewable energies to mitigate CO₂ emissions in the short to mid term, towards a future in which renewable energy is enough to sustain growth (inherently needed in the actual socio-economic system).⁸ Thorium reactors (nuclear fission based technology, with potentially higher sustainability and safety compared to Uranium-based fission) were discarded in the past in comparison to

the efficiency produced by Uranium counterparts, however could be a promising future for nuclear energy,⁹ in part driven by the possibility to adapt old Uranium reactors to the Thorium cycle, and to further reduce nuclear waste to storage times of ~100 years, becoming a technology bridge between the fossil-fuels era to new renewable based era.^{10,11}

Regarding the main energy source for brute production, future seems to be dominated, at least ideally, by fusion reactors. In this context, the scientific community is doing a hard effort worldwide and across frontiers, to give rise to the first fusion reactor, mainly dominated by the ITER project, based on a Tokamak reactor.^{12,13} Although the problem of specific fuel usage is and will be a critical point, specifically concerning tritium (3.5 kg total in Earth).¹⁴

Nevertheless, while there is already proven a reduction in cost of the photovoltaics, and a renewable mix for substitute fossil fuels is possible,¹⁵ some authors even propose that renewable energy alone (plus hydrothermal and hydroelectric) could perfectly handle the world energy demand.¹⁶⁻¹⁸ This is of course not assuming the challenges and nuances of an electrical grid that could handle such an intermittent production of energy, and most importantly energy storage.¹⁹ Huge political efforts are starting to be made regarding world or at least intercountry high voltage energy grid interconnections, in order to reduce transport costs, and possibly could be applied to avoid some of the fluctuations present in renewable energies. This plans are inherently positive, politically and energetically, as the solar power could be normalised if several time-zones are interconnected.²⁰ But so far, the only possible short time solution to green-house emissions is still a balance between firm energy production with natural gas, fission, and renewable sources.¹⁹ This is a naive comparison between the potential of the solar energy with the classical brute energy production, but in reality, the power of this technology lies further away. The easiness of adaptation of the PV technology to a plethora of applications such as building integration (BIPV),^{21,22} powering up sensors,²³ internet of things (IOT)²⁴ and autonomous systems,²⁵ this is, where small scale, delocalized and easy to implement energy

1 - Introduction

production is needed is the most promising aspect of the PV technology.

Even more, at present times, the evolution of the electrical share of renewable energies, including solar, wind and hydro power, is expected to increase by 5 % at the end of 2020, being the most reliable source of energy during Covid-19 lockdown. This is mainly driven by an increase of 100 GW of solar PV, due to the end of several installation projects in 2019 achieving a total share of 28 % in Q1 2020, and a cumulative installation capacity of 600 GW in 2019 with conservative predictions of 750 GW in 2020 (Figure 3).^{26,27} Where the International Energy Agency (IEA) forecast an addition of around 530 GW in the period between 2019-2024, which will consist on an increment of 250% during that time window (Figure 4), although as it is pointed before, the expectation is that the major growth may be on the off-grid applications.²⁸ The resilience that this technology shows in crisis periods is mostly due to their passive nature (as an example no fuel has to be transported) and once installed, the maintenance can be mostly autonomous.

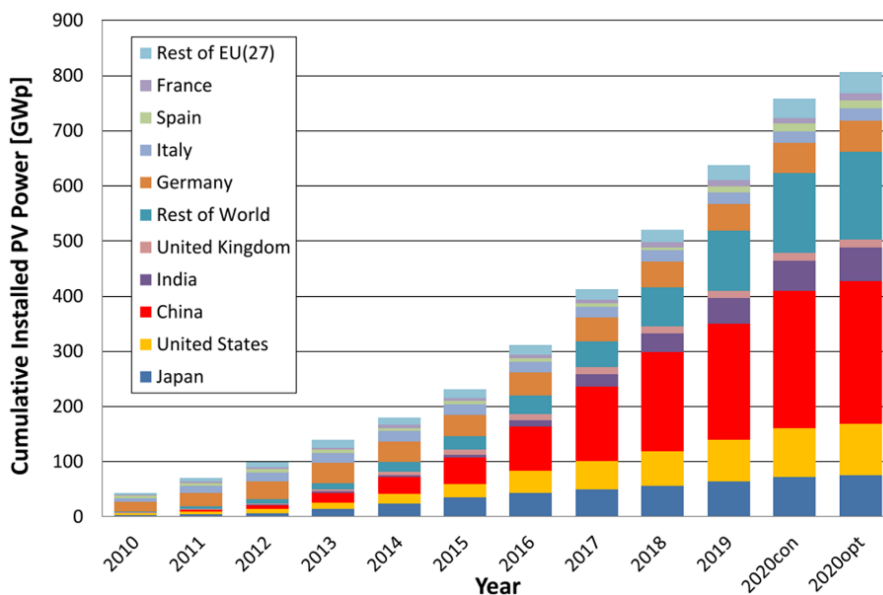


Figure 3: Cumulative photovoltaic installations from 2010 to 2019 plus conservative and optimistic scenarios for 2020. Extracted from ref.²⁷

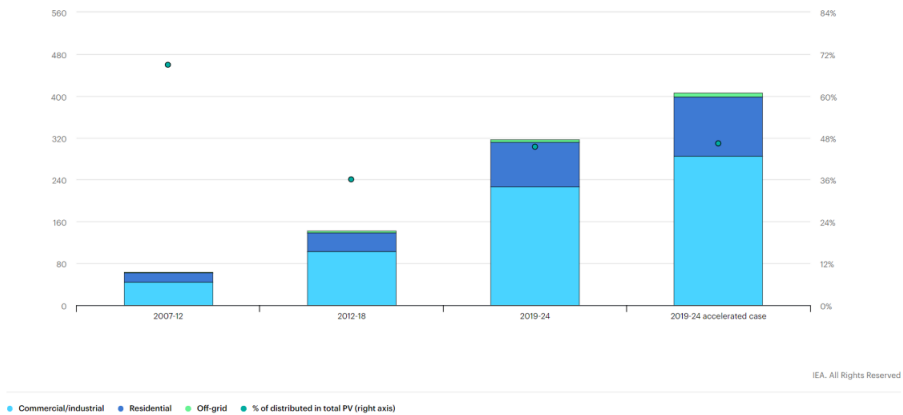


Figure 4: Distributed PV capacity growth by segment, 2007-2024, source IEA.²⁸

With all the previous data in hand, the evidence indicates that, at least to gratify the current standard of living, assuming no socio-economic system change, if the society follows a never ending growth process, the technology development should match this growth.²⁹ The requirement of maintaining this energy production that cannot be sustained by technologies based on fossil fuels, where nuclear fusion-based technologies are still in viability demonstration stage and cannot be integrated in spread energy structures, point towards the necessity of a paradigm change. Within this framework, the possibility of disengagement of renewable energies is a key factor for the stability of the society.

1.2 - PV state of the art

At this point we have to tackle the evolution of the PV technologies, to be able to speak outside the point of view of the energy sector and macro-values of energies, and focus in explicit examples of operating systems, from the already commercial materials to state-of-the-art research level solutions, where the main driving factors of a future proof energy production are found. In this Thesis the focal point is placed on inorganic materials, as the technology that is nowadays leader in terms of industrialization, mostly regarding its inherent stability. In addition, it will not be taken into account GaAs solar cells as this technology, although really close to its maximum potential, has a dramatic cost, only assumable for really specific tasks such as space applications, and thus making it unsuitable for mass deployment.

The first steps of the PV technology were made with a solid state photocell device with photo-generation efficiency of 1 % invented by Charles E. Fritts in 1883, it was based on selenium as the absorber material sandwiched between a copper and gold contacts.³⁰ This research was published 22 years before the theoretical explanation by Albert Einstein of the photoelectric effect in 1905.³¹ While the first silicon cell was developed by Daryl Chapin, et al. in the Bells laboratories in the 1954 achieving a 4 % power conversion efficiency (PCE),³² and thus starting the dominance of this technology in the future years, reaching production values of ~143 GW in 2020 spread across multi-Si and mono-Si (Figure 5).³³

1 - Introduction

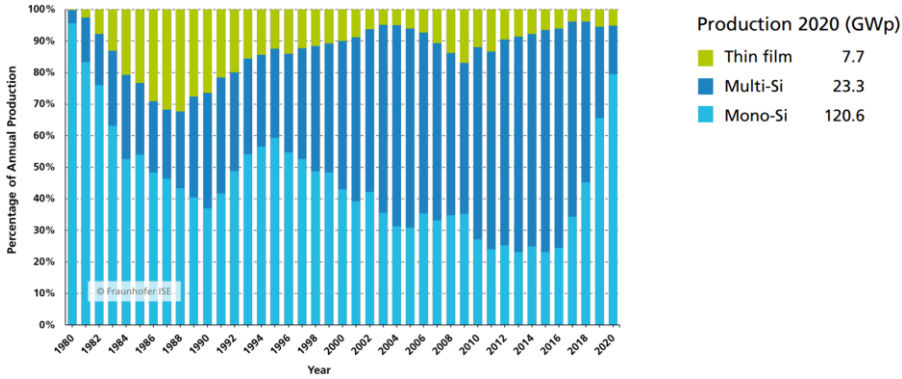


Figure 5: Percentage of global annual production per silicon PV technology. Extracted from ref.³³

Silicon

Silicon has a main advantage, it is not a critical raw material (CRM) it is refined from SiO_2 , basically sand. The production cost is then not coming from the raw material, but from the refining procedure. Metallurgical grade silicon needs to reach around 98 % of purity (1800 °C required) while photovoltaic grade silicon needs to reach standards of 7N (99.99999 %) to have a low degree of impurities that alter the electrical properties of the material. The main synthesis procedure is the Czochralski method, in which a monocrystalline cylinder is casted from a spinning needle inserted in melting silicon at 1425 °C, and subsequently cut in sections or wafers.³⁴ This material, is widely employed in all kinds of electronics, due to the high level of know-how, allowing for a competitive production with low costs even if the synthesis procedure is highly energy intensive. It is, without any doubt, the standard of PV industry to beat.

Silicon presents close to optimal properties for a PV absorber material including near optimal bandgap energy ($E_g = 1.12 \text{ eV}$),³⁵ and very good stability. The main drawback is its indirect bandgap, that implies a low absorption coefficient (α),³⁶ and thus require more material for the photons to interact and generate electron-hole pairs. As a consequence, the minimum thickness a monocrystalline or poly-crystalline silicon technology has achieved is in the range of $\sim 100 \mu\text{m}$ even with the

implementation of anti-reflective coatings and back reflectors. This thickness imposes another fundamental limitation to the maximum achievable *PCE*, where from the Shockley Queisser efficiency limit (SQ limit, where the bandgap value and black body radiation from the sun are taken into account) a potential 33.9 % power conversion efficiency is calculated, if the thickness is taken into consideration the long radiative recombination lifetimes implies an unavoidable contribution of Auger recombination which further limits the *PCE* to a theoretical 29 %.^{35,37,38}

Two main crystalline silicon technologies exist: crystalline silicon (c-Si) and polycrystalline silicon (p-Si). The first one has reached *PCEs* of around 26.3 %, with the employment of a really sophisticated structure HJ-IBC (hetero-junction interdigitated back contact) Figure 6.³⁹

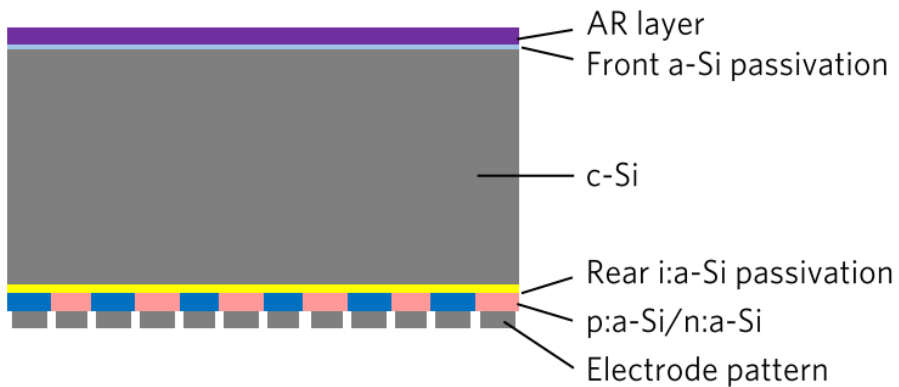


Figure 6: Schematics of a high efficiency silicon HJ-IBC cell Reprinted by permission from Springer Nature: Publisher Nature, *Nature Energy*: Yoshikawa, K. et al., *Silicon Heterojunction Solar Cell with Interdigitated Back Contacts for a Photoconversion Efficiency over 26%*. *Nat. Energy* 2017, 2 (5), 17032. <https://doi.org/10.1038/nenergy.2017.32>, ©(2017).³⁹

This PV technology is near to its SQ limit and the material optimization seems to be close to an end (at laboratory scale). As we depicted before, the high energy cost of purification and the loss of material in the wafer cutting process comprises around 50 % of the total price.⁴⁰ Even if the cost is low nowadays, lower than 0.30 \$/W, due to the highly developed industry surrounding it, the amount of material employed, the lack of flexibility of the technology that difficult its integration in

1 - Introduction

different applications/conditions (mechanical rigidity, high weight, low shape customizability, impossibility to modify the bandgap, etc...), and the indirect nature of the bandgap that force the high thickness are the driving forces towards next generation photovoltaics.

Second generation photovoltaics are defined as thin film photovoltaics, the main driving factor of these technologies is to overcome the Silicon limitations, and thus expand the framework of the PV industry by enabling the possibility of lower material usage. The main technologies in the thin film categories include: amorphous silicon, CIGS and CdTe. These technologies are defined by very high absorption coefficients ($\alpha > 10^4 \text{ cm}^{-1}$) which permits the reduction of its thickness to the order of 1 μm . The smaller width allows these technologies to widen the range of applications of PV by the possibility of flexible substrates (eg, portable electronics, BIPV, space applications, automotive industry, etc, and most importantly for their industrialization to allow roll-to roll process.^{21,41-46}

a-Si

Amorphous silicon came to the market due to the beneficial high throughput and large area process employed for its fabrication, combined with low cost and earth abundant elements. It is normally seen, since a long time ago, on small self-powered electronics like watches and calculators in late eighties. The main advantages over crystalline silicon are that, when in amorphous state, the nature of the bandgap of the material shifts to direct, enabling a more efficient collection of photons, also accompanied with an energy shift to $E_g = 1.7 \text{ eV}$.⁴⁷ An amorphous material has, as expected, a huge drawback due to the high amount of dangling bonds present in the structure, the recombination of the carriers and thus minority carrier diffusion length gets heavily deteriorated. This was solved by a process called hydrogen passivation, that propel the efficiency to 8.04 % (a-Si:H).^{48,49} After the stabilisation by hydrogenation, the evolution of the PCE was driven by adopting tandem structures mainly consisting in a-Si:H/a-SiGe:H/ $\mu\text{C-Si:H}$ structures reaching 13.4 %, ⁵⁰ and a-Si/ $\mu\text{C-Si:H}$ / $\mu\text{C-Si:H}$ with

13.6 % efficiency by the introduction of textured honey-comb substrates.⁵¹

The technique employed for obtaining the best performing devices is plasma-enhanced chemical vapour deposition (PECVD).⁵² This technique is employed to synthesize thin films from chemicals in gas state, where the chemical reaction between the gas molecules starts when the free electrons in the plasma, generated by means of DC or AC current, dissociate the precursor molecules generating free radicals that finally react in the substrate.

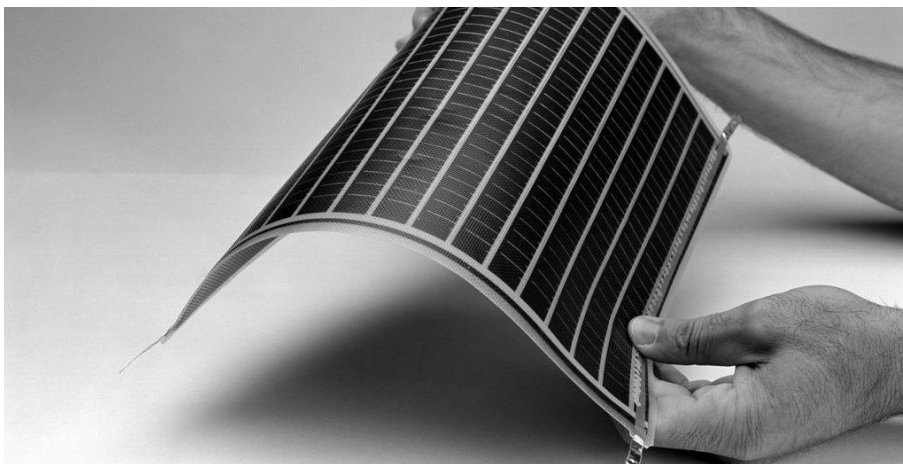


Figure 7: Example of an a-Si flexible module.

CdTe

Regarding the material properties of the CdTe, it belongs to the II-VI semiconductor family among CdS ($E_g = 2.4$ eV),⁵³ and CdSe ($E_g = 1.7$ eV),⁵⁴ it presents a very high absorption coefficient, a direct band gap energy of $E_g = 1.48$ eV.⁵⁵

Cadmium telluride thin film solar cells were the first thin film solar cells ever fabricated with a very promising efficiency of 6 % in 1972 by Bonnet et al.⁵⁶ The structure consisted in a p-type CdTe absorber layer plus a n-type CdS. The synthesis procedure of these samples already consisted in a high quality single crystalline CdTe growth by

1 - Introduction

the Bridgman method, onto which the CdS buffer layer was deposited by thermal evaporation.⁵⁶

Several techniques were employed for the fabrication of CdTe films but the most employed and promising is the close-space sublimation (CSS), this technique allows for low vacuum and low temperature process (Figure 8).⁵⁷⁻⁵⁹ Consisting on the evaporation of a CdTe source close (2-3 mm) to the substrate were its going to be deposited, with a high temperature gradient generated by halogen lamps at both sides (source and substrate), this technique is suitable because CdTe evaporate and sublime in the correct stoichiometry.

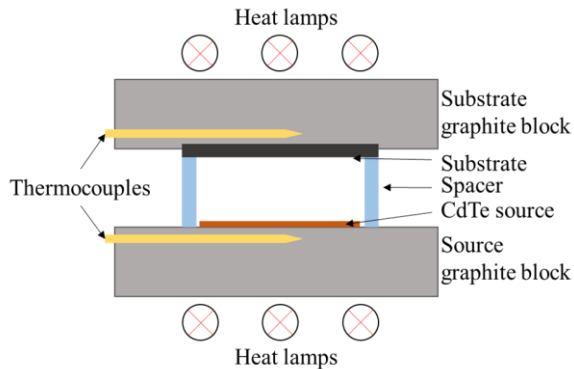


Figure 8: Schematics of a close space sublimation (CSS) technique employed for the fabrication of superstrate CdTe thin film solar cells.

One of the key steps for device efficiency improvement was the inclusion of a CdCl₂ treatment by thermal evaporation and reactive annealing or directly dipping in a solution, although the latter not being suitable for large scale applications, this treatment allow to surpass the efficiency barrier of 16 % improving the grain size, achieving a high degree of boundary passivation and thus improving PL-yield and carrier lifetimes.^{57,60} The technology *PCE* increase has been led by private research from First Solar since 18.7 % to nowadays 22.1 % *PCE*'s.⁶¹

The main limitation to the future deploy of this technology is its constituent elements, the cadmium and tellurium. The former is a highly toxic element, while the CdTe compound present low toxicity, high stability and low solubility in water, the induced decomposition

by fire or not correct recycling process limit strongly they integration in several niches (BIPV, ViPV, APV, etc) and countries where the legislation have strong regularization of the Cd. The latter is a CRM that limit a potentially wide implementation.

CIGSSe

Chalcopyrite semiconductors have dragged a lot of attention in the thin film community, due to the flexibility in bandgap modulation by element interchange with a huge range of values from $E_g = 1 - 3.49$ eV.⁶²⁻⁶⁴ This lets an incredible flexibility in the range of absorption, and thus the possibility to tailor the materials to the specific device applications.

Table 1: Chalcopyrite semiconductor family bandgap energies

Material	E_g (eV)
CuInSe ₂	1.00
CuInS ₂	1.53
CuGaSe ₂	1.68
CuGaS ₂	2.43
CuAlSe ₂	2.71
CuAlS ₂	3.49

From these materials the most relevant for PV energy conversion are the CuInSe₂ (CISE) and CuInS₂ (CIS). While the former has shown efficiencies of ~15 % and the later of around ~12 %, ⁶⁵ the bandgap being tuneable from 1 eV to 1.5 eV allows for a fine selection for a specific application. This family of compounds have evolved to what is recognized as a mature, industrial level technology, the Cu(In,Ga)(S,Se)₂. The most important steps to achieve the record values of this material where mainly 3. The inclusion of Na as doping/alloying, or rather to realise that the films growth on soda-lime glass (with Na) were more efficient than those synthesized onto non containing Na substrates;⁶⁶ where sodium incorporation will interact

1 - Introduction

with Se during the reactive annealing and thus acting as a Se reservoir in the grain boundaries, thus increasing the homogeneity of the films.^{67,68} The alloying with gallium,^{69,70} that occupies indium positions, also generates a bandgap energy shift from 1.0 eV for CuInSe₂ to 1.7 eV for CuGaSe₂ and an almost linear evolution with Ga inclusion for CuIn_{1-x}Ga_xSe₂. The combination of the partial substitution of In with Ga and S with Se gives rise to the best performing devices so far,⁷¹ enabled by the bandgap grading generated by a not homogeneous composition in depth (across the thickness of the absorber layer), where the front surface bandgap energy is increased with increasing sulphur over selenium content,⁷² this leads to a lower energy loss due to $E_{ph} > E_g$ for the short wavelength photons (low penetration) thus to higher V_{oc} ; and back contact grading is controlled by increased gallium to indium content,⁷³ which generates a barrier for electrons in the back contact and thus reduced recombination and higher J_{sc} . Last breakthrough in the technology was the alkaline post deposition treatments, this has shown that it is possible to modify the defect properties, thus improving the carrier density in the surface, passivate lattice defects, improving CdS coverage. Specifically, treatments with heavy alkali elements like Rb and Cs, are the last game-changer in the technology.⁶⁷

The standard structure of a high efficiency CIGS solar cell is as shown in the Figure 9, established in substrate configuration as opposed to CdTe solar cells and composed by a molybdenum back contact layer, a CdS buffer layer (N-type), and a window layer of ZnO/AZO transparent conductive oxides.

This technology presents a high degree of adaptability due to the aforementioned properties and high *PCE* potential even comparable with silicon technologies. Nevertheless, this system presents a drawback in the shape of the scarcity of gallium and the high demands of indium in different industrial fields such as LCD displays.

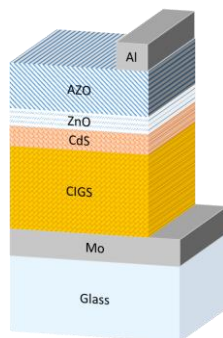


Figure 9: Schematics of a CIGS basic device substrate configuration.

CZTSSe

This absorber material was born as a substitute of the CIGS technology, as a result of the increasing concerns of critical raw material (CRM) usage, due to indium and gallium being considered as such.⁷⁴ Instead in CZTS, zinc and tin are employed, forming a compound with a kesterite crystal structure $\text{Cu}_2\text{ZnSn}(\text{S}_x\text{Se}_{1-x})_4$ (Figure 10). The research field took as reference layer stack the CIGS structure,⁷⁵ or with slight variations,⁷⁶ in accordance to the similarities between the materials.

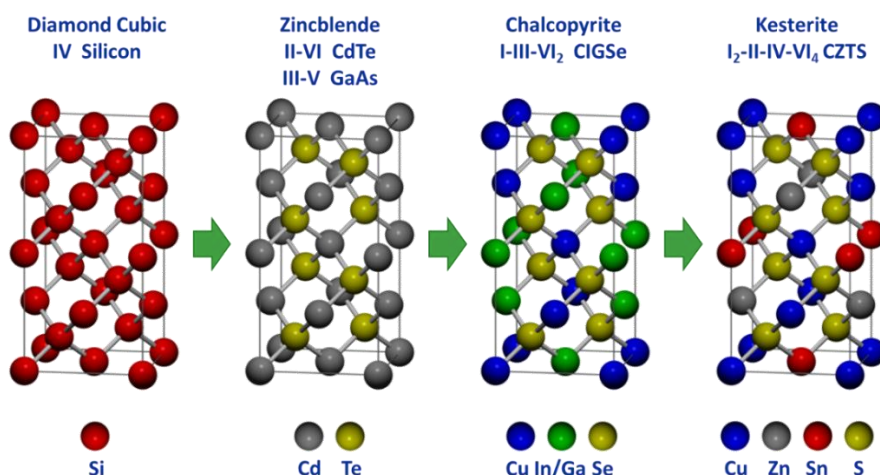


Figure 10: Crystal structures of some semiconductor materials employed in photovoltaics. Extracted from <https://www.pveducation.org/es/fotovoltaica/czts> (Courtesy of Dr. Bryce Walker).

1 - Introduction

Like in the case of CIGS the bandgap energy can be tuned in the range of 1-1.5 eV by varying the sulphur to selenium content in the films,⁷⁷ thus enabling the possibility to tailor the bandgap in depth.⁷⁸ It has, like the rest of the thin film technologies, a high absorption coefficient ($> 10^4 \text{ cm}^{-1}$).⁷⁹ When synthesized out of stoichiometry conditions, in particular copper poor, the material has an intrinsic p-type conductivity, These features and the adaptability of all the know-how of the CIGS technologies promotes the kesterite absorbers to a promising candidate for PV applications.

But some drawbacks are still present. The complex defect chemistry of the material (Figure 11)⁸⁰ is more intricate than in the case of CIGS due to Sn-Zn interchange in the lattice planes, even forming a totally different compound (stannite),⁸¹ together with a myriad of secondary phases that form in the different compositional regimes.⁸² From an industrial perspective this is a mayor no-go point, but from the research and scientific point of view is an orchard of in-deep characterization and knowledge for the material science.⁸³⁻⁸⁷ Even with those limitations the PCE of the CZTSSe system has been raised to 12.6 % and still follows a promising development curve if the research interest does not decrease over time.^{88,89}

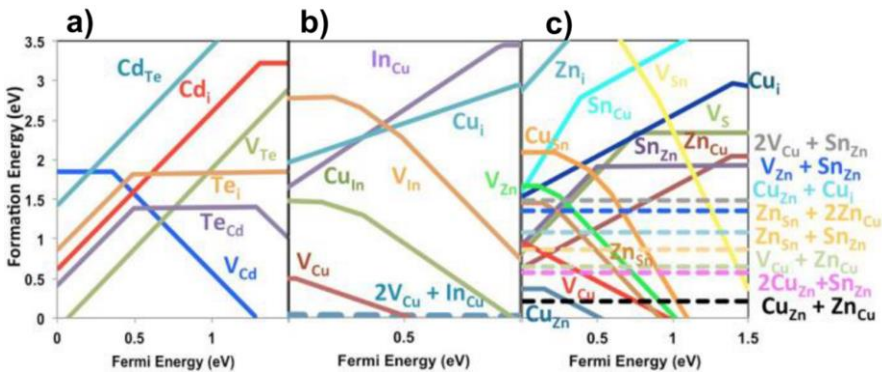


Figure 11: Defect densities of: a) CdTe, Te-rich, b) CIGS Cu-poor, and c) CZTS Cu-poor. ©[2016] IEEE. Reprinted, with permission, from [Ingrid Repins, Wild band edges: The role of bandgap grading and band-edge fluctuations in high-efficiency chalcogenide devices, 2016 IEEE 43rd Photovoltaic Specialists Conference (PVSC)].⁸⁰

Once we have complete a general overview of the most relevant inorganic PV technologies from the industrial ones to the state of the art we can summarize them in the Table 2 where there are presented the main efficiencies achieved for each technology together with their advantages and limitations.

Table 2: Summary of the aforementioned PV technologies with their maximum PCE values of cell and module scale at laboratory, together with their main advantages and limitations.

Technology	PCE Record Laboratory	PCE Record Laboratory Module	Advantages	Limitations
c-Si	26.7% ³⁹	24.4% ⁹⁰	Close to SQ	Indirect Eg/ Material usage/ weight/flexibility
p-Si	23.3% ⁹¹	20.4% ^{*90}	Cheaper than c-Si	Indirect Eg/ Material usage/ weight/flexibility
CdTe	22.1% ⁶¹	19.0% ⁹⁰	Material usage/direct Eg	Toxicity of Cd Te is a CRM
CIGS	23.35% ⁷¹	19.2% ⁹²	Material usage/direct Eg tunnable	In and Ga are CRM
a-Si	14.0% ^{**90}	12.3% ^{*93}	Material usage	Bandgap Eg, PCE, stability
CZTS	12.6 ⁸⁸	xxx	CRM free/ material usage	Defects/ PCE

* *a-Si/nc-Si tandem*. ** *a-Si/ nc-Si/nc-Si*

1.3 - New emerging photovoltaics: the case of Sb_2Se_3

1.3.1 - Evolution and state of the art of Sb_2Se_3

As we have pointed out in the previous section, all the present technologies, even the mature ones, show at least one limiting factor in their fundamental properties, development or in their implementation. In the case of Silicon, is the material usage and high temperatures needed for purification. For the CdTe is the toxicity of cadmium and scarcity of tellurium. Equivalent limitations for CIGSSe with the shortage of gallium and availability of indium (CRMs) due to employment in other technologies. CZTSSe seem like a promising earth abundant alternative but the defect properties of such a multi-compound material is nowadays difficult to assess. With this in mind, several new materials have dragged the attention of the PV community and one of the most promising materials for direct light harvesting are the family of $\text{Sb}_2(\text{Se,S})_3$ (Figure 12).

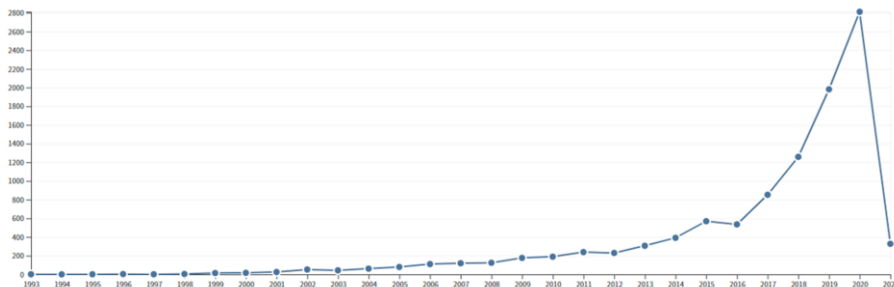


Figure 12: Number of publications under the search " Sb_2Se_3 thin film" extracted from Web of science.

Sb_2Se_3 is composed of abundant materials in the earth crust unlike CIGSSe,⁹⁴ although poorly spread across the world, being the main reservoirs of antimony located in China with 74 % of the world's reservoirs, followed by Tayikistán (8 %) and Russia (4 %), and being Turkey the main supplier to the EU; luckily it is the third most recycled material in the EU.⁹⁵ First scientific evidence of the utilization of Sb_2Se_3 as a photoactive layer was in a photoelectrochemical cell in 1981.⁹⁶ But it was not until 2014 that a competitive *PCE* of 3.2 % was

1 - Introduction

published by Choi et al.⁹⁷ on a m-TiO₂/Sb₂Se₃-sensitized heterojunction solar cell. First planar devices based on thin films were obtained by Zhou et al.⁹⁴ with TiO₂/Sb₂Se₃ heterojunction and a device *PCE* of 2.26 % and Liu et al. that explored CdS/Sb₂Se₃ heterojunction with 2.1 % *PCE*. Two main ways of device structure have been investigated up to now superstrate (based on CdTe technology) and more frequently used, and substrate (based on CIGS technology), so far these two main approaches have shown *PCE*'s of 7.9 %⁹⁸ and 9.2 %⁹⁹ respectively. Further discussion lies in the record *PCE* device of 9.2% reported in 2019 by Z. Li et al.,⁹⁹ this device shows an improved J_{sc} and FF but no improvement in V_{oc} , whether this result lies on the field of device engineering or in the improvement of the material itself is discussible. The nanoribbon structure of the film leads, to an increased amount of photons that reach the space charge region, as this is distributed along the ribbon depth, and thus to an increased J_{sc} due to decreased bulk recombination (more minority carriers are generated close to the SCR). The light trapping effect is also reported by the authors as a reduction in reflection. This leaves these results in the field of engineering of the final device, and not in the material properties. Therefore, even if the result is respectable and representative of what can be achieved with this technology, it must be treated carefully for the correct development of the technology.

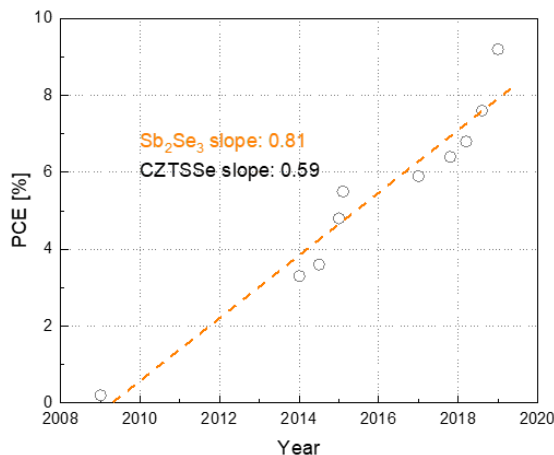


Figure 13: *PCE* evolution of Sb₂Se₃ devices. CZTSSe data is calculated from data in ref⁸⁹, Sb₂Se₃ data is extracted from ref¹⁰⁰.

1.3 - New emerging photovoltaics: the case of Sb_2Se_3

Figure 13 shows the evolution of the *PCE* of the Sb_2Se_3 devices as function of time, if we calculate the trend we can observe how it is increasing faster than that of CZTSSe⁸⁹ (note here only Sb_2Se_3 data is taken into account) this improvement is really promising for a low maturity system with only 7 years from the first respectable device *PCE*. Further impressive improvement has been show for the solid solution of $\text{Sb}_2(\text{S},\text{Se})_3$ with a certified *PCE* >10 % at cell level^{101,102} and 7.4 % at minimodule level (15 cm²),¹⁰³ synthesized in superstrate configuration by hydrothermal deposition, stablishing it as a futureproof technology.

1.3.2 - But why Sb_2Se_3 is so interesting?

First of all, it has a relatively low melting point $T = 590\text{ }^\circ\text{C}$ and low vapour pressure.^{104,105} which guarantees the possibility of low temperature synthesis (< 400 °C), consequently reducing the cost in the manufacturing and ensuring a high degree of integration (Tandem, different substrates, hybrid technologies, etc...).¹⁰⁶ Evaporates congruently like CdTe, ensuring the same composition in the deposit. Is has only one stable phase in contrast to CZTSSe, with no presence of polymorphs (Figure 14), which guarantees that the only secondary phases in the synthesis will be the elemental components and antimony oxides.^{105,107}

1 - Introduction

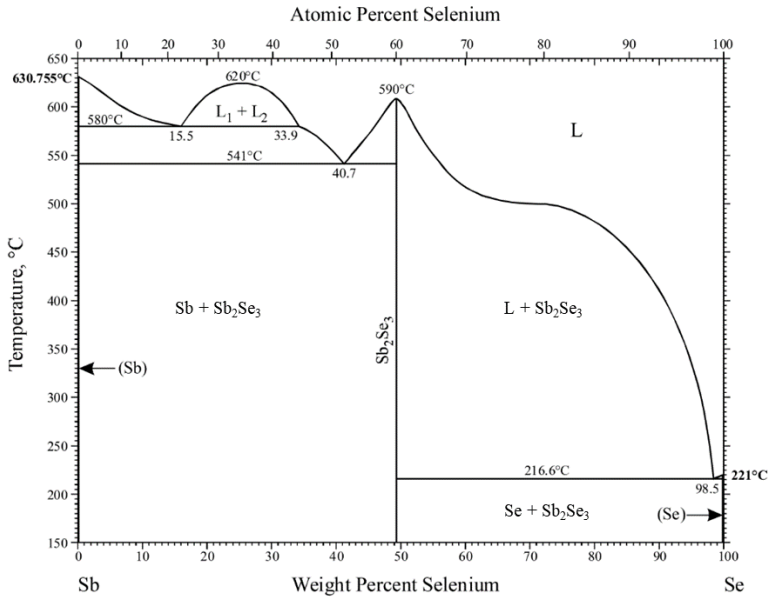


Figure 14: Phase diagram Sb_2Se_3 . Reprinted with permission of ASM international from *Sb (Antimony) Binary Alloy Phase Diagrams*, Ghosh, G.; Olesinski, R. W.; Abbaschian, G. J.; *Diagrams, A. P.*, Vol. 6, pp 585–590, 2016; permission conveyed through Copyright Clearance Center, Inc.¹⁰⁵

This material is an indirect band-gap material, however the peculiar band structure that presents provide to the material a quasi-direct bandgap property, thus translating into high absorption coefficient. The direct and indirect bandgap in the Sb_2Se_3 are close to each other in energy, being the lowest one the indirect one $E_{g,i} = 1.03 - 1.2$ eV and a direct one close to it $E_{g,d} = 1.17 - 1.3$ eV (Figure 15).^{106,108–112} The material present several valence band maximums (VBM) close in energy and momentum between each other, that indicates a lot of possible transitions.¹⁰⁹ The fact that the smaller energy transitions is an indirect transition, is normally associated with poor collection properties (ex. silicon), but in the case of Sb_2Se_3 , it is possible that the presence of a direct bandgap, close in energy-momentum to the indirect one, is the responsible of the high absorption coefficient ($> 10^5$ cm⁻¹),¹⁰⁸ this feature of a lower indirect bandgap could reduce the radiative recombination and thus lead to higher *PCE* devices, although it is a question still open to debate.^{108,113}

1.3 - New emerging photovoltaics: the case of Sb_2Se_3

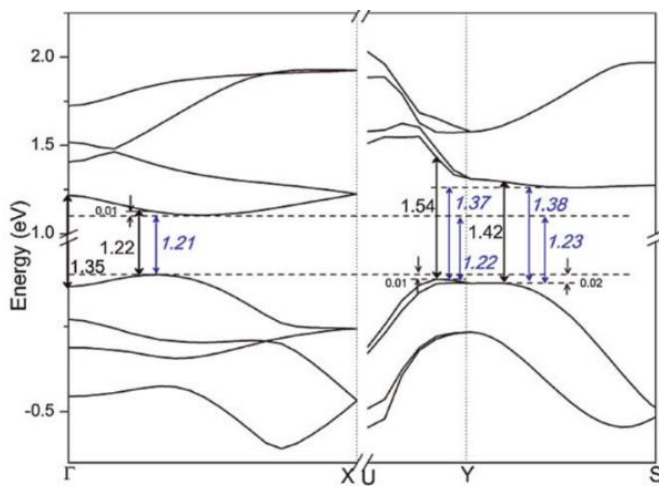


Figure 15: Detail of the Energy band diagram of Sb_2Se_3 calculated by DFT by generalized gradient approximation (GGA). Reprinted with permission of John Wiley & Sons.¹⁰⁹

1 - Introduction

Table 3: main parameters of Sb_2Se_3

Property	Symbol [units]	Value	Ref
Space group		orthorhombic	107
		Pnmb 62	
Lattice parameters	a [Å]	11.63636(9)	107
	b [Å]	11.78446(6)	
	c [Å]	3.97882(3)	
Density	ρ [g·cm ⁻³]	5.84	114
Melting point	T_m [K]		
Absorption coef.	α [cm ⁻¹]	>10 ⁵	108
Relative dielectric constat	ϵ_r [ϵ_0]	14.3-19.8	108
Minority carrier lifetime	τ_e [ns]	67	113
Mobility		a 1.17	113
	μ_h [cm ² ·V ⁻¹ ·s ⁻¹]	b 0.69	
		c 2.59	
	μ_e [cm ² ·V ⁻¹ ·s ⁻¹]	c >16.9	
Diffusion length	L_e [µm] [001]	1.7	113
	L_e [µm] [221]	0.29	
Indirect bandgap	$E_{g,l}$ [eV]	1.03 - 1.2	106,108-
Direct bandgap	$E_{g,d}$ [eV]	1.17 - 1.3	112

1.3 - New emerging photovoltaics: the case of Sb_2Se_3

Antimony selenide pertains to a material category described as Van der Waals solids, where the most known representative of the family is the thinnest material in existence, graphene.¹¹⁵ This kind of materials have the peculiarity to present a crystallographic structure in which at least the atoms along one of their crystallographic directions is held together via van der Waals forces, which permits the exfoliation of the material in single atomically flat layers (i.e. 2D materials).^{95,116–118} In the case of the Sb_2Se_3 , its structure, represented by the space group $\text{Pnmb } 62$, is composed of one dimensional ribbons where the atoms are connected to each other by covalent bonds in the c direction and by soft Van der Waals bonds in the a and b directions (Figure 16).^{107,119} This creates a highly anisotropic material with particular conduction properties, the diffusion length across the c direction is much higher than across the other two directions even by one order of magnitude (Table 3),¹¹³ which directly implies that the films must be properly aligned to obtain successful devices, and this has become a main focus of the research in this material.^{99,119,120} The most desired arrangement is along the $[002]$ orientation (i.e. ribbons completely perpendicular to the substrate), thus if the film is aligned with this orientation, the two metallic contacts will be connected by covalent bonds across the Sb_2Se_3 layer and the charge transport will be optimal (i.e. reduced recombination). It is considered as a general rule, that the crystallographic orientations with $[hkl]$ with $l \neq 0$ are beneficial for carrier transport, as they define planes were the ribbons are tilted at some angle, the more tilted the less beneficial, but they will still connect both front and back contacts.¹¹³ The opposite orientation of the ribbons will imply that the carriers would need to follow a hopping process through the ribbons, thus suggesting a slow tunnelling effect that effectively enhances cross-section recombination. This feature by itself is not desirable, in comparison with homogeneous conduction properties which are easier to live with if one thinks in a perfect single crystal material. What is really important is the speculated reduced recombination in between the ribbons and even the absence in dangling bonds in the grain boundaries, due to this ending surfaces not producing interfacial states, thus not increasing SRH recombination.¹¹⁹ This is a major feature to take into account as recombination in grain

1 - Introduction

boundaries in polycrystalline systems are really difficult to characterize and eliminate.¹²¹

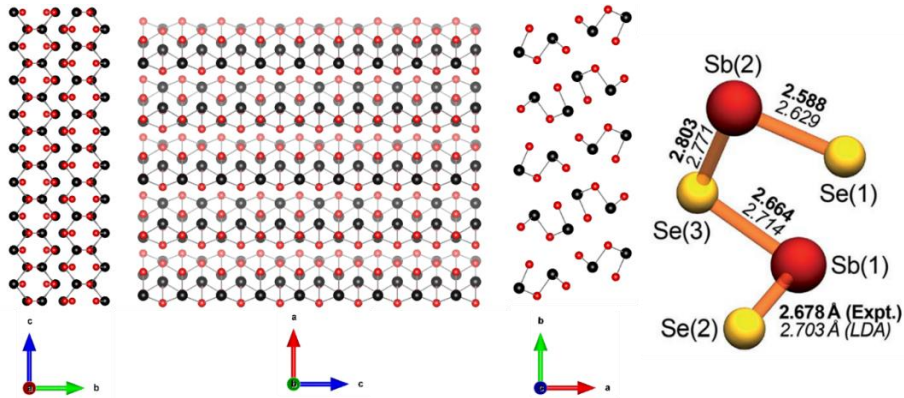


Figure 16: Left) Crystal structure of Sb_2Se_3 along different crystallographic axes. Right) Non-equivalent atom positions. Right figure reproduced from Ref. ¹²² with permission from the Royal Society of Chemistry.

1.3.3 - Defect properties and limitations

Regarding the defect properties of the system, one would expect a simple defect chemistry from a binary compound with only one stable phase, however some authors have proven this to be totally the opposite.^{122,123} We can see how the high anisotropy in the crystal structure also reflects in a lack of symmetry in the atom positions of the constituent elements, thus, not all selenium and antimony atoms behave the same positions, and the defects associated to them are quantitatively different (Figure 16). This arises for the different environment for each atom, i.e. Sb_1 bonds with five Se atoms, while Sb_2 bonds with only two.^{123,124} This implies that a Sb atom on a position of Se_1 (Sb_{Se1}) is not equivalent with a Sb atom on a Se_2 (Sb_{Se2}) position. This generates at the end a complicated defect chemistry for a binary semiconductor for which the defects expected are two Sb vacancies (V_{Sb1} , V_{Sb2}) three Se vacancies (V_{Se1} , V_{Se2} , V_{Se3}), three Sb antisites (Sb_{Se1} , Sb_{Se2} , Sb_{Se3}), two Se antisites (Se_{Sb1} , Se_{Sb2}), Sb and Se interstitials; also the high interatomic distance between the covalently bonded ribbons allows for presence of $2Se_{Sb1}$ and $2Se_{Sb2}$ defects to

1.3 - New emerging photovoltaics: the case of Sb_2Se_3

occur Figure 17.^{123,124} It is important to note that the conduction properties (P or N type conductivity) are defined by the intrinsic defects present when the system is synthesised as Se-poor or Se-rich, where, for the later, the presence of $\text{Se}_{\text{Sb}2}$ and $2\text{Se}_{\text{Sb}1}$ determine the P-type conductivity on the film. These defects although less damaging than the donor ones, still pin the quasi fermi level of holes to 0.4 eV over the valence band maximum, possibly explaining the large V_{oc} deficit and fixing the V_{oc} to around ~ 0.4 V reported by several authors including our research.^{99,106,123–129} Several attempts to measure the exact energy levels of the defects report the presence of three main defects but the energies at what they are formed are still not clear to this point, being: D1 with energy 0.18 – 0.48 eV and density of $\sim 10^{14} - 10^{16} \text{ cm}^{-3}$, D2 with energy 0.29 – 0.62 eV and density of $10^{14} - 10^{16} \text{ cm}^{-3}$, D3 with energy 0.44 – 0.71 eV and density $10^{14} - 10^{16} \text{ cm}^{-3}$. These values although really dissimilar between them, present high concentrations even in devices reaching 7.5% *PCE*, which is something that should be addressed as soon as possible.^{129–135}

1 - Introduction

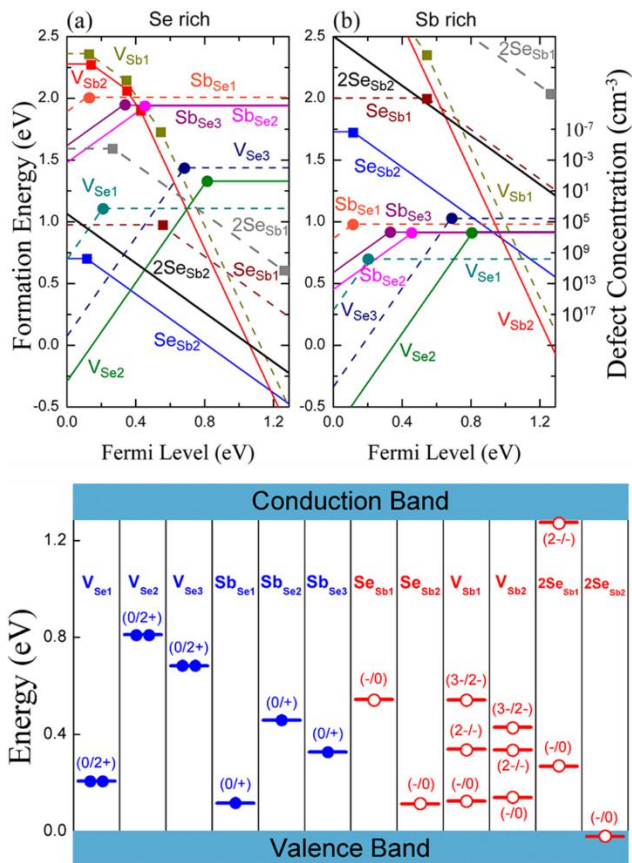


Figure 17: Top) Formation energies and equilibrium concentrations of different defects as a function of the Fermi level under (a) Se and (b) Sb rich conditions. Bottom) Transition energy levels of intrinsic defects on different atomic sites in the bandgap of Sb_2Se_3 . Reprinted (adapted) with permission from Huang, M.; Xu, P.; Han, D.; Tang, J.; Chen, S. *Complicated and Unconventional Defect Properties of the Quasi-One-Dimensional Photovoltaic Semiconductor Sb_2Se_3* . ACS Appl. Mater. Interfaces **2019**, 11 (17), 15564–15572. <https://doi.org/10.1021/acsami.9b01220>.¹²³ Copyright 2019 American Chemical Society.

Other theoretical and experimental works have tried to identify possible ways to modify the doping levels by introducing Cl, I and Br to obtain N-type conductivity in the film, while Cu and Sn may prove to be suitable for P-type conductivity even achieving working devices with a structure of $\text{I:Sb}_2\text{Se}_3/\text{Cu:Sb}_2\text{Se}_3$.^{124,136}

In a different manner, other authors have shown how the surface states of the ending planes in the Sb_2Se_3 system could reorganize (as with all

1.3 - New emerging photovoltaics: the case of Sb_2Se_3

other materials), but in the case of these elements, seems to be without deep defect states generated in the bulk of the films. In principle due to the flexibility provided by the ribbon structure and the lone electron pair in the Sb cation, assisting the benign reorganization.¹³⁷ This has been shown to happen also at the grain boundaries where the relaxation of the atoms in the termination between one grain and the other relax and thus eliminate possible dangling bonds and intermediate states in the bandgap.¹³⁸

C. Chen and J. Tang also investigated where the limitations of the antimony chalcogenides came from.¹³⁹ In their article, they depicted that mostly all state of the art devices presented interfacial and space charge region recombination as principal limitation, as in the case of the devices presented in this thesis. They also investigated where the problem of V_{oc} deficit is arising from low carrier lifetime (τ). This is a difficult property to assess (normally PL measurements) in an indirect bandgap semiconductor and the only reports are those of time resolved THz spectroscopy (TRTS) and transient absorption (TA) spectroscopy giving systematic measurements of $\tau = 0.1-1$ ns^{129,131,132,140-142} way lower than other technologies like CZTSSe.¹⁴³

1.3.4 - Device strategies

Several modifications to the traditional CIGS and CdTe structures have been explored in the literature. As mentioned before, record efficiency in substrate configuration is based on a nanoribbon structure covered by TiO_2 and CdS, but aside from the nanostructure the layers are the same as in CIGS base devices with:

SLG/Mo/MoSe₂/Sb₂Se₃(nano)/TiO₂/CdS/ZnO/Al:ZnO.⁹⁹

In the case of the superstrate configuration the record efficiency is obtained with and structure:

SLG/ITO/CdS/Sb₂Se₃/Spiro oMe-TAD/Au device.⁹⁸

As a starting point several groups have been investigating alternatives to the standard configurations in a pursuit of a specific structure for the

1 - Introduction

Sb₂Se₃ system. First research interest was placed in finding a suitable buffer layer to eliminate the toxic but really well developed CdS. Normally the point of view is a not optimized band alignment in the CdS/Sb₂Se₃ interface and a reduced absorption of UV photons due to the small bandgap of CdS (2.4 eV),¹⁴⁴ with this in mind several groups obtained really promising efficiencies with CdS:O,⁵³ SnO₂,¹⁴⁵ ZnO,¹⁴⁶ TiO₂,^{147,148} CdZnS,¹⁴⁹ In₂S₃.¹⁵⁰

In the same perspective general interest has been placed in the development of back contacts or more specifically hole transport layers. These layers consist of a heavily p-type doped layer or at least a sufficiently high energy barrier for the electrons to reach the back contact and recombine.¹⁵¹ With this kind of layers a more intrinsic absorber material is desirable and a N-i-P structure is normally adopted where the Fermi level is defined by the N and P type layers, as an example, the Sb₂Se₃ absorber (intrinsic) is placed in between two highly doped materials (N-type CdS and P-type T-Se) in this case reaching efficiencies of 7.45 %.¹⁵² Hole transport materials, including organic and inorganic compounds, employed in literature with promising results are: MoSe₂,⁹⁹ CZ-TA,¹²⁸ CuSCN,¹⁵³ PbS-CQD,¹⁵³ NiO_x,¹⁵⁴ PCBM,⁹⁷ WSe₂.¹⁵⁵

The device configuration used during the PhD has been based in:

SLG/Mo/Sb₂Se₃/CdS/i-ZnO/ITO (Figure 18)

This configuration has been chosen due to the experience in the SEMs research group in the development of CIGS and CZTSe technologies. This allowed to focus the effort in the optimization of the Sb₂Se₃ synthesis and characterization. However, the results obtained during the PhD have evidenced that this configuration is suboptimal and a modification is necessary to optimize the front and back interfaces and minimize the recombination and maximize carrier transport.

1.3 - New emerging photovoltaics: the case of Sb_2Se_3

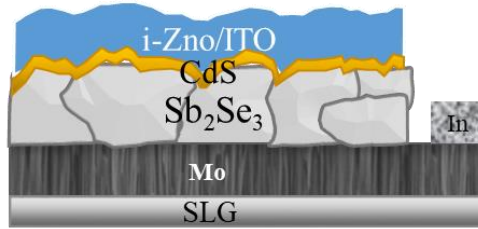


Figure 18: Schematic of the basic solar cell device substrate structure implemented in this thesis.

1.4 - Fundamentals of solar cells

This section is founded in previous knowledge obtained in the bachelor degree in Physics of Pedro Vidal Fuentes, the knowledge acquired during the development of the present PhD studies, plus information extracted from several reference books such as: Würfel P.,¹⁵⁶ Scheer H. and Schock H.,¹⁵⁷ Smets A. et al.,¹⁵⁸ Kittel C.,¹⁵⁹ Yu P. Y. and Cardona M.¹⁶⁰

1.4.1 - What is a solar cell?

The objective of a solar cell is to generate an opto-electrical energy conversion. If we think as the Sun as a source of energy, this will emit electromagnetic radiation closely represented by the black body spectrum, that will depend on its temperature, around $T = 5800$ K. The emission (Figure 19) is not homogenous in wavelength and there is a predominant spectral irradiance in the visible range.

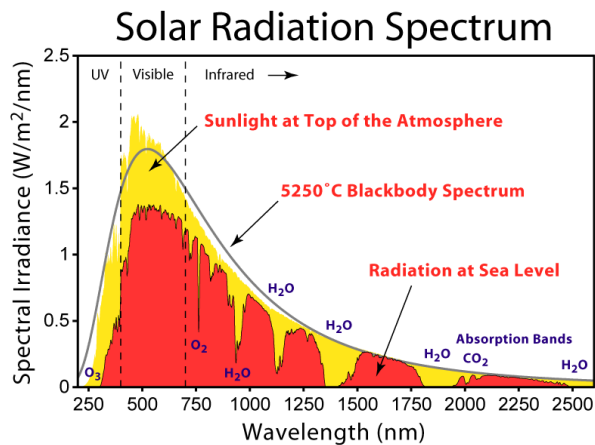


Figure 19: Solar radiation spectrum. (author: CC BY-SA 3.0, <https://commons.wikimedia.org/w/index.php?curid=2623187>).

With this in mind, a solar cell has to absorb as efficiently as possible the solar spectrum. First limitation occurs when the photons emitted by the sun surpass the atmosphere of the Earth, the interaction of the

1 - Introduction

photons via different process with the molecules that compose the atmosphere reduce the final irradiance spectrum in the Earth surface to what is depicted in red (Figure 19).

Several material structures have been employed to harvest light but one of the most employed, and the one implemented in this work are the PN based devices, and the theoretical framework herein presented will be dedicated to its understanding and basic physical properties.

A semiconductor presents, as a main differential property, the presence of a bandgap energy (E_g) which is the minimum energy required for an electron to be excited from the valence band (bound state), to the conduction band (free carrier). The electrons excited with higher energy will lose this extra energy over the E_g by thermalisation into the bottom of the conduction band. The electron once is excited to the conduction band will leave a ‘space’ in the valence band, the subsequent movement of the electrons in the valence band to occupy this empty space can be depicted as a theoretical moving particle, a ‘hole’, that will have a positive charge associated to it (Figure 20). This effect is happening constantly in semiconductors that are at temperatures different from absolute zero ($T \neq 0$ k), and it is defined as the intrinsic doping (n_i) of a semiconductor following Equation (1).

$$n_i = 2 \left(\frac{m^* k_B T}{2\pi \hbar^2} \right)^{3/2} e^{\frac{-(E_c - E_f)}{k_B T}} \quad (1)$$

Where m^* is the effective mass, k_B is the Boltzman constant, \hbar is the reduced Plank’s constant, E_c is the conduction band energy and E_f is the Fermi energy level, which describes a virtual state for the electrons with a 50 % probability of being in an occupied state following the Fermi Dirac distribution (Equation (2)).

$$f(E) = \frac{1}{e^{(E - E_f)/k_B T} + 1} \quad (2)$$

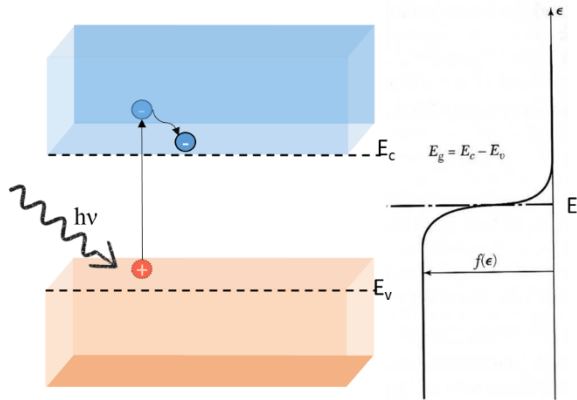


Figure 20: Schematics of the energy band diagram of a semiconductor material with Fermi energy level identified.

If the material is doped (i.e. electrons are introduced or removed from the system) the Fermi level will shift towards the conduction band (more electrons, N-type) or to the valence band (less electrons, P-type), as an example in the case of silicon technology, these behaviours are achieved when the material is extrinsically doped with a group V atom (extra electron, N-type) or a group III atom (missing electron, P-type). All semiconductors must obey the charge balance equation $n_{op}o = n_i^2$, that establish a direct correlation between minority (holes in N-type) and majority carriers (electrons in N-type).

Furthermore, several physical parameters are key to define a semiconductor as a suitable candidate for solar cell construction. Firstly, the absorption coefficient ($\alpha(\lambda)$ [cm^{-1}]), this quantity represents the depth at which an electromagnetic wave of specific wavelength can penetrate a semiconductor before it is absorbed. It is desirable to have a value as high as possible, to be able to reduce to a minimum the material employed to harvest the light, and to generate the charge carriers in the less amount of volume to avoid their recombination. It is one of the key parameters that make semiconductor materials such as CIGS enable the possibility of development of Thin-film photovoltaics. The value of $\alpha(\lambda)$ is heavily influenced by the nature of the bandgap of the semiconductor material employed, if the bandgap is direct, no momentum \mathbf{k} is necessary for the electrons in the system to interact with the impinging photon, and the process is more probable (above the E_g), the effect is the opposite for indirect bandgap

1 - Introduction

semiconductors. From the inverse of $\alpha(\lambda)$ we can obtain the penetration depth in function of the wavelength of the specific photon.

Another relevant parameter is the drift velocity of the charge carriers per unit of electric field or mobility $\mu = |v|/E$ [$\text{cm}^2/(\text{V}\cdot\text{s})$]. This value will represent how quickly an electron (μ_e) or a hole (μ_h) will move through the material when an electric field is applied and will ultimately define how much current density (J) can flow through the system for a given concentration of holes (p) and electrons (n) and electric field (E) following Equation (3). Take into account that mobility values for each carrier may be different in the same material, as mobility itself depends on effective masses of electrons (m_e^*) and holes (m_h^*) in this manner $\mu_{e/h} = q\bar{\tau}/m_{e/h}^*$ where $\bar{\tau}$ is the average scattering time of the carriers.

$$J_x = q(n\mu_e + p\mu_h)E_x \quad (3)$$

But how these junctions of semiconductors work to harvest light? In order to generate power, they should be able to generate a voltage and a current ($P = I \cdot V$). The voltage is needed to separate the charge carriers (electrons and holes) if they are not ‘spatially’ separated the electron will return again to the valence band by several process that we will discuss later on. One of the strategies to separate the photo-generated charges is to create a structure that has a built in potential difference, a PN or P-i-N junctions are the more common structures to achieve this (Figure 21), we will focus our analysis in the first one as it is on which the devices synthesized for this thesis are based.

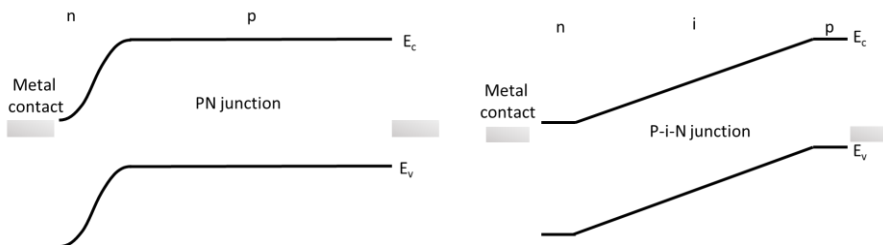


Figure 21: Simplified band diagram of a PN (left) and P-i-N (right) structures.

When two opposite doped semiconductors N and P are brought together, the charge balance between the ionized atoms that conform the lattice of the element and the free charges is broken, and the large

difference between electron concentration in the two materials can be seen as chemical potential that will drive the electrons from the N-type (majority carriers) to the P-type (minority carriers), this charge movement generates a current called *diffusion current*. When the electrons in the N-type semiconductor move to the P-type semiconductor, the positively ionized atoms stay in their positions, and thus a positively net charge is present in the *surface* of the N-type semiconductor and with opposite sign in the P-type semiconductor with a superficial negative charge (Figure 22). This region between the two materials is denoted as the space charge region (SCR or w) or depletion region. This SCR that has been depleted from majority carriers is no longer in charge equilibrium and therefore an electric field (E) is generated from the N-type to the P-type semiconductor and consequently a built-in voltage (V_{bi} , Equation (4)). This field will force the carriers in the opposite direction (*drift current*) to the *diffusion current* until an equilibrium is reached between the two contributions, nevertheless for $T \neq 0$ K there are carriers that cross the junction to the opposite side. When the two semiconductors are brought together, their carrier population will be equilibrated, so their band diagram will be aligned along the Fermi level, and as the conduction and valence bands must be continuous (although not derivable, as spikes may be formed) they will bend as depicted in Figure 23, as an example of a more realistic heterojunction device. From the resolution of the Poisson equation in one dimension, the Electric field across the junction can be obtained, and hence the V_{bi} can be calculated as follows:

$$V_{bi} = \frac{q}{2\epsilon_r\epsilon_0} (N_D l_n^2 + N_A l_p^2) \quad (4)$$

Where N_D and N_A are the donor and acceptor density, and l_n and l_p are the extension of the SCR in the N-type and the P-type semiconductor respectively. The V_{bi} can also be derived from the band diagram of the semiconductors with a final result:

$$V_{bi} = \frac{k_B T}{q} \ln \left(\frac{N_A N_D}{n_i^2} \right) \quad (5)$$

And therefore:

1 - Introduction

$$l_n = \sqrt{\frac{2\epsilon_r\epsilon_0 V_{bi}}{q} \frac{N_A}{N_D} \left(\frac{1}{N_A + N_D} \right)} \quad (6)$$

$$l_p = \sqrt{\frac{2\epsilon_r\epsilon_0 V_{bi}}{q} \frac{N_D}{N_A} \left(\frac{1}{N_A + N_D} \right)} \quad (7)$$

$$SCR = l_n + l_p = \sqrt{\frac{2\epsilon_r\epsilon_0}{q} V_{bi} \left(\frac{1}{N_A} + \frac{1}{N_D} \right)} \quad (8)$$

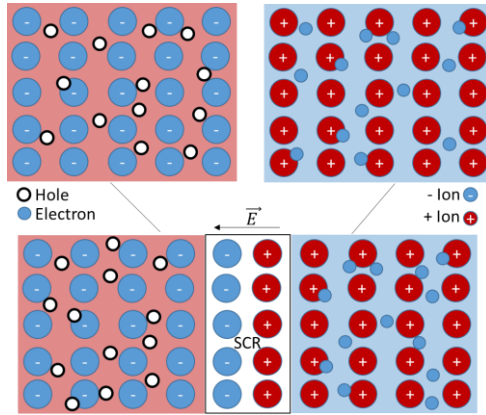


Figure 22: Schematics of formation of the space charge region (SCR) when an N and P semiconductors are brought together.

As it can be seen from the Equations (6) and (7), the space charge region is not homogeneously distributed across the two materials and it will be subjected to the doping concentrations in each material, with increasing doping the $l_{p/n}$ gets smaller. This expression is for a homojunction (i.e. N-type Si / P-type Si). For a heterojunction of two different materials (for example CdS/Sb₂Se₃) the dielectric constants, and the specific doping concentrations need to be taken into account and the resulting Equation (9) will then stand for the SCR width:

$$SCR = l_n + l_p = \sqrt{\frac{2\epsilon_0\epsilon_n\epsilon_p(N_{ap} + N_{dn})^2 V_{bi}}{qN_{ap}N_{dn}(\epsilon_p N_{ap} + \epsilon_n N_{dn})}} \quad (9)$$

When a PN junction of any type is subjected to an external applied voltage (V_a), this voltage will work into reducing or increasing the V_{bi} of the junction, depending on the sign of the applied voltage, and the potential across the region will become ($V_{bi} - V_a$). When the potential across the junction is increased, and thus the SCR, we define this situation as *reverse-biased voltage*, when the potential is decreased the system is in *forward-bias voltage*. For any of these out of equilibrium conditions the Fermi level for each carrier splits into what is called quasi-Fermi energy for electrons E_{fn} and holes E_{fp} . When this external voltage is applied the junction is no longer at equilibrium and the forces responsible for *drift* and *diffusion* are imbalanced. When in situation of forward-bias, some minority carriers will be able to flow through the reduced potential and recombine, this is named *carrier injection*, and generates a net current flow between the generation of the carriers and their recombination, is characteristic from the junction and is expressed as follows:

$$J(V_a) = J_{rec}(V_a) - J_{gen}(V_a) = J_0 \left[\exp\left(\frac{qV_a}{k_B T}\right) - 1 \right] \quad (10)$$

This equation is the Shockley equation and describes the current-voltage characteristics of an ideal PN diode, where J_0 is the *saturation current density* or *dark current density* and is a measure of the recombination in a diode and therefore a figure of merit to reduce.

1 - Introduction

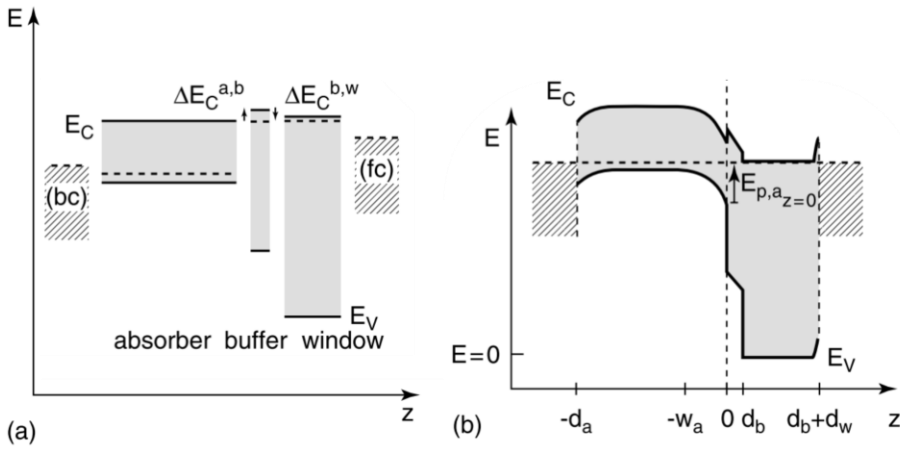


Figure 23: Realistic schematic of the formation of the band structure of a heterojunction solar cell with its main constituents, back contact (bc), absorber, buffer, window and front contact (fc). a) energy band as they will be calculated theoretically or measured experimentally. b) Band diagram once the materials are in contact and the Fermi energy levels are aligned. Image reproduced and adapted with permission of John Wiley and Sons from ref.¹⁵⁷

This constitutes the basic of a solar cell. So what happens when it is illuminated? Upon illumination, minority charge carriers are generated and flow from the P-type to the N-type (reverse for holes), this net current flow is the *photogenerated current* that is added to the J_{gen} . Consequently, the charge balance is again broken, and the distribution of the holes and electrons will once more be defined by the Fermi level splitting. The difference between the quasi-fermi levels between the P-type contact and N-type contact when in open circuit conditions will be qV_{oc} and will define the voltage that is obtained as the *open-circuit voltage*.

When a load is placed in the circuit the electrochemical potential of the holes and electrons will be reduced and the recombination will increase

$$\begin{aligned} J(V_a) &= J_{rec}(V_a) - J_{gen}(V_a) - J_{ph} \\ &= J_0 \left[\exp\left(\frac{qV_a}{k_B T}\right) - 1 \right] - J_{ph} \end{aligned} \quad (11)$$

As it can be seen from Equation (11), the *photogenerated current* is not dependent with the voltage applied to the junction V_a and it is only defined by:

$$J_{ph} = qG(L_N + SCR + L_P) \quad (12)$$

Where G is the generation rate of the carriers, and L_N and L_P are the minority carrier diffusion length.

With this in hand, we can now illustrate the main parameters of a solar cell.

1.4.2 - Opto-electronic parameters of a solar cell

There are 4 parameters that characterize a functional solar cell: the short circuit current density (J_{sc}), the open circuit voltage (V_{oc}), the fill factor (FF), the power conversion efficiency (PCE), all of these parameters can be extracted from the J-V characteristics of a solar cell (Figure 24), and the external quantum efficiency (EQE).

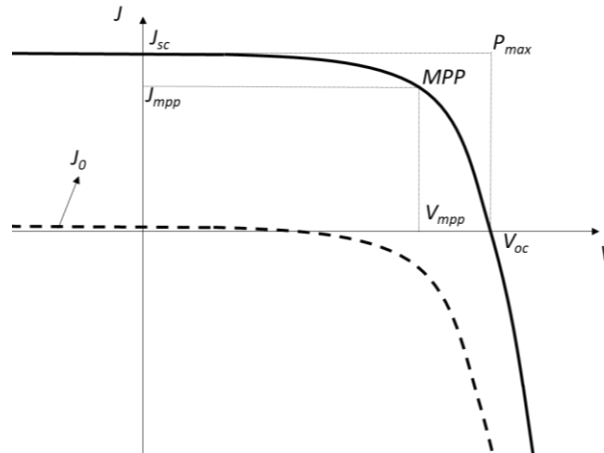


Figure 24: current-voltage characteristics of a solar cell.

The *short-circuit current* (J_{sc}) is obtained when the device is connected without any load and thus $V_a = 0$, ideally its value will be the same as the photo-generated current (J_{ph}) and the value can be derived from Equation (12).

1 - Introduction

The *open-circuit voltage* (V_{oc}) is the maximum voltage obtained when no current flows through the circuit, assuming Equation (11) to be 0 it can be derived that:

$$V_{oc} = \frac{k_B T}{q} \ln \left(\frac{J_{ph}}{J_0} + 1 \right) \approx \frac{k_B T}{q} \ln \left(\frac{J_{ph}}{J_0} \right) \text{ if } J_{ph} \gg J_0 \quad (13)$$

The *fill factor* (FF) is a ratio or normalization of the maximum achievable power of the solar cell, that is the point of the J - V curve for which the product $P = J \cdot V$ is maximum (mpp = maximum power point), divided by the maximum theoretical value that could be obtained:

$$FF = \frac{J_{mpp} V_{mpp}}{J_{sc} V_{oc}} \quad (14)$$

In conclusion, the *power conversion efficiency* (PCE or η) of a photovoltaic device is a ratio between the incident power and the generated power by the cell:

$$\eta = \frac{P_{mpp}}{I_{in}} = \frac{J_{mpp} V_{mpp}}{I_{in}} = \frac{J_{sc} V_{oc} FF}{I_{in}} \quad (15)$$

The *external quantum efficiency* ($EQE(\lambda)$) will define the ratio of photons per wavelength that are able to generate an electron-hole pair in a functional device and collect it, this will give us the short circuit current J_{sc} if integrated over λ pondered by the photon flux of AM 1.5 spectrum at $V_a = 0$ V (Equation (16)), the range of wavelength must at least contain the range for which the cell has photovoltaic response.

$$J_{sc} = -q \int_{\lambda_1}^{\lambda_2} EQE(\lambda) \Phi_{ph,\lambda}^{AM1.5} d\lambda \quad (16)$$

So far we have defined an ideal solar cell and their main parameters, on the other hand a real device will never behave in such fashion and several limiting factors must be taken into account, now we will depict how these equations shift from ideality to a real world operating solar cell.

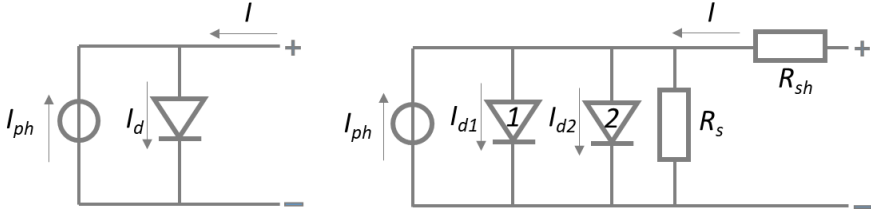


Figure 25: Solar cell equivalent circuit. Left) one diode ideal solar cell. Right) two diode closer to a real solar cell.

Equation (11) will define a circuit with the characteristics of the one depicted in Figure 25 left. In a real circuit (Figure 25 right), we have to take into account resistive losses and recombination on different parts of the circuit. The two added resistances in the Equation (17) account for the *series resistance* (R_s) of the overall layer stack that constitute the cell. A *shunt or parallel resistance* (R_{sh}) that will be low if different conductive paths than across the PN junction are allowed. Here was also included another recombination path or non-ideal diode that will account for other types of recombination present in the device and not only from band to band transitions but from interfacial defects also, then there are two dark saturation current densities J_{01} and J_{02} . When a J - V characteristic curve is measured experimentally and fitted to this equation the values obtained for n will define the dominant path of recombination in the sample by having a value comprised between $n = [1-2]$, if the value obtained lies outside this range other considerations must be taken into account, like non-homogeneous distribution of trap defects in the space charge region.¹⁶¹

$$J(V) = J_{01} \left\{ \exp \left[\frac{q(V - AJR_s)}{n_1 k_B T} \right] - 1 \right\} + J_{02} \left\{ \exp \left[\frac{q(V - AJR_s)}{n_2 k_B T} \right] - 1 \right\} + \frac{V - AJR_s}{R_{sh}} - J_{ph} \quad (17)$$

where A is the area of the device, J_0 can be defined as:

$$J_0 = J_{00} \exp \left[\frac{-E_A}{n k_B T} \right] \quad (18)$$

where j_{00} is the reference current density which is only weakly temperature dependant.

1.4.3 - Fundamental limits and recombination paths

In order to analyse out of ideality cases, first we can analyse what is the upper limit for efficiency in an ideal case, the most accepted definition of the ideal case for a solar cell is defined by the Shockley-Queisser limit (SQ limit).¹⁶² In this theoretical limit, a solar cell is seen as a thermodynamic system between the temperature of the Sun and the temperature of the sample. Only taking into account the non-avoidable radiative recombination, i.e. minority carrier band to band recombination by emission of a photon, the efficiency limit is then calculated by detailed balance¹⁶³. This theoretical limit assumes 100% absorption of photons and 1 to 1 generation of carriers, infinite mobility of the carriers, perfect carrier collection and perfect positioning of the sun. First limitation to PCE is that photons with higher energy than the $E_{ph} > E_g$ of the absorber material will deliver exactly the same energy than E_g , and photons with lower $E_{ph} < E_g$ are directly not absorbed. These considerations give as a result Figure 26. Other authors have pursued the same theoretical limits from a thermodynamic approach following energy and entropy fluxes like De Vos et al.¹⁶⁴

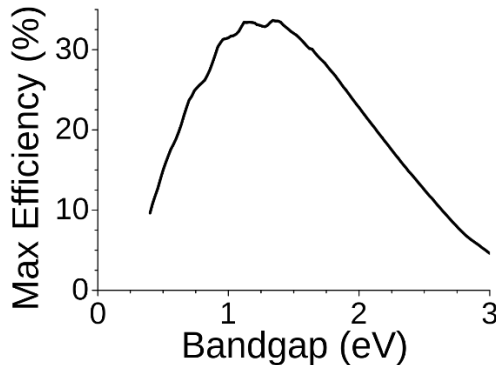


Figure 26: Maximum efficiency based in the SQ limit in function of the bandgap energy of the absorber material (figure extracted from Wikipedia article Shockley-Queisser limit, credits to Steve Byrnes).

Really interesting is the analytical approach of Hirst and Ekins-Daukes (Figure 27) deriving the limits from the intrinsic properties of the semiconductors.¹⁶⁵ From their approach there are 5 main intrinsic

limiting factors in a solar cell with a single bandgap energy defined by the analytical solutions of the Planck equation Equation (19), which includes the chemical potential μ on emission to calculate the total photon emission flux n per energy interval dE and unit of solid angle Ω :

$$n(E, T_S, \mu, \Omega) = \frac{2\Omega}{c^2 h^3} \frac{E^2}{e^{\left(\frac{E-\mu}{k_B T}\right)} - 1} \quad (19)$$

Where T is the temperature of the emitting body, c is the speed of light, h is the Plank's constant and k_B is the Boltzmann's constant. Other parameters to take into account are the solid angle of absorption Ω_{abs} and emission Ω_{emit} respectively, the temperature of the sun and the absorber T_s and T_A . The maximum efficiency is thus achieved evaluating the equation in relation to E_g and V , then all the factors presented herein are the losses in power due to each of the specified process:

- i) Below $E_{ph} < E_g$ loss, these photons do not have enough energy to excite an electron to the conduction band, affects J_{sc} :

$$\int_0^{E_g} E \cdot n(E, T_S, 0, \Omega_{abs}) dE \approx \Omega_{abs} \left(\chi(0, T_S) - \exp\left(\frac{-E_g}{k_B T_S}\right) \chi(E_g, T_S) \right) \quad (20)$$

- ii) Thermalisation loss $E_{ph} > E_g$ the extra energy is loss due to interaction of the charge carriers to lattice phonons affects V_{oc} :

$$\int_{E_g}^{\infty} E \cdot n(E, T_S, 0, \Omega_{abs}) dE - E_g \int_{E_g}^{\infty} n(E, T_S, 0, \Omega_{abs}) dE \approx \Omega_{abs} \exp\left(\frac{-E_g}{k_B T_S}\right) \left(\chi(E_g, T_S) - E_g \cdot \gamma(E_g, T_S) \right) \quad (21)$$

- iii) Emission loss, extracted from Kirchoff's law, all absorbers are also emitters, affects mostly J_{sc} :

1 - Introduction

$$\begin{aligned}
 E_g \int_{E_g}^{\infty} E \cdot n(E, T_A, eV_{opt}, \Omega_{emit}) dE \\
 \approx \Omega_{emit} E_g \gamma(E_g, T_A) \exp\left(\frac{eV_{opt} - E_g}{k_B T_A}\right) \quad (22) \\
 \approx \Omega_{abs} E_g \gamma(E_g, T_A) \exp\left(\frac{-E_g}{k_B T_S}\right)
 \end{aligned}$$

- iv) A solar cell operating as a thermodynamic system between the sun $T_s = 6000$ K and the cell itself $T_c = 300$ K will have a loss factor called the Carnot factor,¹⁶⁶ affects V_{oc} :

$$E_g \left(\frac{T_A}{T_S}\right) J_{opt} \quad (23)$$

- v) Difference between absorption and emission angles of the photons lead to an entropy generation process, therefore generating irreversibility, named Boltzmann loss, affects V_{oc} :

$$kT_A \ln\left(\frac{\Omega_{emit}}{\Omega_{abs}}\right) J_{opt} \quad (24)$$

Where, χ and γ are functions of (E and T) obtained from the resolution of Equation (19); V_{opt} and J_{opt} are the voltage and current obtained at the optimal bandgap energy ($E_g = 1.31$ eV, small deviations in the power losses are obtained for different values, especially for $E_g < 0.5$ eV)

$$\chi(E, T) = \frac{2k_B T}{c^2 h^3} (E^3 + 3E^2 k_B T + 6E k_B^2 T^2 + 6k_B^3 T^3) \quad (25)$$

$$\gamma(E, T) = \frac{2k_B T}{c^2 h^3} (E^2 + 2k_B T E + 2k_B^2 T^2) \quad (26)$$

$$eV_{opt} = E_g \left(1 - \frac{T_A}{T_S}\right) - T_A k_B \ln\left(\frac{\Omega_{emit}}{\Omega_{abs}}\right) \quad (27)$$

$$\begin{aligned}
 J_{opt} &= e \int_{E_g}^{\infty} n(E, T_S, 0, \Omega_{abs}) dE \\
 &= e \int_{E_g}^{\infty} E \cdot n(E, T_A, eV_{opt}, \Omega_{emit}) dE \approx \\
 &\approx e\Omega_{abs} \left[\gamma(E_g, T_S) \exp\left(\frac{-E_g}{k_B T_S}\right) \right. \\
 &\quad \left. - \gamma(E_g, T_A) \exp\left(\frac{-E_g}{k_B T_S}\right) \right]
 \end{aligned} \tag{28}$$

Thus, these limitations will contribute to the reduction of the J_{sc} or the V_{oc} modifying then J - V characteristics as shown in Figure 27 and therefore limiting the effective power output of any device. These factors depicted here are intrinsic and therefore unavoidable, where other limiting factors such as internal resistance or reflection are theoretically possible to solve.

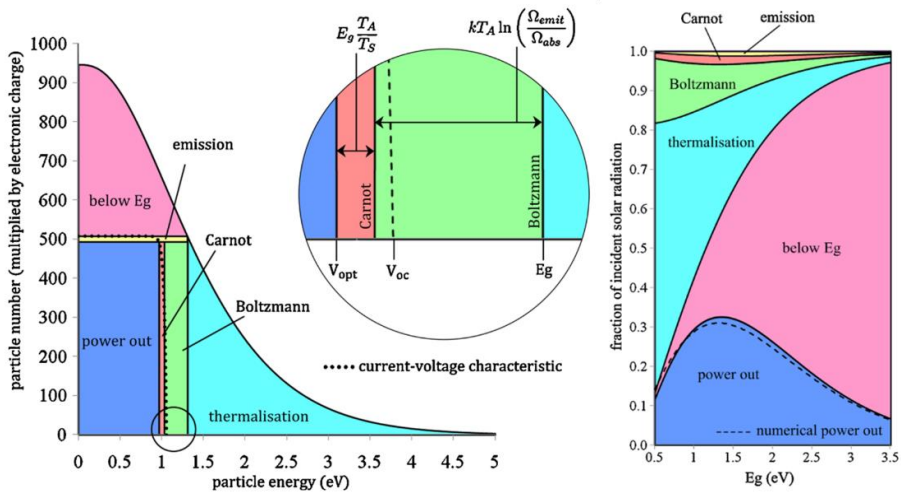


Figure 27: Deviation from ideality of a solar cell due to unavoidable losses. Left) Intrinsic losses of a device with optimal E_g . Right) Translation of the loss process to final power output depending on the bandgap of the device. Reproduced and adapted with permission of John Wiley and Sons.¹⁶⁵

So far we have described the theoretical or intrinsic limiting factors of a solar cell, but there are several parameters that must be optimized “externally”. These elements are easily spotted by quantum efficiency measurements. When the External quantum efficiency is measured the

1 - Introduction

resulting curve (Figure 28) gets far from ideality (i.e. 100% photon-electron conversion). In the example image there are pinpointed these defects, collection in the CdS N-type semiconductor generates no photocurrent as the $SCR \approx l_p$ so no charge separation occurs in the Buffer layer ideally. Reflection and absorption losses can be tailored by engineering of the front surfaces of the cell. Finally lack of complete collection of the carriers in the long-wavelength region, close to the E_g of the absorber layer, can be due to generation outside of the SCR + diffusion length of the charge carriers and thus no effective charge separation is achieved.

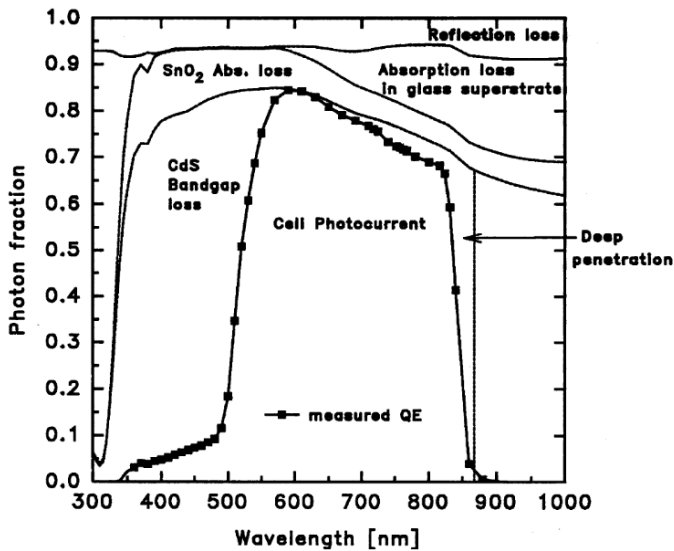


Figure 28: Specific loss mechanisms from a perfect EQE spectra. Reprinted from Publication title, SITES, J., *Quantification of Losses in Thin-Film Polycrystalline Solar Cells*, 75 (1–2), 243–251, Copyright (2003), with permission from Elsevier.¹⁶⁷

Capacitance measurements (C - V) are a good utility to characterise diode junctions and therefore solar cells. This characterization technique is suitable to calculate space charge region width and carrier density in the solar cells. This is normally achieved by measuring the equivalent capacitor that is generated in the P-N junction space charge region. If one considers that the N-type semiconductor is orders of magnitude more doped than the P counterpart, the space charge region can be assumed to be completely shifted to the P side, and thus only parameters for this material are needed for the calculation such as

relative dielectric permittivity ϵ_r , and this way the value of the charge $Q(x)$ can be assumed to be equal to $N(x)$, where x is the SCR width. If a voltage sweep is performed the electric field E through the junction will vary, and this can be represented as the amount of charges that now are inside the SCR as such:

$$dE = \frac{dV}{x} = \frac{q}{\epsilon_0 \epsilon_r} N(x) dx \quad (29)$$

If a standard planar parallel capacitor of area A and capacitance C is considered, then

$$C = \frac{\epsilon_0 \epsilon_r A}{x} \Rightarrow dx = \frac{\epsilon_0 \epsilon_r A}{C^2} dC \quad (30)$$

Combining the previous equations, the resulting carrier concentration is:

$$\begin{aligned} N(x) &= -\frac{C^2}{qxA} \frac{dV}{dC} = -\frac{C^3}{q\epsilon_0 \epsilon_r A^2} \frac{dV}{dC} = -\frac{C^3}{q\epsilon_0 \epsilon_r A^2} \left(\frac{dC}{dV}\right)^{-1} \\ &= -\frac{2}{q\epsilon_0 \epsilon_r A^2} \left(\frac{d(C^{-2})}{dV}\right)^{-1} \end{aligned} \quad (31)$$

Where $x = \epsilon_0 \epsilon_r A / C$

Thus by modifying the voltage applied to the junction and measuring the obtained capacitance the one-dimensional net charge concentration can be obtained as a function of the SCR.

There is a further limitation to device efficiency due to recombination of the charge carriers by several paths. The elimination of these charge carriers principal effect is to modify the shape of the diode current under illumination in relation to the diode current in dark. They can be classified in 3 categories depending on the particles involved: (a) radiative recombination of electrons into photons, (b) Auger recombination of electrons or (c) phonon mediated recombination of electrons. Each one of these contributions (that can happen simultaneously with different ponderation) will modify the diode current of the devices by contributing with specific values of the factors n and J_0 .

1 - Introduction

As a brief description:

- (a) The opposite process of optical absorption, an electron from the conduction band and a hole in the valence band directly recombine emitting a photon. This process is unavoidable and fundamentally limits device *PCE*.
- (b) In contrast with radiative recombination in this process the energy liberated in the recombination of an electron with a hole is transferred directly to another electron/hole promoting it to an excited state. It is also an intrinsic recombination process that cannot be avoided and becomes one of the main limiting factors for example in silicon technologies. Its contribution increases with doping density.
- (c) Recombination by phonons requires defects inside the bandgap of the absorber. This recombination by defect states was defined by Shockley, Read and Hall (SRH)^{168,169}. This is the main limiting process of the three. There are four main regions of recombination: (1) in the PN interface, (2) in the SCR, (3) in the quasi neutral region, which is defined as the region between the SCR and the flat band condition, (4) in the back contact.

Thus, the total diode current will be defined by the combination of all the possible recombination paths Eq. (32), where for specific bias conditions or cell structure one specific path will dominate.

$$J_{diode} = \sum_{i=1}^N J_{0i} \exp \left[\frac{qV}{n_i k_B T} \right] \quad (32)$$

1.5 - Fundamentals of Raman spectroscopy

This thesis is firmly based in Raman spectroscopy measurements and two of the publications rely in the interpretation of the data obtained with this characterization technique. In this subsection a brief summary of the basic theoretical concepts needed to understand the articles is given. The reason of the implication with this technique for the development of the thesis is mainly due to several reasons. First, is a reliable method to analyse the physico-chemical properties of materials and specifically thin films solar cells, due to the spatial precision achievable. Second, the possibility of a non-destructive analysis eases the experimental process and enables the possibility to characterize specific points in a still functional device. Lastly the wavelength dependant penetration and transparency of some of the layers enables the characterization of buried layers in a PV device.

The Raman effect is a scattering effect in which a photon interacting with the mediums losses or gains frequency with a lattice phonon. This is a consequence of a second order effect in which the electric susceptibility of the material (χ) is modified by the vibrations of the atoms, quantized in phonons and the atomic displacement associated with them is denoted by a plane wave $\mathbf{Q}(\mathbf{r}, t)$. As ω_0 is much smaller than the lattice constant, thus χ can be expanded as a Taylor series in \mathbf{Q} .

$$\mathbf{Q}(\mathbf{r}, t) = \mathbf{Q}(\mathbf{q}, \omega_0) \cos(\mathbf{q} \cdot \mathbf{r} - \omega_0 t) \quad (33)$$

$$\chi(\mathbf{k}_i, \omega_i, \mathbf{Q}) = \chi_0(\mathbf{k}_i, \omega_i, \mathbf{Q}) + \left(\frac{\partial \chi}{\partial \mathbf{Q}} \right)_0 \mathbf{Q}(\mathbf{r}, t) + \dots \quad (34)$$

Any incident photon with its associated electromagnetic field will generate a polarization sinusoidal plane wave (\mathbf{P}) depending on the χ of the medium, thus:

$$\mathbf{P}(\mathbf{r}, t, \mathbf{Q}) = \mathbf{P}_0(\mathbf{r}, t) + \mathbf{P}_{ind}(\mathbf{r}, t, \mathbf{Q}) \quad (35)$$

Where \mathbf{P}_0 and \mathbf{P}_{ind} are the polarization of the medium without atomic vibrations and the induced polarization of the coupling of the incident

1 - Introduction

photon with the lattice phonon respectively. Taking into account that the amplitude of the polarization is:

$$\mathbf{P}(\mathbf{k}_i, \omega_i) = \chi(\mathbf{k}_i, \omega_i) \mathbf{F}_i(\mathbf{k}_i, \omega_i) \quad (36)$$

Where \mathbf{F}_i is the amplitude of the incident plane wave. Therefore, \mathbf{P}_{ind} can be expressed as:

$$\begin{aligned} \mathbf{P}_{ind}(\mathbf{r}, t, \mathbf{Q}) &= \left(\frac{\partial \chi}{\partial \mathbf{Q}} \right)_0 \mathbf{Q}(\mathbf{q}, \omega_0) \cos(\mathbf{q} \cdot \mathbf{r} - \omega_0 t) \\ &\quad \times \mathbf{F}_i(\mathbf{k}_i, \omega_i) \cos(\mathbf{q} \cdot \mathbf{r} - \omega_i t) = \\ &= \frac{1}{2} \left(\frac{\partial \chi}{\partial \mathbf{Q}} \right)_0 \mathbf{Q}(\mathbf{q}, \omega_0) \mathbf{F}_i(\mathbf{k}_i, \omega_i) \{ \cos[(\mathbf{k}_i + \mathbf{q}) \\ &\quad \cdot \mathbf{r} - (\omega_i + \omega_0 t)] \\ &\quad + \cos[(\mathbf{k}_i - \mathbf{q}) \cdot \mathbf{r} - (\omega_i - \omega_0 t)] \} \end{aligned} \quad (37)$$

Where it can be distinguished to different out coming waves one with frequency $\omega_s = \omega_i - \omega_0$ Stokes scattered and a second one $\omega_{as} = \omega_i + \omega_0$ anti-Stokes scattered light. Thus, the difference in frequency between the incident light (ω_i) and the scattered light (ω_s or ω_{as}) is called the Raman shift that corresponds to the frequency of the phonon in question (ω_0). Furthermore, wavevector is also conserved so due to the usual values of refractive index in semiconductors \mathbf{q} is much smaller than the Brillouin zone so the only probed phonons will be zone-centre phonons.

The Raman scattering process intensity depends on the polarization of the incident photons in the following fashion

$$I_s \propto |\mathbf{e}_i (\partial \chi / \partial \mathbf{Q})_0 \mathbf{Q}(\omega_0) \mathbf{e}_s|^2 \quad (38)$$

Where the \mathbf{e}_i and the \mathbf{e}_s are the polarization of the incident and scattered photons respectively. If we define a unitary vector $\hat{\mathbf{Q}}(\omega_0) = \mathbf{Q}(\omega_0) / |\mathbf{Q}(\omega_0)|$, then it can be defined what is called the Raman tensor \mathcal{R}

$$I_s \propto |\mathbf{e}_i \cdot \mathcal{R} \cdot \mathbf{e}_s|^2 \quad (39)$$

This second order tensor can be used to define the frequency and the symmetry of a zone centre phonon. Due to the symmetries present in

1.4 - Fundamentals of Raman Spectroscopy

the crystal structures the vibrational modes or phonons will be defined by these structures and these will define the scattering conditions, furthermore for certain polarizations of the incident light (e_i) the intensity may be 0. These modifications to the final intensity can be calculated by the *Raman selection rules*. The appearance or not of the Raman modes depend also in the configuration of the system, i.e. in the wavevector of incident and scattered light (k_i, k_s). This is indeed a rude classical approximation to the real Raman effect for which several nuances have to be accounted for, a full description of the physics can be found in Ref.¹⁶⁰

One of the different effects that are used in the first and third publications is what is called *resonant Raman effect*. Without entering in too much detail, the Raman effect if quantum considerations are taken is a combination of several process that can happen (are happening) at the same time. By selecting an appropriate wavelength of the incident photons one can excite a specific electronic inter band transition, thus neglecting several of the side effects and thus enhancing the Raman cross section. Further increase in the Raman efficiency is achieved if the coupling of the electronic state is with in the vicinity of the bandgap of the material (E_g), in this case what is called a *exciton-mediated multiphonon resonant Raman scattering*, where not only the one phonon mode gets heavily enhanced, but also higher order multiphonon modes get increased. This effect is really suitable for example, to determine the presence of secondary phases in the surface of a thin film, while the presence of these phases can be negligible in relation to the actual amount of the desired material, if the incident photon energy is coupled to the bandgap energy of these secondary phases, the Raman signal can be enhanced orders of magnitude (even using low power density), thus, permitting the detection of these phases even when other techniques such as XRD may not detect them.

Now it will be described briefly the experimental setup needed to perform Raman measurements. First of all, the excitation source must be highly monochromatic, a laser source is normally employed nowadays in contrast to discharge lamps used in the past. The lower the dispersion in energy of a laser line the lower it will be the widening

1 - Introduction

of the detected peaks due to incident photons having frequencies in a continuum range ($\omega_i \pm \Delta\omega$).

Due to the low frequency difference between the laser line and the outgoing photon a high dispersive system is needed, this is normally achieved by a spectrometer with high line density (line/mm) diffraction gratings, even higher for inorganic materials in comparison with organic molecules, and a cut off filter in the entrance of the spectrometer to eliminate as much as the laser signal as possible. An schematic of a Czerny Turner spectrometer used for the measurements performed at IREC is presented in Figure 29.

The final requirements for the system include some optical management system or probe to guide the light coming from the laser line to the sample, normally on a back scattering configuration in the case of semiconductors ($\mathbf{k}_s = -\mathbf{k}_i$) due to the high absorption coefficient α that they present. A collection system of the scattered line and again some light management optics to carry the signal to the spectrometer, where the detector system is placed, the low amount of photons that suffer Raman Scattering generates the necessity to use high signal/noise ratio systems in this case with highly refrigerated CCD systems. Special attention has to be made to reduce the amount of parasitic light inside the system to reduce the background noise.

1.4 - Fundamentals of Raman Spectroscopy

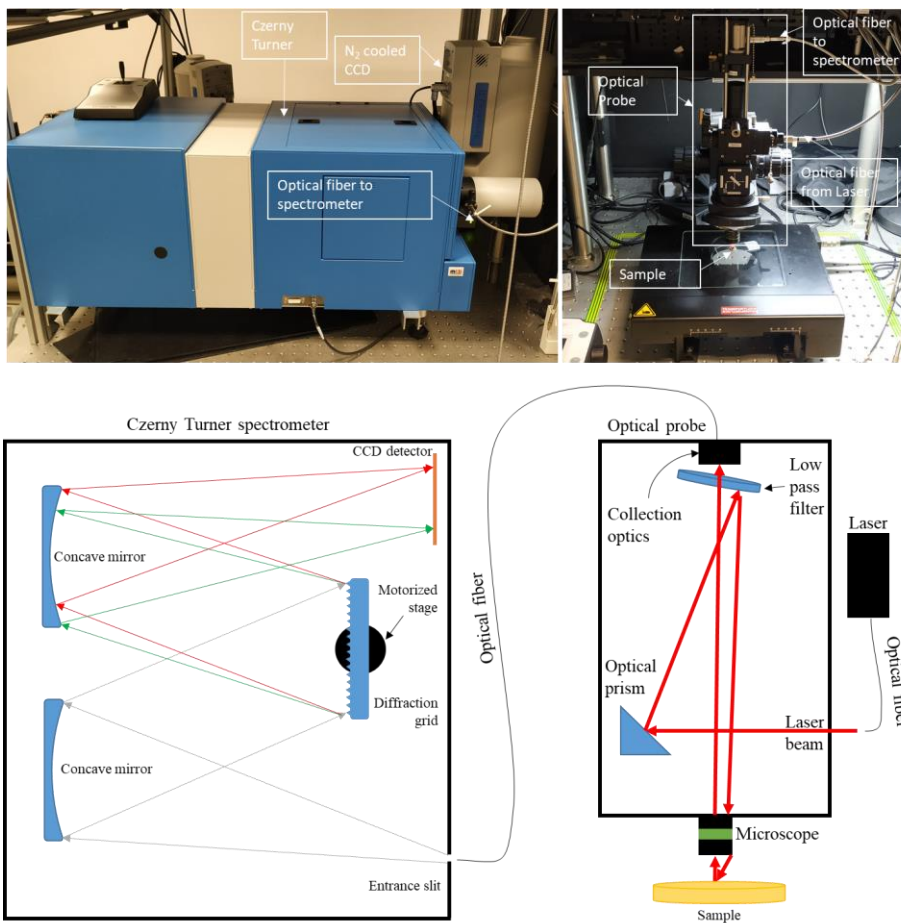


Figure 29: Diagram of the Raman measurement system composed of a top view of the spectrometer and side view of the optical probe.

1.6 - Objectives of the thesis

The fundamental objectives of this doctoral thesis under the title “Antimony Chalcogenides for High Efficiency Thin Film Solar Cell” is to analyse in deep the fundamental properties and develop knowledge of the Sb_2Se_3 compound and explore its potential as an absorber layer in thin film technology for photovoltaic application. In this context three main objectives are proposed:

1. Characterize and develop efficient methodologies for the understanding of the fundamental properties and fast evaluation of the Sb_2Se_3 materials using spectroscopic, structural, and optoelectronic techniques.
2. Develop process and techniques for a controlled synthesis of Sb_2Se_3 based functional devices based in a sequential two-step process consistent in precursor deposition by physical routes followed by a reactive annealing under selenium atmosphere.
3. In depth exploration of the standard SLG/Mo/ Sb_2Se_3 /CdS/i-ZnO/ITO structure limitations, potential performance loss mechanisms, and stability. Proposition of solutions and alternative structures.

2 - Chapter 2: Methodology

In this section an overall view of the fundamentals of the processes and methodologies used for the consecution of this thesis will be introduced. A first section is focused in the layers and device fabrication methodologies. Then a second section focused in the introduction of the characterization techniques used for the analysis of the synthesized layers and devices. Additionally, in chapter 3 in the “experimental section” of each article are explained in detail the techniques and methodologies used for each study regarding the fabrication and characterization performed in the respective articles.

Thus herein there is a summary of the techniques and knowledge acquired that has allowed the achievement of the researcher skills related to synthesis of inorganic thin film layers, fabrication of optoelectronic devices, their electrical and physico-chemical characterization and evaluation. Additionally, the development of new routes of Sb related layer deposition and device fabrication has allowed the attainment of skills to drive a novel research, manage resources and in-depth specific knowledge.

2.1 - Layer synthesis and device fabrication

Standard device employed for the research performed in this thesis is defined as a layered stack of SLG/Mo/Sb₂Se₃/CdS/i-ZnO/ITO. First of all, device fabrication starts with soda lime glass (SLG) substrates, these substrates present very low surface roughness (in order of tens of nanometers) in short spatial ranges (order to tens of μm^2), which is ideal for thin film application due to the overall thickness of the devices ($< 2 \mu\text{m}$). This reduced thickness also implies a necessary thorough cleaning of the dust and small particles from the substrate, this is carried out with by mechanical cleaning with soap and then submitted to a three-step ultrasonic bath cleaning in acetone, isopropanol and deionized water (18.2 M Ω) for a duration of 10 min each, dried with argon and immediately

2 - Methodology

introduced in the sputtering chamber for the Mo back contact deposition in order to avoid any debris to accumulate in the cleaned surface.

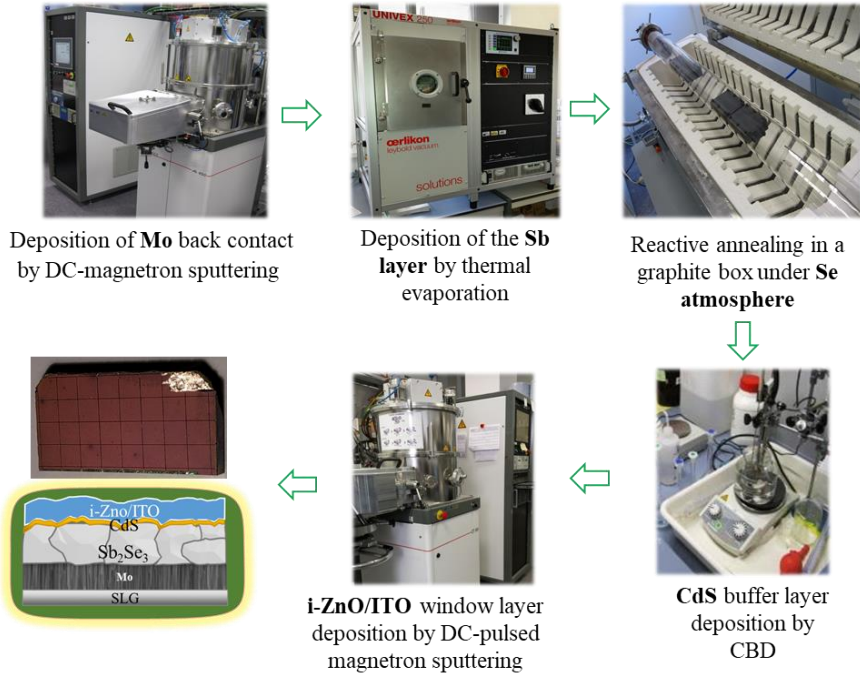


Figure 30: Basic synthesis protocol and structure of a substrate Sb_2Se_3 device.

The clean glasses were then coated with a molybdenum tri-layer structure (around 800 nm full thickness) acting as an electrical back metallic contact, the process of synthesis of this layer was not explored in this thesis and was already optimized in the research group. Its purpose is to act as an electrical back contact, with a controlled superficial selenization using a sacrificial Mo layer (generation of $MoSe_2$ layer) and a dense Mo layer as barrier for this process. This molybdenum staked tri-layer is deposited using a DC-magnetron sputtering machine (Alliance Concept AC450) onto the cleaned SLG substrates following the next steps: i) a first named MoA layer (500 nm) deposited at higher power (4.2 W cm^{-2}) and low pressure ($1.3 \times 10^3 \text{ mbar}$), ii) a second named MoB layer (250 nm), resistant to selenization, deposited at lower power (2.8 W cm^{-2}) and higher pressure ($5.0 \times 10^3 \text{ mbar}$), and finally, iii) a third MoA layer (50 nm) used for sacrificial purposes with the same characteristics as the first one, the total sheet resistance of the trilayer being $\approx 0.3 \text{ } \Omega \text{ sq}^{-1}$. The back contact was

2.1 - Layer synthesis and device fabrication

further completed (at the final step of device fabrication) by thermal soldering of an Indium contact in the exposed Mo surface (achieved by mechanical scratching of the subsequent layers), to ensure Ohmic connection to the measuring tips employed in the optoelectronic characterization.

The Sb_2Se_3 absorber precursor layer consists of a Sb metallic layer deposited by thermal evaporation (Oerlikon Univex 250) onto the Mo tri-layer. Two commercial Sb precursors were employed. First from elemental powder (Alfa Aesar, 99.5%), although this method was highly unreliable since the powder, in some occasions, heavily reacted with the boat, ending on the material getting propelled off the boat, most probably due to sublimation of the Sb directly in contact with the boat. A second Sb precursor was successfully implemented based in elemental Sb pellets (Alfa Aesar, Sb shots 1–3 mm, Puratronic, 6N metal basis), these were much more suitable for the purpose with reliable evaporation. The boat material was also changed from a pure tungsten boat to a Molybdenum coated tungsten boat, although literature seems not to be clear on the preferred boat material and do not recommend thermal evaporation for Sb metal, the evaporation was carried out without any problem for both materials with slight more problem-free deposition for the latter option.

The Sb thermal evaporation was performed with the following conditions: the SLG/Mo layers (up to $10 \times 10 \text{ cm}^2$) were fixed in a rotation plate which was maintained at 10 rpm during the whole process in order to achieve thickness homogeneity, the evaporation rate was measured by a quartz sensor properly calibrated and the rate of deposition was adjusted by a proportional–integral–derivative (PID) controller embedded in the evaporator system, several deposition rates ($0.1\text{--}30 \text{ \AA s}^{-1}$) were explored as presented in the next section. Electrical power flowing through the precursor boat was maintained around $\approx 50 \text{ W}$, although this parameter heavily depends on the boat size, material, precursor type and quantity (first or last evaporation). Base pressure was maintained at $\approx 10^{-5} \text{ mbar}$ by a turbo-molecular pump. In order to corroborate a successful deposition of the Sb metallic layers, the thickness of the as deposited layers were measured by XRF previously calibrated by reference samples.

The Sb coated sample(s) was then cut into pieces of different sizes, but limited to $2.5 \times 2.5 \text{ cm}^2$ maximum sample size. This size is limited by the

2 - Methodology

available volume in the graphite box (26.5 cm^3 with functional $2.5 \times 2.5 \text{ cm}^2$ area) which are used in the reactive selenization annealing process. These graphite boxes were employed due to the high thermal homogeneity they provide, and to guarantee a control over the Se partial pressure at which the reaction takes place with the Sb metallic film. Despite the advantages of the graphite boxes they present some drawbacks, such as accumulation of Se chalcogen excess, almost impossible to eliminate, mostly due to the porous nature of the graphite, due to the same reason no chemicals could be employed for the cleaning process. Only physical cleaning process were utilized to clean the boxes, by a maintained annealing at $T = 650 \text{ }^\circ\text{C}$ during one hour in constant vacuum conditions to de-gas the selenium excess, this selenium excess in the boxes was tracked down and the boxes were cleaned systematically.

The selenization process is performed introducing the samples in the graphite boxes with some selenium mass (Alfa Aesar Puratronic, 99.9995 %) in powder form, where 25 mg was the experimentally best performing amount of material for the thermodynamic conditions explored in this thesis. The boxes were introduced in a sealed quartz tubular furnace, the tube was filled with argon to provide an inert atmosphere and to control the system pressure, several de-gas procedures were carried out by a mechanical pump before each process, to ensure no oxygen was present in the atmosphere. After the atmosphere is controlled inside of the tube, a thermal routine based in 1 step is performed at the desired temperature with a fixed initial Ar pressure that is specified based on the final pressure desired during the dwell time. Samples were let to cool down naturally after the treatment, and were not taken out of the boxes before being cool down to room temperature to avoid any possible increase in the oxidation of the surface. After this process a homogeneous layer of Sb_2Se_3 with thickness in the range of 0.2 and $2 \text{ }\mu\text{m}$ is obtained, where the thickness is dependent of the thickness of the Sb precursor

Once the Sb_2Se_3 absorber is synthesized The heterojunction was then completed with an n-type CdS buffer layer (50 nm) deposited by chemical bath deposition (CBD), being the Cd source $\text{Cd}(\text{NO}_3)_2$, with conditions $[\text{Cd}(\text{NO}_3)_2] = 0.12 \text{ M}$, [thiourea] 0.3 M, pH = 9.5, $T = 80 \text{ }^\circ\text{C}$, the full process with a duration of 40 min.

2.1 - Layer synthesis and device fabrication

The front transparent conductive window layer formed by i-ZnO (50 nm) and In₂O₃:SnO₂ (90/10 wt%) (150 nm) layers were deposited by DC-pulsed magnetron sputtering (Alliance Concept CT100) at $\approx 50^{\circ}\text{C}$ due to parasitic radiative heating by the plasma. Individual solar cells (3 x 3 mm²) were then insulated using a manual mechanical scriber (Micro Diamond MR200 OEG) with a scribed line width of 20 μm .

2.2 - Layers and device characterization

Physicochemical and optoelectronic characterization of the different layers and final devices was performed systematically during the development of this thesis. The objective of these characterization is the identification of the origin of the loss mechanisms in the device performance, and the impact of the synthesis and device fabrication parameters in the properties of the layers and devices. The characterization techniques utilised for this work are based in the following techniques:

X-Ray fluorescence spectroscopy (XRF): Compositional measurements and thickness estimation of the different layers were determined with an X-Ray fluorescence (XRF) equipment (Fischerscope XVD) calibrated by inductively coupled plasma (ICP); the measurements were normally conducted in a 4 x 4 point grid covering the full area of the samples, individual 3 x 3 mm cells were occasionally measured to discretely calculate composition in the cell in question. The measurements are done using a 50 kV accelerating voltage, a Ni10 filter to reduce background signal, and an integration time per measuring point of 45 s. The equipment in question comes equipped with a measurement analyser software that permits the estimation of compositions and thickness of the layer stacks by calculating attenuations in the subsequent layers, this required sample calibration that was achieved by inductively coupled plasma (ICP)

Field emission Secondary electros microscope (FE-SEM): The FE-SEM micrographs have been performed to evaluate the morphology of the layers and full devices with nanometric resolution (order 20nm). The micrographs were acquired using a Zeiss Series Auriga field-emission equipment. All the images presented in the thesis are mainly performed by

2 - Methodology

analysis of secondary electron emission collected by an Everhart-Thornley detector. Top view images and cross sectional images were normally acquired for the experimental samples. The former permits the analysis of the sample surface, and the later allows the analysis of the layered structure, previous cleavage of the sample. Normal operating conditions consist on an acceleration voltage of 5 kV, and working distances ranging between 3 and 5 depending on the sample.

High resolution transmission electron microscopy (HRTEM): The HRTEM and low magnification DF-BF cross-sectional micrographs were employed to assess the interfaces of the standard devices and analyse in detail the layered structure, the analysis was performed by Javier Blanco-Portals, Francesca Peiró and Sònia Estrade at the LENS-MIND *Departament d'Enginyeria Electrònica i Biomèdica* of the University of Barcelona, were acquired in a JEOL-2010F with a field emission gun at 200 keV. The high resolution HAADF (STEM) images and EELS spectrum images were acquired in a JEOL- ARM-F with field emission gun at 200 keV (FEG electron source and Cs aberration correction in the condenser lens system).

X-ray diffraction (XRD): XRD measurements were performed in order to evaluate the crystal structure, the micro structure and the phase formation. The XRD analysis were performed routinely with the equipment available at IREC facilities, a Bruker D8 Advance equipment in Bragg–Brentano configuration from 10° to 90° with a step size of 0.02° and using a 1D detector, this allowed quality assessment of the films and preferred orientation estimation. High signal noise ratio and high angle resolution measurements were acquired in collaboration with the CCTiUB University of Barcelona, obtained with a PANalytical X'Pert PRO MPD alpha Bragg-Brentano powder diffractometer using a Cu tube operating at 45 kV and 40 mA, a Johansson type Ge (111) primary focalizing monochromator and a solid state strip 1D PIXcel^{1D} detector. High resolution, high statistics, full angular range Cu K α_1 $\theta/2\theta$ scans were normally performed. An automatic divergence slit system and a mask enabled a constant irradiated surface (10×12 mm²) over the analyzed samples. Full profile analysis was performed in the UB by applying Rietveld refinement for all the crystalline structure phases observed.¹⁷⁰ The refinements have been performed through the TOPAS v6 software.¹⁷¹ The peak width of each phase was

2.1 - Layer synthesis and device fabrication

modelled with the Double-Voigt Approach by considering both the Lorentzian contribution of the crystallite size effect and the Gaussian contribution of the microstrain to the peak width.¹⁷² Preferential orientation corrections were applied by spherical harmonics.¹⁷³ The background was modelled with a 15th order Chebyshev polynomial. The instrumental contribution to the diffraction profile was calculated with the Fundamental Parameters Approach.¹⁷⁴

Raman spectroscopy: Raman measurements have been performed using IREC developed Raman setups (Figure 29) optimized for the UV–Visible spectral region (based on Horiba Jobin Yvon FHR640 monochromator) and NIR–IR region (based on Horiba Jobin Yvon iHR320 monochromator). The first system is coupled with an open electrode CCD detector cooled down to 75 °C and the second with NIR enhanced CCD detector cooled down to 75 °C, also an InGaAs array detector cooled to liquid nitrogen temperature (-132 °C) was used for the measurements obtained with the 1064 nm excitation wavelength. For the last publication a high resolution low signal/noise ratio open electrode CCD cooled to liquid nitrogen temperature was employed (-132 °C). The measurements were performed in back scattering configuration through a specific probe designed at IREC. Solid state lasers ($\lambda_{ex} = 532, 633, 785, 1064$ nm), and gas He-Cd lasers ($\lambda_{ex} = 335, 442$ nm) were used as excitation sources. Different gratings for the light dispersion were employed to optimize the spectral resolution. The measurements were always performed with laser power density below 25 W cm^{-2} by using a macrospot with a diameter in the range of 50–70 μm depending on the excitation wavelength due to the high instability of the system with temperature. Finally, the use of unpolarised laser beam allowed to minimize the impact of the crystalline orientation in the Raman spectra. Measurements under different polarization conditions were performed at the University of Barcelona using the LabRam HR800UV system from Horiba Jobin Yvon with polarization filters.

Current density-voltage (J–V): J–V measurements were performed under illumination and in dark conditions has been performed to evaluate the final device performance. J–V characteristics were acquired on complete devices using a Sun 3000 AAA solar simulator from Abet Technology (uniform illumination area of $15 \times 15 \text{ cm}^2$) calibrated with a Si reference

2 - Methodology

solar cell under AM1.5 illumination. An extension of the J-V technique has been performed in order to identify the activation energy (E_a) of specific recombination process. The current density–voltage–temperature (J–V–T) analysis was performed by introducing the sample into a cryostat (Cold-Head model RDK-101D Sumitomo Heavy Industries Ltd.) cooled by a Helium closed cycle compressor (Zephyr HC-4A from Sumitomo cryogenics). Samples were illuminated with a solar simulator (Oriel LCS AM1.5 model 94011A). Samples were attached with silver paste to the cold finger and a temperature sensor was placed aside on top of a 3 mm SLG piece to mimic the conditions of the film. Electrical contacts were performed on a four-probe configuration. The same cryostat was employed to perform low temperature Raman measurements without the electrical contacts.

Impedance (C–V): The C-V measurements were performed with the objective to evaluate the defects density (doping level) and its distribution in the heterojunction (Sb₂Se₃-CdS interface). C-V characterization were performed with a Keysight E4990A impedance analyzer and a homemade faraday cage four-probe setup. Samples were kept in dark conditions during the measurement. The equivalent circuit model used is composed of a series resistance, a parallel resistance and a capacitor.

4-point probe: 4-point measurements were performed to assess the sheet resistance of the conducting layers as a figure of merit to check their quality, this was employed only to measure Molybdenum and ITO front contact layers.

Quantum efficiency (QE): QE characterization was performed in order to evaluate the electrical photo response in function of the excitation wavelength in the range of the UV-IR. The QE measurements were conducted with a Bentham PVE300 spectral response system in the 300-1600 nm range calibrated with Si and Ge reference photodiodes. Reflectance measurements were also performed with an integration sphere, available on the system's optics, in order to obtain the Internal quantum efficiency (IQE). Voltage dependant measurements were achieved by connecting a keythley 2400 as a voltage source to the measuring tips

3 - Chapter 3: Publications

This thesis is structured in the shape of article compendium, where the scientific articles in which this manuscript is founded, are collected in this section and will constitute the following subchapters. These articles have been published in high impact factor journals under the titles:

- Multiwavelength excitation Raman scattering study of Sb_2Se_3 compound: fundamental vibrational properties and secondary phases detection. **2D Mater.**, vol. 6, no. 4, p. 045054, Sep. 2019, doi: 10.1088/2053-1583/ab4029. **IMPACT FACTOR (IF): 7.14 (Q1).**
- Efficient Se-Rich $\text{Sb}_2\text{Se}_3/\text{CdS}$ Planar Heterojunction Solar Cells by Sequential Processing: Control and Influence of Se Content. **Sol. RRL**, p. 2000141, May 2020, doi: 10.1002/solr.202000141. **IMPACT FACTOR (IF): 8.582 (Q1).**
- Insights on the Thermal Stability of the Sb_2Se_3 Quasi-1D Photovoltaic Technology. **Sol. RRL**, p. 2100517, 2021, doi: 10.1002/solr.202100517. **IMPACT FACTOR (IF): 8.582 (Q1).**

3.1 - Introduction to publications and side experiments

In this sub-section is presented a general introduction to the three main articles that summarize the work performed during the 2017-2021 period in the frame of the PhD researcher formation at IREC. The activities were performed in the frame of an internal project at IREC with the following objective: innovation in new PV materials and explore their potential for new generation of PV applications. The results obtained during the 4 years of this internal IREC project permitted to open a new research line based in the $\text{Sb}_2(\text{S},\text{Se})_3$ absorber family of materials that currently involves to 6 researchers at IREC (including 4 pre-doctoral and 2 post-doctoral researchers). The presentation of these three works compose this thesis. Herein the works are presented with an introduction including the motivation for each one inside the workflow that led to the article publication. Furthermore, in the discussion of the different works, additional supporting research no published are presented.

The first article (Section 3.2), compiles the developed Raman Spectroscopy characterization to understanding the vibrational properties of the Sb_2Se_3 layers and the development of new methodologies for a correct characterization of the Sb_2Se_3 system. Before this work, a clear identification of the Raman fingerprint of the antimony selenide was not available in the literature across different fields of research. The unclear identification of the Raman signature observed in the bibliography was reflected normally in two kinds of spectra repeatedly reported in the literature as proper spectrums for the Sb_2Se_3 system, taking into consideration same stoichiometry and crystal structure. Additionally, the spectra reported didn't have enough quality/resolution to contrast the peaks observed with the expected theoretical phonons. In Figure 31 are shown two examples of the main finger prints reported in the bibliography.¹²² In the first period the thesis doctoral a strong effort has been performed to clarify the Sb_2Se_3 fingerprint. This was performed by a systematic characterization of a single crystalline Sb_2Se_3 with all the possible wavelengths available show that indeed the left spectrum of Figure 31 corresponded to Sb_2Se_3 plus elemental amorphous selenium (a-Se), and the right spectrum correspond to a heavily decomposed Sb_2Se_3 plus $\alpha\text{-Sb}_2\text{O}_3$ and $\beta\text{-Sb}_2\text{O}_3$. Several authors reported the left spectrum, that clearly show

3 - Publications

presence of a-Se (254.4 cm^{-1}), as the spectrum of the pure Sb_2Se_3 system and possibly compromising their hypothesis. The right spectrum is normally a consequence of high power density in the sample resulting in the degradation of the material in oxidizing atmosphere, we quickly detected this malpractice in the measurement procedure and it was soon reported by Shongalova et al.¹⁷⁵

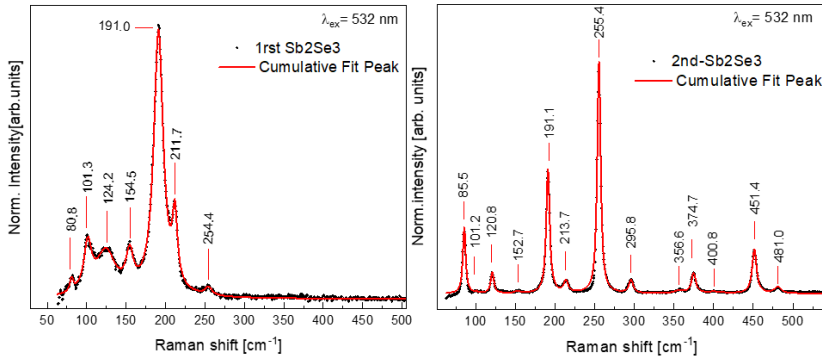


Figure 31: Examples of Sb_2Se_3 decomposition under laser power. Left) Sb_2Se_3 phase plus a-Se (254.4 cm^{-1}). Right) decomposed Sb_2Se_3 in $\alpha\text{-Sb}_2\text{O}_3$ and $\beta\text{-Sb}_2\text{O}_3$.

Thin film technologies are heavily dependent on the interfacial properties of the layers and Raman spectroscopy has proven to be a key characterization technique for thin film technologies from the characterization of structural modifications, defects and secondary phases detection in very few nanometers depth, where this information gets shaded by the bulk information with techniques like XRD. With this in mind we fully characterize a single crystal sample in the article “*Multiwavelength excitation Raman scattering study of Sb_2Se_3 compound: fundamental vibrational properties and secondary phases detection*”. Where we were able to deconvolute 28 Raman modes of 30 possible in the structure, by means of simultaneous fitting using a different spectra acquired under different excitation conditions including multiwavelength excitation, polarization and low temperature (10 K) measurements. This, and above, the characterization of the possible secondary phases present in the synthesis procedures, and the hypothesis of ribbon orientation assessment by polarization measurements (proposed during the first experiments of this doctoral thesis and posteriorly confirmed-developed by Nicole Fleck et al.¹⁷⁶) enables the utilization of the technique as a tool

3.1 - Introduction to publications and side experiments

to assess surface alignment of the 1D ribbons, with the preferred orientation being translated into a reduction of the 110-160 cm^{-1} area in the Sb_2Se_3 fingerprint. These points place Raman spectroscopy as a robust, fast, non-destructive characterization technique, even after synthesis of the complete devices if the proper wavelength is selected.

At the same time, the focus was placed on the synthesis of thin films with Sb_2Se_3 absorber layers by a sequential process based in the reactive annealing under selenium atmosphere of physically evaporated antimony layers and then followed by deposition of the emitter layer of CdS by a CBD process and completed by sputtering of the window/contact layer as described in section 2, Figure 30. The development of efficient devices using substrate configuration (similar structure to other mature thin films technologies like to CIGS, CZTSe) allows an accelerated transference to the PV industry.

The optimization of the Sb layer was done by modifying the evaporation rate employed in the thermal evaporation process, the visual aspect was explored by SEM show differences in the deposition ratio (Figure 32). Raman measurements were performed on the precursor layer, where the same crystal quality was observed regardless of the evaporation rate. However, for the main antimony peak, it can be noticed a shift towards lower frequencies for the 5, 10 and 30 $\text{\AA}/\text{s}$ that at first approximation it could be related to a constrain in the structure (Figure 32). Even with the modifications presented, up to date, no correlation has been found with final device quality (Figure 33), so 10 $\text{\AA}/\text{s}$ was adopted for a compromise in a fast but reliable in thickness process.

3 - Publications

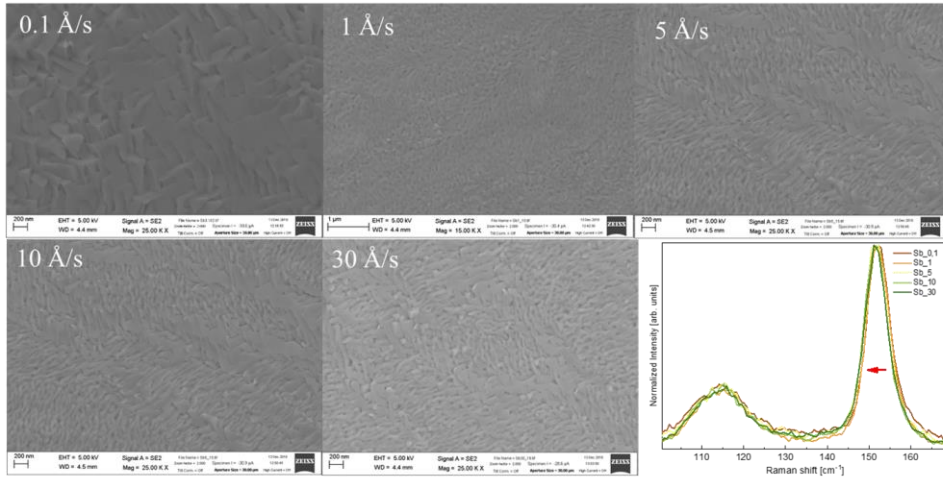


Figure 32: Sb metallic layers evaporated at different rates. Bottom right) Raman scattering of Sb metallic layers with different deposition rates.

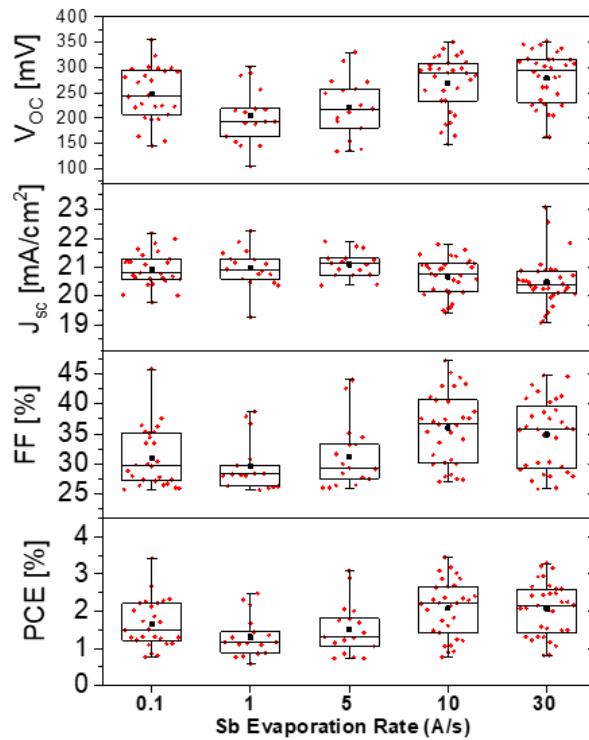


Figure 33: Optoelectronic parameters in function of the deposition rate.

3.1 - Introduction to publications and side experiments

The final Sb_2Se_3 absorber layers present a homogeneous thickness with well packed grains of lateral sizes between 100-300nm but continuous through the thickness of the device (Figure 34a,b). The composition of the final Sb_2Se_3 films was normally assessed by XRF measurements and this were confirmed by ICP and EDX measurements, the later can be observed in Figure 34c. As explored in the second article “*Efficient Se-Rich $\text{Sb}_2\text{Se}_3/\text{CdS}$ Planar Heterojunction Solar Cells by Sequential Processing: Control and Influence of Se Content*”, the best performing devices were the ones with a final Se rich composition and structure like those presented in Figure 34.

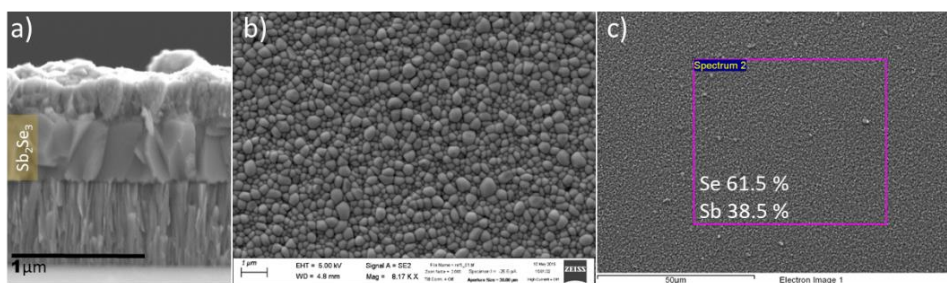


Figure 34: a) Cross-section image of a complete device with the Sb_2Se_3 layer identified. b) Top view of a pristine Sb_2Se_3 layer. c) EDS measurement on the surface of a Sb_2Se_3 layer.

The control of the final thickness of the absorber layer is determined by this antimony precursor layer approximately in a x2.5 factor (Figure 35a). It was observed a clear dependence between the Sb precursor thickness with the final $3[\text{Sb}]/2[\text{Se}]$ ratio (with a fixed Se quantity of 25 mg of the standard process), resulting in selenium poor absorber films for Sb precursor thickness far from the optimal range. The possibility to saturate the atmosphere is also discarded, due to the formation of high amounts of elemental selenium in the surface of the film if the partial pressure of Se is elevated. At this point, to obtain the higher thicknesses, the amount of Se in the graphite box had to be increased to obtain proper composition, where for the 611, 817 and 1000 nm Sb precursor films, 35, 45 and 55 mg of selenium powder where added respectively (Figure 35b).

The thickness optimization was carried out in order to explore the optical limit of absorption in the devices, to find then the optimal compromise between material usage and collection efficiency for the longer

3 - Publications

wavelengths, with the doubt of losing long wavelength photons by the observed triangular shape of the external quantum efficiency. However, were a collection problem is clearly observed for absorber thickness under 600 nm no representative increase in the collection efficiency for longer wavelengths is found for absorbers of 1500 nm (Figure 36), so further on, the optimized thickness was set up in the range of 700-800 nm, in order to reduce material usage, and prevent and reduce bulk recombination without compromising the *PCE*, this result is also consistent with numerical calculations.¹⁷⁷ Additionally, bias voltage internal quantum efficiency (*IQE(V)*) measurements were performed (Figure 36b), and the measurements highlighted a collection problem of the charge carriers generated by IR photons, that are not able to reach the front contact. Notice how the *IQE* reaches values higher than > 90 % between 600-700 nm implying a perfect collection in the first nanometers of the Sb_2Se_3 layer (inside the space charge region). These two facts together: the constant *IQE* with increasing absorber thickness and the increased *IQE(-1V)*, pointing towards a clear limitation in the diffusion length/lifetime of the charge carriers or a small space charge region.¹³⁹

3.1 - Introduction to publications and side experiments

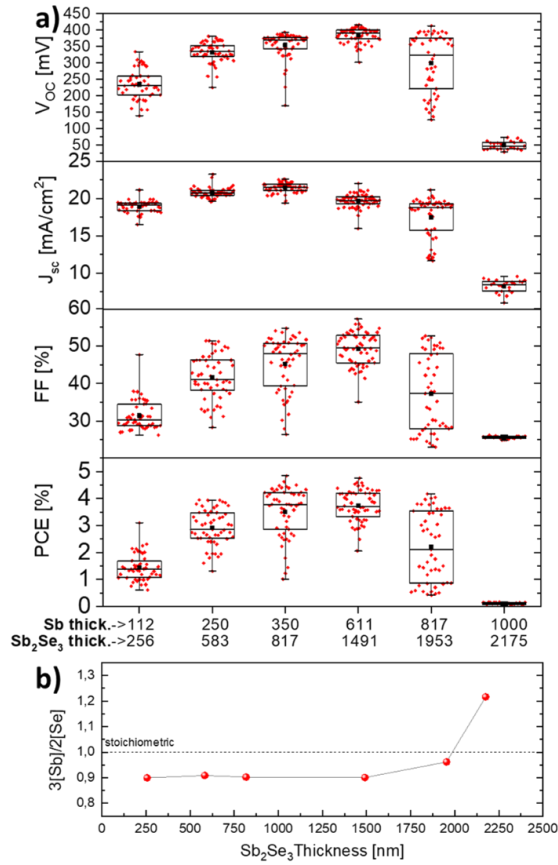


Figure 35: a) Thickness dependence of the optoelectronic properties. b) Average compositional ratio extracted from XRF measurements vs final Sb_2Se_3 thickness.

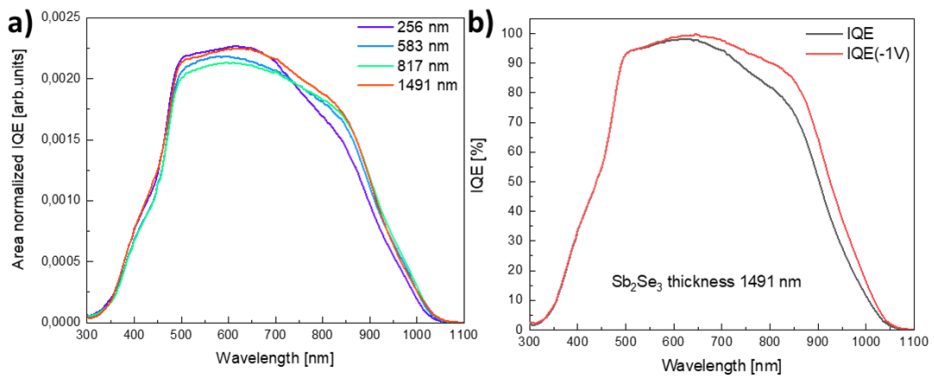


Figure 36: a) Area normalized IQE of different thickness Sb_2Se_3 devices. b) IQE and IQE(-1V) of best performing device with $\sim 1.5 \mu m$ absorber thickness.

3 - Publications

Further explanation and analysis of the basic limitations found in this kind of devices, with structure SLG/Mo/Sb₂Se₃/CdS/i-ZnO/ITO, with already optimized reactive annealing process can be found in second article “*Efficient Se-Rich Sb₂Se₃/CdS Planar Heterojunction Solar Cells by Sequential Processing: Control and Influence of Se Content*”, where the nominal composition dependent performance of the system is explored, and its implications in the material properties (as mentioned in the introduction section) for which a p-type conductivity is desired and obtained through off-stoichiometry doping of Se excess. It is also shown that an excessive increase in Se content lead to a counter-intuitive decrease in performance,¹²³ that has been explained as a strange defect compensation by the same group in a recent publication (M. Huang et al.¹⁷⁸) pointing towards an increase of V_{Se2} donor defects with increasing Se content. Furthermore, we tried to find the limitations of this basic device structure.

Additional experiments were carried out regarding the optimization of the device structure. As it is presented in Figure 36b (and further discussed in the second article), the limitations in the collection efficiency in the longer wavelength may come from a non-optimized back contact or lack of a collection barrier, which could increase the recombination in the back interface, subsequently reducing the lifetime/diffusion length of the minority carriers. First of all, we explored the synthesis mechanisms, a screening of substrates was performed where tungsten (W), silver (Ag), gold (Au) and aluminum (Al). and several thickness were tested on top of the Mo layer. Somehow the Sb₂Se₃ was not formed with silver back contact and an low crystal quality material was obtained. In the case of Al, the back contact heavily reacted with the CdS CBD process and peel off occurred. In contrast, Au and W back contact give functional devices but with decreasing performance with increasing layer thickness.

With the objective of improve the back contact collection and promote the hole extraction, different hole transport layers (HTL) were explored and deposited through thermal evaporation. Among them six oxides were studied MoO₂, MoO₃, WO₃, V₂O₅, NiO₂ and Nb₂O₅, this last one peeled off during the CdS CBD meaning a bad adhesion to the Mo layer or reaction to the chemical bath. Three thickness were explored for each layer (2, 5 and 10 nm) with a decreasing performance with increasing thickness.

3.1 - Introduction to publications and side experiments

Even though, none of the aforementioned layers presented relevant impact in the optoelectronic parameters, all of them ending in a degradation of the optoelectronic parameters (Figure 37).

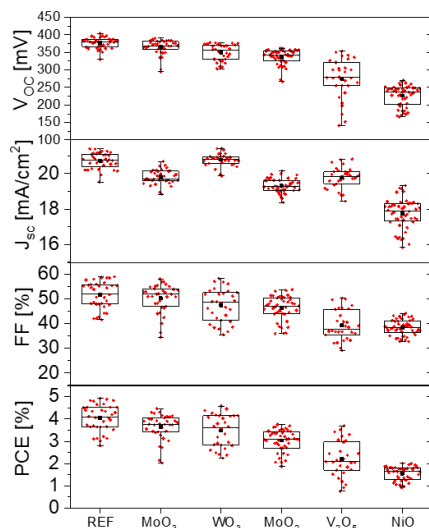


Figure 37: Optoelectronic parameters of different HTL materials with 2 nm thickness.

The standard hole transport layer in CIGS and CZTS structure is the molybdenum selenide/sulfide ($\text{Mo}(\text{S},\text{Se})_2$), depending on the chalcogen in which the absorber is based),^{179–182} in the context of these technologies it is mostly considered as way to ensure ohmic back contact but serves also as an electron blocking layer (or hole transport layer). In this systems the layers normally self-generate during the reactive annealing process. In our case the low temperatures employed (~ 320 °C) generate, at best, a residual tenths of nanometers of MoSe_2 in the back contact. In this regard, pre synthesis of the MoSe_2 layers was explored by reactive annealing of the Molybdenum substrate at different temperatures, with 20 mg of selenium powder mass and ~ 1 bar static pressure. Increasing homogeneity in the optoelectronic properties of the devices is found with the pre-synthesis of this layer that finds its optimal synthesis temperatures at 400 °C Figure 38a, temperature at which the synthesis of the Sb_2Se_3 is suboptimal, further increase in the temperature lead to underperforming devices. The observed improvement is clearly reflected from the increased homogeneity in the V_{oc} of all the devices in each of the samples, and an increase in the FF of the devices.^{106,183} Structural characterization of the MoSe_2 layer was done

3 - Publications

prior to synthesis of the Sb_2Se_3 layer by means of Raman spectroscopy. Here a clear correlation between areas of the peaks marked in Figure 38b, is found with the synthesis temperature of the MoSe_2 layer, and is further correlated with the median FF values of the devices (Figure 38c), standing for the most prominent effect in the final PCE . This observation can have two implications, or the resistance of the MoSe_2 is reducing by proper alignment of the 2D foils, or it is affecting the alignment of the Sb_2Se_3 ribbons themselves. The modification of the areas of the peaks in the MoSe_2 Raman spectra and its translation to foil alignment is related to the symmetry of the selected peaks.^{117,184}

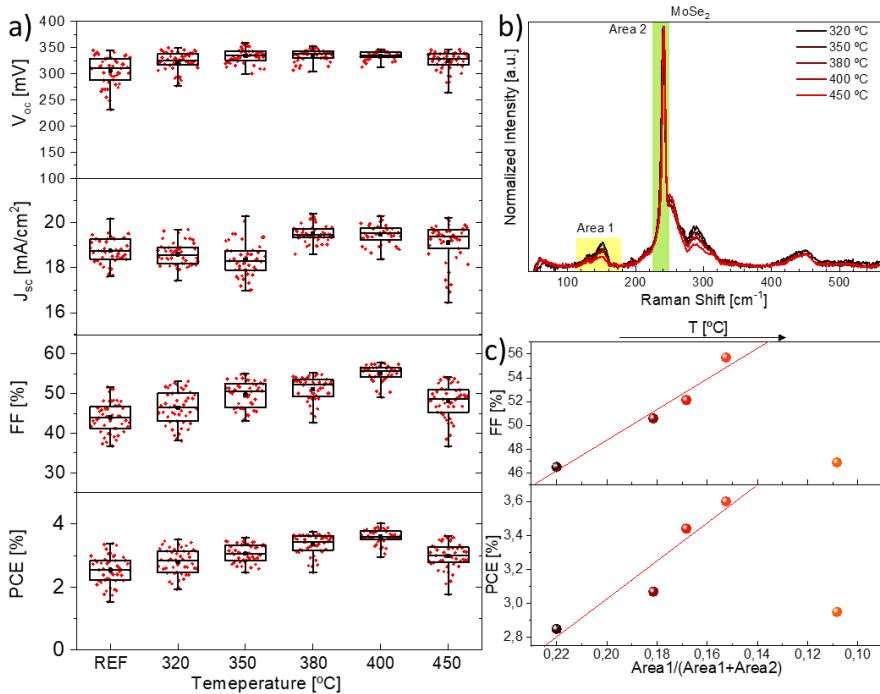


Figure 38: a) MoSe_2 pre-synthesis temperature and impact on optoelectronic properties. b) Raman measurements with excitation wavelength $\lambda_{ex} = 633$ nm performed on the as-synthesized MoSe_2 layer. c) Relation of the areas marked in figure b with the FF factor and PCE of the final devices.

Nevertheless, the pre-synthesis of this layer seems to improve a non-homogenous back contact but if the reference sample already has optimal homogeneity no improvement is then achieved, thus, it may be considered a safety process but with no overall improvement.

3.1 - Introduction to publications and side experiments

Further modification of this layer was achieved with the inclusion of a germanium nanometric layer on top of the pre-synthesized MoSe₂ layer. Although these are preliminary results, a clear modification of the optoelectronic properties is found with increased V_{oc} and J_{sc} but a decrease in the FF (Figure 39a), most probably due to a noticeable relation in the device surface texture with the increased Ge content towards a non-desirable or less [hk1] preferred orientation (Figure 39b, calculated from Raman spectroscopy analysis), thus increasing the resistance of the devices. Increased of the V_{bi} and SCRw are observed without a clear decrease in the doping level in which is a good sign of increased device quality. In the FE-SEM micrographs (Figure 40) the pre-synthesized MoSe₂ layer is clearly visible, where a unclear transition from this layer to the Sb₂Se₃ layer points towards the presence of an intermediate layer associated with a Ge-Se phase.

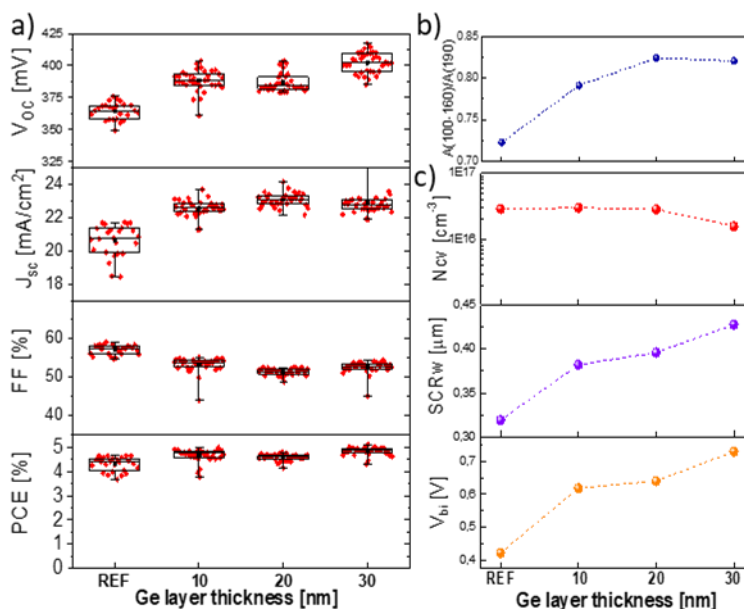


Figure 39: Effects of the inclusion of a Ge layer on top of pre-synthesized MoSe₂: a) On the optoelectronic parameters, b) on the ribbon alignment, c) on the density charge carrier density (N_{cv}), the space charge region width (SCRw) and built-in voltage (V_{bi}).

3 - Publications

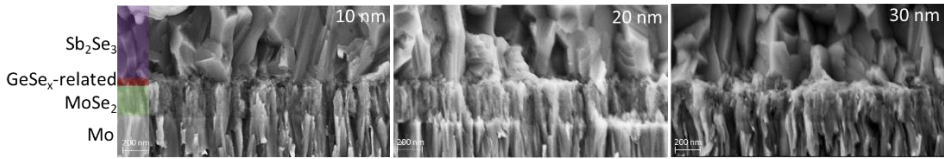


Figure 40: FE-SEM micrographs of the back contact of Sb_2Se_3 samples with different deposited Ge thickness.

Regarding the front interface some attempts were done to improve the cadmium sulphide buffer layer or to completely remove it (due to its toxic nature), in order to achieve a more future proof technology. Two modifications to the CdS reference layer were explored by adding alkaline elements (Li and K), and its substitution for ZnS and In_2S_3 ; and the combination of both with CdS were also tested, all the layers were synthesized by CBD. Analysing the optoelectronic parameters (Figure 41), the best results are for CdS:Li but the results are really comparable with the reference sample although showing less dispersion on the V_{oc} of the cells but higher dispersion in the FF and thus PCE .

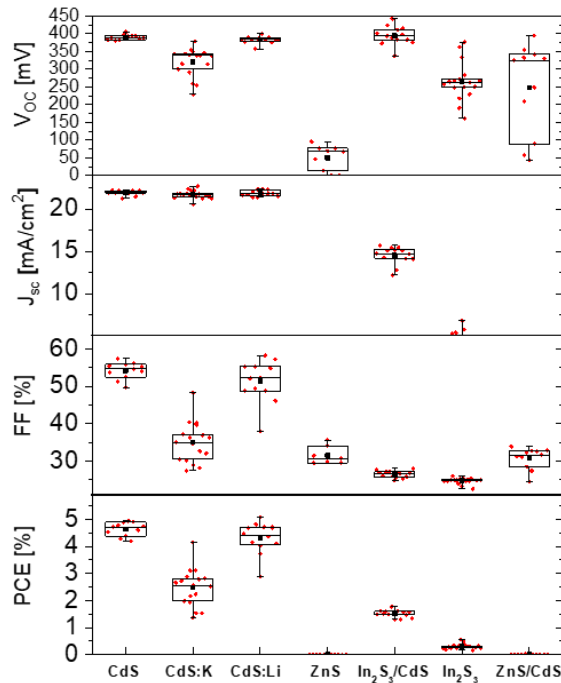


Figure 41: Optoelectronic parameter of the different electron transport layers studied.

3.1 - Introduction to publications and side experiments

Further modifications of the front interface were performed by alkaline treatment of the Sb_2Se_3 surface, this was done with knowledge of the previously shown beneficial effects for CIGS technology.¹⁸⁵ The objective of this research is to find an approach in which the applied treatment only affects the surface of the material, in contrast to bulk treatments, or inclusion of the alkaline elements during synthesis. In order to fulfil the approach, alkaline fluorides (LiF, NaF, KF) of different thickness were deposited by means of thermal evaporation on top of pristine SLG/Mo/ Sb_2Se_3 samples (Figure 42). Afterwards the samples were subjected to an annealing in selenium atmosphere at 250 °C. This treatment is tailored in temperature in order to not modify the composition of the Sb_2Se_3 layer. The objective of the Selenium atmosphere is to avoid the loss of any selenium in the structure during the PDT process as previously demonstrated.¹⁸⁶ In the next section the evaluation of the structural modifications is presented.

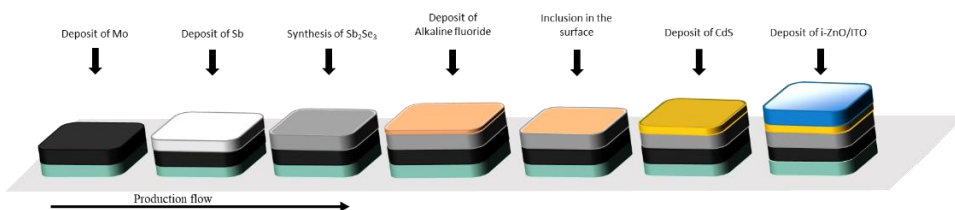


Figure 42: Schematics of the alkaline PDT process.

For the lighter alkali elements (Li and Na) all the devices present a decrease in the optoelectronic properties mainly FF and V_{oc} for the smallest alkaline-fluoride thickness employed (10 nm), this could be related to an inhomogeneous coverage of the surface during the thermal evaporation or induced defects in the surface. In the case of potassium, all parameters decrease linearly with increased deposited thickness. With increasing thickness of the Na and Li, the V_{oc} increases for both species and staggers for 30 nm deposit, while the J_{sc} grows monotonically with increased alkaline content.

3 - Publications

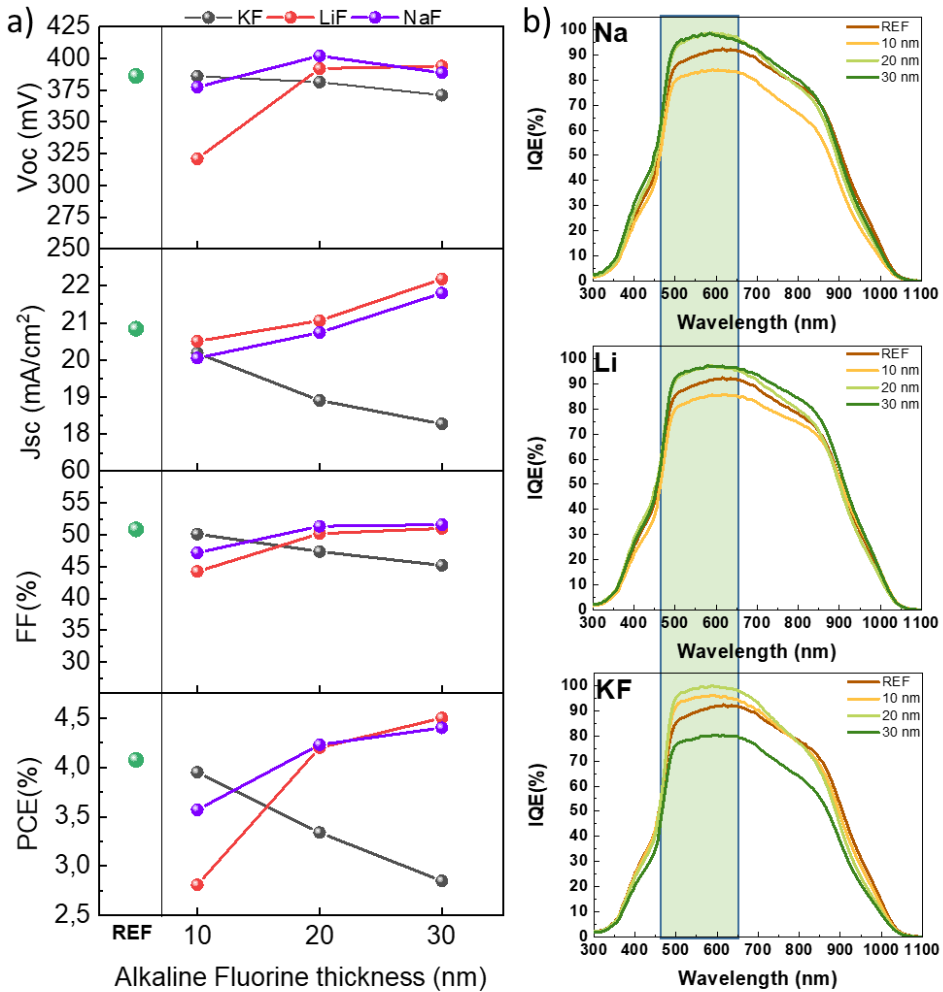


Figure 43: Effect of the alkali PDT treatment in the: a) median values of the optoelectronic parameters. b) in the internal quantum efficiency.

The increase in the short circuit current was also explored by means of spectral response measurements (Figure 43b), here the data of the internal quantum efficiency of the best performing devices in each sample is presented. An increase in the short wavelength collection efficiency is seen for increasing alkaline content from 20 and 30 nm for all the elements tested (Li, Na, K). This could be explained as a less degree of recombination of the photo-generated charges in the upper interface (CdS/Sb₂Se₃) or due to passivation of surface defects after the PDT treatment.

3.1 - Introduction to publications and side experiments

Furthermore, the compositional analysis was extended with glow discharge optical emission spectroscopy (GD-OES) characterization. With this technique the aim was to assess the element distribution across the films in order to determine if the treatment was only altering the surface of the film. In Figure 44 it can be observed the element profile, in order to simplify the analysis the left panel shows the normalized compositional ratio of the Sb_2Se_3 compound for each alkaline thickness, where the right panel shows the distribution of the alkaline elements in the samples subjected to treatment. First of all, we can notice how the compositional ratio stays constant in the bulk for all the alkaline elements (Li, Na and K) treatments and it clearly follows an increase in the Se content correlated to alkaline thickness. The increase in the Se content towards the back contact stands for the self-generation of the MoSe_2 layer. Regarding the alkaline distribution (Figure 44 right), it is clearly observed how all the alkaline elements are detected in the front interface and, even more, we can state that the elements are inside the space charge region of the films (~ 200 nanometers),¹⁰⁶ which corroborates the efficacy of the surface treatment. The elemental profiles also follow consistently the amount of alkaline introduced in the system, with increasing signal proportional to the alkaline introduced in the PDT. As a side effect it seems that all the alkaline elements aside from sodium, diffuse to the back interface, with higher diffusion volume of the Li, most probably due to the reduced atom size in comparison to the other alkali. In the case of the Li, K a double feature can be observed, this could be related to an accumulation of the alkaline elements in between the $\text{Sb}_2\text{Se}_3/\text{MoSe}_2$ and MoSe_2/Mo interfaces, or in the MoSe_2 layer itself. The path followed by the alkaline elements towards the back interface is still unclear being possible a diffusion trough the grain boundaries or the inter-chain Van de Waals space, although this is unlikely. The effects in the crystalline structure of the alkaline treatment needs further investigation.

3 - Publications

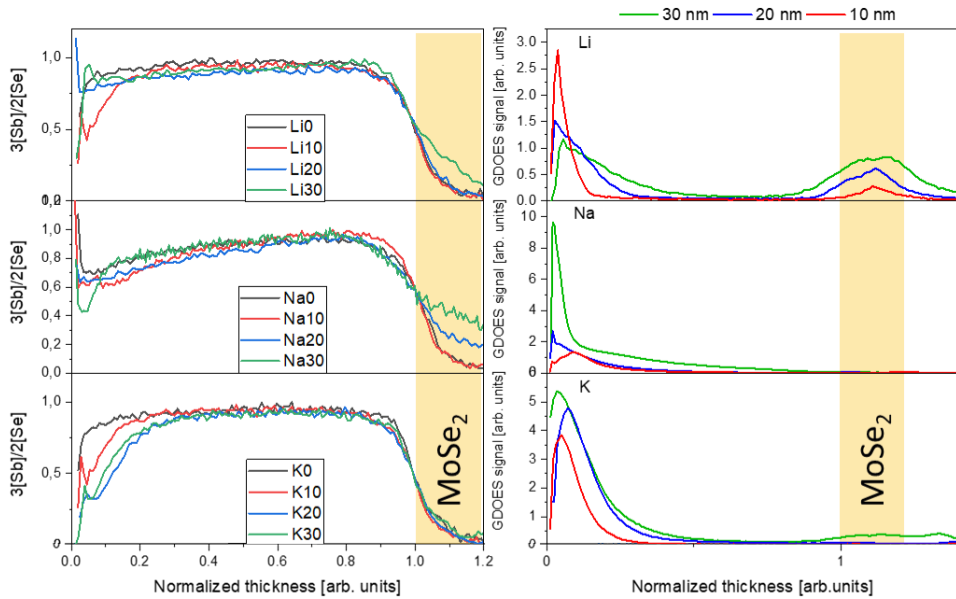


Figure 44: GDOES analysis of the alkaline PDT treatments. Left) normalized ratio between Sb and Se and its distribution through the thickness of the Sb_2Se_3 layer for each alkaline and thickness. Right) distribution of alkaline through the thickness of the Sb_2Se_3 layer for each different thickness.

Finally, we focused on the homogeneity of the basic structure (SLG/Mo/ Sb_2Se_3 /CdS/i-ZnO/ITO) that give the best results overall, several reports throughout the literature reported migration of species between the different layers of the device and specially between the CdS buffer layer and the Sb_2Se_3 . In order to elucidate if the V_{oc} deficit was a consequence of this element inter diffusion we performed TEM microscopy measurements on standard devices.

3.1 - Introduction to publications and side experiments

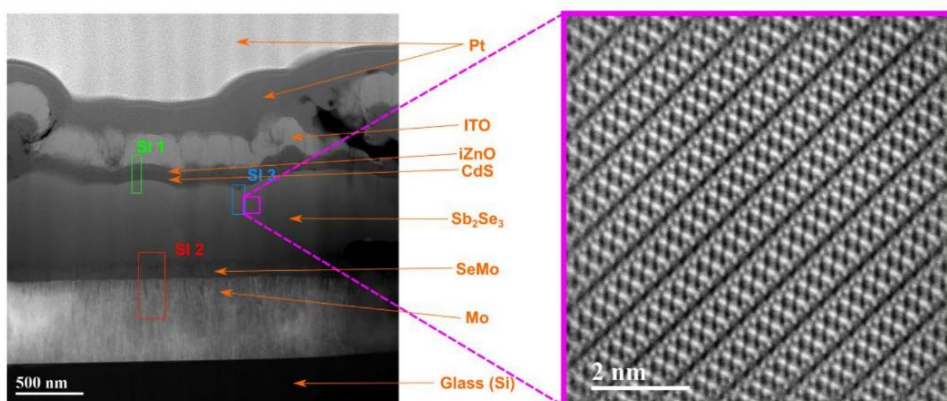


Figure 45: Low magnification HAADF image of the X-section of a standard SLG/Mo/Sb₂Se₃/CdS/i-ZnO/ITO device. Several areas are marked in green, red and blue, where several X-EDS spectrum images were acquired. Right: Processed atomic resolution HAADF image. It corresponds to a single grain in the Sb₂Se₃ layer, marked in the low magnification image in the left with a purple box.

In the left image of Figure 45, a cross section of the device is presented, where all the layers that compose the device are identified. As we can observe this sample present a really defined layer of MoSe₂ that previously was hard to detect. The image in the right of Figure 45 is obtained from the bulk of the Sb₂Se₃ layer and presents continuous ribbons related to good quality films.

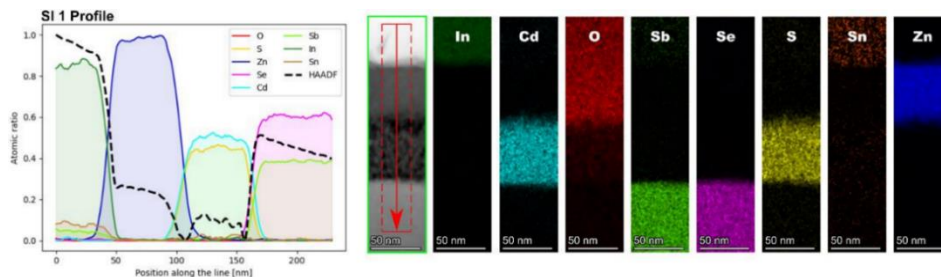


Figure 46: Elemental mappings extracted from the X-EDS signals for the SI area marked in green in Figure 45.

Further characterization of the layer was performed by X-EDS, in order to elucidate the presence of element inter diffusion between the layers. The First zone analysed is the buffer/absorber interface identified by the green square (SI 1) in Figure 45, the probed region does not show any appreciable or clearly distinguishable intermixing of species in the front interface.

3 - Publications

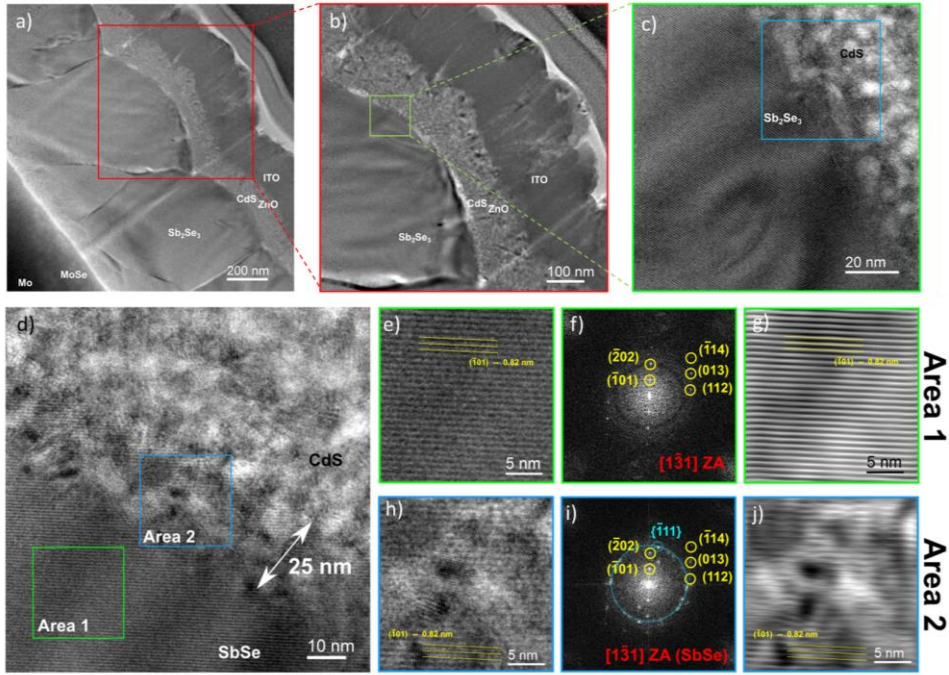


Figure 47: (a) Low resolution image of the whole sample cross-section, (b) magnified image of the front interfaces $Sb_2Se_3/CdS/i-ZnO/ITO$ and (c) high resolution image of the CdS/Sb_2Se_3 interface. (d) HRTEM image of the blue square in figure (c) with two analysis regions in the CdS/Sb_2Se_3 interface. (e) magnification of area 1 (f) fast Fourier transforms (FFT) of the selected area. (g) Inverse FFT filtered by the diffraction pattern of the Sb_2Se_3 . (h) magnification of area 2. (i) fast Fourier transforms (FFT) of the selected area. (j) Inverse FFT filtered by the diffraction pattern of the Sb_2Se_3 .

Further high resolution exploration was performed in the front interface, to elucidate the possible element inter diffusion, Figure 47 (a-b) shows the low magnification images of the areas observed along the CdS/Sb_2Se_3 interface. From a careful observation of these images an overlapping between the Sb_2Se_3 and CdS crystalline structures seem to be present (Figure 47c). Figure 47(d-j) shows a HRTEM image of the CdS/Sb_2Se_3 interface and detailed HRTEM images extracted from two different areas in the region observed. The overlapping between CdS and Sb_2Se_3 is quite notorious, ranging in length up to 25 nm. Two areas are carefully studied in this figure. The first one is far from the interface and the second one is in the overlapping area in the CdS/Sb_2Se_3 interface, in order to analyse any

3.1 - Introduction to publications and side experiments

evolution of the interplanar distances in the Sb_2Se_3 structure. In both cases, the measured distances remained the same, within the resolution limits, around the theoretical 0.82 nm for the $\{-101\}$ family of planes. In both regions it is calculated the inversed FFT (IFFT) image of the area (Figure 47 (f) and (i)), filtering the FFT of both areas by the Sb_2Se_3 crystalline structure spots. The extra spots detected in Area 2 are due to the overlapped CdS crystalline structure and do not show any modification of the Sb_2Se_3 crystal structure, pointing towards a stable interface with no element intermixing in as-deposited devices.

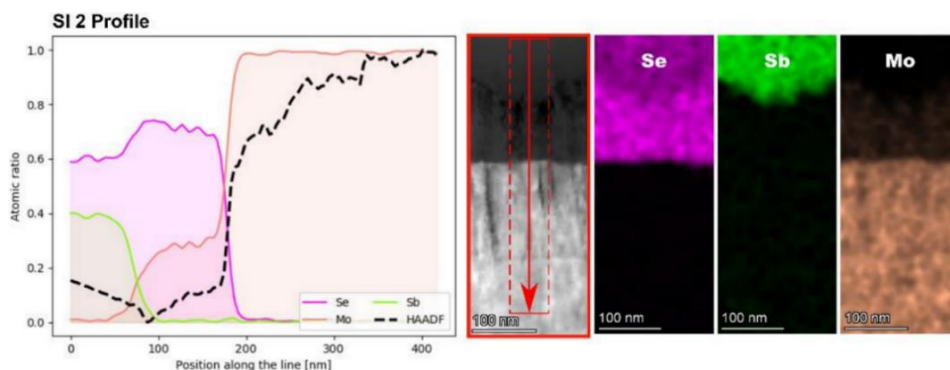


Figure 48: Elemental mappings extracted from the X-EDS signals for the SI 2 red area marked in Figure 45.

Regarding the back contact, the SI 2 analysed in Figure 48 shows the existence of an intermediate MoSe_2 (SeMo in the Figure 45) layer between the Sb_2Se_3 and the Mo contact. The ratios for the Sb and Se in the active Sb_2Se_3 layer are in good agreement with the expected stoichiometry (0.4 Sb – 0.6 Se), which is a good indicator. No stoichiometry variations were neither observed across the GB.

As a summary of the HRTEM characterization:

- Bulk quality is high without visible defects dislocations and with homogeneous composition indicating good quality Sb_2Se_3 .
- Front CdS/ Sb_2Se_3 interface does not show any visible intermixing of species.
- Back Sb_2Se_3 /Mo interface shows formation of a MoSe_2 phase which in principle is beneficial for the device performance.

3 - Publications

To further analyse the basic devices, an attempt on post deposition annealing was performed. This has shown to be essential for high *PCE* devices, such as CIGSSe and CZTSSe, even applied at industrial level in the former.¹⁸⁷⁻¹⁹⁰ At the same time the thermal stability of the system should be in deep tested in order to identify possible limitations in the application of subsequent layers in the device, including buffer and window layer deposition, antireflective coatings or post deposition treatments that may use low temperatures (50-300 °C). In this regard, as we observed a sufficient stability in as growth devices in contrast to literature, we decided to explore the thermal stability of the system, this research is collected in the last publication: *Insights on the Thermal Stability of the Sb₂Se₃ Q1D Photovoltaic Technology*. Where several interesting findings are observed, at low temperature a clear continuous degradation is present in the samples leaded by a reduction in the crystal cell volume of the system, further increasing the temperature high amounts of selenium migrate to the buffer interface generating a CdS_{1-x}Se_x and thus killing the device *PCE*, furthermore segregation of secondary phases in the system occur at lower temperatures in comparison with bulk results, most probably due to the high surface area of the nanostructured devices.

The next three articles that constitute the main body of the thesis are reprinted with permission as described herein: Republished with permission of © IOP Publishing, from Multiwavelength excitation Raman scattering study of Sb₂Se₃ compound: fundamental vibrational properties and secondary phases detection, M. Guc, X. Alcobe, T. Jawhari, M. Placidi, A. Pérez-Rodríguez, E. Saucedo, V. Izquierdo-Roca, vol. 6, no. 4, p. 045054, Sep. 2019; permission conveyed through Copyright Clearance Center, Inc. © IOP Publishing (article 1). John Wiley and Sons license nr 5177590750842 (article 2). John Wiley and Sons license nr 5178140777107 (article 3)

3.2 - Article 1

PAPER

Multiwavelength excitation Raman scattering study of Sb_2Se_3 compound: fundamental vibrational properties and secondary phases detection

To cite this article: Pedro Vidal-Fuentes *et al* 2019 *2D Mater.* **6** 045054

View the [article online](#) for updates and enhancements.

2D Materials



PAPER

Multiwavelength excitation Raman scattering study of Sb₂Se₃ compound: fundamental vibrational properties and secondary phases detectionRECEIVED
25 June 2019REVISED
12 August 2019ACCEPTED FOR PUBLICATION
30 August 2019PUBLISHED
23 September 2019Pedro Vidal-Fuentes^{1,4}, Maxim Guc^{1,4}, Xavier Alcobe², Tariq Jawhari², Marcel Placidi³,
Alejandro Pérez-Rodríguez^{1,3}, Edgardo Saucedo¹ and Victor Izquierdo Roca⁴¹ Catalonia Institute for Energy Research (IREC), Jardins de les Dones de Negre 1, 08930 Sant Adrià de Besòs, Spain² Centres Científics i Tecnològics de la Universitat de Barcelona (CCiTUB), Lluís Solé i Sabarís 1-3, 08028 Barcelona, Spain³ IN²UB, Departament d'Enginyeria Electrònica i Biomèdica, Universitat de Barcelona, C. Martí i Franquès 1, 08028 Barcelona, Spain⁴ Authors to whom correspondence should be addressed.E-mail: pvidal@irec.cat (P Vidal-Fuentes) and mguc@irec.cat (M Guc)**Keywords:** Sb₂Se₃, 1D material, Raman scattering, vibrational properties, single crystal, thin film, solar cellSupplementary material for this article is available [online](#)**Abstract**

This work presents a complete analysis of Raman active modes of Sb₂Se₃ measured by six different excitation wavelengths from NIR to UV, under different polarization configurations and at low temperature. Simultaneous fitting of spectra allowed the deconvolution and identification of the 28 Raman peaks obtained in monocrystalline Sb₂Se₃ sample from the 30 modes predicted by the group theory analysis for this crystalline structure. Analysis of the spectra measured under different polarization configurations yielded the preliminary assignment of the peaks symmetry, while the measurements under low temperature resulted in a fine resolution of the peaks in Raman spectra. Additionally, evaluation of the spectra of the most probable secondary phases under different excitation wavelengths allowed to define the most appropriate measurement conditions for experimental discrimination of their Raman peaks in the spectra of Sb₂Se₃ based thin films solar cells. The combination of different wavelength allows a non-destructive methodology for high sensitivity detection of main secondary phases of the Sb₂Se₃.

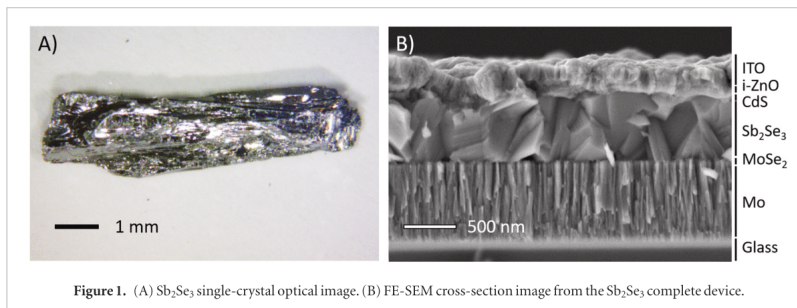
Introduction

Recently, Sb₂Se₃ (Antimonelite) has become a relevant earth abundant semiconductor material with different possible technological applications such as superconductivity [1], electronic components [2], electrode for sodium ion batteries [3], photodetectors [4] and as emerging thin film solar cell absorber [5–8]. In particular, in case of photovoltaic application, the material has shown remarkable improvement in the last few years, demonstrating solar cells in substrate configuration with conversion efficiencies exceeding 9% [9]. This, together with appropriate material properties [10], has opened the perspectives for its use in solar energy conversion application.

One of the most interesting peculiarities of Sb₂Se₃ is that this material is a one dimensional (1D) semiconductor, and is formed by [Sb₄Se₆]_n ribbons where the {Se–Sb–Se–Sb–Se} chains present a strong covalent bonding between Sb and Se atoms, but the different

[Sb₄Se₆]_n ribbons are bonded through relatively weak van der Waals forces. This 1D structure confers interesting anisotropic properties that can be very relevant for photovoltaic applications, because in one direction it exhibits an electrical conductivity much higher than in two other directions [10, 11]. In addition, the material has orthorhombic structure (space group *Pnmb*, with *a* = 11.62 Å, *b* = 11.77 Å and *c* = 3.962 Å) [12], which is the solely Sb–Se known stable phase at typical conditions required for the synthesis and crystallization of the material (temperature and pressure). This is of key importance because implies that no structural polymorphs, neither large amount of secondary phases are expected in this system, simplifying thus its synthesis and technological applications.

In fact, Sb₂Se₃ has shown a high degree of flexibility in terms of synthesis methods as it is typical for other chalcogenide materials, and it can be easily grown by chemical [13–15] and physical [5, 6, 16, 17] routes. Nevertheless, Sb₂Se₃ evaporates congruently,



presenting a relatively high vapour pressure at common processing temperatures [18]. This makes very attractive all the physical vapour deposition methods that can be employed at relatively low temperatures (300–400 °C), for the growth of high-quality thin films. Indeed, most of the solar cells with decent efficiencies reported so far, have been prepared using physical vapour deposition methods [5–8, 19–22].

Even if the material presents a single stable phase at normal conditions, and the occurrence of secondary phases is minimal in binary compounds, the relatively complex structure of the material organized in 1D ribbons as well as the relatively low temperatures required for its synthesis (~350 °C), suggest the possibility of formation of point defects (antisites, interstitials etc), and possible contaminating phases (like elemental Se, Sb and its oxides), that can be detrimental for the overall performance of the solar cells. In this sense, and considering the early stages on the development of the compound, a deep analysis on the fundamental structural properties of Sb_2Se_3 is of high importance.

In this context Raman spectroscopy has demonstrated to be a powerful tool for characterization of new chalcogenide compounds for thin film photovoltaic application [23–26]. It has proven also its suitability as a tool for the deep characterization of the denoted as van der Waals solids or 2D materials such as graphene, MoS_2 , WS_2 , As_2S_3 , and 1D materials such as Te [27–30]. This suitability is related to the strong impact in the vibrational properties of the anisotropic character of these materials. For example, due to the modifications in the obtained spectra with the amount of layers present in the sample, being able to differentiate the effects of the interlayer coupling to investigate the fine structure, atomic bonds, and mechanical and thermal properties of 2D materials [29]. In the case of 1D materials, like Te, it has been reported a shift in some of the Raman modes associated to the presence of strain [30]. Under our knowledge few materials have been evaluated, however the high anisotropy is expected to induce strong effects in the Raman spectra allowing the use of this tool for the characterization of 1D structures, like $\text{Sb}_2(\text{S,Se})_3$.

Furthermore, sensibility of phonon to the crystallographic changes allows to provide relevant information

about the presence of secondary phases, composition, crystal quality and presence of defects in the analysed material. However, a fingerprint spectrum of the Sb_2Se_3 measured under different conditions is missing up to date, and only few works are available with very limited information [12, 31]. In this work, a complete multi-wavelength Raman scattering analysis of the Sb_2Se_3 thin films and commercial single crystal, as well as of the possible secondary phases, using excitation wavelengths from the NIR (1064 nm) down to UV (325 nm) was carried out. In addition, the measurements on a monocrystalline sample were measured under different polarization configurations and at low temperatures. As result the complete identification of most of the Raman modes of the compound was performed, as well as the most appropriate conditions for the detection of possible secondary phases were proposed.

Experimental details

The study presented in this work was achieved using both, a commercial Sb_2Se_3 single crystal from 2D semiconductors (figure 1(A)), as well as thin films synthesized at IREC (figure 1(B)). The synthesis was performed onto Mo coated soda-lime glass (SLG/Mo) substrate, with a Mo tri-layer metallic contact preparation as it has been described elsewhere [32]. Sb_2Se_3 was synthesized using a sequential process consisting in the thermal evaporation of 200 nm of Sb (Alfa Aesar, Sb shots 1–3 mm, Puratronic, 6N metal basis) using an Oerlikon Univex 250 evaporator, with a base vacuum of 5×10^{-5} mBar and an evaporation rate of 0.7 \AA s^{-1} . The SLG/Mo/Sb precursors were then submitted to a reactive annealing in a tubular furnace under Se atmosphere using semi-closed graphite boxes (23 cm^3). For this purpose, $2.5 \times 2.5 \text{ cm}^2$ in area samples were heated up to 320 °C, with a heating ramp of 20 °C s^{-1} , and kept at this temperature during 30 min, and then cooled down naturally (taking approximately 1 h). During the annealing, 30 mg of Se (Alfa Aesar, Se powder 200 mesh, 5N metal basis) were used and 500 mBar of total Ar pressure was imposed. Half of the sample was used to produce and characterize solar cells (SLG/Mo/ Sb_2Se_3 /CdS/i-ZnO/ITO), and the other half for the fundamental characterization.

The solar cells were characterized by illuminated J - V curves using a calibrated AAA class Abet Sun 3000 solar simulator.

Additionally, the Sb shots and Se powder converted into pellets and described before, as well as Sb_2O_3 (Alfa Aesar, powder, 5N puratronic metal basis), were also used for the complete Raman characterization.

X-ray diffraction (XRD) results were obtained with a PANalytical X'Pert PRO MPD Bragg-Brentano powder diffractometer equipped with a Cu tube operating at 45 kV and 40 mA, a Ge (111) Johansson type primary focalizing monochromator and a silicon strip ID X'Celerator detector. High resolution, high statistics, full angular range $\text{Cu K}\alpha_1$ $\theta/2\theta$ scans are obtained: $2\theta/\theta$ scans from 4 to $145^\circ 2\theta$; step size 0.0166° ; measuring time per step 200 s (X'Celerator active length 2.113°); five consecutive repeated scans; total measuring time per sample 19 h. Two samples were measured: a fine powder sample obtained after grinding, in an Agate mortar, a small piece of the commercial Sb_2Se_3 single crystal, mounted in the cylindrical cavity (0.15 mm of height and 16 mm of diameter) of a zero-background silicon single crystal sample holder; a thin film sample, on a piece of about $1.5 \times 1.5 \text{ mm}^2$, with a stack SLG/Mo/ Sb_2Se_3 . Full profile analysis, Rietveld method [33], have been done in both Sb_2Se_3 powder and SLG/Mo/ Sb_2Se_3 XRD data. The refinements have been performed by the TOPAS v5 software [34]. The background is modelled with a 20th order Chebyshev polynomial. The instrumental contribution to the diffraction profile is calculated with the Fundamental Parameters Approach [35].

Raman measurements have been performed using IREC developed Raman setups optimized for the UV-Visible spectral region (based on Horiba Jobin Yvon FHR640 monochromator) and NIR-IR region (based on Horiba Jobin Yvon iHR320 monochromator). The first system is coupled with an open electrode CCD detector cooled down to -75°C and the second with NIR enhanced CCD detector cooled down to -75°C and also an InGaAs array detector cooled to liquid nitrogen temperature for the measurements obtained with the 1064 nm excitation wavelength. The utilization of different gratings for the light dispersion allows to optimize the spectra resolution, achieving a full width at half maximum (FWHM) of the main peak of monocrystalline silicon at 520 cm^{-1} of $4\text{--}6 \text{ cm}^{-1}$ for most of the excitation wavelengths, except for UV measurements (325 nm) where silicon FWHM was about 8 cm^{-1} . The study was performed with laser power density below 25 W cm^{-2} by using a macro-spot with a diameter in the range of $50\text{--}70 \mu\text{m}$ depending on the excitation wavelength. Finally, the use of unpolarised laser beam allowed to minimize the impact of the crystalline orientation in the Raman spectra. Measurements under different polarization conditions were performed using the LabRam HR800-UV system from Horiba Jobin Yvon with polarization filters. A close cycle helium cryostat was used to decrease the sample

temperature down to 10 K while obtaining the Raman spectra using the FHR640 based system.

Results and discussion

Structural characterization of single crystal and thin film Sb_2Se_3

Sb_2Se_3 Antimonelite is isostructural with Sb_2S_3 Stibnite. The crystal structure is orthorhombic, space group $Pnmb$ (#62), $Z = 4$, with twenty atoms in the primitive unit cell, all the atoms of the asymmetric unit (two non-equivalent Sb cation sites and three non-equivalent Se anions sites) in the Wyckoff Position $4c$ ($x, y, 1/4$) [36]. The Rietveld analysis, in the XRD data of the Sb_2Se_3 powder sample from the single crystal, confirms that the sample shows only one phase with the expected above described structure. The structure has been refined with the values of $R_{\text{wp}} = 7.65$ and $R_{\text{B}} = 3.18$ and the Rietveld plot is presented in the figure 2(A). In the table S1 (stacks.iop.org/TDM/6/045054/mmedia) are reported the XRD indexation. The 18 refined structural parameters, three cell parameters, ten atomic coordinates and five isotropic temperature parameters, are listed in table 1 and 2 together with the resulting bond distances. Crystallographic results agree with previous publications [36]. The crystal structure and detailed atomic base, with indication of non-equivalent positions, and the distance between them obtained from the Rietveld analysis are shown in figure 3. It is interesting to mention, that all the bonds in the $[\text{Sb}_4\text{Se}_6]_n$ ribbons have relatively close distance [36], which shrinks the distribution of phonons energy and makes them hardly resolvable.

In contrast to powder samples, the phase analysis in the x-ray diagram of the thin film stack of SLG/Mo/ Sb_2Se_3 (figure 2(B)), confirms the presence of Sb_2Se_3 as the main observed phase in the layer and the Mo back contact underneath. Additionally, minor contributions identified as elemental Se secondary phase of the Sb_2Se_3 layer and the formation of small amount of MoSe_2 in the $\text{Sb}_2\text{Se}_3/\text{Mo}$ interface are observed. All four observed phases were included in the Rietveld analysis. All the structural parameters of Sb_2Se_3 , but the a , b and c unit cell parameters, i.e. the atomic coordinates and the six temperature parameters, are fixed equal to the obtained ones in the crystal structure refinement of the powder Sb_2Se_3 sample (see table 2). The Rietveld refinement is fully reasonable with excellent agreement factors $R_{\text{wp}} = 6.51$; $R_{\text{B}}(\text{Mo}) = 3.18$; $R_{\text{B}}(\text{Sb}_2\text{Se}_3) = 2.81$ and Rietveld plot is shown in figure 2(B). The Sb_2Se_3 Antimonelite is the main phase of the analysed absorber and does not show strong preferential texture, indicating close to random orientation distribution of the crystals that can be observed in the random orientation of the crystal's facets in the SEM (image figure 1(B)). On the other hand, no significant peak broadening is observed in comparison with the single crystal powder. This suggest a high crystal

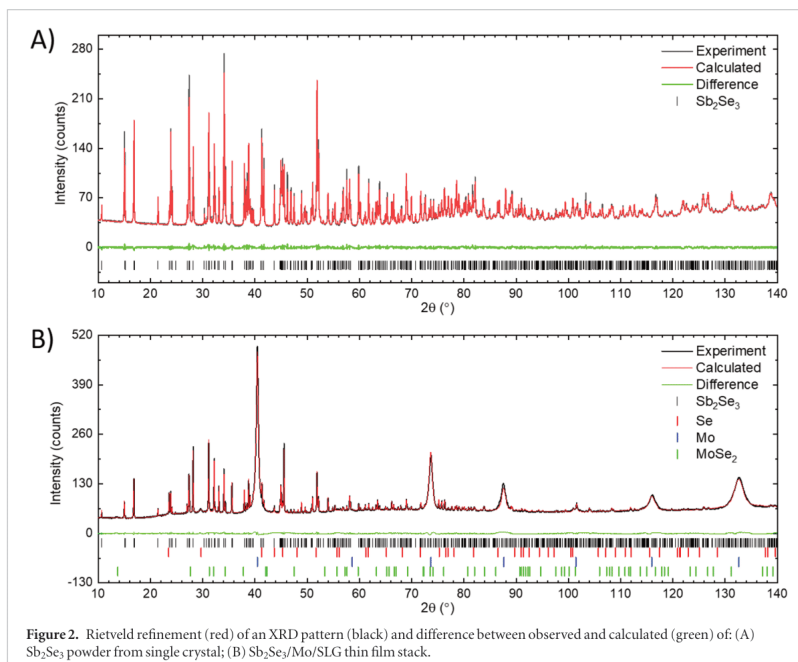
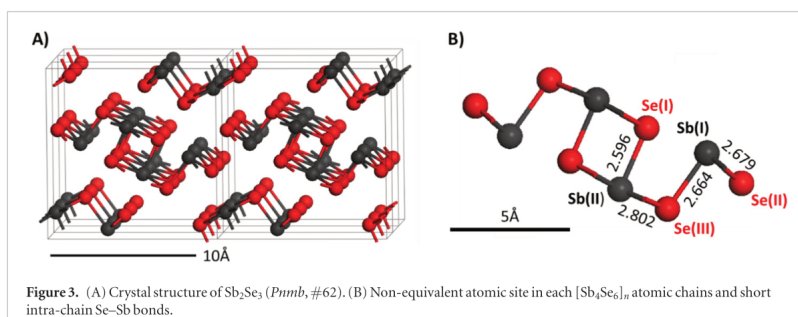


Table 1. Sb_2Se_3 crystallographic parameters and refinement agreement factors.

	Structure, space group, Z	R_{wp}	R_B	a (Å)	b (Å)	c (Å)	V (Å ³)	V/Z (Å ³)
Powder	Orthorhombic, $Pnmb$, 4	7.65	3.178	11.636 36(9)	11.784 46(6)	3.978 82(3)	545.607(7)	136.4
Thin film	Orthorhombic, $Pnmb$, 4	6.51	2.809	11.6286(2)	11.776 36(14)	3.976 17(4)	544.506(13)	136.1



quality of the Sb_2Se_3 crystals, in agreement with large size (>500 nm) and geometrical shape of the Sb_2Se_3 grains observed in SEM cross-section (figure 1(B)). The obtained cell parameters and volume of the Sb_2Se_3 thin film were found to be slightly compressed in respect to the ones of the powder sample (see table 1).

Vibrational properties of Sb_2Se_3 single crystal

Group theory analysis of the Sb_2Se_3 with $Pnmb$ space group yields 60 different phonon modes split on three acoustic modes, and fifty-seven optical modes, including thirty Raman active, twenty-two IR active and five silent modes [37, 38]:

Table 2. Atomic coordinates, site occupation factor and Wyckoff positions of the non-equivalent atoms, and bond distances in between them obtained from the refinement of the diffractogram of monocrystalline powder sample.

Name	Element	X	Y	Z	B_{eq}	Sof	Wyck.	Bound	Dist. (Å)
Sb(I)	Sb	0.32796(11)	0.02997(7)	0.25000	1.18(3)	1.00	4c	Sb(I)–Se(II)	2.679
Sb(II)	Sb	0.03938(12)	0.14743(8)	0.75000	1.23(3)	1.00	4c	Sb(I)–Se(III)	2.664
Se(I)	Se	0.87102(18)	0.05430(12)	0.25000	0.92(4)	1.00	4c	Sb(II)–Se(I)	2.596
Se(II)	Se	0.44461(17)	0.12954(11)	0.75000	0.93(4)	1.00	4c	Sb(II)–Se(III)	2.802
Se(III)	Se	0.1950(2)	0.21399(12)	0.25000	1.07(4)	1.00	4c		

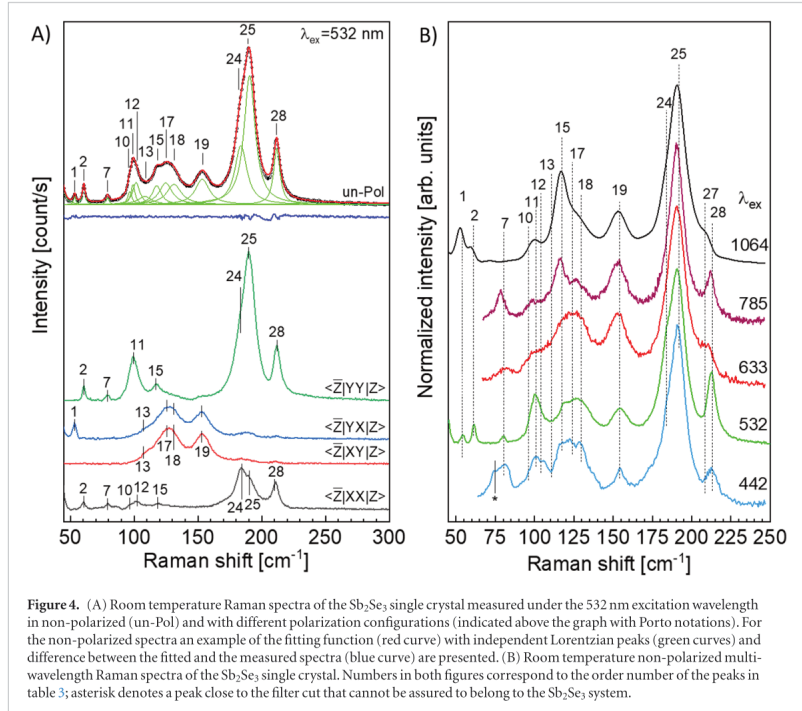


Figure 4. (A) Room temperature Raman spectra of the Sb_2Se_3 single crystal measured under the 532 nm excitation wavelength in non-polarized (un-Pol) and with different polarization configurations (indicated above the graph with Porto notations). For the non-polarized spectra an example of the fitting function (red curve) with independent Lorentzian peaks (green curves) and difference between the fitted and the measured spectra (blue curve) are presented. (B) Room temperature non-polarized multi-wavelength Raman spectra of the Sb_2Se_3 single crystal. Numbers in both figures correspond to the order number of the peaks in table 3; asterisk denotes a peak close to the filter cut that cannot be assured to belong to the Sb_2Se_3 system.

$$\begin{aligned} \Gamma_{\text{acoustic}} &= B_{1u} \otimes B_{2u} \otimes B_{3u}; \\ \Gamma_{\text{Raman}} &= 10A_g \otimes 5B_{1g} \otimes 10B_{2g} \otimes 5B_{3g}; \\ \Gamma_{\text{IR}} &= 9B_{1u} \otimes 4B_{2u} \otimes 9B_{3u}; \\ \Gamma_{\text{silent}} &= 5A_u. \end{aligned}$$

The Raman spectrum of Sb_2Se_3 single crystal measured under 532 nm excitation wavelength is shown in figure 4(A). In the range 45–300 cm^{-1} the non-polarized (un-Pol) spectrum is dominated by a large band at 190 cm^{-1} and seven less intense bands, some of them being strongly overlapped. For higher wavenumbers no additional fundamental bands are observed and only second order of the main band can be detected. Detection of only eight bands contradicts the expected thirty Raman active modes and is related to a complex structure of the observed bands with a high overlapping of the individual peaks. In order to decompose the

observed bands and analyse the symmetry type of the peaks, measurements using different polarization configurations were obtained, presented in the bottom of figure 4(A). The Raman polarizability tensors for the point group $m\bar{3}m$ (D_{2h}) are:

$$\begin{aligned} A_g &: \begin{pmatrix} a & & \\ & b & \\ & & c \end{pmatrix} & B_{1g} &: \begin{pmatrix} d & & \\ & d & \\ & & \end{pmatrix} \\ B_{2g} &: \begin{pmatrix} & & \\ & e & \\ e & & \end{pmatrix} & B_{3g} &: \begin{pmatrix} & & \\ & f & \\ & & f \end{pmatrix}. \end{aligned}$$

Taking these tensors into account the following selection rules for the primitive crystal planes, like (100), (010) and (001), for the peak symmetry

assignment can be deduced using the Porto notations [39]:

- (i) The Raman peaks which show maximum intensity in parallel polarization configurations, $\langle \bar{Z} | XX | Z \rangle$ and $\langle \bar{Z} | YY | Z \rangle$, and conversely less intensity in cross polarization configurations, $\langle \bar{Z} | XY | Z \rangle$ and $\langle \bar{Z} | YX | Z \rangle$, can be assigned to A_g modes.
- (ii) The peaks with the inverse behaviour, maximum intensity in $\langle \bar{Z} | XY | Z \rangle$ and $\langle \bar{Z} | YX | Z \rangle$ configurations and minimum in $\langle \bar{Z} | XX | Z \rangle$ and $\langle \bar{Z} | YY | Z \rangle$ configurations can be assigned to B_{1g} , B_{2g} or B_{3g} modes.

Assuming that strong change in the peaks intensity in parallel and cross polarization is related with the measurements from one of the primitive crystal plains, the tentative assignment of the peaks is proposed in table 3. Note, that the measurements were performed on the relatively small crystal plane, which prohibited to measure its strict crystallographic orientation with a conventional XRD equipment. However, a strong difference in the spectra measured in parallel and cross polarizations allows to suppose that one of the primitive crystal planes was used in the case. Further, the differences in intensities between the $\langle \bar{Z} | XX | Z \rangle$ and $\langle \bar{Z} | YY | Z \rangle$ configurations can be explained by differences between a , b and c elements of the Raman tensor of A_g modes. Due to the high anisotropic properties of the 1D material, the polarizability tensor elements of the A_g symmetry modes may be quite different which would explain the difference in intensity of the peaks assigned to this modes in spectra measured along different crystallographic orientations. This way, the highest difference is expected between the spectra measured along and across to the orientation of the ribbons. On the other hand, no significant changes in the intensity of B_{3g} ($x = 1-3$) symmetry peaks are expected in the spectra measured along or across to the 1D ribbons. This opens the possibility of estimation of the preferential orientation of the ribbons in a polycrystalline sample, which is one of the critical points of Sb_2Se_3 material [10]. However, an analysis of the samples with different ribbon orientation should be performed to prove the proposed application of the Raman spectroscopy.

The origin of the Raman peaks overlapping come from the strong similarities between the different Sb and Se atoms in non-equivalent positions with very similar but non-equal bond length (figure 3(B) and table 2). Aside with the non-equivalent positions, the presence of the 30 expected Raman modes in a very small region ($20-220 \text{ cm}^{-1}$) brings the necessity of high-resolution Raman spectroscopy for the proper observation of the Raman modes. Therefore, the available gratings with higher dispersive power for the different excitation wavelengths were used in order to

achieve the highest resolution possible in this work. Furthermore, the Raman spectra of Sb_2Se_3 single crystal were measured using six different excitation wavelengths. The methodology of simultaneously fitting using a multi-wavelength excitation reported by Dimitrievska *et al* [23, 36] allowed to perform a precise deconvolution of the Raman spectra to the Lorentzian peaks, assuming the good crystal quality of the single crystal. Using this methodology, 15 peaks from the total 30 theoretically expected Raman modes were resolved at room temperature. Different intensities of the peaks or even appearance of new peaks can be observed in figure 4(B), depending on the excitation wavelength. Enhancement of different peaks under different excitations is due to the coupling of the excitation wavelength with an inter-band optical transition at the Γ point. Based on theoretical calculations the latter were found to have the energies $\Gamma_1 = 1.21 \text{ eV}$, $\Gamma_3 = 1.5 \text{ eV}$, $\Gamma_5 = 2.0 \text{ eV}$, $\Gamma_7 = 2.25 \text{ eV}$, $\Gamma_{14} = 2.8 \text{ eV}$ that can be coupled with $\lambda_{\text{ex}} = 1064, 785, 633, 532$ and 442 nm respectively [12]. Even assuming small discrepancies of the theoretically calculated values with the real position of the energy levels a close to resonant effect is still expected for the mentioned excitation wavelengths. Herein the non-equivalent enhancement of the peaks in resonant conditions can be explained by difference in the atoms, producing the specific vibrational phonon, and their involvement in creation of specific energy level.

As it is mentioned above, a simultaneous Lorentzian fitting of the Raman spectra measured under different excitations was performed for the fine spectra deconvolution. This was done by using the minimum number of peaks, which can describe the whole measured spectrum. Additionally, the FWHM of the peaks was maintained between spectra, allowing to achieve similar fitting equation for all excitation wavelengths. The observed differences between spectra are summarized hereafter. First, an asymmetric broadening towards the lower wavenumber side of the main peak was observed in the spectra measured with 442 and 532 nm excitation wavelengths, suggesting the existence of a peak at the red side of the main peak found at 184.7 cm^{-1} . The peaks at $80.1, 100.1$ and 132.2 cm^{-1} are found to be better resolved in the spectra measured under 442 nm excitation wavelength in comparison with the other wavelengths. Additionally, a shoulder at the red side of the main peak can be seen around 174 cm^{-1} , although the fitting of this peak was not possible. The measurement performed with the usual 532 nm excitation wavelength resulted in one of the richest spectra and its fitting is presented as example in figure 4(A). Here, the peaks at $80.1, 100.1, 132.2$ and 212.8 cm^{-1} can be finely resolved. For the 633 nm wavelength a broad band close to 153 cm^{-1} has the highest intensity, also the contrast with FWHM of this band measured under 442 nm excitation wavelength and a red shift mean the presence of more than one peak at this frequency. An enhancement of

Table 3. Frequency of the Raman peaks obtained from the multi-wavelength analysis of spectra measured at room temperature (RT) and at low temperature (10 K), best excitation conditions and tentative symmetry assignment. Previously published experimental and theoretical results are presented for comparison.

#	Symm.	λ_{ex} [nm]	This work				References			
			Raman shift (RT) [cm ⁻¹]	FWHM (RT) [cm ⁻¹]	Raman shift (10 K) [cm ⁻¹]	FWHM (10 K) [cm ⁻¹]	[37] ^b [cm ⁻¹]	[46] [cm ⁻¹]	[38] [cm ⁻¹]	[1] [cm ⁻¹]
1	B_{2g}	532	54.4	2.0			20/29/40/44/45/46/48			
							55/56			
2	A_g	532	61.6	2.4			58/59/60 × 2/61			
3		532 ^a			71.9	1.3	69 × 2			
4		532 ^a			74.7	2.4				
5		532 ^a			76.0	1.6	76			
6		532 ^a			78.5	0.4	77			
7	A_g	785	80.1	2.9	83.4	1.7	84	80	84	
8		532 ^a			91.2	1.9	92			
9		532 ^a			94.9	1.0	93/94			
10	B_{2g}	532	97.6	3.8	99.5	2.0	99			
11	A_g	442/532	100.1	3.8	103.3	2.5	102/103			105
12	B_{2g}	442	102.6	6.7	107.2	1.3	110			
13	B_{2g}	785	109.3	13.0	111.4	1.8	113			
14		532 ^a			114.7	2.1				
15	A_g	1064/785	118.7	8.7	119.0	2.4	118/119	120	117	
16		532 ^a			122.9	1.0	124/125			122.6
17	B_{2g}	633	125.7	12.3	130.0	2.7	129/131/132/134 × 3			131
18	B_{2g}	532	132.2	14.0	138.7	1.0	142/145/146 × 2			
19	B_{2g}	532	154.4	13.2	157.4	3.5	158	151		155.2
20		532 ^a			164.0	4.3	164			
21		532 ^a			168.3	0.9	170			
22		532 ^a			174.7	6.9	174/175 × 2			
23		532 ^a			182.7	6.4	179 × 2			181
24	A_g	532	184.7	11.5	189.1	2.0	188			
25	A_g	532	191.5	10.6	195.8	2.9	194/195	189	193	189.6
26		532 ^a			203.7	3.9	200/201			
27	—	633/1064	207.8	7.3	209.0	3.3	207			
28	A_g	532	212.8	6.0	215.6	3.1	214	210		213.3

^a The peak was resolved only in the spectra measured at 10 K.

^b Position of all optical modes, both IR and Raman active, were extracted from the phonon branch diagram at the zone centre Γ -point.

the peaks intensity at 80.1, 118.7 and 212.8 cm⁻¹ was found in the spectra measured under 785 nm excitation wavelength. Additionally, under this excitation conditions the most intense band at 191.5 cm⁻¹ has the lowest FWHM from all the investigated spectra, which assumes the weak intensity of the peaks around the main mode. Finally, excitation with the 1064 nm wavelength implies near resonant conditions due to close energy of the laser with the optical bandgap of the material. Under this measurement conditions the best signal to noise ratio was observed and the peak at 118.7 cm⁻¹ exhibits the higher intensity comparing to spectra measured with other excitation wavelengths. In the table 3 wavenumbers of all found peaks are summarized together with the most suitable excitation wavelength for observation. The latter were determined after overlapping of measured spectra normalized to the peak at 191.5 cm⁻¹ (see figure 5). Some of the Raman peak frequencies

were previously published in different works (see the references in table 3) and are in agreement with the present study, and with the theoretical predictions of the peaks wavenumbers from DFT calculations (extracted from phonon branch diagram collecting all modes: acoustic, infrared and Raman active) [40]. However, in our study, no peak around 250 cm⁻¹ was detected under any excitation conditions, and no vibrational mode was predicted in the theoretical calculations close to this position, indicating the misinterpretation of the spectra analysis reported previously by many authors [2, 15, 16, 41–48].

The sixth excitation wavelength used in the present study is the 325 nm laser line. Under this excitation conditions, a degradation of the material is observed starting from the lowest laser power density available 0.25 W cm⁻² (figure 6). This degradation is characterized by the reduction of the intensity and broadening of the FWHM of the Sb₂Se₃ Raman peaks, and

Table 4. Position of the Raman peaks in the characterized secondary phases, with the main modes highlighted in bold, and the best wavelength for specific phase detection.

Secondary phase	Raman shift [cm^{-1}]	E_g (direct) [eV]	λ_{ex} [nm], [eV] ^a	Reference
β -Sb ₂ O ₃	75.4, 104.0, 140.2 , 186.2, 215.4, 224.5, 257.6, 283.1, 296.2 , 443.4, 488.6, 502.3, 597.2, 685.7	≈ 2.7	442, 2.72 (R)	This work [51]
α -Sb ₂ O ₃	84, 124, 188 , 253 , 355, 372, 450 , 712	≈ 3.5	442, 2.72	[49, 51]
Se (trigonal)	81.0, 112.7, 144.9, 236.4 , 240.7	≈ 1.9	633, 1.96 (R)	This work [52]
Se (amorphous)	254.8	≈ 1.7 –2.0	633, 1.96 (R)	This work [52]
Sb	114.3 , 127.9, 151.3 , 255.9, 275.2	—	633, 1.96	This work [53]

^a (R) indicate conditions when resonant Raman scattering is expected.

by a concomitant increase of the intensity of peak at 254.8 cm^{-1} associated with amorphous Se (a-Se) secondary phase (figure 6). The observed time evolution of the spectra suggests a decomposition of the Sb₂Se₃ phase due to break of the compound bonds under UV excitation.

Apart from the peaks' frequency, their FWHM is also presented in the table 3. Here the strong difference in the peaks width could be an indication for the more complex structure of the wide peaks (FWHM > 10 cm^{-1}). In order to resolve the complex structure mentioned above low temperature Raman measurement at $\sim 10 \text{ K}$ were carried out (see figure 7). The reduction on thermal dispersion of the phonon states ($\Gamma_0 + \Delta\Gamma(T)$) (anharmonic contributions) minimizes the overlapping of the different peaks, thus reducing the FWHM, allowing the identification of 26 peaks under 532 nm excitation wavelength. In addition, the reduction of thermal agitation of the lattice implies a blue-shift in frequencies for the peaks, meaning that this analysis is useful for fundamental characterization of the material's vibrational properties, but not as a quality control tool for sample analysis purposes like the multi-wavelength study at room temperature described above. Nevertheless, the measurement at low temperature is suitable to corroborate the peak assignment to the room temperature measurements. All these new peaks detected at low temperature are added in table 3. For example, in spectra measured at low temperature a series of new peaks in the spectral range 60 – 80 cm^{-1} were found (at 71.9 , 74.7 , 76.0 , 78.5 cm^{-1}), while only two peaks (at 61.6 and 80.1 cm^{-1}) were resolved in the spectra measured at room temperature. We can observe the corroboration of the predictions done for the band around 100 cm^{-1} at room temperature and under different excitations, which correlate well with the low temperature measurements (taking into account the blue-shift), confirming the hypothesis of three peaks which form this band. The band between 100 – 140 cm^{-1} is also properly identified in the multi-wavelength analysis and two peaks more can be resolved at positions 114.7 and 122.9 cm^{-1} . The broad peak at 154.4 cm^{-1} is deconvoluted into two different peaks at positions 157.4 and 164.0 cm^{-1} . The shoulder on the low wavenumbers side of the main peak at low temperatures is resolved into two different peaks at

168.3 and 174.7 cm^{-1} . The main mode as stated in the analysis above is composed of three peaks at positions 182.7 , 189.1 and 195.8 cm^{-1} , the latter being the most intense one. Finally the higher energy peaks are confirmed by the low temperature analysis and another peak is found at 203.7 cm^{-1} . The FWHM of the peaks is considerably lower than the room temperature measured ones, and very consistent ranging from 0.4 to 4.3 cm^{-1} with the exception of the peaks at 174.7 and 182.5 cm^{-1} with FWHM of 6.5 cm^{-1} that could account for the two peaks left to find. As it can be seen in table 3 there is strong correlation of the theoretically calculated frequencies of Raman modes and the peaks positions measured in the low temperature spectra. These 26 obtained peaks, plus two peaks at low wavenumbers 54.4 and 61.6 cm^{-1} , give a total of 28 resolved peaks from 30 predicted by group theory analysis.

Secondary phase analysis

The only stable phase of Sb–Se system has orthorhombic Sb₂Se₃ (*Pnmb*, #62) structure and no other structural or compositional polymorphs has been reported to our knowledge. The only expected secondary phases are pure selenium (amorphous or trigonal), pure antimony and antimony oxide Sb₂O₃. The later, antimony oxide, is alike to selenium containing compound has three different crystallographic structures, α -Sb₂O₃, β -Sb₂O₃, γ -Sb₂O₃, which are the most stable polymorphs, and no less energetically favourable Sb₂O₄ and Sb₂O₅ phase are expected to form as secondary phases in Sb₂Se₃ [50].

The main Raman peaks of some of the mentioned secondary phases are summarized in table 4, with indication of the most suitable wavelength for their detection. Taking into account the temperature conditions usually used for the Sb₂Se₃ synthesis ($< 400 \text{ }^\circ\text{C}$) the most stable oxide contain polymorph is cubic α -Sb₂O₃ (senarmonite). However, formation of high temperature stable orthorhombic β -Sb₂O₃ (valentinite) polymorph cannot be excluded. The Raman spectra of both phases were studied by Cody *et al* [51] and the spectra from commercial powder of β -Sb₂O₃ was measured in the present study, and a 442 nm excitation wavelength was found as the most suitable for these secondary phases detection. The third possible γ -Sb₂O₃ was found only under specific high-pressure

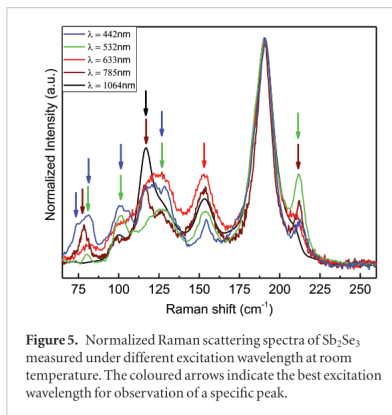


Figure 5. Normalized Raman scattering spectra of Sb_2Se_3 measured under different excitation wavelength at room temperature. The coloured arrows indicate the best excitation wavelength for observation of a specific peak.

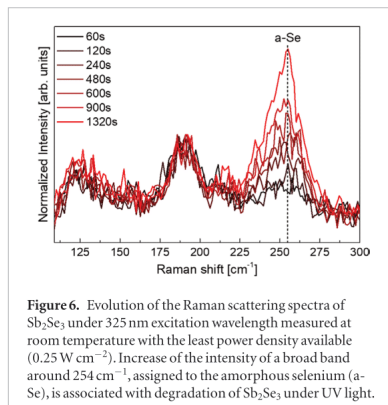


Figure 6. Evolution of the Raman scattering spectra of Sb_2Se_3 under 325 nm excitation wavelength measured at room temperature with the least power density available (0.25 W cm^{-2}). Increase of the intensity of a broad band around 254 cm^{-1} , assigned to the amorphous selenium (a-Se), is associated with degradation of Sb_2Se_3 under UV light.

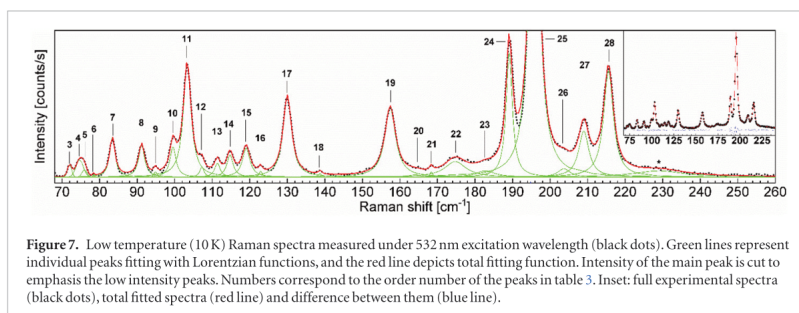


Figure 7. Low temperature (10K) Raman spectra measured under 532 nm excitation wavelength (black dots). Green lines represent individual peaks fitting with Lorentzian functions, and the red line depicts total fitting function. Intensity of the main peak is cut to emphasize the low intensity peaks. Numbers correspond to the order number of the peaks in table 3. Inset: full experimental spectra (black dots), total fitted spectra (red line) and difference between them (blue line).

conditions and is not expected to be formed during the Sb_2Se_3 synthesis, with the actual state of the art processes. Measurements of elemental Se and Sb were performed under 633 nm excitation wavelength, which showed to be the most appropriate for detection of these phases. In case of elemental selenium two phases, crystalline trigonal selenium (t-Se) and amorphous selenium (a-Se), can be distinguished. The main peaks of each phase are highlighted with bold in table 4.

Finally, to show the possible influence of the used laser's power density to the Raman spectra of Sb_2Se_3 compound, the measurements at high power density of 785 nm laser were performed. In figure 8 it is seen that the evolution of the spectra for the low power densities from 21 to 42 W cm^{-2} is reflected mainly in broadening of the peaks due to small local heating. With increasing of the power density up to 164 W cm^{-2} the main mode became broad enough to reduce the resolution of the modes at 207 and 212 cm^{-1} , and the shift of the main peak to the lower wavenumbers becomes more relevant. Under the 180 W cm^{-2} of laser power density the Sb_2Se_3 compound starts to decompose into $\alpha\text{-Sb}_2\text{O}_3$, which is evident due to appearance of new peaks at 253, 372 and 450 cm^{-1} . Additionally, an increased asymmetry of the main peak at the low wavenumber side can be associated to appearance of

the peak at 188 cm^{-1} from $\alpha\text{-Sb}_2\text{O}_3$ phase. As it was mentioned above, the former peak around 250 cm^{-1} is the one usually observed by many researchers, and from the present study it adherence to a secondary phase is not discussible, either being $\alpha\text{-Sb}_2\text{O}_3$ 253 cm^{-1} , Se-trigonal $236.4, 240.7 \text{ cm}^{-1}$ or Se-amorphous 254.8 cm^{-1} peaks. Detection of $\alpha\text{-Sb}_2\text{O}_3$ phase is compromised by overlapping of its most intense peaks at 188 and 253 cm^{-1} with the main peaks of the Sb_2Se_3 and the Se amorphous phases, but appearance of the less intense peaks at 370 and 450 cm^{-1} is a clear evidence of the formation of this phase. Note, that used laser power density at which the decomposition of Sb_2Se_3 starts is relatively low ($\sim 180 \text{ W cm}^{-2}$), comparing to the common used laser power in micro Raman configuration with a spot diameter close to $1 \mu\text{m}$ ($\sim 30 \text{ kW cm}^{-2}$), which implies the necessity to select very carefully the excitation laser power density.

Vibrational characterization of complete devices

Multi-wavelength Raman analysis was applied to the Sb_2Se_3 thin films and solar cells based on this absorber, synthesized in the way described in the Experimental section. Note, that the power conversion efficiency of the obtained device was 4.5%, which is the typical range published for Sb_2Se_3 based

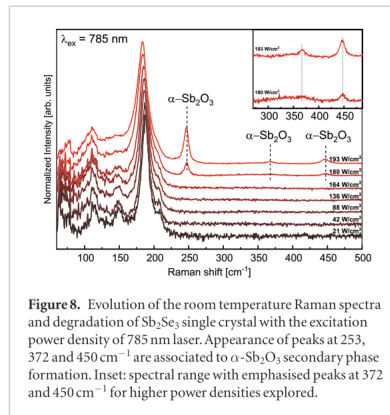


Figure 8. Evolution of the room temperature Raman spectra and degradation of Sb_2Se_3 single crystal with the excitation power density of 785 nm laser. Appearance of peaks at 253, 372 and 450 cm^{-1} are associated to $\alpha\text{-Sb}_2\text{O}_3$ secondary phase formation. Inset: spectral range with emphasised peaks at 372 and 450 cm^{-1} for higher power densities explored.

devices (figure 9(A)). Previously the high potential of the Raman spectroscopy for the complete solar cell characterization was established [26, 54, 55]. Indeed, clear methodologies for controlling the properties of different layers in thin film solar cells were shown [51]. However, a fine reference Raman spectrum should be measured before developing any methodologies. The spectra measured on the bare absorber and on complete device under different excitation wavelengths are presented in figure 9(B), together with the reference spectra measured on monocrystalline sample. In the spectra of complete device excited with 442 and 532 nm lasers the peak at 300 cm^{-1} is related to the CdS buffer layer. Here the use of the 442 nm excitation leads to a resonant condition with the CdS material and thus, a strong signal of its Raman peak do not allow to detect any peaks of the absorber layer before completing the cell for the detection of possible Sb_2O_3 secondary phase. The spectra of the bare absorber measured under mentioned wavelengths were found to be different from the spectra of single crystal by a clear presence of a peak at 237 cm^{-1} , related to a trigonal selenium (t-Se) secondary phase. Widening of the main peak is observed in bare absorber layer, which is explained by expected worsening of the crystal quality in the thin film versus single crystal. Additionally, small variation of the relative intensity of some of the Sb_2Se_3 peaks indicates difference in the preferential orientation of the thin film structure and the crystal plain of the monocrystalline sample, which, as it was mentioned above, can be potentially used for the control of thin film texture, i.e. the ribbons orientation.

Raman spectra measured under 633 nm excitation wavelength show an increase intensity of the trigonal selenium peak. This is mainly attributed to the resonant conditions for this secondary phase ($E_g(\text{Se}) \approx 1.9\text{ eV}$, $E_{633\text{ nm}} = 1.96\text{ eV}$). This proves the preceded statement that measurement under 633 nm

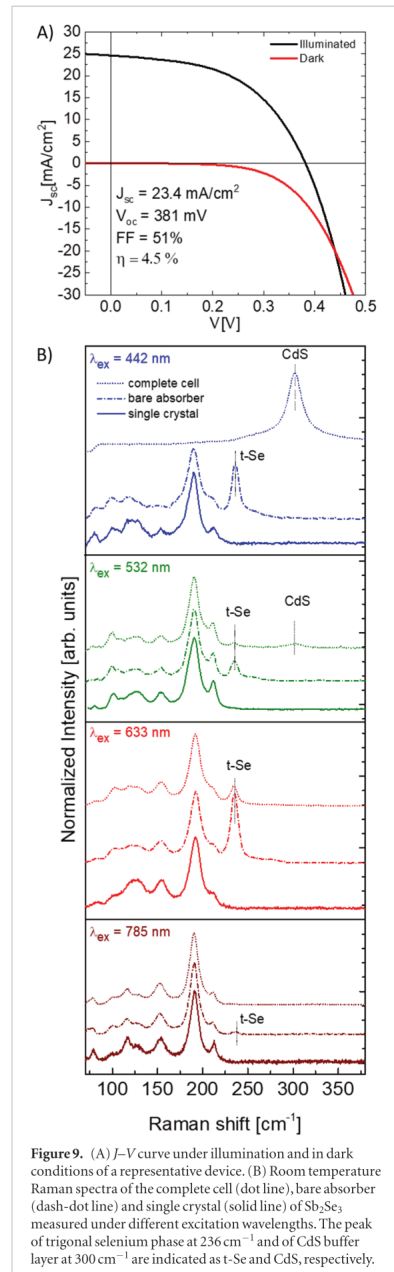


Figure 9. (A) J - V curve under illumination and in dark conditions of a representative device. (B) Room temperature Raman spectra of the complete cell (dot line), bare absorber (dash-dot line) and single crystal (solid line) of Sb_2Se_3 measured under different excitation wavelengths. The peak of trigonal selenium phase at 236 cm^{-1} and of CdS buffer layer at 300 cm^{-1} are indicated as t-Se and CdS, respectively.

excitation is the most suitable for detection of low concentration of the elemental Se. In contrast, no clear evidences of peaks of elemental Sb were found

in the measured spectra, which can be an indicator of the complete antimony incorporation in the Sb_2Se_3 structure. Taking into account observed presence of elemental selenium, the real chemical composition of the absorber could be closer to stoichiometric or even poor in selenium, which strongly influence the concentration of Se_{Sb} and V_{Sb} defects, which were found to be critical for the device performance [20]. Finally, in the spectra measured under 785 nm excitation wavelength the spectra of complete device, bare absorber and single crystal are highly similar and with a high signal to noise ratio. This allows to propose this excitation wavelength as the most suitable for the detection and analysis of Sb_2Se_3 compound, reducing the influence of the secondary phases contribution.

The combination of the different wavelengths provide a sensitive and non-destructive methodology for characterization of the absorber and/or full device based on Sb_2Se_3 thin film with a high sensitivity to detection of the most possible secondary phases.

Conclusions

In this work, 15 of 30 Raman peak position have been resolved at room temperature by multi-wavelength analysis and polarization study, and their symmetry was tentatively assigned. From the low temperature measurements, 13 peaks more were found in good agreement with theoretical predictions, and the positions at room temperature were confirmed. A good identification of the Raman peaks is crucial for the correct characterization of the material for all possible applications, and enables the possibility to potential evaluation of the concentration and type of atomic defects in the structure along with doping and other modifications of the structure. As a 1D material with a strong anisotropy of electrical conductivity, the assessment of the chain alignment is of a high importance, and the polarization Raman spectroscopy study opens the door to micro characterization of the material orientation with a fast and non-destructive technique.

The incongruences in the literature regarding the position and phase assignment of the material's Raman peaks has been treated in the secondary phase section. The importance of elemental selenium presence in the structure of the material and its effects on the electronic behaviour must be taken into account not to fall into the wrong interpretation of the experimental results. Additionally it is proposed a methodology based in multi-wavelength excitation for complete assessment of Sb_2Se_3 compound and their main secondary phases. Thus, we propose that characterization of the Sb_2Se_3 material could be properly performed under 785 nm excitation wavelength with minimal contribution of peaks from secondary phases. For the secondary phase detection and evaluation, the 442 nm excitation wavelength was found to be optimal for the antimony oxide species (only applicable in bare

absorber), and the most suitable laser wavelength for elemental selenium detection was 633 nm (compatible with full devices characterization).

Acknowledgments

This research was supported by the H2020 Programme under the project INFINITE-CELL (H2020-MSCA-RISE-2017-777968), by the DURACIS project from the SOLAR-ERA.NET International program (subproject ref. PCIN-2017-041 funded by Spanish MINECO) by the Spanish Ministry of Science, Innovation and Universities under the WINCOST (ENE2016-80788-C5-1-R), and by the European Regional Development Funds (ERDF, FEDER Programa Competitivitat de Catalunya 2007–2013). Authors from IREC and the University of Barcelona belong to the SEMS (Solar Energy Materials and Systems) Consolidated Research Group of the 'Generalitat de Catalunya' (Ref. 2017 SGR 862). MP thanks the Government of Spain for the Ramon y Cajal Fellowship (RYC-2017-23758).

ORCID iDs

Pedro Vidal-Fuentes  <https://orcid.org/0000-0001-5776-9986>

Maxim Guc  <https://orcid.org/0000-0002-2072-9566>

Xavier Alcobe  <https://orcid.org/0000-0001-7854-6052>

Tariq Jawhari  <https://orcid.org/0000-0002-5398-4766>

Marcel Placidi  <https://orcid.org/0000-0001-5684-9669>

Alejandro Pérez-Rodríguez  <https://orcid.org/0000-0002-3634-1355>

Edgardo Saucedo  <https://orcid.org/0000-0003-2123-6162>

Victor Izquierdo Roca  <https://orcid.org/0000-0002-5502-3133>

References

- [1] Kong P P et al 2015 Superconductivity in strong spin orbital coupling compound Sb_2Se_3 *Sci. Rep.* **4** 6679
- [2] Malligavathy M, Ananth Kumar R T, Das C, Asokan S and Pathinettam Padiyan D 2015 Growth and characteristics of amorphous Sb_2Se_3 thin films of various thicknesses for memory switching applications *J. Non-Cryst. Solids* **429** 93–7
- [3] Ge P, Cao X, Hou H, Li S and Ji X 2017 Rodlike Sb_2Se_3 wrapped with carbon: the exploring of electrochemical properties in sodium-ion batteries *ACS Appl. Mater. Interfaces* **9** 34979–89
- [4] Li G, Li Z, Chen J, Chen X, Qiao S, Wang S, Xu Y and Mai Y 2018 Self-powered, high-speed $\text{Sb}_2\text{Se}_3/\text{Si}$ heterojunction photodetector with close spaced sublimation processed Sb_2Se_3 layer *J. Alloys Compd.* **737** 67–73
- [5] Yuan C, Jin X, Jiang G, Liu W and Zhu C 2016 Sb_2Se_3 Solar cells prepared with selenized Dc-sputtered metallic precursors *J. Mater. Sci. Mater. Electron.* **27** 8906–10
- [6] Li Z, Chen X, Zhu H, Chen J, Guo Y, Zhang C, Zhang W, Niu X and Mai Y 2017 Sb_2Se_3 thin film solar cells in substrate configuration and the back contact selenization *Sol. Energy Mater. Sol. Cells* **161** 190–6

- [7] Chen C *et al* 2017 6.5% certified efficiency Sb₂Se₃ solar cells using PbS colloidal quantum dot film as hole-transporting layer *ACS Energy Lett.* **2** 2125–32
- [8] Chen C *et al* 2017 Accelerated optimization of TiO₂/Sb₂Se₃ thin film solar cells by high-throughput combinatorial approach *Adv. Energy Mater.* **7** 1700866
- [9] Li Z *et al* 2019 9.2%-efficient core-shell structured antimony selenide nanorod array solar cells *Nat. Commun.* **10** 125
- [10] Chen C *et al* 2017 Characterization of basic physical properties of Sb₂Se₃ and its relevance for photovoltaics *Frontiers Optoelectron.* **10** 18–30
- [11] Song H, Li T, Zhang J, Zhou Y, Luo J, Chen C, Yang B, Ge C, Wu Y and Tang J 2017 Highly anisotropic Sb₂Se₃ nanosheets: gentle exfoliation from the bulk precursors possessing 1D crystal structure *Adv. Mater.* **29** 1700441
- [12] Vadapoo R, Krishnan S, Yilmaz H and Marin C 2011 Electronic structure of antimony selenide (Sb₂Se₃) from GW calculations *Phys. Status Solidi* **248** 700–5
- [13] Maghraoui-Meherzi H, Ben Nasr T and Dachraoui M 2013 Synthesis, structure and optical properties of Sb₂Se₃ *Mater. Sci. Semicond. Process.* **16** 179–84
- [14] Costa M B, de Souza Lucas F W and Mascaro L H 2017 Thermal treatment effects on electrodeposited Sb₂Se₃ photovoltaic thin films *ChemElectroChem* **4** 2507–14
- [15] Lai Y, Han C, Lv X, Yang J, Liu F, Li J and Liu Y 2012 Electrodeposition of antimony selenide thin films from aqueous acid solutions *J. Electroanal. Chem.* **671** 73–9
- [16] Liu X *et al* 2014 Thermal evaporation and characterization of Sb₂Se₃ thin film for substrate Sb₂Se₃/CdS solar cells *ACS Appl. Mater. Interfaces* **6** 10687–95
- [17] Luo M, Leng M, Liu X, Chen J, Chen C, Qin S and Tang J 2014 Thermal evaporation and characterization of superstrate CdS/Sb₂Se₃ solar cells *Appl. Phys. Lett.* **104** 173904
- [18] Piacente V, Scardala P and Ferro D 1992 Total vapour pressure of solid Sb₂Se₃ *J. Mater. Sci. Lett.* **11** 855–7
- [19] Wen X *et al* 2017 Magnetron sputtered ZnO buffer layer for Sb₂Se₃ thin film solar cells *Sol. Energy Mater. Sol. Cells* **172** 74–81
- [20] Liu X *et al* 2017 Enhanced Sb₂Se₃ solar cell performance through theory-guided defect control *Prog. Photovolt., Res. Appl.* **25** 861–70
- [21] Wang L *et al* 2017 Stable 6%-efficient Sb₂Se₃ solar cells with a ZnO buffer layer *Nat. Energy* **2** 17046
- [22] Zakutayev A 2017 Brief review of emerging photovoltaic absorbers *Curr. Opin. Green Sustain. Chem.* **4** 8–15
- [23] Dimitrievska M, Fairbrother A, Fontané X, Jawhari T, Izquierdo-Roca V, Saucedo E and Pérez-Rodríguez A 2014 Multiwavelength excitation Raman scattering study of polycrystalline kesterite Cu₂ZnSnS₄ thin films *Appl. Phys. Lett.* **104** 021901
- [24] Dimitrievska M, Gurieva G, Xie H, Carrete A, Cabot A, Saucedo E, Pérez-Rodríguez A, Schorr S and Izquierdo-Roca V 2015 Raman scattering quantitative analysis of the anion chemical composition in kesterite Cu₂ZnSn(S_{1-x}Se_x)₄ solid solutions *J. Alloys Compd.* **628** 464–70
- [25] Dimitrievska M, Fairbrother A, Pérez-Rodríguez A, Saucedo E and Izquierdo-Roca V 2014 Raman scattering crystalline assessment of polycrystalline Cu₂ZnSnS₄ thin films for sustainable photovoltaic technologies: phonon confinement model *Acta Mater.* **70** 270–80
- [26] Oliva F, Arqués L, Acebo L, Guc M, Sánchez Y, Alcobé X, Pérez-Rodríguez A, Saucedo E and Izquierdo-Roca V 2017 Characterization of Cu₂ZnSn₄ polymorphism and its impact on optoelectronic properties *J. Mater. Chem. A* **5** 23863–71
- [27] Placidi M *et al* 2015 Multiwavelength excitation Raman scattering analysis of bulk and two-dimensional MoS₂: vibrational properties of atomically thin MoS₂ layers *2D Mater.* **2** 035006
- [28] Liang E, Xu H, Wu X, Wang C, Luo C and Zhang J 2018 Raman spectroscopy characterization of two-dimensional materials *Chin. Phys. B* **27** 037802
- [29] Mamedov S and Drichko N 2018 Characterization of 2D As₂S₃ crystal by Raman spectroscopy *MRS Adv.* **3** 385–90
- [30] Du Y, Qiu G, Wang Y, Si M, Xu X, Wu W and Ye P D 2017 One-dimensional van Der Waals material tellurium: Raman spectroscopy under strain and magneto-transport *Nano Lett.* **17** 3965–73
- [31] Kostadinova O and Yannopoulos S N 2009 Raman spectroscopic study of Sb₂Se_{100-x} phase-separated bulk glasses *J. Non-Cryst. Solids* **355** 2040–4
- [32] Lopez-Marino S *et al* 2016 The importance of back contact modification in Cu₂ZnSnSe₄ solar cells: the role of a thin MoO₂ layer *Nano Energy* **26** 708–21
- [33] Rietveld H M A 1969 Profile refinement method for nuclear and magnetic structures *J. Appl. Crystallogr.* **2** 65–71
- [34] Coelho A A, Evans J, Evans I, Kern A and Parsons S 2011 The TOPAS symbolic computation system *Powder Diffr.* **26** S22–5
- [35] Cheary R W, Coelho A A and Cline J P 2007 Fundamental parameters line profile fitting in laboratory diffractometers *J. Res. Natl Inst. Stand. Technol.* **109** 1–25
- [36] Voutsas G P, Papazoglou A G, Rentzeperis P J and Siapakas D 1985 The crystal structure of antimony selenide, Sb₂Se₃ *Z. Krist.—Cryst. Mater.* **171** 261–8
- [37] Rousseau D L, Bauman R P and Porto S P S 1981 Normal mode determination in crystals *J. Raman Spectrosc.* **10** 253–90
- [38] Liu Y, Eddie Chua K T, Sum T C and Gan C K 2014 First-principles study of the lattice dynamics of Sb₂S₃ *Phys. Chem. Chem. Phys.* **16** 345–50
- [39] Porto S P S and Krishnan R S 1967 Raman effect of corundum *J. Chem. Phys.* **47** 1009–12
- [40] Deringer V L, Stoffel R P, Wuttig M and Dronskowski R 2015 Vibrational properties and bonding nature of Sb₂Se₃ and their implications for chalcogenide materials *Chem. Sci.* **6** 5255–62
- [41] Efthimiopoulos I, Zhang J, Kucway M, Park C, Ewing R C and Wang Y 2013 Sb₂Se₃ under pressure *Sci. Rep.* **3** 2665
- [42] Ma X, Zhang Z, Wang X, Wang S, Xu F and Qian Y 2004 Large-scale growth of wire-like Sb₂Se₃ microcrystallines via PEG-400 polymer chain-assisted route *J. Cryst. Growth* **263** 491–7
- [43] Wang J, Deng Z and Li Y 2002 Synthesis and characterization of Sb₂Se₃ nanorods *Mater. Res. Bull.* **37** 495–502
- [44] Zhai T, Ye M, Li L, Fang X, Liao M, Li Y, Koide Y, Bando Y and Golberg D 2010 Single-crystalline Sb₂Se₃ nanowires for high-performance field emitters and photodetectors *Adv. Mater.* **22** 4530–3
- [45] Yang J, Lai Y, Fan Y, Jiang Y, Tang D, Jiang L, Liu F and Li J 2015 Photoelectrochemically deposited Sb₂Se₃ thin films: deposition mechanism and characterization *RSC Adv.* **5** 85592–7
- [46] Zhou Y *et al* 2014 Solution-processed antimony selenide heterojunction solar cells *Adv. Energy Mater.* **4** 1301846
- [47] Lu J, Han Q, Yang X, Lu L and Wang X 2008 Preparation of ultra-long Sb₂Se₃ nanoribbons via a short-time solvothermal process *Mater. Lett.* **62** 2415–8
- [48] Hu X *et al* 2018 Improving the efficiency of Sb₂Se₃ thin-film solar cells by post annealing treatment in vacuum condition *Sol. Energy Mater. Sol. Cells* **187** 170–5
- [49] Shongalova A, Correia M R, Vermang B, Cunha J M V, Salomé P M P and Fernandes P A 2018 On the identification of Sb₂Se₃ using Raman scattering *MRS Commun.* **8** 865–70
- [50] Allen J P, Carey J J, Walsh A, Scanlon D O and Watson G W 2013 Electronic structures of antimony oxides *J. Phys. Chem. C* **117** 14759–69
- [51] Cody C A, Dicarlo L and Darlington R K 1979 Vibrational and thermal study of antimony oxides *Inorg. Chem.* **18** 1572–6
- [52] Yannopoulos S N and Andrikopoulos K S 2004 Raman scattering study on structural and dynamical features of noncrystalline selenium *J. Chem. Phys.* **121** 4747–58
- [53] Wang X, Kunc K, Loa I, Schwarz U and Syassen K 2006 Effect of pressure on the Raman modes of antimony *Phys. Rev. B* **74** 134305
- [54] Oliva F *et al* 2016 Optical methodology for process monitoring of chalcopyrite photovoltaic technologies: application to low cost Cu(In,Ga)(S,Se)₂ electrodeposition based processes *Low Energy Mater. Sol. Cells* **158** 168–83
- [55] Guc M, Oliva F, Kondrotas R, Alcobe X, Placidi M, Pistor P, Saucedo E, Perez-Rodríguez A and Izquierdo-Roca V 2019 Cu₂ZnInSe₄-based solar cells: impact of copper concentration on vibrational and structural properties and device performance *Prog. Photovolt., Res. Appl.* **27** 716–23

3.3 - Article 2

Efficient Se-Rich $\text{Sb}_2\text{Se}_3/\text{CdS}$ Planar Heterojunction Solar Cells by Sequential Processing: Control and Influence of Se Content

Pedro Vidal-Fuentes,* Marcel Placidi, Yudania Sánchez, Ignacio Becerril-Romero, Jacob Andrade-Arvizu, Zacharie Jehl, Alejandro Pérez-Rodríguez, Víctor Izquierdo-Roca, and Edgardo Saucedo*

Quasi-1D chalcogenides are under the spotlight due to their unique properties for several technological applications including computing, photonic, sensing, and energy conversion. In particular, antimony chalcogenides have recently experienced incredible progresses as emerging photovoltaic materials. Herein, the fabrication by a sequential process of Sb_2Se_3 solar cells is addressed, and the annealing temperature is found to be the main parameter controlling the composition of the Se-rich absorbers. Building on this, a systematic study of the evolution of the optoelectronic parameters of the solar cells as a function of the Se excess is presented together with a thorough characterization of the devices that sheds light on their main limiting factors. A record power conversion efficiency of 5.7% is achieved, the highest reported value using reactive annealing on a metallic precursor for this material.

(such as Cd in CdTe), which will hamper their deployment beyond the Terawatt level.^[3,4] The past 10 years have shown the emergence of new chalcogenide materials for TFPV applications which, while inspired by CdTe and CIGS, alleviate the material scarcity issue by being based on abundant elements. Although important progresses were made in that regard, the large complexity of the most successful earth-abundant chalcogenide compounds, $\text{Cu}_2\text{SnZn}(\text{S,Se})_4$ (CZTSSe or kesterite) has led to stalling performances that remain below 13%,^[5] resulting in a declining interest from the industry. In that context, returning toward simpler compounds with less than four elements present an attractive path for the development

1. Introduction

Thin-film photovoltaic (TFPV) chalcogenide absorbers such as cadmium telluride (CdTe) and $\text{Cu}(\text{In,Ga})(\text{S,Se})_2$ (CIGS) are reaching maturity with record power conversion efficiencies (PCEs) of 22.1% and 23.35%, respectively, leading to an increase in their industrial deployment and module production.^[1,2] Although these technologies are achieving remarkable results among TFPV materials approaching the values of those of silicon solar cells, they contain elements that are considered either scarce (such as In and Ga in CIGS, or Te in CdTe) or toxic


of further TFPV technologies. Several of these simpler materials have recently attracted a lot of interest, such as the binary compounds SnS, GeSe, and $\text{Sb}_2(\text{S,Se})_3$, the ternary compounds $\text{CuSb}(\text{S,Se})_2$, $\text{Cu}_2\text{Sn}(\text{S,Se})_3$, and even elemental Se.^[3,6–18]

Among them, quasi-1D (Q-1D) antimony chalcogenide compounds have demonstrated a promising performance increase within a short timeframe (Table 1), with a very recent record of 9.2% PCE reported for a Sb_2Se_3 device in a nonplanar configuration.^[18] In addition, Q-1D Sb_2Se_3 is formed by earth-abundant and low-toxicity constituents, and has shown various properties that position it as a strong candidate for low-cost TFPV applications: its single stable phase (similar to CdTe, hence avoiding issues with secondary-phase formation), an almost optimal bandgap (1.0–1.20 eV indirect and 1.17–1.30 eV direct), a large absorption coefficient above the bandgap (around 10^5 cm^{-1}), and a carrier lifetime of 67 ns, higher than that of kesterite and most chalcopyrite materials.^[42–44]

An important characteristic of this material is its Q-1D crystal structure forming ribbons stacked by van der Waals forces that confer it anisotropic conduction properties, and in principle benign grain boundaries (absence of dangling bonds) possibly leading to preferential carrier transport along the ribbons and low recombination losses in solar cell devices.^[15,20] Moreover, recent works have demonstrated the possibility of controlling the orientation during the Sb_2Se_3 growth by choosing an adequate substrate, a crucial step for high performance.^[45,46] However, little is known about the influence of the film

P. Vidal-Fuentes, Dr. M. Placidi, Dr. Y. Sánchez, Dr. I. Becerril-Romero, J. Andrade-Arvizu, Dr. Z. Jehl, Prof. A. Pérez-Rodríguez, Dr. V. Izquierdo-Roca, Dr. E. Saucedo
Advanced Materials for Energy
Catalonian Institute for Energy Research (IREC)
Jardin de les Dones de Negre 1, Sant Adrià de Besòs 08930, Barcelona, Spain
E-mail: pvidal@irec.cat; esaucedo@irec.cat

Prof. A. Pérez-Rodríguez
Departament d'Enginyeria Electrònica i Biomèdica
IN2UB
Universitat de Barcelona
c. Martí i Franquès 1, 08028 Barcelona, Spain

 The ORCID identification number(s) for the author(s) of this article can be found under <https://doi.org/10.1002/solr.202000141>.

DOI: 10.1002/solr.202000141

Table 1. Summary of the best planar Sb₂Se₃ solar cells (works using organic layers as hole transport layer have not been reported in the table).

Ref.	Technique	Configuration	Device structure	Eff. [%]	FF [%]	J _{sc} [mA cm ⁻²]	V _{oc} [mV]	N _d [cm ⁻³]	w [nm]	Comments
[19]	RTE ^{a)}	SS ^{b)}	Glass/ITO/CdS/Sb ₂ Se ₃ /Au	7.04	59.3	–	–	–	–	CuCl ₂ treatment + (NH ₄) ₂ S etching
[20]	TE ^{c)}	S ^{d)}	SLG/Mo/MoSe ₂ /Sb ₂ Se ₃ /CdS/ZnO/ITO/Au	4.25	58.1	17.1	427	3.2 × 10 ¹⁶	–	Mo selenization
[21]	CE ^{e)}	SS	SLG/FTO/CdS/Sb ₂ Se ₃ /Au	3.47	41.3	23.1	364	2.2 × 10 ¹⁵	–	
[22]	RTP ^{f)}	S	SLG/Mo/Sb ₂ Se ₃ /CdS/Al/ZnO:Al	3.47	52	16.0	414	8.8 × 10 ¹³	–	
[23]	VTD ^{g)}	SS	Glass/ITO/CdS/Sb ₂ Se ₃ /Au	7.6	60.4	29.9	420	–	–	
[24]	RTE	SS	Glass/FTO/TiO ₂ /Sb ₂ Se ₃ /Au	5.6	55.1	28.3	358	2 × 10 ¹⁷	67	(NH ₄) ₂ S etching
[25]	CSS ^{h)}	SS	Glass/ITO/CdS/Sb ₂ Se ₃ /CZ-TA/Au	6.84	57.1	28.4	421	–	256	n-i-p structure
[26]	RTE	SS	Glass/ITO/CdS/Sb ₂ Se ₃ /PbS(CQD)/Au	6.5	59.3	25.5	427	–	214	n-i-p structure
[27]	RTE	SS	Glass/FTO/ZnO/Sb ₂ Se ₃ /Au	5.93	57.8	26.2	391	2 × 10 ¹⁶	220–280	ZnO orientation control
[28]	Sp-Se ⁱ⁾	S	Glass/Mo/Sb ₂ Se ₃ /CdS/ITO/Ag	6.06	47.7	25.91	494	9 × 10 ¹⁶	160	
[29]	SpSb-Se ^{j)}	S	Glass/Mo/Sb ₂ Se ₃ /CdS/ITO/Ag	6.15	59.5	22.75	455	1 × 10 ¹⁶	222	
[30]	VTD	S	Mo/MoSe ₂ /Sb ₂ Se ₃ /In ₂ S ₃ /i-ZnO/ITO/Au	5.35	51.9	28.22	370	1 × 10 ¹⁶	250–300	Flexible substrate
[31]	CSS	S	SLG/Mo/Sb ₂ Se ₃ /Cd _{0.9} Zn _{0.1} S/ZnO/ZnO:Al	6.71	64.8	25.7	403	–	–	
[32]	TE	SS	Glass/ITO/CdS/Sb ₂ Se ₃ /Au	4.8	52.5	25.3	353	1.4 × 10 ¹⁵	–	O ₂ addition
[33]	RTE	SS	Glass/FTO/ZnO/Sb ₂ Se ₃ /Au	4.08	44.5	28.0	328	–	–	Air annealed
[34]	RTE	SS	Glass/FTO/ZnO/Zn _{1-x} Mg _x O/Sb ₂ Se ₃ /Au	4.45	48.0	26.2	360	–	153	Zn _{0.9} Mg _{0.1} O
[35]	VTD	SS	Glass/ITO/CdS/Sb ₂ Se ₃ /Au	5.72	55.7	26.0	371	1 × 10 ¹⁷	450	Postannealing in vacuum 200 °C
[36]	VTD	SS	Glass/ITO/SnO ₂ /CdS/Sb ₂ Se ₃ /Au	5.91	58.4	27.3	355	–	–	
[37]	CSS	SS	Glass/FTO/SnO ₂ /CdS/Sb ₂ Se ₃ /Au	5.18	55.0	24.5	385	7.6 × 10 ¹⁵	–	
[38]	CSS	SS	Glass/FTO/TiO ₂ /Sb ₂ Se ₃ /Au	5.5	49.0	25.4	450	3 × 10 ¹⁶	250	TiO ₂ buffer
[39]	VTD	SS	Glass/ITO/CdS/Sb ₂ Se ₃ /Au	7.0	57	29.4	417	–	–	NiO _x back contact proof of concept
[40]	TE	SS	Glass/FTO/CdS/Sb ₂ Se ₃ /Au	3.7	46.8	24.4	335	2.6 × 10 ¹⁶	343	Postselenization
[41]	RTE	SS	Glass/FTO/CdS/p-Sb ₂ Se ₃ /p-Sb ₂ Se ₃ /Al ₂ O ₃ /Au	6.7	57.8	28.6	406	3 × 10 ¹⁵	–	Oxygen plasma + Al ₂ O ₃
[18]	CSS	S	Glass/Mo/MoSe ₂ /Sb ₂ Se ₃ -nanorods/TiO ₂ /CdS/ZnO/AZO	9.2	70.3	32.6	400	–	–	Nanorod Sb ₂ Se ₃ + ALD TiO ₂

^{a)}Rapid thermal evaporation; ^{b)}Superstrate; ^{c)}Thermal evaporation; ^{d)}Substrate; ^{e)}Coevaporation; ^{f)}Rapid thermal process; ^{g)}Vapor transport deposition; ^{h)}Close space sublimation; ⁱ⁾Sputtering of Sb₂Se₃ and selenization; ^{j)}Sputtering of Sb and selenization;

composition on the photovoltaic (PV) response of the Sb₂Se₃ devices, and previous studies on CIGS and CZTS have demonstrated how critical it can be in controlling the presence of defects within the layer.^[47,48] Typically, the best Sb₂Se₃ reported solar cells are achieved under Se-rich conditions which tends to reduce the presence of Se vacancies (V_{Se}) and substitutional defects (especially Sb_{Se}) acting as donor impurities. Se vacancies have been widely reported as the main recombination centers and ascribed to performance degradation, especially in thermally evaporated devices.^[49] Nevertheless, postdeposition steps such as selenization have been reported to be highly effective in reducing the density of Se vacancies.^[31]

It is shown in Table 1 that most of the record devices are fabricated through evaporation or closed space sublimation, and in superstrate configuration.^[18,19,21–30,32–41,45,50] Very few groups have been focusing on a substrate configuration, and only one study reported a sequential route based on selenization of a

sputtered Sb precursor which resulted in a promising efficiency of 6.15%.^[28] In this work, we aim at extending the Sb₂Se₃ technology toward substrate configuration and sequential processing, which is of high importance for future development of cost-effective applications based on this technology.

As such, a sequential route based on the selenization of thermally evaporated Sb layers is proposed. This work is divided into two main parts. First, a broad analysis is conducted and the most relevant process parameters that lead to good-quality Se-rich Sb₂Se₃ PV absorbers with an adequate orientation and no secondary phases are identified. The composition of the layers is shown to be controllable through the temperature of the reactive annealing, demonstrating the optimal elemental ratio and leading to the fabrication of a glass/Mo/Sb₂Se₃/CdS/i-ZnO/indium tin oxide (ITO)-based solar cell with a 5.7% PCE. The second part of the work focuses on a deep analysis of the optoelectronic properties of the best device. From these results, the main PCE limitations

of the Sb_2Se_3 absorber are identified, and strategies for further improvement of the device architecture are proposed.

2. Results and Discussion

2.1. Synthesis of Sb_2Se_3 Absorbers by a Sequential Process: How to Control the $3[\text{Sb}]/2[\text{Se}]$ Ratio

Sb_2Se_3 thin-film solar cells were fabricated in substrate configuration (in contrast to most of the works reported with this material, as shown in Table 1) by a sequential process, as described in Section 4 (Figure S1, Supporting Information). The annealing atmosphere was controlled by fixing the amount of Se powder (25 mg) and by varying several other parameters such as temperature, pressure, and time. Due to the lack of information about Sb_2Se_3 processing through reactive annealing of a Sb layer, the first part of the work is focused on understanding the influence of the different annealing parameters on relevant structural properties of this Q-1D material.

The influence of reactive annealing temperature on the composition of the Sb_2Se_3 layer was first investigated by varying it from 300 up to 400 °C while fixing the rest of the parameters. This way, the heating ramp was fixed to 20 °C min^{-1} , the processing time to 30 min, and the pressure to 500 mbar. Figure 1a

shows the change in composition in the range of temperatures investigated determined by X-ray fluorescence (XRF) measurements. The results show that the layers are consistently Se-rich ($3[\text{Sb}]/2[\text{Se}] < 1$) and, interestingly, the $3[\text{Sb}]/2[\text{Se}]$ ratio is found to decrease with the increasing annealing temperature. This is an important result because it implies that it is possible to adjust the absorber composition within a wide range in a simple way by varying the annealing temperature. Despite the observed Se excess, X-ray diffraction (XRD) and Raman spectroscopy measurements (under Se resonant conditions) (Figure 1b,c) show no evidence of elemental Se secondary phases in the samples processed in the 300–380 °C range. Therefore, it can be assumed that the selenium excess is completely assimilated into the structure of the absorber. In contrast, both elemental Se and $\alpha\text{-Sb}_2\text{O}_3$ secondary phases are clearly detected in the sample processed at 400 °C, the peak assignment of the different phases can be found elsewhere.^[51] Thus, it seems that such high amount of Se exceeds the assimilation capacity of the lattice and leads to the segregation of elemental Se at the surface of the film.^[52,53] In contrast, the presence of $\alpha\text{-Sb}_2\text{O}_3$ detected in the samples annealed at 400 °C is probably arising from the selective oxidation of the Sb-rich surface due to the partial Se loss at 400 °C. Sb detection in such case is impossible as the characterization is performed after oxidation, but Sb_2O_3 is fully detectable thanks to the high sensitivity of Raman spectroscopy to this phase,

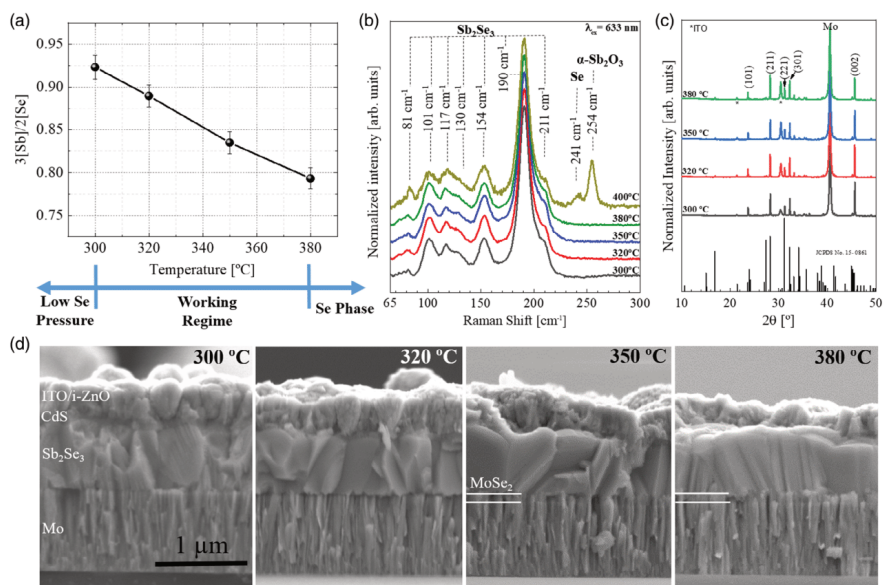


Figure 1. Effect of synthesis temperature on Sb_2Se_3 absorber layers: a) compositional ratio $3[\text{Sb}]/2[\text{Se}]$ obtained at different temperatures showing an optimal range (working regime) comprised between 300 and 380 °C. b) Raman spectra ($\lambda_{\text{ex}} = 633 \text{ nm}$) showing the presence of Se and $\alpha\text{-Sb}_2\text{O}_3$ for the absorber processed at 400 °C. c) XRD diffractograms with preferential orientation around [001] for all the temperatures. d) Cross-section SEM images of the samples processed at different temperatures.

the detection accounts for a small and superficial presence of this secondary phase. Nevertheless, this is just a hypothesis that requires for further analysis and confirmation, to be addressed in subsequent works.^[29,49,54] It can thus be inferred that the optimum annealing temperature range to obtain Se-rich single phase Sb_2Se_3 lies within a broad temperature range from 300 to 380 °C.

The XRD measurements were performed on the different samples to identify the preferential orientation of the Sb_2Se_3 layers (Figure 1c) (only data from 10° to 50° is presented for the sake of clarity). Interestingly, no noticeable texture change is observed for annealing temperatures between 300 and 380 °C, in agreement with the apparent stability of the process up to this point. A clear preferential $[hk1]$ orientation (JCPDS no. 15-0861) is observed in all the cases. This orientation is ascribed to vertically aligned ribbons, with negligible presence of undesirable $[hk0]$ planes.^[18] Thus, the sequential process developed in this work for the synthesis of Sb_2Se_3 layers (and using glass/Mo as substrate) results in $[hk1]$ oriented ribbons regardless of the annealing temperature. In addition, both Raman and XRD measurements demonstrate that in the $0.78 \leq 3[\text{Sb}]/2[\text{Se}] \leq 0.92$ composition region, only orthorhombic (Pnmb #62) Sb_2Se_3 phase is observed.^[51]

Regarding the morphology of the absorbers, cross-sectional scanning electron microscopy (SEM) micrographs on completed devices are shown in Figure 1d. Independently from the annealing temperature, the grains maintain a uniform appearance, without voids or substrate delamination issues, and generally large grains with clear facets forming compact layers. This aligns well with previous reports on this material.^[45] In addition, a clear increase in grain size is observed for annealing temperature of 380 °C.

In contrast, it is also possible to observe the formation of a thin layer in the interface between the Mo and the Sb_2Se_3 absorber layer in the samples synthesized at 350 and 380 °C. This layer, which increases with the annealing temperature from ≈ 75 to ≈ 130 nm, is associated with the formation of a MoSe_2 phase, which could enhance the contact ohmicity at the back interface, as widely reported for other chalcogenides,^[55] and more recently for Sb_2Se_3 devices.^[45]

The influence of the annealing pressure and duration were also investigated (Figure 2 and Figure S2, Supporting Information). Figure S2, Supporting Information, shows that at pressures below 500 mbar, the obtained Sb_2Se_3 absorbers display a degraded absorber morphology with very low homogeneity. This effect could be related to a fast Se evaporation at the beginning of the annealing routine, hindering chalcogen availability during the rest of the process. In contrast, for pressures comprised between 500 and 1000 mbar, no inhomogeneity is observed. As shown in Figure 2a, the highest pressures (500 and 1000 mbar) lead to similar absorber compositions. In addition, the crystalline quality remains unchanged with the increasing annealing pressure as can be deduced from the analysis of the full width at half maximum (FWHM) of the main XRD 211 and 002 reflections (Figure 2c). These results indicate that the suitable pressure range for the synthesis of Sb_2Se_3 is broad, between 500 and 1000 mbar, with negligible variations within this range.

Regarding the annealing duration, six different dwell times (from 5 to 60 min) were tested. The annealing temperature was fixed to 320 °C (this temperature was selected based on the performance of the solar cell devices that will be presented in the next section). No significant changes are observed neither

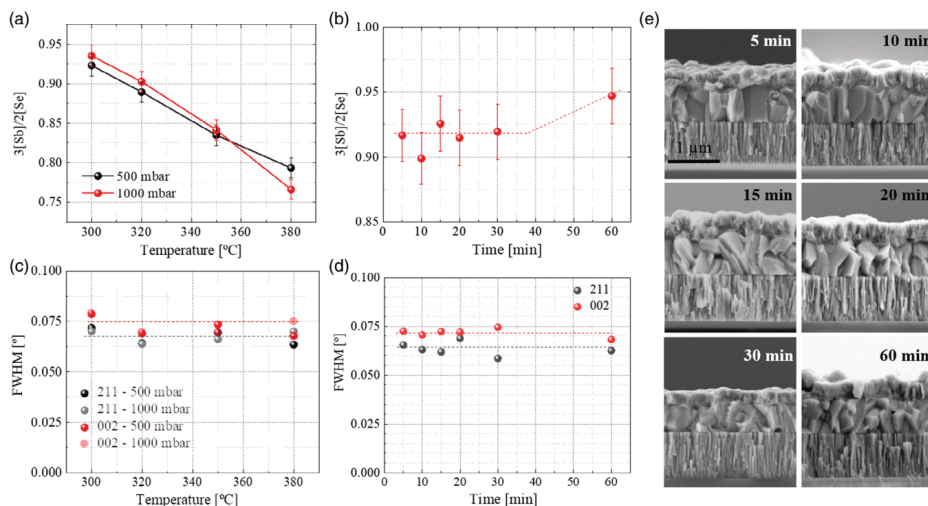


Figure 2. Effect of the pressure and time for the synthesis of the Sb_2Se_3 absorber layers: a,b) composition ratios dependence with pressure and time. c,d) FWHM dependence with pressure and time of the 002 and 211 reflections. e) Cross-section SEM images of the samples for different processing times.

in composition (Figure 2b) nor in the FWHM of the 211 and 002 reflections (Figure 2d) for dwell durations ≤ 30 min. This indicates that for short processing times (up to 30 min), there is almost no Se loss in contrast to what is typically reported in the literature using other deposition techniques, especially with thermal evaporation.^[50] However, longer annealing times (60 min), increase the 3[Sb]/2[Se] ratio of the synthesized absorbers close to stoichiometry, suggesting a significant Se loss. Figure 2e shows cross-sectional SEM images of the samples processed using different dwell durations. The only noticeable difference between them is a lower grain size for longer processing times, especially for the 60 min annealing. It is interesting to note that large grains and an absence of voids are obtained with annealing durations as short as 5 min.

Thus, from the results shown previously, it can be concluded that it is possible to obtain good-quality Se-rich Sb_2Se_3 layers by reactive annealing of Sb layers. In addition, it has been demonstrated that the annealing temperature can be used to control the composition of the absorber layers, whereas the annealing pressure and duration exhibit a minor influence. In the following

section, the impact of the absorber composition on the optoelectronic parameters of the solar cells is investigated.

2.2. The Impact of the 3[Sb]/2[Se] Ratio on the $\text{Sb}_2\text{Se}_3/\text{CdS}$ Planar Heterojunction Properties

Following the previous results, all the absorbers synthesized at 500 and 1000 mbar were processed into solar cells to investigate on the correlation between the absorber composition and the PV properties of the completed devices. A 30 min dwell time was used to minimize the effects of small variations in the reactive annealing step, which could have higher impact for shorter times; thus, ensuring a better comparability between samples is achieved. The results are shown in Figure 3 where the most relevant optoelectronic parameters of the single solar cells are plotted as a function of the 3[Sb]/2[Se] ratio of the absorbers including dark and illuminated current density–voltage (J – V), together with capacitance–voltage (C – V) analysis. Observing the evolution of the PCE with the composition (Figure 3a), three

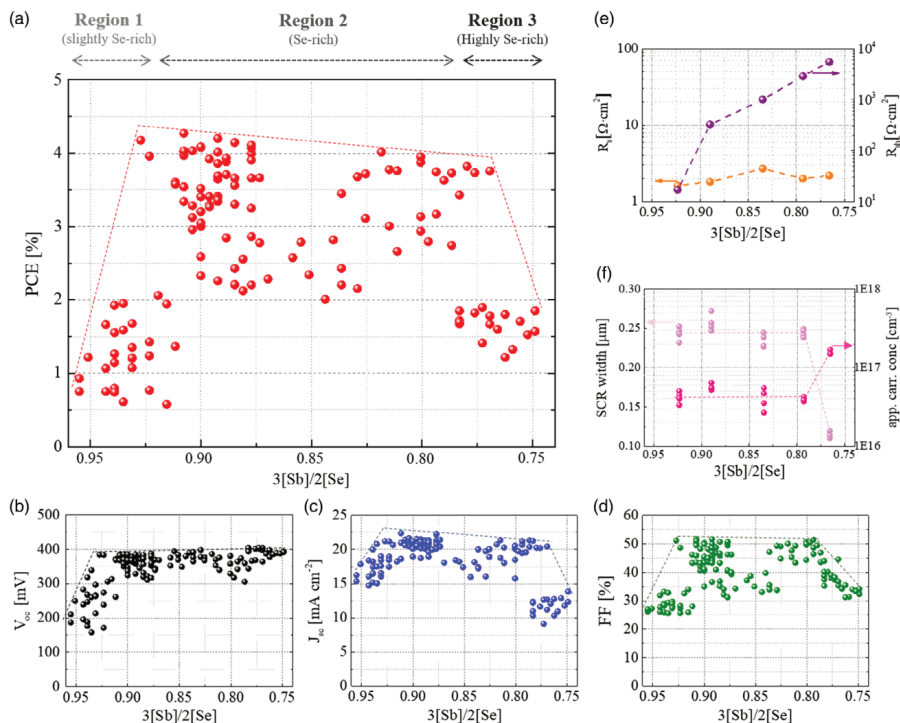


Figure 3. Effect of the composition on the device performance of $\text{Sb}_2\text{Se}_3/\text{CdS}$ planar heterojunction solar cells: a) PCE; b) open-circuit voltage; c) short-circuit current; d) fill factor; e) series and shunt resistances; and f) apparent carrier concentration and SCR width, as a function of the 3[Sb]/2[Se] composition ratio.

different regions are clearly distinguished. The main characteristics of each compositional region are now surveyed:

Region 1 (slightly Se-rich conditions, $0.95 \geq 3[\text{Sb}]/2[\text{Se}] > 0.90$): All the optoelectronic parameters are below the maximum values obtained in this set of samples with V_{oc} (around 100 mV, Figure 3b), J_{sc} (around 3 mA cm⁻², Figure 3c), and fill factor (FF) (around 15% absolute, Figure 3d). Looking at the analysis of dark J - V curves (Figure 3e, raw dark J - V curves can be found in Figure S4, Supporting Information), it is clear that the samples in this region suffer from a very low shunt resistance (R_{sh}), only one order of magnitude higher than series resistance (R_{s}). This correlates with the low V_{oc} and deteriorated FF. Because no pinholes were observed in these samples that could imply an interconnection between the ITO and the Sb_2Se_3 layer or even with the Mo back contact, and there is no evidence of secondary phases by XRD or Raman spectroscopy that could account for some conductive paths in the sample, our hypothesis is that such an unusually low R_{sh} may be arising from direct conduction through unpassivated grain boundaries. In contrast, the series resistance of the devices can be considered low (1.5 Ω cm²), consistent with the good crystalline quality and the beneficial [001] preferential orientation of the absorbers. Likewise, the apparent carrier concentration estimated from C - V measurements is in the range of 10^{16} - 10^{17} cm⁻³ (Figure 3e, raw data can be found in Figure S5, Supporting Information) typical for Sb_2Se_3 and other high-efficiency chalcogenide devices.^[18,56] The space charge region (SCR) width around 250 nm is comparable with other Sb_2Se_3 devices shown in Table 1, which we consider low and could account for collection problems for photo-generated carriers near the back contact. In summary, the main identified problems for this region of slightly Se-rich composition are a low R_{sh} and a narrow SCR.

Region 2 (Se-rich conditions, $0.90 \geq 3[\text{Sb}]/2[\text{Se}] > 0.80$): In this region, the V_{oc} (Figure 3b) and FF (Figure 3d) are remarkably increased, whereas J_{sc} is only slightly enhanced (Figure 3c). This is accompanied by a higher R_{sh} (up to two orders of magnitude) as extracted from the dark J - V curves. Furthermore, the R_{sh} of the devices follows an almost exponential increase with Se content (Figure 3e). Considering that neither the crystalline quality nor the orientation of the absorber grains are modified with the increasing Se content and that no secondary Se phases are detected, it seems that Se-excess is accumulated within the structure of Sb_2Se_3 . In fact, a recent work proposes that Sb_2Se_3 can accept high concentrations of defects due to weak van der Waals interactions and the large interspace between the different $[\text{Sb}_4\text{Se}_6]_{\text{n}}$ atomic chains of the Q-1D structure.^[52] The presence of electrically inactive Se_i^{31} or even of wide bandgap crystalline elemental Se could hinder electronic hopping in this region, and drastically reduce the conduction at the grain boundaries which could lie at the origin of the improved R_{sh} observed in this region.

Region 3 (very Se-rich conditions, $3[\text{Sb}]/2[\text{Se}] \leq 0.80$): Further increase of the Se content leads to a deterioration of the PCE, due to degraded J_{sc} and FF (V_{oc} is not affected). In this case, the resistances of the devices present favorable values for solar cell performance and thus seem unrelated to the observed low PCE's. However, important changes are observed from the C - V analysis (Figure 3f). In particular, the apparent carrier concentration increases, and the SCR width strongly decreases to

values as low as 0.10 μm . The latter observation could lead to a lower collection efficiency and an increased recombination at the SCR which is in good agreement and with the low J_{sc} and FF observed in this region. Therefore, it seems clear that a too high Se content somehow affects the $\text{Sb}_2\text{Se}_3/\text{CdS}$ heterojunction, modifying the electrical properties of the absorber.

In contrast to the large impact of the composition on the optoelectronic parameters of the solar cell devices, the bandgap of the absorber (both the indirect and the direct bandgaps) calculated by the derivative method from the external quantum efficiency (EQE) of the devices (Figure S3, Supporting Information) is not affected by the $3[\text{Sb}]/2[\text{Se}]$ ratio.

In the last part of the article, a detailed characterization of a high PCE device is presented to further study the relation between Se content and solar cell performance.

2.3. Limiting Factors for PCE in a High-Efficiency $\text{Sb}_2\text{Se}_3/\text{CdS}$ Planar Heterojunction Solar Cell

In the previous section, it has been demonstrated that the highest PCE are obtained for absorber compositions in the Se-rich region of the Sb_2Se_3 phase diagram ($3[\text{Sb}]/2[\text{Se}] = 0.8$ - 0.9) with the record performance obtained for $3[\text{Sb}]/2[\text{Se}] = 0.88$. This section presents a complete optoelectronic characterization of one of these record devices (5.7% PCE). Raman spectroscopy measurements (Figure S6, Supporting Information) and XRD data (Figure S7, Supporting Information) suggest that the absorber of the selected device is free of secondary phases (neither Se nor $\alpha\text{-Sb}_2\text{O}_3$ are detected) and shows good crystal quality with a predominant (002) and (301) texture that implies a preferential [001] orientation (although not uniaxial). Thus, this analysis will focus on the intrinsic properties of the absorber and the interfaces of the device to discriminate among the possible factors limiting its PCE.

Figure 4 shows the illuminated and dark J - V curves of the selected Sb_2Se_3 device. In addition, Table 2 shows a summary

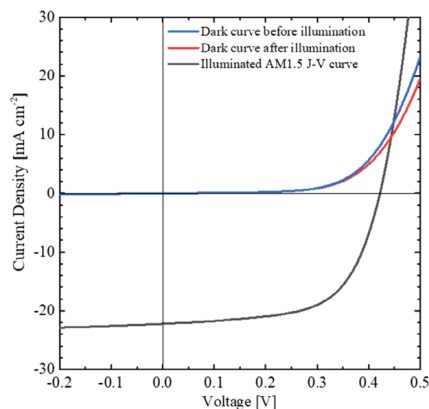


Figure 4. Dark and illuminated J - V characteristics of the best solar cell obtained in this study.

Table 2. Summary of the optoelectronic parameters obtained for the champion solar cell obtained in this study. The parameters are extracted from Figure 4–6.

Parameter	Value	Units
3[Sb]/2[Se]	0.88	–
PCE	5.7	%
V_{oc}	422	mV
J_{sc}	21.9	mA cm^{-2}
FF	61.7	%
R_s	2	$\Omega \text{ cm}^2$
R_{sh}	1143	$\Omega \text{ cm}^2$
J_0	0.001	mA cm^{-2}
A	1.605	–
App. carr. conc.	5.3×10^{16}	cm^{-3}
SCR	212	Nm
$E_{g,ind}$	1.26	eV
$E_{g,dir}$	1.37	eV
E_U	17.4	meV
Ext. V_{oc} (0 K)	0.94	eV

of the most relevant optoelectronic parameters extracted from the J – V analysis as well as from EQE, C – V , and J – V – T measurements. The following information on the figures of merit of the device can be extracted from these data:

Open-circuit voltage: The device presents a V_{oc} of 422 mV. This value is in the range of the best ones reported in the literature (Table 1). Nevertheless, considering that the indirect bandgap of the material is estimated to be 1.26 eV (Figure 5), a large voltage deficit still exists and should be considered the main limitation of the device (and of Sb_2Se_3 devices in general). Such a large V_{oc} deficit can be related either to intrinsic defects, to interface recombination, to a combination of both or to absorber/buffer band alignment.^[32]

Fill factor: The device exhibits a FF of 61.7%, which, again, is among the best FF reported in the literature (Table 1). This is a clear indication of the formation of a good CdS/ Sb_2Se_3 heterojunction. The low series resistance R_s ($2 \Omega \text{ cm}^2$), favored by the [001] preferential orientation of the film (Figure S5, Supporting Information),^[18] and the high R_{sh} ($1143 \Omega \text{ cm}^2$) further support the favorable properties of the heterojunction.

Short-circuit current: In contrast to the V_{oc} and FF, the J_{sc} of this record device (21.9 mA cm^{-2}) is low compared with the state of the art of the Sb_2Se_3 technology. This could be related to the narrow SCR systematically observed in all the samples presented in this work (around 212 nm), although is comparable with those shown in Table 1, the fact of not using a front metallic contact could affect the extracted current in a deeper way. Furthermore, the low J_{sc} reveals a current leakage problem at the heterojunction that may be pointing toward the degradation of the absorber surface during the deposition of the CdS buffer layer (chemical bath deposition) or even toward an unstable Sb_2Se_3 /CdS interface due to element interdiffusion.^[18] Figure 4 also shows a clear cross-over between the light and dark J – V curves

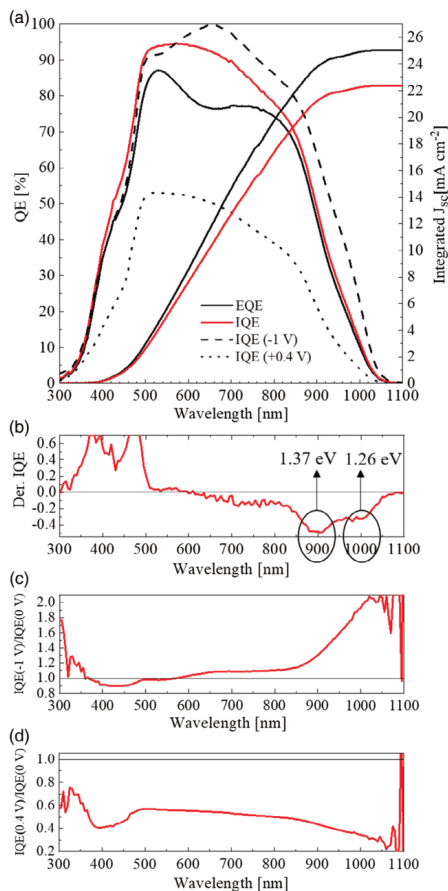


Figure 5. Spectral response characterization of the best device: a) external, internal, and biased internal (reverse at -1 V and forward at $+0.4 \text{ V}$) quantum efficiency, along with the integrated J_{sc} for EQE and IQE. b) Bandgap calculation from the derivative method. c) Ratio between IQE (-1 V)/IQE (0 V). d) Ratio between IQE ($+0.4 \text{ V}$)/IQE (0 V).

of the device which is aggravated after first illumination. This can be attributed to the presence of photoactive defects at the Sb_2Se_3 /CdS heterojunction interface or within the bulk of the CdS that translates into a high density of acceptor-like traps.^[57] These traps can be the result of partial interface degradation/modification during the CdS or even during the i -ZnO/ITO deposition.

Regarding other parameters extracted from the dark J – V curve, the reverse saturation current (J_0) can be considered relatively high compared with high PCE chalcogenide devices

such as CIGS.^[58] A high J_0 is often related to the recombination through interface defects at the p–n junction which supports the idea of $\text{Sb}_2\text{Se}_3/\text{CdS}$ interface recombination being one of the main problems of the devices fabricated in this work. In contrast, the diode quality factor remains below 2 (1.605) which indicates that a single diode model is a reasonably accurate representation of the selected device and that recombination is most probably occurring at the interfaces.

The C–V measurements show an apparent carrier concentration of $5.3 \times 10^{16} \text{ cm}^{-3}$ and a SCR width of 212 nm. The carrier concentration is a bit higher than in other works but still compatible with the fabrication of high PCE solar cells.^[45,59] On the contrary, the SCR width is narrow, suggesting that either the absorber properties are not optimal, and/or that the SCR width is being influenced by the CdS layer.

Complementary to the previous optoelectronic characterization, EQE, internal quantum efficiency (IQE), and biased IQE measurements were also performed on the record device (Figure 5a). The bandgap of the Sb_2Se_3 absorber was extracted from the IQE using the derivative method (Figure 5b).^[60] A “double feature” is clearly observed which may correspond to the double bandgap (direct and indirect) structure of the material. Values of $E_{g,\text{direct}} = 1.37 \text{ eV}$ and $E_{g,\text{indirect}} = 1.26 \text{ eV}$ were calculated (as also shown in Table 2), which are in good agreement with the experimental^[42,44,50] and theoretical^[61] bandgap values reported in the literature.

In contrast, the EQE shows a gradual deterioration of charge collection for wavelengths higher than 500 nm. This feature has been previously reported even in high PCE devices.^[18] Studying the EQE and IQE curves, it is clear that in the 300–500 nm region the collection losses are mainly influenced by parasitic absorption on the window/buffer layer and, in the 500–800 nm range to reflections, an increase in the integrated J_{sc} of 2.9 mA cm^{-2} is observed between the IQE and EQE measurements, if we assume a device without reflections the PCE of the device will increase to 6.5%, this could be achieved by the inclusion of an antireflective coating. For wavelengths higher than 500 nm (just below the typical bandgap of our CdS),^[62] electrical losses become the dominant collection limiting factor as can be deduced from the reverse-biased (–1 V) IQE being considerably

higher than the IQE at zero voltage. Considering that under reverse-biased IQE, the SCR is being further depleted toward the absorber, the observed difference between the IQE and the reverse-biased IQE points toward an incomplete carrier collection in the 550–1000 nm region. The IQE (–1 V)/IQE (0 V) ratio plot in Figure 5c shows a severe deterioration of the collection starting from 600 nm, which indicates that the $\text{Sb}_2\text{Se}_3/\text{CdS}$ interface is playing a major role in this issue. This result matches the low SCR width (at 0 V) estimated by C–V measurements and could arise from a band mismatch at the p–n interface, nonoptimized carrier concentrations, and/or high interface recombination at the heterojunction. Similarly, the IQE was also measured under forward bias (+0.4 V, below the flat band voltage which is typically a bit higher than V_{oc}) (Figure 5a). The ratio between forward biased and unbiased IQE curves (Figure 5d) shows a relatively constant value, which suggests a good-quality absorber. Nevertheless, there is a noticeable reduction for wavelengths below 500 nm that can be associated to recombination at the CdS layer or nearby regions. In particular, for a high photogeneration of charge carriers in the CdS, the higher concentration of holes at the heterojunction can contribute to increasing recombination at the interface. Considering that the absorber exhibits good properties and that the main problems observed in the record sample can be ascribed to the narrow SCR width, these results suggest that the properties of the CdS buffer layer may be significantly affected by the solar cell fabrication process.

Figure 6a shows the V_{oc} versus T plot where it can be observed that the linear extrapolation toward 0 K intercepts the y-axis at 0.94 V. This is well below the bandgap of the material determined previously from the EQE (1.26 eV) and confirms that the device is bulk and/or interface limited. Thus, further optimization of the $\text{Sb}_2\text{Se}_3/\text{CdS}$ heterojunction is required. Figure 6b shows the Urbach energy (E_U) of the device (estimated from the IQE as presented in Equation S(1), Supporting Information). The E_U is related to structure/composition/temperature disorder,^[63] and manifests itself as tail states or potential fluctuations in the materials.^[61] Surprisingly, the E_U found is very low (17.4 meV). This is at the same level or even lower than that of other high PCE chalcogenide materials such as CIGS and CZTSe.^[64–66]

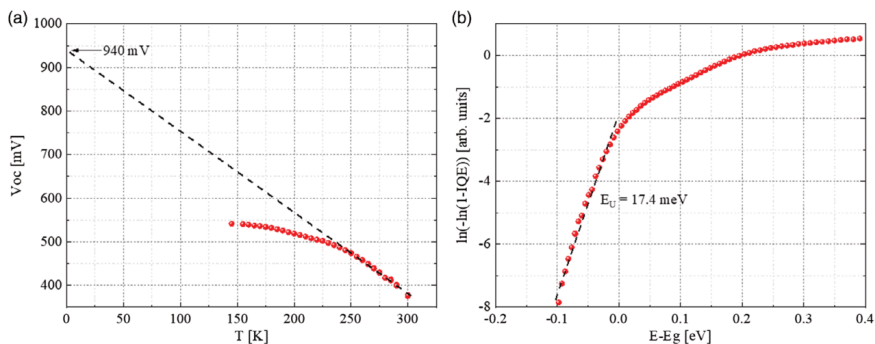


Figure 6. a) V_{oc} versus T plot. b) Urbach plot for the determination of E_U from the IQE.

This indicates that the absorber itself does not present severe disorder problems, and that recombination at the heterojunction arises from a combined effect of the Sb_2Se_3 absorber and the CdS buffer.

Therefore, all the previous data suggest that there is a strong modification of the $\text{Sb}_2\text{Se}_3/\text{CdS}$ interface during processing, and that this interface is largely limiting the PCE of the devices. Alternative n-type buffer layers have been used in the literature, although the best reported values are still observed with CdS. This is probably related to the fact that CdS has been extensively researched by the PV community. As such, we believe that investigating strategies such as barrier layer between CdS and Sb_2Se_3 may be a better approach that can help avoiding interface instability in $\text{Sb}_2\text{Se}_3/\text{CdS}$ and lead to further development of this technology.

3. Conclusion

This work proves the feasibility of synthesizing PV-quality Sb_2Se_3 layers using a sequential process based on reactive annealing under Se atmosphere of elemental Sb layers deposited by thermal evaporation. This technique has been demonstrated to be well suited for an accurate control of the $3[\text{Sb}]/2[\text{Se}]$ ratio in the Se-rich part of the phase diagram by varying the annealing temperature and the relevance of this parameter in the device optoelectronic performance. In this work, a deep study is presented on the effects of selenium content in the performance of Se-rich $\text{Sb}_2\text{Se}_3/\text{CdS}$ planar heterojunction solar cells and an in depth characterization of the best performing device obtained to shed light of their main limiting factors. Medium and high Se-excess has been found to increase the shunt resistance of the devices, although the highest contents have been observed to affect the Sb_2Se_3 heterojunction. However, through a compositional tuning ($3[\text{Sb}]/2[\text{Se}] = 0.88$), a champion solar cell device with PCE = 5.7%, FF = 61.7%, $V_{oc} = 422$ mV, and $J_{sc} = 21.9$ mA cm^{-2} has been obtained that could potentially be increased to 6.5% using an antireflecting coating in the structure. Finally, further $J-V-T$ and QE measurements in our record devices suggest that the main limiting factor of this technology is the heterojunction.

4. Experimental Section

Device Preparation: The 10×10 cm^2 soda-lime glass (SLG) substrates were cleaned with soap and then submitted to a three-step ultrasonic bath cleaning in acetone, isopropanol, deionized water (18.2 M Ω), for a duration of 10 min each, and dried with argon. The clean glasses were then coated with a molybdenum trilayer structure (around 800 nm full thickness), using a DC-magnetron sputtering machine (Alliance Concept AC450). The Mo trilayer is composed by a first named MoA layer (500 nm) deposited at higher power (4.2 W cm^{-2}) and low pressure (1.3×10^{-3} mbar), a second named MoB layer (250 nm), resistant to selenization, deposited at lower power (2.8 W cm^{-2}) and higher pressure (5.0×10^{-3} mbar), and finally a third MoA layer (50 nm) used for sacrificial purposes with the same characteristics as the first one, the total sheet resistance of the trilayer being $\approx 0.3 \Omega \text{sq}^{-1}$.^[35] A thin Sb metallic layer was then deposited by thermal evaporation (Oerlikon Univex 250) from elemental powder (Alfa Aesar, 99.5%) using a tungsten boat (10 rpm, rate of 0.6 Å s^{-1} , power ≈ 57.4 W, base pressure $\approx 10^{-5}$ mbar). The thickness of the Sb layers was determined by XRF (Fisherscope XDV) being

250 ± 10 nm, which was previously calibrated with several samples of known thicknesses. The samples were then cut into pieces of 1.25×2.5 cm^2 and were annealed in a three-zone tubular furnace using a graphite box (26.5 cm^3 volume) containing 25 mg of selenium powder (Alfa Aesar Puratronic, 99.9995%); the tube was filled with argon to provide an inert atmosphere and to control the system pressure. Several thermal processes were performed at different temperatures, times, and pressures as described throughout the main text. In all the cases, the heating ramp was 20 $^\circ\text{C min}^{-1}$ and the cooling down to room temperature was allowed to occur naturally (around 1 h).

The heterojunction was then completed with an n-type CdS buffer layer (50 nm) deposited by chemical bath deposition, being the Cd source $\text{Cd}(\text{NO}_3)_2$, with conditions $[\text{Cd}(\text{NO}_3)_2] = 0.12$ M, [thiourea] 0.3 M, pH = 9.5, $T = 80$ $^\circ\text{C}$.^[60] The front transparent conductive window layer formed by i-ZnO (50 nm) and $\text{In}_2\text{O}_3:\text{SnO}_2$ (90/10 wt%) (150 nm) layers were deposited by DC-pulsed magnetron sputtering (Alliance Concept CT100) at 200 $^\circ\text{C}$. Individual solar cells (3×3 mm^2) were then insulated using a manual mechanical scribe (Micro Diamond MR200 OEG) with a scribed line width of 20 μm .

Film and Device Characterization: The composition of the absorber layers was determined with an XRF equipment (Fisherscope XVD) calibrated by inductively coupled plasma (ICP); the measurements were conducted in a 4×4 point grid covering the full area of the individual 3×3 mm cells using a 50 kV accelerating voltage, a Ni10 filter to reduce background signal, and an integration time per measuring point of 45 s. The SEM micrographs were acquired in cross-section configuration (by mechanical cleavage of the full samples) using a Zeiss Series Auriga field-emission equipment, an acceleration voltage of 5 kV, and working distances ranging between 3 and 5 depending on the sample. Raman scattering measurements were performed using a Raman probe developed at Institut de Recerca en Energia de Catalunya (IREC) coupled with optical fiber to an FHR640 Horiba Jobin Yvon spectrometer and in back scattering configuration using 633 nm excitation wavelength with the laser spot focused onto the surface. The measurements were performed using a laser power density below 10 W cm^{-2} and using a macro-spot with a diameter of around 50 μm . The XRD patterns were obtained using a Bruker D8 Advance equipment in Bragg-Brentano configuration from 10 $^\circ$ to 90 $^\circ$ with a step size of 0.02 $^\circ$ and using a 1D detector, for the Rietveld analysis of the best device, results were obtained with a PANalytical X'Pert PRO MPD Bragg-Brentano powder diffractometer equipped with a Cu tube operating at 45 kV and 40 mA, a Ge (111) Johansson-type primary focalizing monochromator, and a silicon strip 1D X'Celerator detector. High resolution, high statistics, full angular range Cu K α_1 $\theta/2\theta$ scans are obtained: 2 θ/θ scans from 4 $^\circ$ to 145 $^\circ$. Current density-voltage ($J-V$) measurements were performed on complete devices using a Sun 3000 AAA solar simulator from Abet Technology (uniform illumination area of 15×15 cm^2) calibrated with a Si reference solar cell under AM1.5 illumination. Quantum efficiency (QE) measurements were conducted with a Bentham PVE300 spectral response system in the 300-1600 nm range calibrated with Si and Ge reference photodiodes.

The $C-V$ measurements were performed with a Keysight E4990A impedance analyzer and a homemade faraday cage four-probe setup. Samples were kept in dark conditions during the measurement. The measurements were performed in a voltage range between $[-1, +0.3]$ V. Selected frequency for data analysis was chosen to be 10 KHz. The equivalent circuit model used is composed of a series resistance, a parallel resistance and a capacitor. Dielectric constant was fixed to 19 based on bibliography ellipsometry measurements, although the reported values assume a very complex dielectric constant and thus the values for carrier concentration will be referred as apparent.^[42,54]

Current density-voltage-temperature ($J-V-T$) analysis was performed by introducing the sample into a cryostat (Cold-Head model RDK-101D Sumitomo Heavy Industries Ltd.) cooled by a Helium closed cycle compressor (Zephyr HC-4A from Sumitomo cryogenics). Samples were illuminated with a solar simulator (Oriol LCS AM1.5 model 94011A). Samples were attached with silver paste to the cold finger and a temperature sensor was placed aside on top of a 3 mm SLG piece to mimic the conditions of the film. Electrical contacts were performed on a four-probe

configuration, two of them connected to the indium-covered Mo back contact and the other two to the front ITO contact by applying silver paste. The range of temperatures probed was from 300 to 145 K (until V_{oc} saturation). Pressure was controlled by a turbo-molecular pump (Varian Mini-TASK AG81) with base vacuum of $\approx 10^{-6}$ mbar.

Supporting Information

Supporting Information is available from the Wiley Online Library or from the author.

Acknowledgements

This research was supported by the H2020 Programme under the project INFINITE-CELL (grant no. H2020-MSCA-RISE-2017-777968), by the DURACIS project from the SOLARERANET International program (subproject ref. PCIN-2017-041 funded by Spanish MINECO), by the Spanish Ministry of Science, Innovation and Universities under the WINCOST (grant no. ENE2016-80788-CS1-R), and by the European Regional Development Funds (ERDF, FEDER Programa Competitividad de Catalunya 2007–2013). Authors from IREC and the University of Barcelona belong to the SEMS (Solar Energy Materials and Systems) Consolidated Research Group of the “Generalitat de Catalunya” (Ref. 2017 SGR 862). M.P. thanks the Government of Spain for the Ramon y Cajal Fellowship (RYC-2017-23758) and Z.J. for the TECNIOspring PLUS Fellowship CLEAR SUN.

Conflict of Interest

The authors declare no conflict of interest.

Keywords

quasi-1D materials, Sb_2Se_3 , sequential process, thin-film solar cells

Received: March 16, 2020

Revised: April 15, 2020

Published online: May 10, 2020

- [1] M. A. Green, Y. Hishikawa, E. D. Dunlop, D. H. Levi, J. Hohl-Ebinger, M. Yoshita, A. W. Y. Ho-Baillie, *Prog. Photovolt. Res. Appl.* **2019**, *27*, 3.
- [2] V. Bermudez, A. Perez-Rodriguez, *Nat. Energy* **2018**, *3*, 466.
- [3] A. Zuser, H. Rechberger, *Resour. Conserv. Recycl.* **2011**, *56*, 56.
- [4] V. Fthenakis, *Renewable Sustainable Energy Rev.* **2009**, *13*, 2746.
- [5] D.-H. Son, S.-H. Kim, S.-Y. Kim, Y.-I. Kim, J.-H. Sim, S.-N. Park, D.-H. Jeon, D.-K. Hwang, S.-J. Sung, J.-K. Kang, K.-J. Yang, D.-H. Kim, *J. Mater. Chem. A* **2019**, *7*, 25279.
- [6] L. H. Wong, A. Zakutayev, J. D. Major, X. Hao, A. Walsh, T. K. Todorov, E. Saucedo, *J. Phys. Energy* **2019**, *1*, 032001.
- [7] B. Krishnan, S. Shaji, R. Ernesto Ornelas, *J. Mater. Sci. Mater. Electron.* **2015**, *26*, 4770.
- [8] A. Kanai, K. Toyonaga, K. Chino, H. Katagiri, H. Araki, *Jpn. J. Appl. Phys.* **2015**, *54*, 08KC06.
- [9] A. Zakutayev, *Curr. Opin. Green Sustain. Chem.* **2017**, *4*, 8.
- [10] F. Oliva, L. Arqués, L. Acebo, M. Guc, Y. Sánchez, X. Alcobé, A. Pérez-Rodríguez, E. Saucedo, V. Izquierdo-Roca, *J. Mater. Chem. A* **2017**, *5*, 23863.
- [11] D. J. Xue, B. Yang, Z. K. Yuan, G. Wang, X. Liu, Y. Zhou, L. Hu, D. Pan, S. Chen, J. Tang, *Adv. Energy Mater.* **2015**, *5*, 1.
- [12] P. Sinsermsuksakul, L. Sun, S. W. Lee, H. H. Park, S. B. Kim, C. Yang, R. G. Gordon, *Adv. Energy Mater.* **2014**, *4*, 1400496.
- [13] D. Lee, J. Y. Cho, H. S. Yun, D. K. Lee, T. Kim, K. Bang, Y. S. Lee, H. Y. Kim, J. Heo, *J. Mater. Chem. A* **2019**, *7*, 7186.
- [14] D. J. Xue, S. C. Liu, C. M. Dai, S. Chen, C. He, L. Zhao, J. S. Hu, L. J. Wan, *J. Am. Chem. Soc.* **2017**, *139*, 958.
- [15] H. Lei, J. Chen, Z. Tan, G. Fang, *Sol. RRL* **2019**, *3*, 1900026.
- [16] T. K. Todorov, S. Singh, D. M. Bishop, O. Gunawan, Y. S. Lee, T. S. Gershon, K. W. Brew, P. D. Antunez, R. Haight, *Nat. Commun.* **2017**, *8*, 682.
- [17] I. Hadar, T. Bin Song, W. Ke, M. G. Kanatzidis, *Adv. Energy Mater.* **2019**, *9*, 1.
- [18] Z. Li, X. Liang, G. Li, H. Liu, H. Zhang, J. Guo, J. Chen, K. Shen, X. San, W. Yu, R. E. I. Schropp, Y. Mai, *Nat. Commun.* **2019**, *10*, 125.
- [19] C. Chen, K. Li, S. Chen, L. Wang, S. Lu, Y. Liu, D. Li, H. Song, J. Tang, *ACS Energy Lett.* **2018**, *3*, 2335.
- [20] Y. Zhou, L. Wang, S. Chen, S. Qin, X. Liu, J. Chen, D. J. Xue, M. Luo, Y. Cao, Y. Cheng, E. H. Sargent, J. Tang, *Nat. Photonics* **2015**, *9*, 409.
- [21] Z. Li, H. Zhu, Y. Guo, X. Niu, X. Chen, C. Zhang, W. Zhang, X. Liang, D. Zhou, J. Chen, Y. Mai, *Appl. Phys. Express* **2016**, *9*, 052302.
- [22] C. Yuan, L. Zhang, W. Liu, C. Zhu, *Sol. Energy* **2016**, *137*, 256.
- [23] X. Wen, C. Chen, S. Lu, K. Li, R. Kondrotas, Y. Zhao, W. Chen, L. Gao, C. Wang, J. Zhang, G. Niu, J. Tang, *Nat. Commun.* **2018**, *9*, 2179.
- [24] C. Chen, Y. Zhao, S. Lu, K. Li, Y. Li, B. Yang, W. Chen, L. Wang, D. Li, H. Deng, F. Yi, J. Tang, *Adv. Energy Mater.* **2017**, *7*, 1.
- [25] D. B. Li, X. Yin, C. R. Grice, L. Guan, Z. Song, C. Wang, C. Chen, K. Li, A. J. Cimaroli, R. A. Awai, D. Zhao, H. Song, W. Tang, Y. Yan, J. Tang, *Nano Energy* **2018**, *49*, 346.
- [26] C. Chen, L. Wang, L. Gao, D. Nam, D. Li, K. Li, Y. Zhao, C. Ge, H. Cheong, H. Liu, H. Song, J. Tang, *ACS Energy Lett.* **2017**, *2*, 2125.
- [27] L. Wang, D. B. Li, K. Li, C. Chen, H. X. Deng, L. Gao, Y. Zhao, F. Jiang, L. Li, F. Huang, Y. He, H. Song, G. Niu, J. Tang, *Nat. Energy* **2017**, *2*, 1.
- [28] R. Tang, Z. Zheng, Z. Su, X. Li, Y. Wei, X. Zhang, Y. Fu, J. Luo, P. Fan, G. Liang, *Nano Energy* **2019**, *64*, 103929.
- [29] Y. Luo, R. Tang, S. Chen, J. Hu, Y. Liu, Y. Li, X. Liu, Z. Zheng, Z. Su, X. Ma, P. Fan, X. Zhang, H. Ma, Z. Chen, G. Liang, *Chem. Eng. J.* **2020**, *393*, 124599.
- [30] C. Wang, S. Lu, S. Li, S. Wang, X. Lin, J. Zhang, R. Kondrotas, K. Li, C. Chen, J. Tang, *Nano Energy* **2020**, p. 104577.
- [31] X. Liu, X. Xiao, Y. Yang, D. J. Xue, D. B. Li, C. Chen, S. Lu, L. Gao, Y. He, M. C. Beard, G. Wang, S. Chen, J. Tang, *Prog. Photovolt. Res. Appl.* **2017**, *25*, 861.
- [32] G. Li, Z. Li, X. Liang, C. Guo, K. Shen, Y. Mai, *ACS Appl. Mater. Interfaces* **2019**, *11*, 828.
- [33] X. Liu, C. Chen, L. Wang, J. Zhong, M. Luo, J. Chen, D.-J. Xue, D. Li, Y. Zhou, J. Tang, *Prog. Photovolt.* **2015**, *23*, 1828.
- [34] X. Wen, Y. He, C. Chen, X. Liu, L. Wang, B. Yang, M. Leng, H. Song, K. Zeng, D. Li, K. Li, L. Gao, J. Tang, *Sol. Energy Mater. Sol. Cells* **2017**, *172*, 74.
- [35] K. Li, R. Kondrotas, C. Chen, S. Lu, X. Wen, D. Li, J. Luo, Y. Zhao, J. Tang, *Sol. Energy* **2018**, *167*, 10.
- [36] X. Hu, J. Tao, S. Chen, J. Xue, G. Weng, Kaijiang, Z. Hu, J. Jiang, S. Chen, Z. Zhu, J. Chu, *Sol. Energy Mater. Sol. Cells* **2018**, *187*, 170.
- [37] X. Hu, J. Tao, G. Weng, J. Jiang, S. Chen, Z. Zhu, J. Chu, *Sol. Energy Mater. Sol. Cells* **2018**, *186*, 324.
- [38] K. Shen, C. Ou, T. Huang, H. Zhu, J. Li, Z. Li, Y. Mai, *Sol. Energy Mater. Sol. Cells* **2018**, *186*, 58.
- [39] L. J. Phillips, C. N. Savory, O. S. Hutter, P. J. Yates, H. Shiel, S. Mariotti, L. Bowen, M. Birkett, K. Durose, D. O. Scanlon, J. D. Major, *IEEE J. Photovolt.* **2019**, *9*, 544.
- [40] J. Zhang, R. Kondrotas, S. Lu, C. Wang, C. Chen, J. Tang, *Sol. Energy* **2019**, *182*, 96.

- [41] H. Guo, Z. Chen, X. Wang, Q. Cang, X. Jia, C. Ma, N. Yuan, J. Ding, *Sol. RRL* **2019**, *3*, 1970033.
- [42] C. Chen, D. C. Bobela, Y. Yang, S. Lu, K. Zeng, C. Ge, B. Yang, L. Gao, Y. Zhao, M. C. Beard, J. Tang, *Front. Optoelectron.* **2017**, *10*, 18.
- [43] C. Chen, W. Li, Y. Zhou, C. Chen, M. Luo, X. Liu, K. Zeng, B. Yang, C. Zhang, J. Han, J. Tang, *Appl. Phys. Lett.* **2015**, *107*, 043905.
- [44] M. Birkett, W. M. Linhart, J. Stoner, L. J. Phillips, K. Durose, J. Alaria, J. D. Major, R. Kudrawiec, T. D. Veal, *APL Mater.* **2018**, *6*, 084901.
- [45] Z. Li, X. Chen, H. Zhu, J. Chen, Y. Guo, C. Zhang, W. Zhang, X. Niu, Y. Mai, *Sol. Energy Mater. Sol. Cells* **2017**, *161*, 190.
- [46] R. Kondrotas, J. Zhang, C. Wang, J. Tang, *Sol. Energy Mater. Sol. Cells* **2019**, *199*, 16.
- [47] F. Oliva, S. Kretschmar, D. Colombara, S. Tomblato, C. M. C. M. Ruiz, A. Redinger, E. Saucedo, C. Broussillou, T. G. T. G. de Monsabert, T. Unold, P. J. P. J. Dale, V. Izquierdo-Roca, A. Pérez-Rodríguez, *Sol. Energy Mater. Sol. Cells* **2016**, *158*, 168.
- [48] M. Dimitrievska, A. Fairbrother, E. Saucedo, A. Pérez-Rodríguez, V. Izquierdo-Roca, *Sol. Energy Mater. Sol. Cells* **2016**, *149*, 304.
- [49] X. Liu, J. Chen, M. Luo, M. Leng, Z. Xia, Y. Zhou, S. Qin, D. J. Xue, L. Lv, H. Huang, D. Niu, J. Tang, *ACS Appl. Mater. Interfaces* **2014**, *6*, 10687.
- [50] M. Leng, M. Luo, C. Chen, S. Qin, J. Chen, J. Zhong, J. Tang, *Appl. Phys. Lett.* **2014**, *105*, 083905.
- [51] P. Vidal-Fuentes, M. Guc, X. Alcobe, T. Jawhari, M. Placidi, A. Pérez-Rodríguez, E. Saucedo, V. I. Roca, *2D Mater.* **2019**, *6*, 045054.
- [52] M. Huang, P. Xu, D. Han, J. Tang, S. Chen, *ACS Appl. Mater. Interfaces* **2019**, *11*, 15564.
- [53] T. Cebriano, B. Méndez, J. Piqueras, *Mater. Chem. Phys.* **2012**, *135*, 1096.
- [54] C. Chen, W. Li, Y. Zhou, C. Chen, M. Luo, X. Liu, K. Zeng, B. Yang, C. Zhang, J. Han, J. Tang, *Appl. Phys. Lett.* **2015**, *107*, 043905.
- [55] S. Lopez-Marino, M. Espindola-Rodríguez, Y. Sánchez, X. Alcobé, F. Oliva, H. Xie, M. Neuschitzer, S. Giraldo, M. Placidi, R. Caballero, V. Izquierdo-Roca, A. Pérez-Rodríguez, E. Saucedo, *Nano Energy* **2016**, *26*, 708.
- [56] M. Neuschitzer, J. Marquez, S. Giraldo, M. Dimitrievska, M. Placidi, I. Forbes, V. Izquierdo-Roca, A. Pérez-Rodríguez, E. Saucedo, *J. Phys. Chem. C* **2016**, *120*, 9661.
- [57] M. Neuschitzer, Y. Sanchez, S. Lopez-Marino, H. Xie, A. Fairbrother, M. Placidi, S. Haass, V. Izquierdo-Roca, A. Perez-Rodríguez, E. Saucedo, *Prog. Photovolt. Res. Appl.* **2015**, *23*, 1660.
- [58] S. R. Kodigala, *Cu(In1-xGax)Se2 Based Thin Film Solar Cells*, Thin Film Nanostructures, Vol. 35, Elsevier **2010**, pp. 505–679.
- [59] M. Luo, M. Leng, X. Liu, J. Chen, C. Chen, S. Qin, J. Tang, *Appl. Phys. Lett.* **2014**, *104*, 173904.
- [60] R. Carron, C. Andres, E. Avancini, T. Feurer, S. Nishiwaki, S. Pisoni, F. Fu, M. Lingg, Y. E. Romanyuk, S. Buecheler, A. N. Tiwari, *Thin Solid Films* **2019**, *669*, 482.
- [61] R. Vadapoo, S. Krishnan, H. Yilmaz, C. Marin, *Phys. Status Solid Basic Res.* **2011**, *248*, 700.
- [62] M. Neuschitzer, Y. Sanchez, S. López-Marino, H. Xie, A. Fairbrother, M. Placidi, S. Haass, V. Izquierdo-Roca, A. Perez-Rodríguez, E. Saucedo, *Prog. Photovolt. Res. Appl.* **2015**, *23*, 1660.
- [63] I. Studenyak, M. Kranj, M. Kurik, *Int. J. Opt. Appl.* **2014**, *4*, 76.
- [64] J. P. Teixeira, P. M. P. Salomé, B. Alves, M. Edoff, J. P. Leitão, *Phys. Rev. Appl.* **2019**, *11*, 054013.
- [65] M. Neuschitzer, M. Espindola-Rodríguez, M. Guc, J. Marquez, S. Giraldo, I. Forbes, A. Perez-Rodríguez, E. Saucedo, *J. Mater. Chem. A* **2018**, *6*, 11759.
- [66] S. Lopez-Marino, Y. Sánchez, M. Placidi, A. Fairbrother, M. Espindola-Rodríguez, X. Fontané, V. Izquierdo-Roca, J. Lopez-García, L. Calvo-Barrio, A. Pérez-Rodríguez, E. Saucedo, *Chem. Eur. J.* **2013**, *19*, 14814.

Supporting Information

Efficient Se-rich $\text{Sb}_2\text{Se}_3/\text{CdS}$ planar-heterojunction solar cells by sequential processing: control and influence of Se content

*Pedro Vidal-Fuentes**, *Marcel Placidi*, *Yudania Sánchez*, *Ignacio Becerril Romero*, *Jacob Andrade-Arvizu*, *Zacharie Jehl*, *Alejandro Pérez-Rodríguez*, *Víctor Izquierdo-Roca*, and *Edgardo Saucedo**

For the synthesis of Se-rich Sb_2Se_3 layers a sequential process is used as described in the corresponding Experimental Section. As is shown in the **Figure S1** the SLG/Mo/Sb precursors are introduced in a graphite box containing elemental Se powder, and then introduced in a tubular furnace under controlled inert atmosphere (Ar atmosphere), for the thermal annealing. The resulting absorbers are processed into solar cell devices with the substrate configuration shown in the same **Figure S1**.

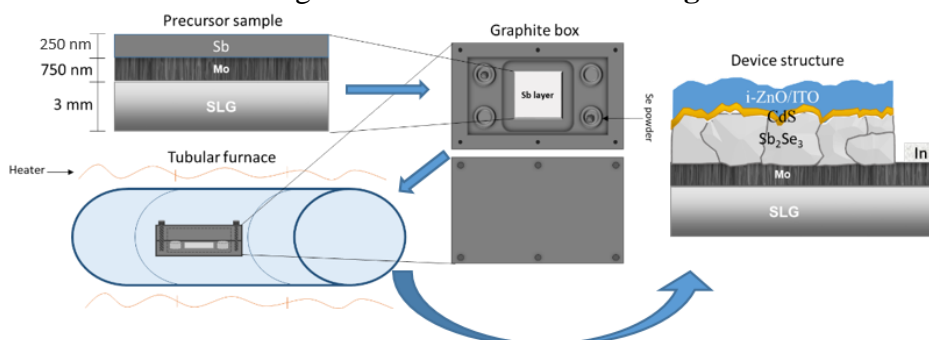


Figure S1. Experimental set-up followed in this work, consisting on the selenization of a metallic thermally evaporated precursor, using a graphite box in a tubular furnace.

The synthesis of Sb_2Se_3 layers at different total Ar pressures was investigated. As can be seen in Figure S2, for pressures below 500 mbar the layers are non-homogenous, presenting peel-off regions and making them useless as PV absorbers.

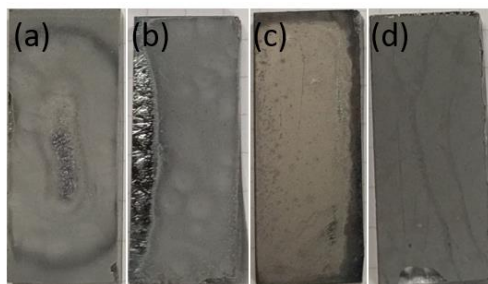


Figure S2. Effect of the processing pressure on the absorber morphology, selenized at a fixed temperature of 320 °C during 30 min with 25 mg of Se at (a) 1 mbar (b) 10 mbar (c) 50 mbar (d) 500 mbar.

Figure S3 shows the IQE of selected devices fabricated with absorbers containing different $3[\text{Sb}]/2[\text{Se}]$ ratios together with the corresponding derivate in order to estimate the indirect and direct bandgaps. As it is clear, both of them does not depend on the composition, and values around 1.24-1.25 eV for the indirect bandgap and 1.37-1.39 eV for the direct one are obtained.

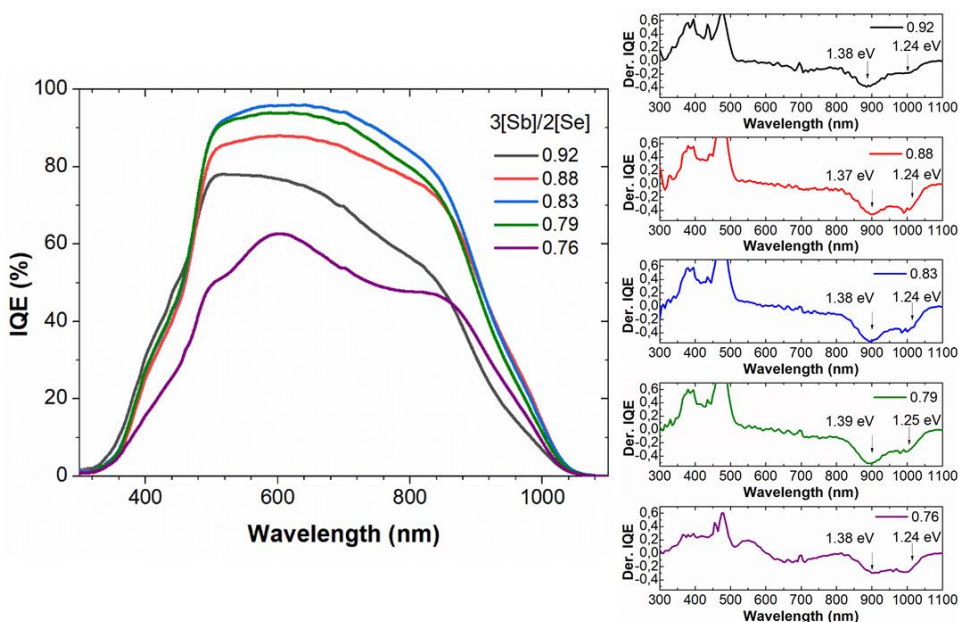


Figure S3. IQE of selected solar cell devices made with absorbers with different $3[\text{Sb}]/2[\text{Se}]$ ratios and corresponding derivate of the IQE to estimate the indirect and direct bandgaps.

3 - Publications

Figure S4 shows the Raman spectrum in which no secondary phases aside for the orthorhombic Sb_2Se_3 phase. **Figure S5** shows the XRD diffractogram of the champion device, demonstrating good crystalline quality, preferential [001] orientation due to a high increase in intensity of the 002 and 004 reflections, although the orientation is not uniaxial being 301 and 211 also promoted in comparison to a non-texturized samples, nevertheless this two reflections also belong to vertically aligned ribbons with some degree of tilt. ^[49]

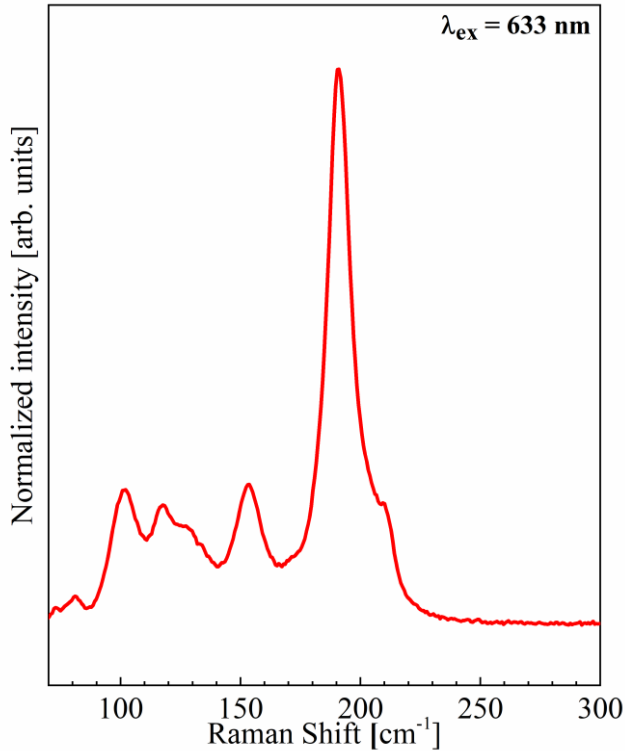


Figure S4. Raman spectrum of the champion solar cell.

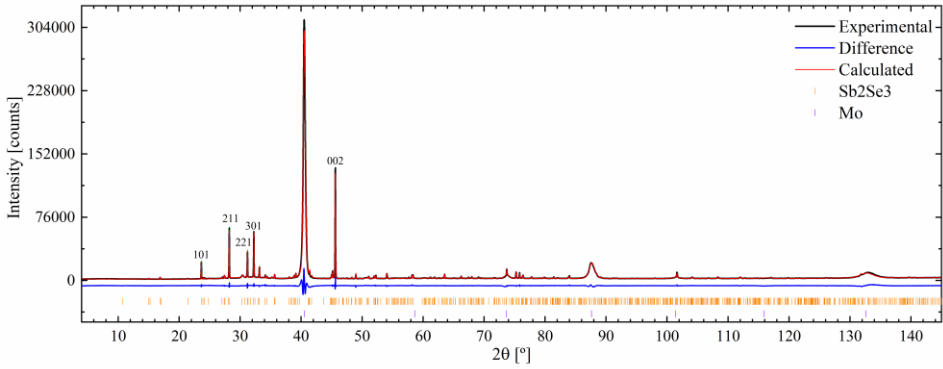


Figure S5. XRD diffractogram and Rietveld refinement of the champion solar cell.

From the linearization of **Equation 1**, that is equivalent to the y-axis on the **Figure 6**, the Urbach energy can be extracted as the inverse of the slope of the linear fit on the region $E - E_g < 0$; that can be understood as the characteristic energy of an exponentially decaying DOS.

$$\alpha(h\nu) = \begin{cases} A_0 \sqrt{\frac{E_U}{2 \exp(1)}} \exp\left(\frac{h\nu - E_G}{E_U}\right) & \text{for } h\nu < E_G + \frac{E_U}{2} \\ A_0 \sqrt{h\nu - E_G} & \text{for } h\nu \geq E_G + \frac{E_U}{2} \end{cases} \quad \text{Equation.}$$

SI

3.4 - Article 3

Insights on the Thermal Stability of the Sb₂Se₃ Quasi-1D Photovoltaic Technology

Pedro Vidal-Fuentes,* Maxim Guc, Ignacio Becerril-Romero, Diouldé Sylla, Xavier Alcobé, Yudania Sánchez, Alejandro Pérez-Rodríguez, Edgardo Saucedo, and Victor Izquierdo-Roca*

This work explores the thermal stability of antimony-based photovoltaic (PV) technologies investigating the effect of low-temperature (50–350 °C) postdeposition annealings (PDAs) on bare Sb₂Se₃ absorbers and complete SLG/Mo/Sb₂Se₃/CdS/i-ZnO/ITO devices (5.7% power conversion efficiency with no anti-reflecting coating or metallic grid). A comprehensive structural analysis by means of X-ray diffraction and Raman spectroscopy, coupled with optoelectronic characterization, reveals clear evidences of a degradation process dominated by selenium diffusion. The degradation process is observed to start at low PDA temperatures as a shrinkage of the Sb₂Se₃ unit cell. Further increasing the PDA temperature above 200 °C leads to the formation of Sb oxides and Se secondary phases in bare absorbers, and of CdS_{1-x}Se_x in complete devices at the Sb₂Se₃ front interface which completely degrade the heterojunction and kill device performance. Furthermore, a clear correlation is found between PV performance decrease and Sb₂Se₃ layer lattice shrinkage with the increasing PDA temperature ($T > 50$ °C). This is the first time that thermal instability is reported for the Sb₂Se₃ compound at temperatures commonly used during PV module fabrication processes such as emitter/transparent conducting oxide deposition or encapsulation.

1. Introduction

The thin film photovoltaic (TFPV) industry is mostly dominated by highly stable chalcogenide compounds such as Cu(In,Ga)(S,Se)₂ (CIGS) and CdTe, which are competing with silicon technologies at industrial level with power conversion efficiencies (PCEs) at laboratory scale reaching 23.35% and 22.1%, respectively.^[1,2] On the contrary, perovskites are another TFPV technology, currently at the preindustrial stage in terms of PCE (25.2%), with potential for surpassing CIGS and CdTe due to its reduced production cost.^[2,3] Nevertheless, all these technologies present important drawbacks. In the case of CIGS and CdTe, the scarcity and/or toxicity of indium, gallium, tellurium, and cadmium sets limits to mass production and will lead to cost volatility in these technologies. In the case of perovskites, their main limitations arise from their low thermal and chemical stability due to their organic composition as well as from their toxicity.^[3–5]

In this regard, the Sb₂(S,Se)₃ compound family represents an interesting alternative for TFPV because it has rapidly reached promising PCEs ≈10% in a short development period.^[6–10] It is composed by low-toxicity inorganic Earth-abundant elements which, in principle, should make it a stable and sustainable technology. In addition, in contrast to other TFPV technologies based on multinary compounds (e.g., kesterites) with a high degree of complexity,^[11] Sb₂(S,Se)₃ offers an attractive binary compound composition. As such, on paper, Sb₂(S,Se)₃ is a very promising candidate to take lead of the TFPV industry in the near future.

Sb₂(S,Se)₃ compounds are van der Waals solids that present a quasi-1D (Q1D) structure in which the atoms are covalently bonded in 1D chains and, in turn, the chains are bonded to each other by van der Waals forces.^[12] This anisotropic bonding causes a high anisotropy in the electronic properties of the material and preferred orientations along $[hkl]$ with $l \neq 0$, i.e., the carrier diffusion length along the covalent bonds is much higher than through the van der Waals bonds.^[13] In the case of polycrystalline systems, this has been proposed to have a direct implication in the absence of dangling bonds at the grain boundaries.^[14,15] Nevertheless, a high number of complex defects are expected in the bulk due to the big interchain nonbonding

P. Vidal-Fuentes, M. Guc, I. Becerril-Romero, D. Sylla, Y. Sánchez, A. Pérez-Rodríguez, V. Izquierdo-Roca
Solar Energy Materials and Systems
Catalonia Institute for Energy Research (IREC)
Jardins de les Dones de Negre 1, 08930 Sant Adrià de Besòs, Spain
E-mail: pvidal@irec.cat; vizquierdo@irec.cat

X. Alcobé
Unitat de Difracció de Raigs X
Centres Científics i Tecnològics de la Universitat de Barcelona (CCiTUB)
Lluís Solé i Sabarís 1-3, 08028 Barcelona, Spain

A. Pérez-Rodríguez
IN2UB, Departament d'Enginyeria Electrònica i Biomèdica
Universitat de Barcelona

C. Martí i Franquès 1, 08028 Barcelona, Spain

E. Saucedo
Electronic Engineering Department
Polytechnic University of Catalonia (UPC)
Campus Besòs, Av. d'Eduard Maristany, 16, 08930 Barcelona, Spain

 The ORCID identification number(s) for the author(s) of this article can be found under <https://doi.org/10.1002/solr.202100517>.

DOI: 10.1002/solr.202100517

spaces, especially Se_{Sb} , 2Se_{Sb} , and V_{Se} .^[16] The interchain regions are of great scientific interest because, theoretically, they can accommodate some excess of chalcogen atoms in the case of chalcogen-rich samples. However, the low-energy van der Waals bonds could also compromise the thermal stability of $\text{Sb}_2(\text{S,Se})_3$ compounds. This is particularly critical in view of the upcoming development of this TFPV technology toward module fabrication in which postdeposition processes of the complete PV devices (e.g., deposition of TCOs or encapsulation process) are normally conducted at relatively low temperatures (200–300 °C) that could affect the weak bonds of the $\text{Sb}_2(\text{S,Se})_3$ material structure and lead to material decomposition.^[17–22]

Despite the important implications of a possible thermal instability of $\text{Sb}_2(\text{S,Se})_3$, up to now, the effect of low-temperature postdeposition treatments has not been systematically studied.^[23,24] Furthermore, no specific works addressing the thermal instability of the $\text{Sb}_2(\text{S,Se})_3$ system can be found in the literature. However, elemental migration between different layers has been observed and reported for $\text{Sb}_2(\text{S,Se})_3$,^[25] Sb_2S_3 ,^[26,27] and Sb_2Se_3 .^[28–31] These observations were mainly related to Cd diffusion into the Sb_2Se_3 layer in $\text{Sb}_2\text{Se}_3/\text{CdS}$ superstrate configuration devices.^[30,32,33] Moreover, the instability of the $\text{Sb}_2\text{Se}_3/\text{CdS}$ junction under light/dark soaking has also been detected.^[34,35]

In view of the mentioned stability concerns, this article is focused on investigating the thermal instability of Sb_2Se_3 thin films and PV devices based on them, in substrate configuration. This issue is analyzed by submitting bare absorber layers (SLG/Mo/ Sb_2Se_3) and full devices (SLG/Mo/ $\text{Sb}_2\text{Se}_3/\text{CdS}/\text{i-ZnO}/\text{ITO}$, no anti-reflecting coating (ARC) or metallic grid) to controlled low-temperature postdeposition annealing (PDA) in ambient atmosphere. The PCE of the complete devices was $\approx 5.7\%$ with the J_{sc} as the only limiting factor in comparison with other state-of-the-art Sb_2Se_3 -based devices.^[7,36] The results presented demonstrate a high instability of the Sb_2Se_3 layers under the applied temperatures (50–350 °C), which is reflected on structural modifications, compound decomposition, and subsequent Se migration from the absorber to the $\text{CdS}/\text{Sb}_2\text{Se}_3$ heterojunction. Structural modifications result in a soft degradation of the optoelectronic parameters due to lattice compression, while compound decomposition and Se migration result in the formation of secondary phases and of a $\text{CdS}_x\text{Se}_{1-x}$ solid solution that drastically degrades PV performance. The observed selenium migration seems to be favored by the excess of Se present in the Sb_2Se_3 selenium-rich samples, which was found to be the optimum compositional range in terms of device PCE. The results presented in this work provide a valuable insight into the instability of $\text{Sb}_2(\text{S,Se})_3$ compounds under low temperatures which is a potential limitation for this PV technology regarding future device stability and development of synthesis routes.

2. Results and Discussion

To study the effect of PDA on the bare layers and on devices, three different sets of samples with different PDA conditions were prepared and analyzed as described in the Experimental Section.

These three sets of samples were mainly analyzed by means of Raman spectroscopy and X-ray diffraction (XRD). Recently, Raman scattering spectroscopy combined with Rietveld profile

analysis of the XRD diffractograms has demonstrated to possess a high potential for the analysis of emergent multicomponent inorganic compounds such as Cu_2SnS_3 , SnS , and Sb_2Se_3 .^[37–43] The close combination of both techniques allows to assess changes not only in the crystalline quality of the samples, but also variations in the chemical and phase composition, in the structure (including different polymorphs and texture), and even in point defect concentrations.^[37–43] Finally, these structural and compositional information extracted by Raman and XRD analyses can be directly correlated with the optoelectronic properties of the individual solar cells. This analysis is structured in four sections: 1) study of the thermal stability of the bare Sb_2Se_3 absorber under different PDA temperatures; 2) extension of the analysis by completing devices with the annealed absorbers and analyzing the effect of the PDA process on the optoelectronic properties; 3) direct application of the PDA to full Sb_2Se_3 devices; and 4) detailed exploration of the degradation mechanisms and the thermal limitations of the Sb_2Se_3 PV technology.

2.1. PDA on the Bare Sb_2Se_3 Absorber: Impact on the Device Properties

To evaluate the impact of the PDA temperature on the structural and compositional properties of the bare Sb_2Se_3 absorber layers, Raman scattering spectra measured under 633 nm excitation were acquired on the reference Sb_2Se_3 bare absorber and analyzed (see Figure 1a). The spectra were measured after each PDA step once the sample had cooled down to RT to exclude any temperature-induced shift or widening of the Raman peaks. The spectrum of the Sb_2Se_3 absorber before performing any PDA treatment on it (black spectrum at the bottom of Figure 1a) can be taken as a fingerprint Raman spectrum of a Sb_2Se_3 absorber with PV grade. This spectrum is characterized by the presence of an intense peak at 192 cm^{-1} on top of a complex band in the spectral range $70\text{--}230\text{ cm}^{-1}$ where a significant amount of small intensity peaks (up to 22 Raman active peaks are expected in this spectral range) are overlapped.^[43] The spectrum does not show any evidence of additional contributions that could be associated with secondary phases on the surface of the film.

After applying the PDA treatment, the Raman spectra acquired at the bare absorber surface exhibit changes that correlate with the annealing temperature. A careful evaluation of the phase formation at the sample surface allows to distinguish three temperature regions: 1) PDA temperature $< 300\text{ }^\circ\text{C}$: no changes are observed in the Raman spectra. 2) PDA temperature in the $300\text{--}350\text{ }^\circ\text{C}$ range: a weak peak at 254 cm^{-1} whose intensity increases with the rising temperature is detected. It is associated with the main peak of the senarmonite $\alpha\text{-Sb}_2\text{O}_3$ phase.^[43,44] 3) PDA temperature $> 350\text{ }^\circ\text{C}$: the intensity of the peak at 254 cm^{-1} increases and additional weaker peaks at 85, 375, and 451 cm^{-1} associated with the $\alpha\text{-Sb}_2\text{O}_3$ phase are also detected which correlates with an increased concentration of this phase at the sample surface.^[43–45]

Moreover, an additional new peak is detected at 240 cm^{-1} which suggests the formation of trigonal Se (t-Se).^[43,46] Finally, a broad band appears at 280 cm^{-1} which can be tentatively assigned to the valentinite $\beta\text{-Sb}_2\text{O}_3$ phase.^[43,47]

Together with the appearance of new Raman peaks after the PDA treatments at temperatures above $300\text{ }^\circ\text{C}$, detectable

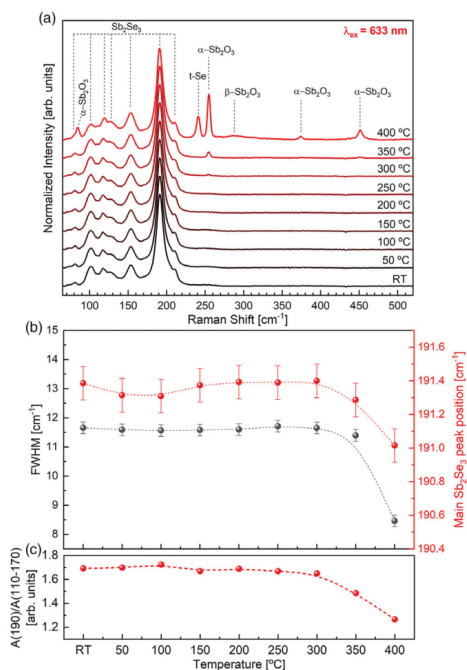


Figure 1. a) Average Raman spectra of the bare Sb_2Se_3 absorber layer measured after applying different PDA temperatures. b) Evolution of the FWHM of the Sb_2Se_3 main Raman peak with the PDA temperature (error bars represent the standard deviation from the mean value calculated for different points measured in the sample). c) Evolution of the relative integrated intensity of the peaks in the 110–170 cm^{-1} range with the PDA temperature.

changes can also be observed in the peaks of the main Sb_2Se_3 phase. These are mainly related to the shift of the most intense peak (190 cm^{-1}) toward lower wavenumbers and to a decrease in its full width at half maximum (FWHM) (see Figure 1b). These changes can be linked to the improvement of the crystalline quality of the main Sb_2Se_3 phase and/or to the variation of its chemical composition. Finally, an increase in the relative integrated intensity of the peaks in the spectral range 110–170 cm^{-1} is also observed (see bottom panel in Figure 1c). This has been proposed as an indicator of the change of the Sb_2Se_3 surface texture,^[38,43] denoting significant changes in the absorber layer for temperatures above 300 °C.

In view of the changes detected in the Raman spectra of the Sb_2Se_3 phase induced by the different PDA treatments, an overview of the published results of thermogravimetric analysis (TGA) and differential thermal analysis (DTA) of this material was performed. On the one hand, a recent publication reported no changes in the mass of a Sb_2Se_3 powder sample submitted to temperatures up to 423 °C.^[48] However, Sekkina conducted a

more detailed TGA and DTA analysis of Sb_2Se_3 powder and its constituent elements reporting a different behavior.^[49] This work observed a gain of mass in the Sb_2Se_3 powder sample from 300 °C (TGA) accompanied by a phase change (DTA) correlated with an oxygen adsorption (oxidation) of the Sb_2Se_3 phase. In addition, this study also found that Se has a complex and rather unpredictable behavior with temperature. Pure Se powder was found to start sublimating already at 60 °C. However, if mixed with Sb powder (2Sb + 3Se mix) the mass of the mixture remained stable up to 340 °C. This can be related to two opposite processes: the oxidation of Sb with the increasing temperature that results in a mass gain, and the sublimation of Se which results in a loss of mass. The compensation of these two processes could explain the observed constant mass of the 2Sb + 3Se mixture up to 340 °C. On the other hand, Sekkina also points toward the oxidation of Sb in the Sb_2Se_3 powder at 300 °C,^[49] which is in agreement with the appearance of $\alpha\text{-Sb}_2\text{O}_3$ Raman peaks in the current work. Finally, the contradictions with the more recent TGA results from Liu et al.^[48] could be simply related to the experimental conditions used because their TGA measurements were conducted under N_2 flow while the TGA analysis by Sekkina seems performed in air,^[49] closer to the PDA conditions used in the current work. Coming back to the results of the current article, at PDA temperatures above 350 °C the appearance of $t\text{-Se}$ Raman peaks suggests that the high Se losses result in the formation of a solid amorphous phase that gets partially crystallized at 400 °C.

2.2. PDA on the Bare Sb_2Se_3 Absorber: Impact on the Device Properties

The influence of the PDA of the bare Sb_2Se_3 absorber on the optoelectronic properties of complete PV devices was studied using the second set of samples (PDA-absorber) as described in the Experimental Section. After performing PDA treatments at a different temperature in each of the samples, X-ray fluorescence (XRF) chemical composition measurements were performed on the bare absorbers to ensure an optimal composition, and after completing the samples into devices (Figure S1, Supporting Information), these were further studied by means of Raman, XRD, and $J-V$.

In a first stage, the Raman spectra of the different samples of the PDA-absorber set were compared with those obtained in the bare absorber annealed at different temperatures (see Section 2.1). Small uncontrolled differences between the preparation conditions of the PDA-absorber set of samples resulted in some deviations in the spectra corresponding to samples with PDA below 250 °C (Figure S2, Supporting Information) compared with the previous analysis where only one sample was sequentially submitted to the different PDAs (Figure 1). Nevertheless, the general trend was observed for the previous set of samples, regarding the appearance of the secondary phases, and the changes in the Raman peaks of the Sb_2Se_3 phase were also clearly observed in this set of samples allowing to transfer the conclusions made earlier about the absorber evolution with the PDA temperature.

To further characterize the crystallinity, the structure, and to estimate about the microstructure and texture of these layer

materials with the PDA treatments, a detailed XRD full profile analysis was performed. **Figure 2** shows the full set of X-ray diffractograms with selected ranges of the complete devices (see Figure S3a, Supporting Information, for the complete diffractograms). Table S1, Supporting Information, relates the main results of Rietveld refinement full profile analysis: the relative mass fraction of the identified crystalline phases, their refined cell parameters and volume, the R_w and R_B agreement factors, the crystallite size, and the microstrain values. The main crystalline phases found are Mo (from the back contact layer) that does not show any significant change with temperature, and the main absorber Sb_2Se_3 phase.^[43] Up to 250 °C, Sb_2Se_3 is highly crystalline showing very narrow peaks and low microstrain values ($\Delta d/d = 1.3 - 2.2 \times 10^{-4}$), with practically only instrumental broadening, and with crystallite size estimated values of 700–1000 nm (this is in agreement with the layer thickness of the films, pointing to single crystallites covering the full thickness across the device). The layers show a quite complex multiaxial [001] (also in the [211] and [301]) dominating preferred orientations, which become slightly less dominant with temperature. Moreover, up to 250 °C, a progressive minor variation of the Sb_2Se_3 structure is determined, mainly reflected by the decrease in the cell parameters and,

consequently, of the cell volume (see Table S1, Supporting Information and **Figure 3a**). At 300 °C, an α - Sb_2O_3 secondary phase appears in the absorber layer and its relative concentration increases (decreasing the Sb_2Se_3 concentration) with the increasing annealing temperature which is in agreement with the Raman analysis. In addition, at the same temperature, the Sb_2Se_3 cell volume decreases sharply after the structure relaxes into secondary phases, and the estimated crystallite size also decreases to around 300 nm. Both parameters remain practically constant at 350 °C.

The changes observed in the Raman peaks of the Sb_2Se_3 phase (Figure S2, Supporting Information) are supported by the change in the structural and textural properties of this phase with the PDA temperature detected by XRD. At the highest temperatures, the slight variation in the texture of the bulk is accompanied with a decrease in the relative integrated intensity of the peaks in the 110–170 cm^{-1} range, which points toward an important change in the texture at the layer surface (see Figure S2c, Supporting Information and Figure 1c).^[38,43]

Finally, $J-V$ curves were measured for all the solar cells of each sample (up to 18 cells per sample). The evolution of their optoelectronic properties with the PDA temperature is shown in Figure 3b–e. A degradation of the optoelectronic properties of the

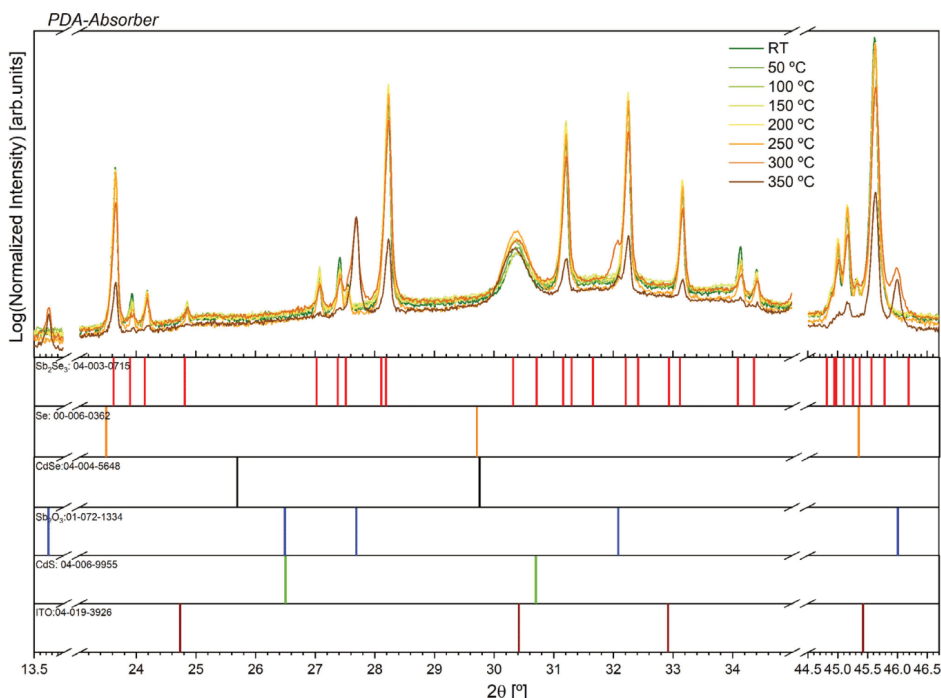


Figure 2. XRD diffractograms of the PDA-absorber set of samples subjected to different PDA temperatures (the intensity of the diffractograms has been normalized to the 110 reflection of Mo). The used ICDD Powder Diffraction File (PDF's) pattern numbers are indicated in each of the reference figures.^[62]

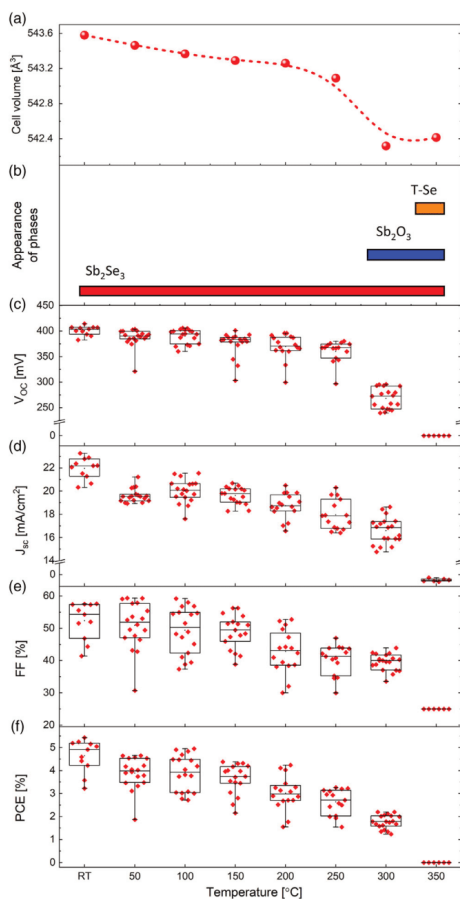


Figure 3. a) Temperature evolution of the cell volume of the Sb_2Se_3 phase. b) Temperature ranges of detection of different phases. c–f) Evolution of the optoelectronic parameters with the PDA temperature in the PDA-absorber set.

devices is observed for PDA temperatures >250 °C. In view of the Raman and XRD results, this is clearly related to the formation of native oxide phases and to accumulation of Se at the interface. The formation of these phases at the interface degrades the p–n junction and increases the recombination rate. On the contrary, a slight reduction of the J_{sc} , V_{oc} , and fill factor (FF) is observed for PDA temperatures lower than 250 °C in clear correlation with the reduction of the Sb_2Se_3 crystalline lattice volume (Figure 3a). This will be further discussed in the next sections.

2.3. PDA of the Sb_2Se_3 -Based Devices: Impact on the Optoelectronic Properties

On a final step, the PDA treatment was applied directly to complete PV devices (PDA-device set of samples). In this case, the upper layers on top of the absorber are expected to protect it from oxidation during the PDA treatment. Analogously to the analysis of the bare Sb_2Se_3 absorbers (Section 2.1 and 2.2), phase formation in the absorber layer was first studied by means of Raman spectroscopy (Figure 4a). As expected, no peaks of Sb–O or elemental Se are detected in the Raman spectra of samples at any PDA temperature under 633 nm excitation wavelength. However, several new peaks can be observed in the samples annealed at temperatures above 200 °C. A more detailed analysis revealed that these new peaks can be associated with the formation of a $\text{CdS}_{1-x}\text{Se}_x$ solid solution phase. It is worth mentioning that the high bandgap, low thickness, and low crystalline quality of the CdS buffer layer used in the analyzed solar cells prevent the detection of its Raman peaks under these excitation conditions (the energy of the 633 nm excitation laser is below the bandgap of CdS). On the contrary, the $\text{CdS}_{1-x}\text{Se}_x$ solid solution possesses a lower bandgap (between ≈ 2.4 and ≈ 1.7 eV which correspond to CdS and CdSe, respectively), leading to quiresonant conditions under 633 nm (1.96 eV) excitation. As such, the formation of even low amounts of this phase results in the appearance of the detected peaks.

To deeply investigate the formation process of the $\text{CdS}_{1-x}\text{Se}_x$ phase, the Raman spectra of the PDA-device set were measured under 532 nm (2.4 eV) excitation wavelength (Figure 4b). Under these resonant excitation conditions, as expected, a clear Raman peak of the CdS buffer layer (LO_{CdS}) can be seen already in the sample without PDA at around 300 cm^{-1} . This peak does not present significant changes for the samples subjected to PDAs up to 200 °C. The increase in the PDA temperature above this limit results in an increased intensity of this CdS peak and in the appearance of a new peak related to the $\text{CdS}_{1-x}\text{Se}_x$ phase at around 200 cm^{-1} (LO_{CdSe} -like peak and several multiphonon peaks).^[50] A more detailed study of the evolution of the $\text{CdS}_{1-x}\text{Se}_x$ phase with the annealing temperature was performed by analyzing the residual spectra (Figure 4c) obtained after subtracting the reference spectrum of Sb_2Se_3 phase (i.e., spectrum of the sample not subjected to PDA treatment). The evolution of the position of the LO_{CdS} and LO_{CdSe} peaks with PDA temperature was calculated (Figure 4d) from the obtained residual spectra. To decrease the possible influence of the strain/stress effects to the position of the $\text{CdS}_{1-x}\text{Se}_x$ Raman peaks, the difference in Raman shift between the two LO peaks was calculated. This difference was found to decrease with the PDA temperature confirming the increase in the Se amount in the formed $\text{CdS}_{1-x}\text{Se}_x$ solid solution from about 20% in the sample annealed at 150 °C up to about 40% in the sample annealed at 350 °C.^[51] It should be noted that the coexistence of the phases (pure CdS and $\text{CdS}_{1-x}\text{Se}_x$ solid solution) in the buffer layer cannot be excluded from the data presented in this work, even for the samples annealed at the highest temperature.

The strong overlapping of the Raman peaks of the $\text{CdS}_{1-x}\text{Se}_x$ phase with the peaks of the Sb_2Se_3 phase in the spectra measured both at 532 and 633 nm excitation wavelengths does not allow to

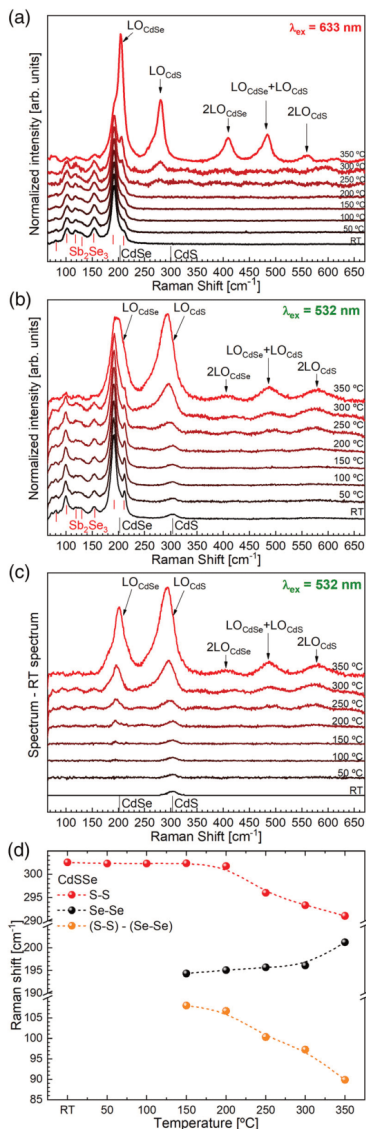


Figure 4. Raman spectra of the PDA-device set of samples measured under a) 633 nm and b) 532 nm excitation wavelength. c) Residual spectra resulting from the subtraction of the RT spectrum from the spectra of each sample (i.e., removal of Sb₂Se₃ peaks). d) Position of the LO_{CdS}, LO_{CdSe} Raman peaks of the CdS_{1-x}Se_x phase, and difference between them (LO_{CdS}–LO_{CdSe}).

detect small changes in the absorber. These could differ from those previously observed in the bare absorbers, in which the surface of the absorber was completely exposed to the air during the PDA. To overcome this limitation, a 785 nm laser was used as excitation source because it has a very low interaction with the buffer and window layers and prevents the appearance of peaks related to these layers in the Raman spectra (see Figure S4a, Supporting Information). The analysis of position and FWHM of the main Sb₂Se₃ peak as well as of the relative integrated intensity of the peaks in the 110–170 cm⁻¹ range does not show any significant changes in the Sb₂Se₃ phase with the annealing temperature (see Figures S4b,c, Supporting Information). This is further confirmed by the detailed XRD structural analysis performed (Figure 5).

From the XRD full profile analysis of the complete devices, it can be concluded that the Sb₂Se₃ layers exhibit a similar dependence with the PDA temperature as in the PDA-absorber set discussed in the previous section, i.e., no modifications in crystal quality, microstrain and overall texture, small cell volume reduction, and formation of the α-Sb₂O₃ secondary phase for temperatures above 300 °C (reduced due to the coverage of the upper layers) (Figure 6a, Table S2, Supporting Information). Nevertheless, some key differences between both sets of samples can be identified. First, the ITO layer shows a low crystal quality for low PDA temperatures and, at 200 °C, it appears to experience a recrystallization process that can be seen from the evolution of the typical ITO XRD reflection at 30.4 °2θ. Second, a clear presence of Se-rich CdS_{1-x}Se_x is detected at 350 °C (Figure 5) in agreement with the Raman observations, and differently from elemental Se formation in the PDA-absorber set of samples. The detection of the CdS_{1-x}Se_x by XRD denotes an increased crystalline quality of this phase.

The clear diminishment of the lattice parameters and, thus, of the cell volume of the Sb₂Se₃ phase allows to conclude that, in both cases, even if the Sb₂Se₃ is protected by the CdS/i-ZnO/ITO layers, structural modifications occur in the absorber layer, pointing toward the instability of the Sb₂Se₃ layer itself. It is worth noticing that while neither the Raman spectroscopy nor XRD analyses show any signs of Cd or S migration from the CdS toward Sb₂Se₃ layer, this possibility cannot be discarded.

The analysis of the optoelectronic properties of the solar cells annealed at different temperatures shows that their performance is relatively stable up to 150 °C and drastically decreases for higher PDA temperatures (Figure 6b–f). The formation of a relatively high amount of CdS_{1-x}Se_x at 200 °C drastically decreases the J_{sc} and FF of the devices as a consequence of the deterioration of the absorber/buffer interface. Beyond this temperature, the increased Se content in the buffer layer results in a close to zero J_{sc} already at 250 °C. On the contrary, the V_{oc} remains almost constant up to 200 °C and sharply decreases for higher temperatures. The latter is comparable with the PDA-absorber set of samples and can be related to a reduction of Se content in the Sb₂Se₃ phase that decreases the concentration of Se_{SB} and 2Se_{SB} intrinsic point defects (responsible of the p-type conductivity of the material) at the absorber surface.^[15] This is also in agreement with the cell volume contraction present in the PDA-absorber set. The C(V) characteristics of the devices were acquired (Figure S5, Supporting Information), showing a clear decrease in the space charge region width (SCRW) of the devices

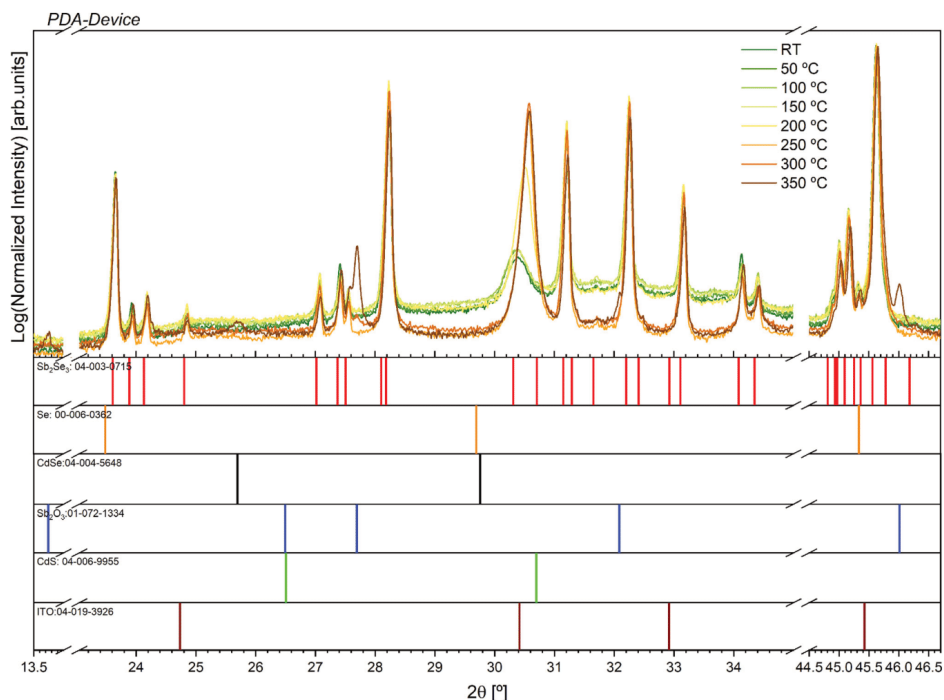


Figure 5. XRD diffractograms of the PDA-device set of samples subjected to different PDA temperatures (the intensity of the diffractograms has been normalized to the 110 reflection of Mo). The used ICDD Powder Diffraction File (PDF's) pattern numbers are indicated in each of the reference figures.^[62]

with PDA temperature up to 200 °C. This supports the hypothesis of the compensation of the sulfur vacancies by Se atoms in the CdS layer, which shifts the SCR inside the buffer layer and consequently reduces its width in the Sb₂Se₃ side of the junction. A further increase in the PDA temperature shows an increment in the apparent doping density of the material, possibly accounting for the increased amount of defects in the degraded devices. In addition, as mentioned earlier, a recrystallization effect of the ITO layer takes place at 200 °C. However, no influence on device performance caused by ITO recrystallization after soft annealing has been observed in other technologies with similar architectures (e.g., CZTSe^[22]), thus it is not expected to have an important influence on device performance in the samples analyzed in this work either.

2.4. Mechanisms of Degradation and Temperature Limitations for the Sb₂Se₃ PV Technology

The analysis presented in the previous sections allowed the development of a model of the degradation of the Sb₂Se₃-based devices by thermal instability. The observed degradation pathways

can be summarized in three main points: 1) A reduction of the volume of the Sb₂Se₃ unit cell starting at 50 °C and associated with the decrease in the Se_{Sb} and 2Se_{Sb}, and the increase in the V_{Se} defects: comparing the evolution of the optoelectronic parameters and the cell volume, prior to segregation into secondary phases, it can be spotted that the two sets of samples analyzed (PDA-absorber and PDA-device) show the same volume-decreasing tendency that clearly correlates with the optoelectronic parameters of the cells (**Figure 7**). This effect seems to affect more strongly the *J*_{sc} and the FF of the devices. The former points toward a reduction in charge carriers concentration and/or mobility, while the latter may be related to a lower shunt resistance.^[52] This effect could be related to the reduction of complex binary defects such as 2Se_{Sb}, previously reported in density functional theory (DFT) calculations as responsible for the p-type conductivity (along with Se_{Sb}) of Sb₂Se₃ in Se-rich conditions.^[16] Thus, the reduction of this kind of defects could be the cause of the observed lattice contraction which could be influencing negatively the V_{oc} of the devices by reducing the Fermi-level splitting. 2) Generation of CdS_{1-x}Se_x at 150 °C: the diffusion of elemental Se from the Sb₂Se₃ absorber layer becomes strong

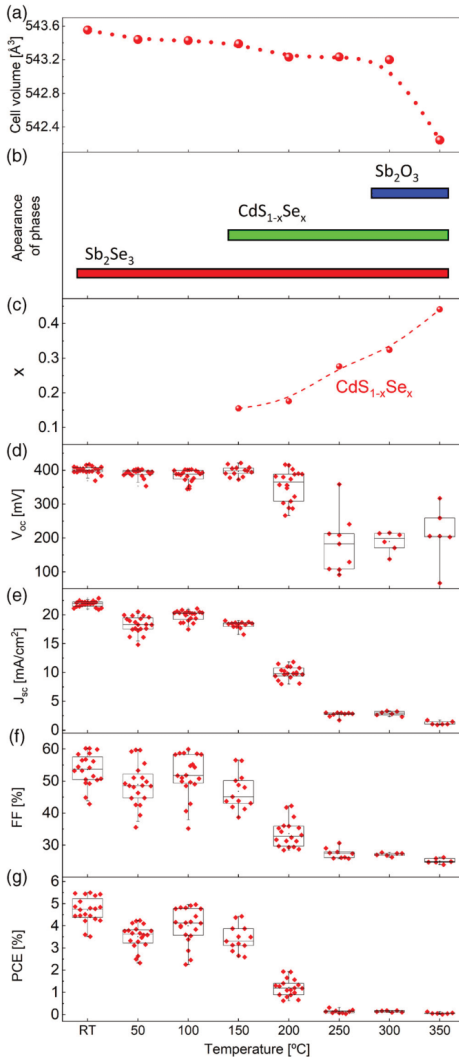


Figure 6. a) Evolution of cell volume of the Sb₂Se₃ phase. b) Temperature ranges of detection of different phases. c) Se content in the CdS_{1-x}Se_x solid solution estimated from the Raman spectra, based on the results reported in the works of Bischof et al.^[50] and Azhniuk et al.^[51] d–g) Evolution of the optoelectronic parameters with the PDA temperature of the complete devices.

enough to start influencing the upper layers (by forming the CdS_{1-x}Se_x phase). A further increase in the PDA temperature up to 300 °C increases the amount of diffused Se which, although hardly detectable in the bare absorber and with a minor influence on the Sb₂Se₃ phase, becomes strong enough to promote changes in the composition of the buffer layer completely degrading the PCE of the PV devices. 3) Further decomposition and generation of secondary phases at 300 °C: large amounts of α-Sb₂O₃ secondary phase are formed in the bare Sb₂Se₃ absorbers enabling their detection both by Raman and XRD. In the case of the complete devices, the protection of the absorber surface from the ambient oxygen by the buffer and window layers reduces the amount of α-Sb₂O₃ phase observed, although, alternatively, the presence of amorphous Sb (a-Sb) as a result of Se loss in the structure is highly likely. Finally, at temperatures above 300 °C, an increased amount of Sb–O phase is observed in both bare absorbers and complete devices. This is accompanied by the recrystallization of the elemental Se and Sb₂O₃ phases in the bare absorbers and complete devices, respectively.

Figure 8 shows the different degradation and secondary phase formation mechanisms observed and proposed in this work based on the results presented earlier about the influence of PDAs on bare Sb₂Se₃ absorbers and complete PV devices.

The observed interdiffusion of Se, that results in a strong degradation of the absorber/buffer interface, significantly restrains the fabrication process of Sb₂Se₃ thin film solar cells with the discussed architecture (SLG/Mo/Sb₂Se₃/CdS/i-ZnO/ITO). This further restricts the use of CdS as buffer layer beyond the high toxicity of Cd. The fact that the absorber/buffer interface presents a low thermal stability and can only withstand temperatures up to ≈200 °C highly limits the necessary postprocessing for fabricating complete PV devices and modules (e.g., deposition of TCOs or encapsulation process). Moreover, this raises questions about the stability of Sb₂Se₃-based PV modules under the standard operating conditions in which temperatures around 100 °C can be reached.^[53,54] Although less pronounced, Se migration effects occur in this temperature range. These could be expected to slowly decrease the doping level of the CdS layer due to the passivation of donor V_S defects by the diffused selenium atoms. This effect becomes more relevant in Se-rich absorber layers which present a higher potential for PV applications due to their increased p-doping.^[16,52] As such, the interdiffusion of Se atoms has a negative effect in both the absorber and buffer layers that acts twofold: 1) reducing carrier density and thus the conductivity of the Sb₂Se₃ layer which results in the degradation of the J_{sc} of the devices, and 2) reducing the quasi-Fermi-level splitting between them which leads to a reduction of the effective V_{oc} of the devices. This could be one of the underlying mechanisms that hampers the development of devices with a lower V_{oc} deficit, issue that is systematically reported for CdS/Sb₂Se₃ solar cells.^[7,14,28,31,36,55,56] The mobility of Se atoms under low temperatures may also be an obstacle to future technology applications such as tandem solar cells structures, for which the Sb₂Se₃ material is a desirable candidate as a bottom

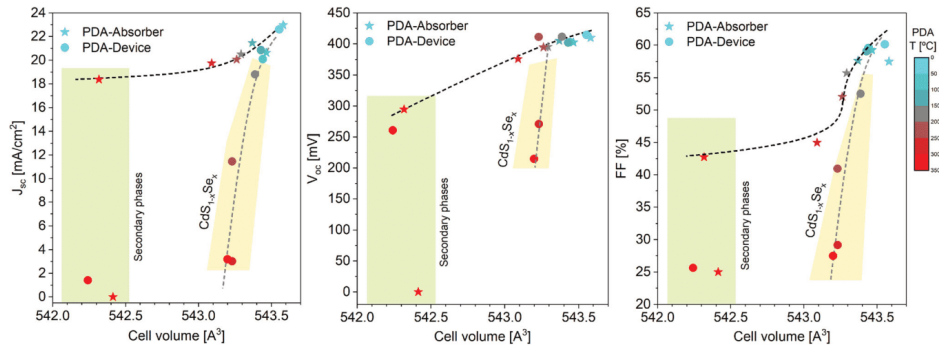


Figure 7. Evolution of the (left) J_{sc} , (center) V_{oc} , and (right) FF of the three best cells median values with the Sb_2Se_3 cell volume. Samples with presence of secondary phases are highlighted. Dashed lines are only intended as an eye guide for the reader.

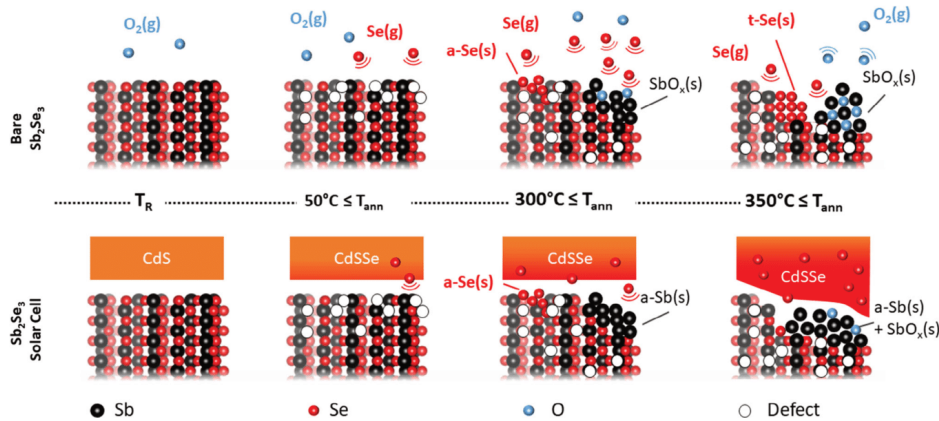


Figure 8. Schematic representation of the decomposition and secondary phase formation mechanisms in the bare Sb_2Se_3 layers (top) and complete PV device (bottom) at different PDA temperatures.

cell and, thus, should withstand the top cell sequential fabrication processes. Moreover, $CdS_{1-x}Se_x$ formation was found to be detrimental also in superstrate configuration devices with CdS electron transport layers during the synthesis process.^[32,33] Thus, a further development of the Sb_2Se_3 -based technology should be focused on finding effective ways of preventing Se migration such as the development of innovative low-temperature postdeposition processes (i.e., transparent conducting oxide (TCO) deposition or encapsulation) and device architectures specifically tailored to the thermal stability limitations of this technology. Finally, it should be taken into account that the observed effects are probably not exclusive for the Sb_2Se_3 compound, but can also be a limiting issue for Sb_2S_3 and $Sb_2(S,Se)_3$ compounds for which comparable formation enthalpies were previously calculated.^[30]

3. Conclusions

This work has presented clear evidences of the thermal instability of Sb-based Q1D layers through a systematic analysis of the effect of low-temperature PDA processes on the stability of bare Sb_2Se_3 absorbers and on Sb_2Se_3 /CdS-based PV devices. The obtained results from thorough compositional, structural, and optoelectronic analyses based on Raman, XRD (Rietveld refinement), and $J-V$ characteristics evidence the thermal instability of the Sb_2Se_3 compound under temperatures in the range of those used in typical device fabrication processes such as TCO deposition or module encapsulation. Significant stability problems related to defect modification (observed by cell volume reduction), decomposition of Sb_2Se_3 into Se and Sb in the bare absorber material, and to the migration of selenium from the Sb_2Se_3 .

4. Experimental Section

Films and Device Preparation: Sb_2Se_3 thin films were prepared using a two-step process. This process consisted in the deposition of a Sb layer by thermal evaporation (Oerlikon Univex 250) on a soda-lime glass (SLG) substrate coated with a molybdenum layer using a DC-magnetron sputtering machine (Alliance Concept AC450). The layers were then introduced into graphite boxes with selenium powder (25 mg) and subjected to a selenization procedure in a 3-zone tubular furnace (temperature 320 °C, time 30 min). After the synthesis of the Sb_2Se_3 layers, devices were completed with an n-type CdS buffer layer (≈ 50 nm) deposited by chemical bath deposition at 80 °C, and a window bilayer formed by i-ZnO (≈ 50 nm) and In_2O_3 : SnO_2 (ITO) (≈ 150 nm) deposited by DC-pulsed magnetron sputtering (Alliance Concept CT100) at low temperature (≈ 50 °C) to avoid inducing thermal effects in the p–n junction. Individual cells (3×3 mm²) were then isolated using a mechanical scribe (Micro Diamond MR200 OEG). This process is described with more detail in the study by Vidal-Fuentes et al.^[52]

To study the PDA effect on the bare layers and devices, three different sets of samples with different PDA conditions were prepared and analyzed: 1) Reference Sb_2Se_3 bare absorber: a single reference sample that sequentially was subjected to PDA process at different temperatures from RT to 400 °C with a 50 °C step. 2) PDA-absorber set: eight different Sb_2Se_3 absorber layers (SLG/Mo/ Sb_2Se_3) synthesized with the same process conditions and exposed to different PDA processes at different temperatures from RT to 350 °C with a 50 °C step. After the PDA, a CdS/i-ZnO/ITO structure was deposited onto the samples to fabricate complete PV devices. 3) PDA-device set: eight different Sb_2Se_3 complete devices (SLG/Mo/ Sb_2Se_3 /CdS/i-ZnO/ITO) with the same absorber, buffer and window layer synthesis procedures as the Set PDA-absorber, that were exposed to PDA processes at different temperatures from RT to 350 °C with a 50 °C step.

The PDAs were performed using a hot plate system with a dwell time of 10 min in all cases inside a fume hood with controlled humidity (<20%) and temperature (25 °C) values.

Thin Film and Device Characterization: The composition of the absorber layers was determined with an XRF system (Fischerscope XVD) calibrated by inductively coupled plasma mass spectroscopy (ICP-MS). The XRF measurements were conducted in a 4×4 point grid covering the full area of the samples (1×2 cm²) using a 50 kV accelerating voltage, a Ni10 filter to reduce background signal, and an integration time per measuring point of 45 s.

Raman scattering spectra were measured using an FHR640 Horiba Jobin Yvon spectrometer coupled with a CCD detector. The measurements were performed in back scattering configuration through a specific probe designed at IREC. Solid-state lasers ($\lambda_{\text{exc}} = 532, 633, 785$ nm) were used as excitation sources. Here, the 532 nm excitation wavelength was used to characterize the Sb_2Se_3 surface and the Cd-based buffer layer in complete devices.^[43] The 633 nm excitation wavelength was used to characterize the Sb_2Se_3 absorber layer avoiding interferences with the upper layers and to detect the possible formation of secondary phases such as elemental Se and SbO_x .^[43] Finally, the 785 nm excitation wavelength is in close to resonant conditions with the Sb_2Se_3 phase and was used to assess the evolution of the crystalline quality and stress of the absorber layer taking advantage of the resulting high signal-to-noise ratio.^[43] In all cases, the power density was kept below 25 W cm⁻² and was concentrated to a macropspot with a diameter of around ≈ 50 μm , which allowed to avoid any thermal effects on the surface of the samples during the measurements. The measurements were performed in five different points in each sample which, in combination with the macropspot used, ensures a general overview of the samples surface, minimizing possible local effects associated with the inhomogeneity inherent to the synthesis process.

XRD data were obtained with a PANalytical X'Pert PRO MPD alpha1 Bragg-Brentano powder diffractometer using a Cu tube operating at 45 kV and 40 mA, a Johansson-type Ge (111) primary focalizing monochromator, and a solid-state strip 1D PIXcel^{1D} detector. High-resolution, high statistics, full angular range Cu K α_1 $\theta/2\theta$ scans were performed with the following parameters: $\theta/2\theta$ scans from 4 to 145°; step size 0.0131°; measuring time per step 200 s (PIXcel^{1D} active length 3.347°); three consecutive repeated scans; and total measuring time per sample 7.2 h. An

automatic divergence slit system and a mask enabled a constant irradiated surface (10×12 mm²) over the analyzed samples. The diffracting volume was also constant regarding the small and finite thickness (<2 μm) of the characterized layers. Measurements were performed on the PDA-absorber and PDA-device sets. Full profile analysis was performed applying Rietveld refinement for all the crystalline structure phases observed.^[57] The refinements have been performed through the TOPAS v6 software.^[58] The peak width of each phase was modeled with the double-Voigt approach by considering both the Lorentzian contribution of the crystallite size effect and the Gaussian contribution of the microstrain to the peak width.^[59] Preferential orientation corrections were applied by spherical harmonics.^[60] The background was modeled with a 15th-order Chebyshev polynomial. The instrumental contribution to the diffraction profile was calculated with the fundamental parameters approach.^[61]

Finally, current density–voltage (J – V) measurements were performed on complete devices using a Sun 3000 AAA solar simulator from Abet Technology (uniform illumination area of 15×15 cm²) calibrated with a Si reference solar cell under AM1.5 illumination.

Supporting Information

Supporting Information is available from the Wiley Online Library or from the author.

Acknowledgements

This research has received funding from the European Union H2020 Framework Programme under grant agreement no. 866018, Low dimensional semiconductors for optically tunable solar harvesters (SENSATE), and by the Spanish Ministry of Science, Innovation and Universities under the WINCOST (ENE2016-80788-C5-1-R), and by the European Regional Development Funds (ERDF, FEDER Programa Competitivitat de Catalunya 2007–2013). Authors from IREC and the University of Barcelona belong to the SEMS (Solar Energy Materials and Systems) Consolidated Research Group of the “Generalitat de Catalunya” (Ref. 2017 SGR 862). M.G. appreciates the funding received from Spanish Ministry of Science, Innovation and Universities within the Juan de la Cierva (IJC2018-038199-I) programs.

Conflict of Interest

The authors declare no conflict of interest.

Data Availability Statement

Research data are not shared.

Keywords

quasi-1D, Sb_2Se_3 , solar cells, thermal stability, thin films

Received: July 8, 2021

Revised: August 2, 2021

Published online:

- [1] V. Bermudez, A. Perez-Rodriguez, *Nat. Energy* **2018**, *3*, 466.
- [2] M. Green, E. Dunlop, J. Hohl-Ebinger, M. Yoshita, N. Kopidakis, X. Hao, *Prog. Photovoltaics Res. Appl.* **2021**, *29*, 3.
- [3] N. Li, X. Niu, Q. Chen, H. Zhou, *Chem. Soc. Rev.* **2020**, *49*, 8235.
- [4] R. Wang, M. Mujahid, Y. Duan, Z. Wang, J. Xue, Y. Yang, *Adv. Funct. Mater.* **2019**, *29*, 1808843.

- [5] L. Meng, J. You, Y. Yang, *Nat. Commun.* **2018**, *9*, 5265.
- [6] R. Tang, X. Wang, W. Lian, J. Huang, Q. Wei, M. Huang, Y. Yin, C. Jiang, S. Yang, G. Xing, S. Chen, C. Zhu, X. Hao, M. A. Green, T. Chen, *Nat. Energy* **2020**, *5*, 587.
- [7] Z. Li, X. Liang, G. Li, H. Liu, H. Zhang, J. Guo, J. Chen, K. Shen, X. San, W. Yu, R. E. I. Schropp, Y. Mai, *Nat. Commun.* **2019**, *10*, 125.
- [8] A. Mavlonov, T. Razykov, F. Raziq, J. Gan, J. Chantana, Y. Kawano, T. Nishimura, H. Wei, A. Zakutayev, T. Minemoto, X. Zu, S. Li, L. Qiao, *Sol. Energy* **2020**, *201*, 227.
- [9] Y. C. Choi, D. U. Lee, J. H. Noh, E. K. Kim, S. Il Seok, *Adv. Funct. Mater.* **2014**, *24*, 3587.
- [10] X. Wang, R. Tang, C. Jiang, W. Lian, H. Ju, G. Jiang, Z. Li, C. Zhu, T. Chen, *Adv. Energy Mater.* **2020**, *10*, 2002341.
- [11] I. Repins, L. Mansfield, A. Kanevce, S. A. Jensen, D. Kuciauskas, S. Glynn, T. Barnes, W. Metzger, J. Burst, C.-S. Jiang, P. Dippo, S. Harvey, G. Teeter, C. Perkins, B. Egaas, A. Zakutayev, J.-H. Alsmeyer, T. Lusky, L. Korte, R. G. Wilks, M. Bar, Y. Yan, S. Lany, P. Zawadzki, J.-S. Park, S. Wei, in *2016 IEEE 43rd Photovolt. Spec. Conf.*, IEEE, Piscataway, NJ **2016**, pp. 0309–0314.
- [12] K. Li, C. Chen, S. Lu, C. Wang, Y. Lu, J. Tang, *Adv. Mater.* **2019**, *31*, 1903914.
- [13] C. Chen, D. C. Bobela, Y. Yang, S. Lu, K. Zeng, C. Ge, B. Yang, L. Gao, Y. Zhao, M. C. Beard, J. Tang, *Front. Optoelectron.* **2017**, *10*, 18.
- [14] Y. Zhou, L. Wang, S. Chen, S. Qin, X. Liu, J. Chen, D.-J. Xue, M. Luo, Y. Cao, Y. Cheng, E. H. Sargent, J. Tang, *Nat. Photonics* **2015**, *9*, 409.
- [15] R. E. Williams, Q. M. Ramasse, K. P. McKenna, L. J. Phillips, P. J. Yates, O. S. Hutter, K. Durose, J. D. Major, B. G. Mendis, *ACS Appl. Mater. Interfaces* **2020**, *12*, 21730.
- [16] M. Huang, P. Xu, D. Han, J. Tang, S. Chen, *ACS Appl. Mater. Interfaces* **2019**, *11*, 15564.
- [17] D. Hironiwa, N. Sakai, T. Kato, H. Sugimoto, Z. Tang, J. Chantana, T. Minemoto, *Thin Solid Films* **2015**, *582*, 151.
- [18] H. Xie, S. López-Marino, T. Olar, Y. Sánchez, M. Neuschitzer, F. Oliva, S. Giraldo, V. Izquierdo-Roca, I. Lauermann, A. Pérez-Rodríguez, E. Saucedo, *ACS Appl. Mater. Interfaces* **2016**, *8*, 5017.
- [19] M. Neuschitzer, Y. Sanchez, T. Olar, T. Thersleff, S. Lopez-Marino, F. Oliva, M. Espindola-Rodríguez, H. Xie, M. Placidi, V. Izquierdo-Roca, I. Lauermann, K. Leifer, A. Pérez-Rodríguez, E. Saucedo, *Chem. Mater.* **2015**, *27*, 5279.
- [20] U. Rau, D. Braunger, R. Herberholz, H. W. Schock, J.-F. Guillemoles, L. Kronik, D. Cahen, *J. Appl. Phys.* **1999**, *86*, 497.
- [21] I. Repins, M. A. Contreras, B. Egaas, C. DeHart, J. Scharf, C. L. Perkins, B. To, R. Noufi, *Prog. Photovoltaics Res. Appl.* **2008**, *16*, 235.
- [22] M. Dimitrievska, S. Giraldo, P. Pistor, E. Saucedo, A. Pérez-Rodríguez, V. Izquierdo-Roca, *Sol. Energy Mater. Sol. Cells* **2016**, *157*, 462.
- [23] X. Hu, J. Tao, S. Chen, J. Xue, G. Weng, Kaijiang, Z. Hu, J. Jiang, S. Chen, Z. Zhu, J. Chu, *Sol. Energy Mater. Sol. Cells* **2018**, *187*, 170.
- [24] V. Kumar, E. Artegiani, A. Kumar, G. Mariotto, F. Piccinelli, A. Romeo, *Sol. Energy* **2019**, *193*, 452.
- [25] W. Wang, X. Wang, G. Chen, L. Yao, X. Huang, T. Chen, C. Zhu, S. Chen, Z. Huang, Y. Zhang, *Adv. Electron. Mater.* **2019**, *5*, 1800683.
- [26] X. Liu, S. Chang, J. Liu, Y. Qiao, E. Jia, X. Shen, S. Li, K. Cheng, Z. Du, *J. Power Sources* **2021**, *491*, 229581.
- [27] X. Jin, Y. Fang, T. Salim, M. Feng, S. Hadke, S. W. Leow, T. C. Sum, L. H. Wong, *Adv. Funct. Mater.* **2020**, *30*, 2002887.
- [28] D.-B. Li, X. Yin, C. R. Grice, L. Guan, Z. Song, C. Wang, C. Chen, K. Li, A. J. Cimaroli, R. A. Awani, D. Zhao, H. Song, W. Tang, Y. Yan, J. Tang, *Nano Energy* **2018**, *49*, 346.
- [29] Y. Zhou, Y. Li, J. Luo, D. Li, X. Liu, C. Chen, H. Song, J. Ma, D.-J. Xue, B. Yang, J. Tang, *Appl. Phys. Lett.* **2017**, *111*, 013901.
- [30] S. Lu, H. Ding, J. Hu, Y. Liu, J. Zhu, R. Kondrotas, C. Chen, J. Tang, *Appl. Phys. Lett.* **2020**, *116*, 241602.
- [31] R. Tang, Z. H. Zheng, Z. H. Su, X. J. Li, Y. D. Wei, X. H. Zhang, Y. Q. Fu, J. T. Luo, P. Fan, G. X. Liang, *Nano Energy* **2019**, *64*, 103929.
- [32] R. E. Williams, Q. M. Ramasse, K. P. McKenna, L. J. Phillips, P. J. Yates, O. S. Hutter, K. Durose, J. D. Major, B. G. Mendis, *ACS Appl. Mater. Interfaces* **2020**, *12*, 21730.
- [33] L. J. Phillips, C. N. Savory, O. S. Hutter, P. J. Yates, H. Shiel, S. Mariotti, L. Bowen, M. Birkett, K. Durose, D. O. Scanlon, J. D. Major, *IEEE J. Photovoltaics* **2019**, *9*, 544.
- [34] L. Wang, D.-B. Li, K. Li, C. Chen, H.-X. Deng, L. Gao, Y. Zhao, F. Jiang, L. Li, F. Huang, Y. He, H. Song, G. Niu, J. Tang, *Nat. Energy* **2017**, *2*, 17046.
- [35] M. Neuschitzer, Y. Sanchez, S. López-Marino, H. Xie, A. Fairbrother, M. Placidi, S. Haass, V. Izquierdo-Roca, A. Pérez-Rodríguez, E. Saucedo, *Prog. Photovoltaics Res. Appl.* **2015**, *23*, 1660.
- [36] X. Wen, C. Chen, S. Lu, K. Li, R. Kondrotas, Y. Zhao, W. Chen, L. Gao, C. Wang, J. Zhang, G. Niu, J. Tang, *Nat. Commun.* **2018**, *9*, 2179.
- [37] S. Lopez-Marino, M. Espindola-Rodríguez, Y. Sánchez, X. Alcobé, F. Oliva, H. Xie, M. Neuschitzer, S. Giraldo, M. Placidi, R. Caballero, V. Izquierdo-Roca, A. Pérez-Rodríguez, E. Saucedo, *Nano Energy* **2016**, *26*, 708.
- [38] N. Fleck, T. D. C. Hobson, C. N. Savory, J. Buckeridge, T. D. Veal, M. R. Correia, D. O. Scanlon, K. Durose, F. Jäckel, *J. Mater. Chem. A* **2020**, *8*, 8337.
- [39] M. Guc, F. Oliva, R. Kondrotas, X. Alcobe, M. Placidi, P. Pistor, E. Saucedo, A. Pérez-Rodríguez, V. Izquierdo-Roca, *Prog. Photovoltaics Res. Appl.* **2019**, *27*, 3150.
- [40] M. Guc, J. Andrade-Arvizu, I. Y. Ahmet, F. Oliva, M. Placidi, X. Alcobé, E. Saucedo, A. Pérez-Rodríguez, A. L. Johnson, V. Izquierdo-Roca, *Acta Mater.* **2020**, *183*, 1.
- [41] S. Schorr, G. Gurieva, M. Guc, M. Dimitrievska, A. Pérez-Rodríguez, V. Izquierdo-Roca, C. S. Schnorr, J. Kim, W. Jo, J. M. Merino, *J. Phys. Energy* **2019**, *2*, 012002.
- [42] P. Pistor, M. Meyns, M. Guc, H.-C. Wang, M. A. L. Marques, X. Alcobé, A. Cabot, V. Izquierdo-Roca, *Scr. Mater.* **2020**, *184*, 24.
- [43] P. Vidal-Fuentes, M. Guc, X. Alcobe, T. Jawhari, M. Placidi, A. Pérez-Rodríguez, E. Saucedo, V. I. Roca, *2D Mater.* **2019**, *6*, 045054.
- [44] A. Shongalova, M. R. Correia, B. Vermang, J. M. V. Cunha, P. M. P. Salomé, P. A. Fernandes, *MRS Commun.* **2018**, *8*, 865.
- [45] J. P. Allen, J. J. Carey, A. Walsh, D. O. Scanlon, G. W. Watson, *J. Phys. Chem. C* **2013**, *117*, 14759.
- [46] S. N. Yannopoulos, K. S. Andrikopoulos, *J. Chem. Phys.* **2004**, *121*, 4747.
- [47] D. Cody, C. A. Cody, L. D. Carlo, R. K. Darlington, *Inorg. Chem.* **1979**, *18*, 1572.
- [48] X. Liu, J. Chen, M. Luo, M. Leng, Z. Xia, Y. Zhou, S. Qin, D.-J. Xue, L. Lv, H. Huang, D. Niu, J. Tang, *ACS Appl. Mater. Interfaces* **2014**, *6*, 10687.
- [49] M. M. A. Sekkina, *J. Therm. Anal.* **1988**, *34*, 749.
- [50] T. Bischof, M. Ivanda, G. Lermann, A. Materny, W. Kiefer, J. Kalus, *J. Raman Spectrosc.* **1996**, *27*, 297.
- [51] Y. M. Azhniuk, A. G. Milekhin, A. V. Gomonnai, V. V. Lopushansky, V. O. Yukhymchuk, S. Schulze, E. I. Zenkevich, D. R. T. Zahn, *J. Phys. Condens. Matter* **2004**, *16*, 9069.
- [52] P. Vidal-Fuentes, M. Placidi, Y. Sánchez, I. Becerril-Romero, J. Andrade-Arvizu, Z. Jehl, A. Pérez-Rodríguez, V. Izquierdo-Roca, E. Saucedo, *Sol. RRL* **2020**, 2000141.
- [53] D. Fairman, *Prog. Photovoltaics Res. Appl.* **2008**, *16*, 307.
- [54] W. Yuan, J. Ji, Z. Li, F. Zhou, X. Ren, X. Zhao, S. Liu, *Energy* **2018**, *148*, 1153.

3 - Publications

- [55] Y.-D. Luo, R. Tang, S. Chen, J.-G. Hu, Y.-K. Liu, Y.-F. Li, X.-S. Liu, Z.-H. Zheng, Z.-H. Su, X.-F. Ma, P. Fan, X.-H. Zhang, H.-L. Ma, Z.-G. Chen, G.-X. Liang, *Chem. Eng. J.* **2020**, 393, 124599.
- [56] J. Zhang, R. Kondrotas, S. Lu, C. Wang, C. Chen, J. Tang, *Sol. Energy* **2019**, 182, 96.
- [57] H. M. Rietveld, *J. Appl. Crystallogr.* **1969**, 2, 65.
- [58] A. A. Coelho, J. Evans, I. Evans, A. Kern, S. Parsons, *Powder Diffr.* **2011**, 26, S22.
- [59] D. Balzar, N. Audebrand, M. R. Daymond, A. Fitch, A. Hewat, J. I. Langford, A. Le Bail, D. Louër, O. Masson, C. N. McCowan, N. C. Popa, P. W. Stephens, B. H. Toby, *J. Appl. Crystallogr.* **2004**, 37, 911.
- [60] P. S. Whitfield, *J. Appl. Crystallogr.* **2009**, 42, 134.
- [61] R. W. Cheary, A. A. Coelho, J. P. Cline, *J. Res. Natl. Inst. Stand. Technol.* **2007**, 109, 1.
- [62] S. Gates-Rector, T. Blanton, *Powder Diffr.* **2019**, 34, 352.

Supporting Information

Insights on the Thermal Stability of the Sb₂Se₃ Q1D Photovoltaic Technology

*Pedro Vidal-Fuentes**, *Maxim Guc*, *Ignacio Becerril-Romero*, *Diouldé Sylla*, *Xavier Alcobé*, *Yudania Sánchez*, *Alejandro Pérez-Rodríguez*, *Edgardo Saucedo*, *Victor Izquierdo-Roca**

P. Vidal-Fuentes, Dr. M. Guc, Dr. I. Becerril-Romero, Dr. D. Sylla, Dr. Y. Sánchez, Dr. V. Izquierdo-Roca

Catalonia Institute for Energy Research (IREC), Jardins de les Dones de Negre 1, 08930 Sant Adrià de Besòs, Spain

E-mail: pvidal@irec.cat, vizquierdo@irec.cat

Dr. X. Alcobé

Centres Científics i Tecnològics de la Universitat de Barcelona (CCiTUB), Lluís Solé i Sabarís 1-3, 08028 Barcelona, Spain

Prof. A. Pérez-Rodríguez

Catalonia Institute for Energy Research (IREC), Jardins de les Dones de Negre 1, 08930 Sant Adrià de Besòs, Barcelona, Spain

IN²UB, Departament d'Enginyeria Electrònica i Biomèdica, Universitat de Barcelona, C. Martí i Franquès 1, 08028 Barcelona, Spain

3 - Publications

Prof. E. Saucedo

Electronic Engineering Department, Polytechnic University of Catalonia (UPC), Campus Besòs, Av. d'Eduard Maristany, 16, 08930 Barcelona, Spain.

Keywords: Sb₂Se₃, Q1D, thin films, solar cells, thermal stability

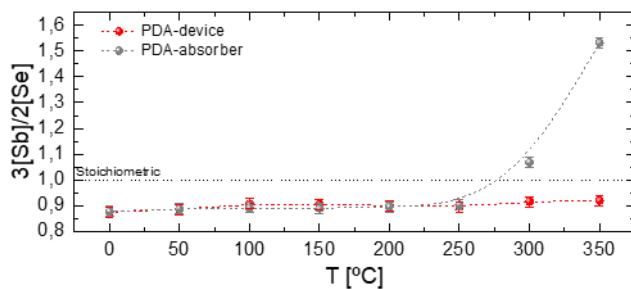


Figure S1: Compositional evolution of both sets of samples from XRF measurements.

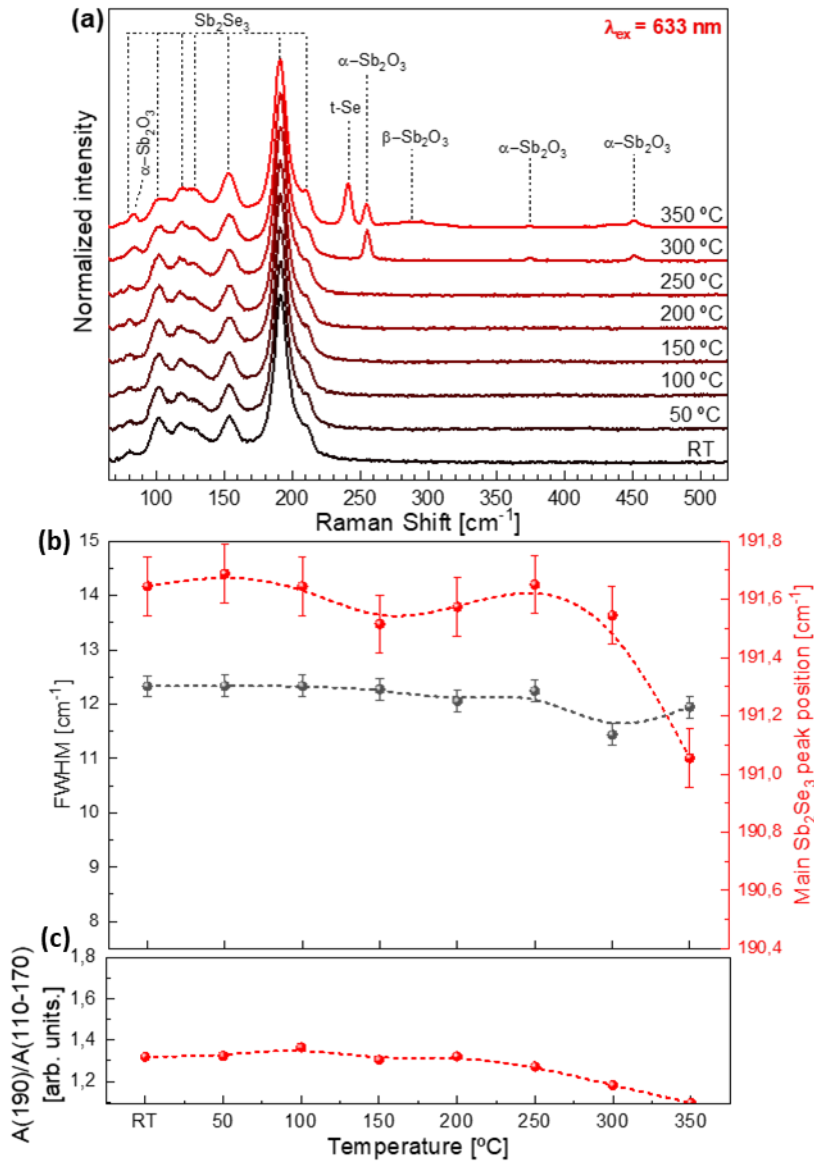


Figure S2: (a) Average Raman spectra of samples from PDA-absorber set after applying different PDA temperatures. (b) Evolution of the FWHM and position of the Sb_2Se_3 main Raman peak with PDA temperature. (c) Change of the relative integrated intensity of the peaks in the range 110 – 170 cm^{-1} with PDA temperature.

3 - Publications

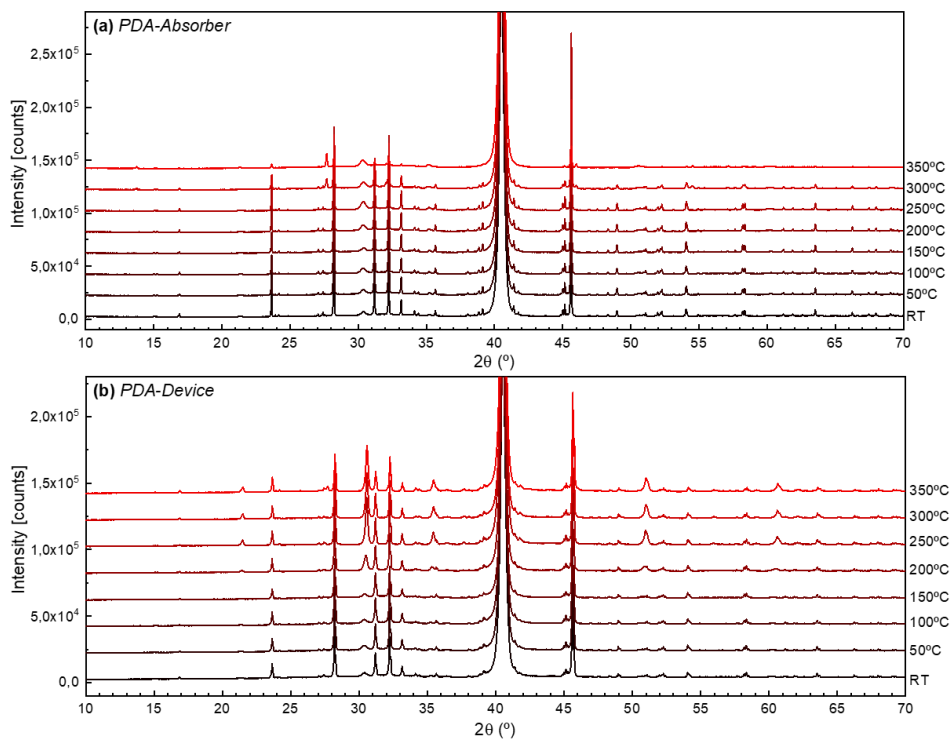


Figure S3: XRD diffractograms of (a) PDA-absorber and (b) PDA-device sets of samples.

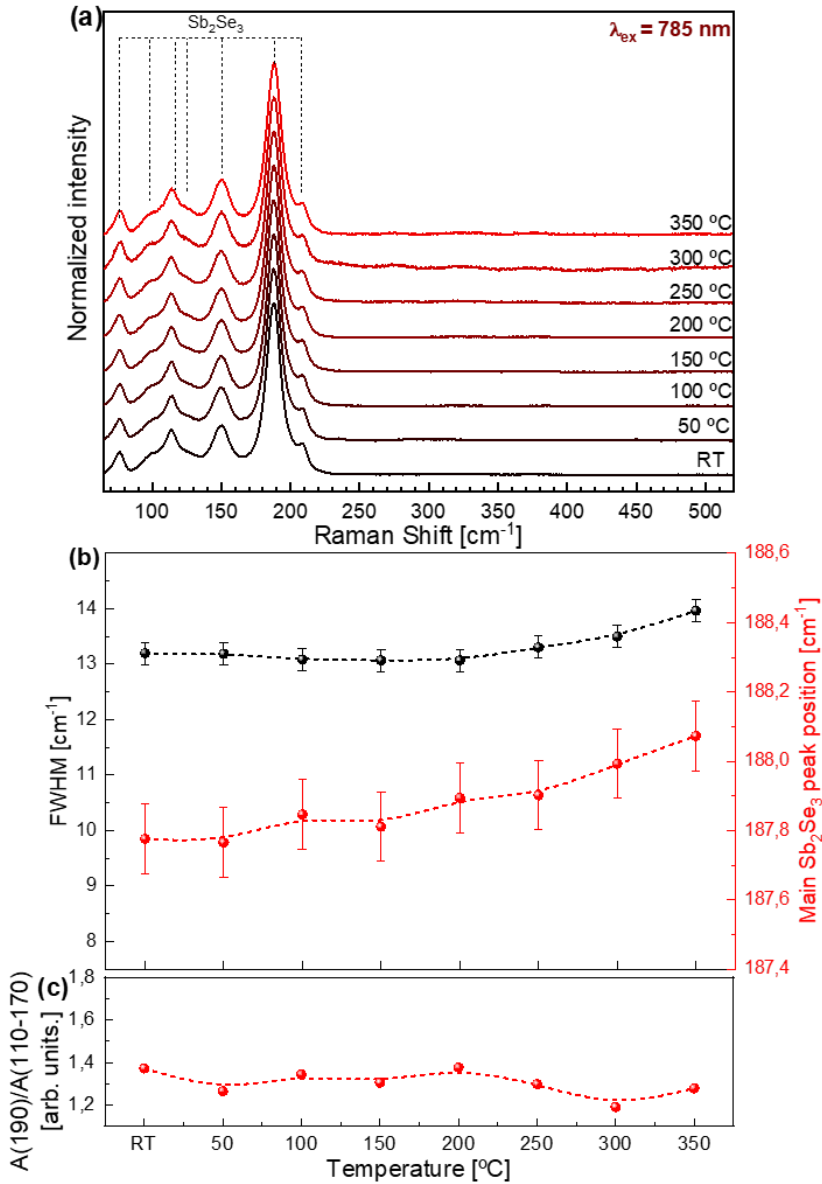


Figure S4: (a) Average Raman spectra of samples from *PDA-device* set after applying different PDA temperatures measured under 785 nm excitation. (b) Evolution of the FWHM and position of the Sb_2Se_3 main Raman peak with PDA temperature. (c) Change of the relative integrated intensity of the peaks in the range 110 – 170 cm^{-1} with PDA temperature.

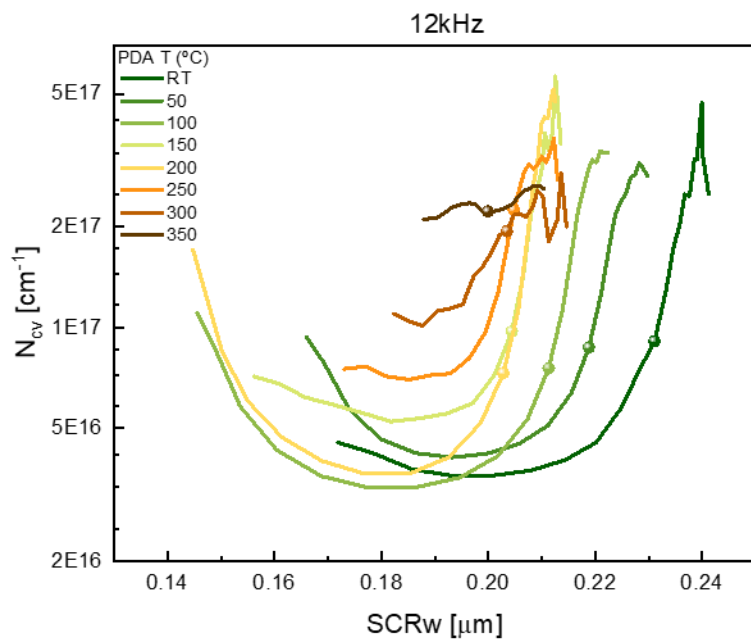


Figure S5: Apparent doping density vs space charge region width measured at 12 kHz. The marked points represent the values at 0 bias voltage.

Table S1: Agreement factors, semi-quantitative phase analysis, cell parameters and averaged microstructure parameters obtained from the Rietveld refinements of the *PDA-Absorber* set of samples.

Temperature (°C)	Mo (<i>Im3m</i>)				ITO (<i>Ia3</i>)				Sb ₂ O ₃ (<i>Fd3m</i>)			
	<i>a</i> (Å)	<i>V</i> (Å ³)	Mass fraction (wt.%)	R _{Bragg}	<i>a</i> (Å)	<i>V</i> (Å ³)	Mass fraction (wt.%)	R _{Bragg}	<i>a</i> (Å)	<i>V</i> (Å ³)	Mass fraction (wt.%)	R _{Bragg}
25	3.1458117	31.13137	43.5	0.46	10.1813641	1055.40197	3.5	1.89	-	-	-	-
50	3.1457227	31.12872	39.1	0.46	10.1838255	1056.16760	4.2	1.60	-	-	-	-
100	3.1454595	31.12091	39.6	0.44	10.1900221	1058.09673	5.4	1.60	-	-	-	-
150	3.1456387	31.12623	42.0	0.50	10.1789117	1054.63952	2.9	1.72	-	-	-	-
200	3.1457799	31.13042	40.2	0.46	10.1842812	1056.30940	4.9	1.55	-	-	-	-
250	3.1457517	31.12959	35.5	0.48	10.1848008	1056.47109	7.8	1.60	-	-	-	-
300	3.1445010	31.09247	45.0	0.41	10.1778320	1054.30394	5.2	1.62	11.1538671	1387.63869	4.4	1.43
350	3.1434290	31.06068	76.4	0.48	10.1888040	1057.71732	9.0	1.45	11.1500000	1386.19588	3.7	1.64

Temperature (°C)	Sb ₂ Se ₃ (<i>Pbnm</i>)									
	<i>a</i> (Å)	<i>b</i> (Å)	<i>c</i> (Å)	<i>V</i> (Å ³)	Mass fraction (wt.%)	R _{Bragg}	Crystal. size (nm)	microstrain $\Delta d/d$	R _{wp}	
25	11.6246317	11.7654534	3.9744436	543.58092	52.9	2.87	992.198	0.00014	5.47	
50	11.6247838	11.763482	3.9742076	543.46471	56.6	2.20	796.726	0.00015	5.39	
100	11.6241014	11.7636134	3.9736957	543.36886	54.9	2.12	707.885	0.00017	5.23	
150	11.6242444	11.7607040	3.9740667	543.29187	55.1	2.19	894.098	0.00014	5.29	
200	11.6237874	11.7609878	3.9739075	543.26185	54.9	2.09	811.530	0.00015	5.34	
250	11.6227082	11.7592886	3.9735920	543.08981	56.7	2.54	859.091	0.00016	5.61	
300	11.6188047	11.7504977	3.9722419	542.31722	45.4	1.93	309.190	0.00022	4.95	
350	11.6187369	11.7531952	3.9720594	542.41363	10.9	2.41	308.759	0.00013	5.27	

3 - Publications

Table S2: Agreement factors, semi-quantitative phase analysis, cell parameters and averaged microstructure parameters obtained from the Rietveld refinements of the *PDA-Device* set of samples.

Temperature (°C)	Mo (<i>Im$\bar{3}m$</i>)				ITO (<i>Ia$\bar{3}$</i>)				CdSe (<i>Fd$\bar{3}m$</i>)			
	<i>a</i> (Å)	<i>V</i> (Å ³)	Mass fraction (wt.%)	R _{Bragg}	<i>a</i> (Å)	<i>V</i> (Å ³)	Mass fraction (wt.%)	R _{Bragg}	<i>a</i> (Å)	<i>V</i> (Å ³)	Mass fraction (wt.%)	R _{Bragg}
25	3.14575	31.130	37.8	0.49	10.18133	1055.390	3.7	2.16	-	-	-	-
50	3.14579	31.131	37.5	0.47	10.18661	1057.033	4.8	1.69	-	-	-	-
100	3.14517	31.112	42.0	0.41	10.18674	1057.075	4.0	1.57	-	-	-	-
150	3.14548	31.122	41.2	0.45	10.17703	1054.056	3.6	1.81	-	-	-	-
200	3.14528	31.115	37.3	0.42	10.14536	1044.243	14.0	2.17	-	-	-	-
250	3.14564	31.126	27.4	0.54	10.12720	1038.646	26.5	3.03	-	-	-	-
300	3.14527	31.115	30.6	0.46	10.12361	1037.543	26.4	2.94	-	-	-	-
350	3.14546	31.121	29.6	0.47	10.11982	1036.378	26.7	2.90	6.00000	216.000	0.8	3.24

Temperature (°C)	Sb ₂ O ₃ (<i>Fd$\bar{3}m$</i>)				Sb ₂ Se ₃ (<i>Pbnm</i>)							R _{wp}	
	<i>a</i> (Å)	<i>V</i> (Å ³)	Mass fraction (wt.%)	R _{Bragg}	<i>a</i> (Å)	<i>b</i> (Å)	<i>c</i> (Å)	<i>V</i> (Å ³)	Mass fraction (wt.%)	R _{Bragg}	Crystal size (nm)		micro Strain $\Delta d/d$
25	-	-	-	-	11.62458	11.76510	3.97438	543.553	58.4	2.85	693.917	0.00017	5.81
50	-	-	-	-	11.62456	11.76298	3.97428	543.442	57.7	2.07	862.434	0.00017	5.52
100	-	-	-	-	11.62424	11.76393	3.97398	543.428	54.0	2.30	640.426	0.00019	5.28
150	-	-	-	-	11.62454	11.76227	3.97414	543.388	55.2	1.93	702.668	0.00017	5.36
200	-	-	-	-	11.62341	11.76116	3.97374	543.230	48.7	1.93	935.390	0.00018	5.42
250	-	-	-	-	11.62242	11.76262	3.97360	543.231	46.2	2.84	917.331	0.00018	6.42
300	11.14963	1386.056	0.2	2.74	11.62219	11.76364	3.97309	543.199	42.9	2.04	952.668	0.00017	5.96
350	11.14967	1386.073	1.7	1.94	11.61471	11.75451	3.97173	542.242	41.3	3.44	809.280	0.00022	6.23

4 - Conclusions and Outlook

The foremost objective of this thesis was to deepen in the Sb_2Se_3 material and explore its applicability in the PV technology field. Additionally, this thesis was accomplished in the framework of the general objective of the SEMS (IREC) research group line devoted to the development of next generation photovoltaic technologies. In this context, the achievement of functional PV devices with promising power conversion efficiencies up to 5.7 %, permitted to consolidate a research line focused in the comprehension and optimization of the Sb_2Se_3 based devices in the research facilities at IREC with the aim to achieve high efficiency devices able to compete in the research field related to the topic.

The low maturity of the Sb_2Se_3 technology at the time of the start in the research performed in this thesis was reflected in the limited number of literature available and lack of a homogeneous consensus about several aspects, characteristics, or fundamental properties of the material, including device structure. In the framework of the SEMS research group, previous to this thesis, little knowledge was developed before regarding the Sb_2Se_3 material and no functional devices were fabricated beforehand. Therefore, considerable amount of time was dedicated to understand the basic material properties, which combined together with the experience of the SEMS research group in the optimized back and front contacts developed for CZTSSe and CIGSSe technologies, served as a strong starting point and permitted to achieve a fast development of the Sb_2Se_3 PV based devices achieving 5.7 % power conversion efficiency in 4 years.

In the first stages of the thesis a physical characterization of the Sb_2Se_3 material itself was performed in order to properly understand its basic structural properties mainly by means of multi-wavelength Raman spectroscopy and supported XRD characterization, were a direct comparison between a single crystalline sample and one of the first devices synthesized at IREC was performed. In this study we found many misconceptions in the literature regarding the Raman fingerprint of the material, were Raman peaks associated with secondary phases were assigned to Sb_2Se_3 phase, thus leading to errors in the analysis. With this technique 28 of 30 Raman modes were detected, the peaks associated with

4 - Conclusions and Outlook

the most common secondary phases were analysed and the most suitable wavelengths for device quality assessment were proposed. In this stage, the fundamental tools for the characterization of the Sb_2Se_3 layers and devices was established.

In the second stage of the thesis, huge effort was placed in the development of the synthesis route. These optimizations mainly in the reactive annealing lead us to the publication of the second article in where the standard configuration device (SLG/Mo/ Sb_2Se_3 /CdS/i-ZnO/ITO) was studied. The main finding of the article is the relation between selenium content in the film, controlled by temperature in the reactive annealing, and device performance, this was supported by previous DFT studies published in the literature where p-type conductivity is obtained for Se rich films,¹²³ where the decrease in performance for heavily Se rich conditions was afterwards also confirmed by DFT.¹⁷⁸ This allowed us to reach a PCE of 5.7 %, close to the literature values for substrate devices (Table 4) especially in V_{oc} and FF, note that no optimization of the front contact was performed in our samples and a PCE of 6.5 % will be achieved if reflection losses are eliminated. Assessment of the device limitations was performed by means of temperature dependant open circuit voltage (V_{oc} - T) measurements and spectral response analysis, were a clear limitation due to recombination mechanisms mainly dominating in the interfaces of the device. Further exploration, in side experiments, of modifications in the interfaces did not yield any substantial benefit aside for increased homogeneity by pre-synthesis of the MoSe_2 layer. Further work relating this topic should comprehensively study surface treatments to reduce interface recombination as it seems to be the main limiting factor for these kind of devices.

Table 4: Device comparative between this work and literature best performing devices.

Optoelectronic properties	This thesis ¹⁰⁶	Planar substrate record ¹⁶¹	Planar superstrate record ⁹⁸	Technology record (nano-structured) ⁹⁹
J_{sc} [mA/cm ²]	21.9(24.8)*	24.91	24.1	32.6
V_{oc} [mV]	422	504	449	400
FF [%]	61.7	54.47	62.1	70.3
PCE [%]	5.7 (6.5)*	6.84	7.89	9.2

*values in parenthesis account for the values expected if reflexion loss of the window layer is eliminated.

The last period of the thesis has combined the optimization of the process with the study of the stability of the Sb_2Se_3 technology. Specific experiments and characterization were performed related to the thermal stability of the basic structure, optimized in the previous work. High instability was found under low temperature post deposition annealing (PDA) both in the absorber itself and in complete devices. This assessment was possible by the previous generated knowledge on Raman and XRD characteristics of the Sb_2Se_3 material. The system was found to be affected at low temperatures starting from 50 °C where a constriction in the lattice parameters was observed and prolonged until the samples segregated in secondary phases, this constrain in the cell volume affected mainly the short circuit current and the fill factor of the samples. Furthermore, the selenium excess of these samples, beneficial as previously reported, seems to be responsible of this lattice constriction and when the temperature of the PDA is raised over 150 °C it manifests itself by reacting with the CdS buffer layer thus generating $\text{CdS}_{1-x}\text{Se}_x$ phase, with higher concentration of selenium with increasing temperature reaching values of 40 % in the solid solution and completely degrading the heterojunction properties. This is proposed as a major drawback that could lead the technology to a dead end if not corrected properly, due to the low temperatures at which this effect is happening, a range of temperatures at which other subsequent layers could be deposited, including buffer, window or antireflective layers. Further studies must be performed in order to elucidate if this effect could be present in highly stoichiometric devices with a P-i-N structure.

As a final remark, the results achieved in this thesis included the development of a two-step synthesis route and implementation of substrate Sb_2Se_3 technology with photovoltaic grade comparable with the record devices in the literature and has provided to the community the knowledge of the fundamental properties (structural and vibrational). The contribution of this research to the scientific community is reflected in the 23 accumulated citations in high impact factor journals. These results provided to the SEMS research group knew knowledge that allowed to participate in several international conferences and obtain new national and european projects, generating new networks with relevant Sb_2Se_3 research centres. Additionally, currently at IREC 6 new researches have been involved in the Sb_2Se_3 research lines exploring new strategies in the

4 - Conclusions and Outlook

synthesis and optimization of devices with the starting point of this manuscript.

5 - Bibliography

- (1) III, E. B. *The Big Story: Human History, Energy Regimes, and the Environment*. *Univ. Calif. Press* **2008**.
- (2) Noor, D. Shell Says It Has Reached Peak Oil Production. *Gizmodo*. **2021**.
- (3) International Energy Agency. *World Energy Balances 2020 Edition - Database Documentation*. **2020**.
- (4) BP. *Statistical Review of World Energy 69th Edition*. **2020**.
- (5) Gaedicke, C.; Franke, D.; Ladage, S.; Lutz, R.; Pein, M.; Rebscher, D.; Schauer, M.; Schmidt, S.; Goerne, G. von. *BGR Energy Study*; **2019**.
- (6) International Energy Agency. *Understanding the World Energy Outlook Scenarios – Analysis - IEA*. 2019.
- (7) Nuclear Energy Agency. *Nuclear Power in 2019 - NEA Activities by Sector General Information*. **2019**.
- (8) EU Technical Expert Group on Sustainable Finance. *Taxonomy Technical Report*. **2019**, *June* (June), 414.
- (9) Humphrey, U. E.; Khandaker, M. U. Viability of Thorium-Based Nuclear Fuel Cycle for the next Generation Nuclear Reactor: Issues and Prospects. *Renew. Sustain. Energy Rev.* **2018**, *97* (January), 259–275. <https://doi.org/10.1016/j.rser.2018.08.019>.
- (10) Ünak, T. What IS the Potential Use of Thorium in the Future Energy Production Technology? *Prog. Nucl. Energy* **2000**, *37* (1–4), 137–144. [https://doi.org/10.1016/s0149-1970\(00\)00038-x](https://doi.org/10.1016/s0149-1970(00)00038-x).
- (11) Cooper, N.; Minakata, D.; Begovic, M.; Crittenden, J. Should We Consider Using Liquid Fluoride Thorium Reactors for Power Generation? *Environ. Sci. Technol.* **2011**, *45* (15), 6237–6238. <https://doi.org/10.1021/es2021318>.
- (12) ITER. *ITER - the Way to New Energy*. **2013**.
- (13) McGuire, K. M.; Adler, H.; Alling, P.; Ancher, C.; Anderson, H.; Anderson, J. L.; Anderson, J. W.; Arunasalam, V.; Ascione, G.;

Ashcroft, D.; Barnes, C. W.; Barnes, G.; Batha, S.; Bateman, G.; Beer, M.; Bell, M. G.; Bell, R.; Bitter, M.; Blanchard, W.; Bretz, N. L.; Brunkhorst, C.; Budny, R.; Bush, C. E.; Camp, R.; Caorlin, M.; Carnevale, H.; Cauffman, S.; Chang, Z.; Chang, C. S.; Cheng, C. Z.; Chrzanowski, J.; Collins, J.; Coward, G.; Cropper, M.; Darrow, D. S.; Daugert, R.; DeLooper, J.; Dendy, R.; Dorland, W.; Dudek, L.; Duong, H.; Durst, R.; Efthimion, P. C.; Ernst, D.; Evenson, H.; Fisch, N.; Fisher, R.; Fonck, R. J.; Fredd, E.; Fredrickson, E.; Fromm, N.; Fu, G. Y.; Fujita, T.; Furth, H. P.; Garzotto, V.; Gentile, C.; Gilbert, J.; Gioia, J.; Gorelenkov, N.; Grek, B.; Grisham, L. R.; Hammett, G.; Hanson, G. R.; Hawryluk, R. J.; Heidbrink, W.; Herrmann, H. W.; Hill, K. W.; Hosea, J.; Hsuan, H.; Hughes, M.; Hulse, R.; Janos, A.; Jassby, D. L.; Jobes, F. C.; Johnson, D. W.; Johnson, L. C.; Kalish, M.; Kamperschroer, J.; Kesner, J.; Kugel, H.; Labik, G.; Lam, N. T.; LaMarche, P. H.; Lawson, E.; LeBlanc, B.; Levine, J.; Levinton, F. M.; Loesser, D.; Long, D.; Loughlin, M. J.; Machuzak, J.; Majeski, R.; Mansfield, D. K.; Marmor, E. S.; Marsala, R.; Martin, A.; Martin, G.; Mazzucato, E.; Mauel, M.; McCarthy, M. P.; McChesney, J.; McCormack, B.; McCune, D. C.; McKee, G.; Meade, D. M.; Medley, S. S.; Mikkelsen, D. R.; Mirnov, S. V.; Mueller, D.; Murakami, M.; Murphy, J. A.; Nagy, A.; Navratil, G. A.; Nazikian, R.; Newman, R.; Norris, M.; O'Connor, T.; Oldaker, M.; Ongena, J.; Osakabe, M.; Owens, D. K.; Park, H.; Park, W.; Parks, P.; Paul, S. F.; Pearson, G.; Perry, E.; Persing, R.; Petrov, M.; Phillips, C. K.; Phillips, M.; Pitcher, S.; Pysher, R.; Qualls, A. L.; Raftopoulos, S.; Ramakrishnan, S.; Ramsey, A.; Rasmussen, D. A.; Redi, M. H.; Renda, G.; Rewoldt, G.; Roberts, D.; Rogers, J.; Rossmassler, R.; Roquemore, A. L.; Ruskov, E.; Sabbagh, S. A.; Sasao, M.; Schilling, G.; Schivell, J.; Schmidt, G. L.; Scillia, R.; Scott, S. D.; Semenov, I.; Senko, T.; Sesnic, S.; Sissingh, R.; Skinner, C. H.; Snipes, J.; Stencel, J.; Stevens, J.; Stevenson, T.; Stratton, B. C.; Strachan, J. D.; Stodiek, W.; Swanson, J.; Synakowski, E.; Takahashi, H.; Tang, W.; Taylor, G.; Terry, J.; Thompson, M. E.; Tighe, W.; Timberlake, J. R.; Tobita, K.; Towner, H. H.; Tuszewski, M.; von Halle, A.; Vannoy, C.; Viola, M.; von Goeler, S.; Voorhees, D.; Walters, R. T.; Wester, R.; White, R.; Wieland, R.; Wilgen, J. B.; Williams, M.; Wilson, J. R.; Winston, J.; Wright, K.; Wong, K. L.; Woskov, P.; Wurden, G. A.; Yamada, M.; Yoshikawa, S.; Young, K. M.; Zarnstorff, M. C.;

- Zavereev, V.; Zweben, S. J. Review of Deuterium–Tritium Results from the Tokamak Fusion Test Reactor. *Phys. Plasmas* **1995**, *2* (6), 2176–2188. <https://doi.org/10.1063/1.871303>.
- (14) Antunes, R. Tritium: A Challenging Fuel for Fusion - EUROfusion. **2019**.
- (15) García-Olivares, A.; Ballabrera-Poy, J.; García-Ladona, E.; Turiel, A. A Global Renewable Mix with Proven Technologies and Common Materials. *Energy Policy* **2012**, *41*, 561–574. <https://doi.org/10.1016/j.enpol.2011.11.018>.
- (16) Jacobson, M. Z.; Delucchi, M. A.; Cameron, M. A.; Mathiesen, B. V. Matching Demand with Supply at Low Cost in 139 Countries among 20 World Regions with 100% Intermittent Wind, Water, and Sunlight (WWS) for All Purposes. *Renew. Energy* **2018**, *123*, 236–248. <https://doi.org/10.1016/j.renene.2018.02.009>.
- (17) Connolly, D.; Vad Mathiesen, B. A Technical and Economic Analysis of One Potential Pathway to a 100 % Renewable Energy System. *Int. J. Sustain. Energy Plan. Manag.* **2014**, *01* (0), 7–28. <https://doi.org/10.5278/ijsepm.2014.1.2>.
- (18) Manish Ram, Dmitrii Bogdanov, A.; Aghahosseini, Solomon Oyewo, A.; Gulagi, M. C. and C. B. *Global Energy System Based on 100% Renewable Energy - Power Sector*; **2017**.
- (19) Gils, H. C.; Scholz, Y.; Pregger, T.; Luca de Tena, D.; Heide, D. Integrated Modelling of Variable Renewable Energy-Based Power Supply in Europe. *Energy* **2017**, *123*, 173–188. <https://doi.org/10.1016/j.energy.2017.01.115>.
- (20) Cornel, P. International Grid Integration: Efficiencies, Vulnerabilities, and Strategic Implications in Asia - Atlantic Council. **2020**.
- (21) Ramanujam, J.; Bishop, D. M.; Todorov, T. K.; Gunawan, O.; Rath, J.; Nekovei, R.; Artegiani, E.; Romeo, A. Flexible CIGS, CdTe and a-Si:H Based Thin Film Solar Cells: A Review. *Prog. Mater. Sci.* **2020**, *110* (November 2019), 100619. <https://doi.org/10.1016/j.pmatsci.2019.100619>.
- (22) Ghosh, A. Potential of Building Integrated and Attached/Applied Photovoltaic (BIPV/BAPV) for Adaptive Less Energy-Hungry

- Building's Skin: A Comprehensive Review. *J. Clean. Prod.* **2020**, 276, 123343. <https://doi.org/10.1016/j.jclepro.2020.123343>.
- (23) Bogue, R. Solar-Powered Sensors: A Review of Products and Applications. *Sens. Rev.* **2012**, 32 (2), 95–100. <https://doi.org/10.1108/02602281211209374>.
- (24) Li, K.; Li, F.; Chen, C.; Jiang, P.; Lu, S.; Wang, S.; Lu, Y.; Tu, G.; Guo, J.; Shui, L.; Liu, Z.; Song, B.; Tang, J. One-Dimensional Sb₂Se₃ Enabling Ultra-Flexible Solar Cells and Mini-Modules for IoT Applications. *Nano Energy* **2021**, 86 (April), 106101. <https://doi.org/10.1016/j.nanoen.2021.106101>.
- (25) Lester, L. F.; Yang, K.; El-Emawy, M. A.; Saiz, T.; Clark, R. A.; Hollowell, A.; Lavrova, O. Flexible Solar Cells for Micro-Autonomous Systems Technology. In *Micro- and Nanotechnology Sensors, Systems, and Applications II*; George, T., Islam, M. S., Dutta, A. K., Eds.; 2010; Vol. 7679, p 76790Y. <https://doi.org/10.1117/12.852598>.
- (26) IEA (2020), Global Energy Review 2020, IEA, Paris <https://www.iea.org/reports/global-energy-review-2020>.
- (27) Jäger-Waldau, A. Snapshot of Photovoltaics—February 2020. *Energies* **2020**, 13 (4), 930. <https://doi.org/10.3390/en13040930>.
- (28) IEA. Distributed Solar PV – Renewables 2019 – Analysis - IEA. *International Energy Agency.* **2019**.
- (29) Jaeger, C. Limits to Growth. In *Encyclopedia of Ecology*; Elsevier, 2008; pp 367–369. <https://doi.org/10.1016/B978-0-444-63768-0.00630-2>.
- (30) Fritts, C. E. On a New Form of Selenium Cell, and Some Electrical Discoveries Made by Its Use. *Am. J. Sci.* **1883**, s3-26 (156), 465–472. <https://doi.org/10.2475/ajs.s3-26.156.465>.
- (31) Einstein, A. Über Einen Die Erzeugung Und Verwandlung Des Lichtes Betreffenden Heuristischen Gesichtspunkt. *Ann. Phys.* **1905**, 322 (6), 132–148. <https://doi.org/10.1002/andp.19053220607>.
- (32) Chapin, D. M.; Fuller, C. S.; Pearson, G. L. A New Silicon P-n Junction Photocell for Converting Solar Radiation into Electrical

- Power. *J. Appl. Phys.* **1954**, 25 (5), 676–677.
<https://doi.org/10.1063/1.1721711>.
- (33) Fraunhofer Institute for Solar Energy Systems. Photovoltaics Report. **2021**, No. July.
- (34) Czochralski Method - Wikipedia.
- (35) Tiedje, T.; Yablonovitch, E.; Cody, G. D.; Brooks, B. G. Limiting Efficiency of Silicon Solar Cells. *IEEE Trans. Electron Devices* **1984**, 31 (5), 711–716. <https://doi.org/10.1109/T-ED.1984.21594>.
- (36) Harbeke, G.; Krausbauer, L.; Steigmeier, E. F.; Widmer, A. E.; Kappert, H. F.; Neugebauer, G. Growth and Physical Properties of LPCVD Polycrystalline Silicon Films. *J. Electrochem. Soc.* **1984**, 131 (3), 675–682. <https://doi.org/10.1149/1.2115672>.
- (37) Green, M. A. Limits on the Open-Circuit Voltage and Efficiency of Silicon Solar Cells Imposed by Intrinsic Auger Processes. *IEEE Trans. Electron Devices* **1984**, 31 (5), 671–678.
<https://doi.org/10.1109/T-ED.1984.21588>.
- (38) Andreani, L. C.; Bozzola, A.; Kowalczewski, P.; Liscidini, M.; Redorici, L. Silicon Solar Cells: Toward the Efficiency Limits. *Adv. Phys. X* **2019**, 4 (1).
<https://doi.org/10.1080/23746149.2018.1548305>.
- (39) Yoshikawa, K.; Kawasaki, H.; Yoshida, W.; Irie, T.; Konishi, K.; Nakano, K.; Uto, T.; Adachi, D.; Kanematsu, M.; Uzu, H.; Yamamoto, K. Silicon Heterojunction Solar Cell with Interdigitated Back Contacts for a Photoconversion Efficiency over 26%. *Nat. Energy* **2017**, 2 (5), 17032.
<https://doi.org/10.1038/nenergy.2017.32>.
- (40) Saga, T. Advances in Crystalline Silicon Solar Cell Technology for Industrial Mass Production. *NPG Asia Mater.* **2010**, 2 (3), 96–102. <https://doi.org/10.1038/asiamat.2010.82>.
- (41) Reinhard, P.; Chirila, A.; Pianezzi, F.; Nishiwaki, S.; Buecheler, S.; Tiwari, A. N. High Efficiency Flexible Cu(In,Ga)Se₂ Solar Cells. *2013 Twent. Int. Work. Act. Flatpanel Displays Devices* **2013**, 79–82.
- (42) Chirilă, A.; Reinhard, P.; Pianezzi, F.; Bloesch, P.; Uhl, A. R.;

- Fella, C.; Kranz, L.; Keller, D.; Gretener, C.; Hagendorfer, H.; Jaeger, D.; Erni, R.; Nishiwaki, S.; Buecheler, S.; Tiwari, A. N. Potassium-Induced Surface Modification of Cu(In,Ga)Se₂ Thin Films for High-Efficiency Solar Cells. *Nat. Mater.* **2013**, *12* (12), 1107–1111. <https://doi.org/10.1038/nmat3789>.
- (43) Kaczynski, R.; Lee, J.; Alsburg, J. Van; Sang, B.; Schoop, U.; Britt, J. In-Line Potassium Fluoride Treatment of CIGS Absorbers Deposited on Flexible Substrates in a Production-Scale Process Tool. **2017**, 1455–1458.
- (44) Mahabaduge, H. P.; Rance, W. L.; Burst, J. M.; Reese, M. O.; Meysing, D. M.; Wolden, C. A.; Li, J.; Beach, J. D.; Gessert, T. A.; Metzger, W. K.; Garner, S.; Barnes, T. M. High-Efficiency, Flexible CdTe Solar Cells on Ultra-Thin Glass Substrates. *Appl. Phys. Lett.* **2015**, *106* (13), 133501. <https://doi.org/10.1063/1.4916634>.
- (45) Kranz, L.; Gretener, C.; Perrenoud, J.; Schmitt, R.; Pianezzi, F.; La Mattina, F.; Blösch, P.; Cheah, E.; Chirilă, A.; Fella, C. M.; Hagendorfer, H.; Jäger, T.; Nishiwaki, S.; Uhl, A. R.; Buecheler, S.; Tiwari, A. N. Doping of Polycrystalline CdTe for High-Efficiency Solar Cells on Flexible Metal Foil. *Nat. Commun.* **2013**, *4*. <https://doi.org/10.1038/ncomms3306>.
- (46) Yan, B.; Yue, G.; Sivec, L.; Yang, J.; Guha, S.; Jiang, C.-S. Innovative Dual Function Nc-SiO_x:H Layer Leading to a >16% Efficient Multi-Junction Thin-Film Silicon Solar Cell. *Appl. Phys. Lett.* **2011**, *99* (11), 113512. <https://doi.org/10.1063/1.3638068>.
- (47) Miles, R. W.; Zoppi, G.; Forbes, I. Inorganic Photovoltaic Cells. *Mater. Today* **2007**, *10* (11), 20–27. [https://doi.org/10.1016/S1369-7021\(07\)70275-4](https://doi.org/10.1016/S1369-7021(07)70275-4).
- (48) Tawada, Y.; Kondo, M.; Okamoto, H.; Hamakawa, Y. Hydrogenated Amorphous Silicon Carbide as a Window Material for High Efficiency A-Si Solar Cells. *Sol. Energy Mater.* **1982**, *6* (3), 299–315. [https://doi.org/10.1016/0165-1633\(82\)90036-3](https://doi.org/10.1016/0165-1633(82)90036-3).
- (49) Tawada, Y.; Tsuge, K.; Kondo, M.; Okamoto, H.; Hamakawa, Y. Properties and Structure of a -SiC:H for High-efficiency a -Si Solar Cell. *J. Appl. Phys.* **1982**, *53* (7), 5273–5281. <https://doi.org/10.1063/1.331363>.

- (50) Kim, S.; Chung, J.-W.; Lee, H.; Park, J.; Heo, Y.; Lee, H.-M. Remarkable Progress in Thin-Film Silicon Solar Cells Using High-Efficiency Triple-Junction Technology. *Sol. Energy Mater. Sol. Cells* **2013**, *119*, 26–35.
<https://doi.org/10.1016/j.solmat.2013.04.016>.
- (51) Sai, H.; Matsui, T.; Koida, T.; Matsubara, K.; Kondo, M.; Sugiyama, S.; Katayama, H.; Takeuchi, Y.; Yoshida, I. Triple-Junction Thin-Film Silicon Solar Cell Fabricated on Periodically Textured Substrate with a Stabilized Efficiency of 13.6%. *Appl. Phys. Lett.* **2015**, *106* (21), 213902.
<https://doi.org/10.1063/1.4921794>.
- (52) Shah, A. Amorphous Silicon Solar Cells. In *Springer Series in Materials Science*; **2020**; Vol. 301, pp 139–161.
https://doi.org/10.1007/978-3-030-46487-5_6.
- (53) Guo, L.; Zhang, B.; Ranjit, S.; Wall, J.; Saurav, S.; Hauser, A. J.; Xing, G.; Li, L.; Qian, X.; Yan, F. Interface Engineering via Sputtered Oxygenated CdS:O Window Layer for Highly Efficient Sb₂Se₃ Thin-Film Solar Cells with Efficiency Above 7%. *Sol. RRL* **2019**, *3* (10), 1900225.
<https://doi.org/10.1002/solr.201900225>.
- (54) Guo, L.; Grice, C.; Zhang, B.; Xing, S.; Li, L.; Qian, X.; Yan, F. Improved Stability and Efficiency of CdSe/Sb₂Se₃ Thin-Film Solar Cells. *Sol. Energy* **2019**, *188*, 586–592.
<https://doi.org/10.1016/j.solener.2019.06.042>.
- (55) Khairnar, U. P.; Bhavsar, D. S.; Vaidya, R. U.; Bhavsar, G. P. Optical Properties of Thermally Evaporated Cadmium Telluride Thin Films. *Mater. Chem. Phys.* **2003**, *80* (2), 421–427.
[https://doi.org/10.1016/S0254-0584\(02\)00336-X](https://doi.org/10.1016/S0254-0584(02)00336-X).
- (56) Mitchell, K. W.; Fahrenbruch, A. L.; Bube, R. H. Evaluation of the CdS/CdTe Heterojunction Solar Cell. *J. Appl. Phys.* **1977**, *48* (10), 4365–4371. <https://doi.org/10.1063/1.323429>.
- (57) Romeo, N.; Bosio, A.; Tedeschi, R.; Romeo, A.; Canevari, V. A Highly Efficient and Stable CdTe/CdS Thin Film Solar Cell. *Sol. Energy Mater. Sol. Cells* **1999**, *58* (2), 209–218.
[https://doi.org/10.1016/S0927-0248\(98\)00204-9](https://doi.org/10.1016/S0927-0248(98)00204-9).

- (58) Chu, T. L.; Chu, S. S. High Efficiency Thin Film CdS/CdTe Solar Cells. *Int. J. Sol. Energy* **1992**, *12* (1–4), 121–132. <https://doi.org/10.1080/01425919208909755>.
- (59) Britt, J.; Ferekides, C. Thin-film CdS/CdTe Solar Cell with 15.8% Efficiency. *Appl. Phys. Lett.* **1993**, *62* (22), 2851–2852. <https://doi.org/10.1063/1.109629>.
- (60) Romeo, N.; Bosio, A.; Romeo, A. An Innovative Process Suitable to Produce High-Efficiency CdTe/CdS Thin-Film Modules. *Sol. Energy Mater. Sol. Cells* **2010**, *94* (1), 2–7. <https://doi.org/10.1016/j.solmat.2009.06.001>.
- (61) Solar, F. First Solar Achieves Yet Another Cell Conversion Efficiency World Record. **2016**, pp 1–4.
- (62) Bekaert, J.; Saniz, R.; Partoens, B.; Lamoen, D. Native Point Defects in $\text{CuIn}_{1-x}\text{Ga}_x\text{Se}_2$: Hybrid Density Functional Calculations Predict the Origin of p- and n-Type Conductivity. *Phys. Chem. Chem. Phys.* **2014**, *16* (40), 22299–22308. <https://doi.org/10.1039/C4CP02870H>.
- (63) Duclaux, L.; Donsanti, F.; Vidal, J.; Bouttemy, M.; Schneider, N.; Naghavi, N. Simulation and Growing Study of Cu–Al–S Thin Films Deposited by Atomic Layer Deposition. *Thin Solid Films* **2015**, *594*, 232–237. <https://doi.org/10.1016/j.tsf.2015.06.014>.
- (64) Castellanos Águila, J. E.; Palacios, P.; Conesa, J. C.; Arriaga, J.; Wahnón, P. Theoretical Band Alignment in an Intermediate Band Chalcopyrite Based Material. *Appl. Surf. Sci.* **2017**, *424*, 132–136. <https://doi.org/10.1016/j.apsusc.2016.12.237>.
- (65) Jehad AbuShama; Noufi, R.; Johnston, S.; Ward, S.; Wu, X. Improved Performance in CuInSe_2 and Surface-Modified CuGaSe_2 Solar Cells. In *Conference Record of the Thirty-first IEEE Photovoltaic Specialists Conference, 2005.*; IEEE, **2001**; Vol. 91, pp 299–302. <https://doi.org/10.1109/PVSC.2005.1488128>.
- (66) Stolt, L.; Hedström, J.; Kessler, J.; Ruckh, M.; Velthaus, K.; Schock, H. ZnO/CdS/CuInSe_2 Thin-film Solar Cells with Improved Performance. *Appl. Phys. Lett.* **1993**, *62* (6), 597–599. <https://doi.org/10.1063/1.108867>.

- (67) Sun, Y.; Lin, S.; Li, W.; Cheng, S.; Zhang, Y.; Liu, Y.; Liu, W. Review on Alkali Element Doping in Cu(In,Ga)Se₂ Thin Films and Solar Cells. *Engineering* **2017**, *3* (4), 452–459. <https://doi.org/10.1016/J.ENG.2017.04.020>.
- (68) Braunger, D.; Hariskos, D.; Bilger, G.; Rau, U.; Schock, H. W. Influence of Sodium on the Growth of Polycrystalline Cu(In,Ga)Se₂ Thin Films. *Thin Solid Films* **2000**, *361*, 161–166. [https://doi.org/10.1016/S0040-6090\(99\)00777-4](https://doi.org/10.1016/S0040-6090(99)00777-4).
- (69) Contreras, M. A.; Romero, M. J.; Noufi, R. Characterization of Cu(In,Ga)Se₂ Materials Used in Record Performance Solar Cells. *Thin Solid Films* **2006**, *511–512*, 51–54. <https://doi.org/10.1016/j.tsf.2005.11.097>.
- (70) Devaney, W. E.; Chen, W. S.; Stewart, J. M.; Mickelsen, R. A. Structure and Properties of High Efficiency ZnO/CdZnS/CuInGaSe₂ Solar Cells. *IEEE Trans. Electron Devices* **1990**, *37* (2), 428–433. <https://doi.org/10.1109/16.46378>.
- (71) Nakamura, M.; Yamaguchi, K.; Kimoto, Y.; Yasaki, Y.; Kato, T.; Sugimoto, H. Cd-Free Cu(In,Ga)(Se,S)₂ Thin-Film Solar Cell With Record Efficiency of 23.35%. *IEEE J. Photovoltaics* **2019**, *9* (6), 1863–1867. <https://doi.org/10.1109/JPHOTOV.2019.2937218>.
- (72) Izquierdo-Roca, V.; Fontañ, X.; Álvarez-García, J.; Calvo-Barrio, L.; Pérez-Rodríguez, A.; Morante, J. R.; Ruiz, C. M.; Saucedo, E.; Bermúdez, V. Electrochemical Synthesis of CuIn(S,Se)₂ Alloys with Graded Composition for High Efficiency Solar Cells. *Appl. Phys. Lett.* **2009**, *94* (6), 10–13. <https://doi.org/10.1063/1.3080654>.
- (73) Gloeckler, M.; Sites, J. R. Band-Gap Grading in Cu(In,Ga)Se₂ Solar Cells. *J. Phys. Chem. Solids* **2005**, *66* (11), 1891–1894. <https://doi.org/10.1016/j.jpcs.2005.09.087>.
- (74) Gian Andrea Blengini, Cynthia EL Latunussa, Umberto Eynard, Cristina Torres de Matos, Dominic Wittmer, Konstantinos Georgitzikis, Claudiu Pavel, Samuel Carrara, Lucia Mancini, Manuela Unguru, Darina Blagoeva, Fabrice Mathieux, D. P. *Study on the EU 's List of Critical Raw Materials*; 2020. <https://doi.org/10.2873/11619>.
- (75) Giraldo, S.; Neuschitzer, M.; Thersleff, T.; López-Marino, S.;

- Sánchez, Y.; Xie, H.; Colina, M.; Placidi, M.; Pistor, P.; Izquierdo-Roca, V.; Leifer, K.; Pérez-Rodríguez, A.; Saucedo, E. Large Efficiency Improvement in Cu₂ZnSnSe₄ Solar Cells by Introducing a Superficial Ge Nanolayer. *Adv. Energy Mater.* **2015**, *5* (21), 1501070. <https://doi.org/10.1002/aenm.201501070>.
- (76) Kim, J.; Hiroi, H.; Todorov, T. K.; Gunawan, O.; Kuwahara, M.; Gokmen, T.; Nair, D.; Hopstaken, M.; Shin, B.; Lee, Y. S.; Wang, W.; Sugimoto, H.; Mitzi, D. B. High Efficiency Cu₂ZnSn(S,Se)₄ Solar Cells by Applying a Double In₂S₃/CdS Emitter. *Adv. Mater.* **2014**, *26* (44), 7427–7431. <https://doi.org/10.1002/adma.201402373>.
- (77) Wang, Y. P.; Levenco, S.; Dumcenco, D. O.; Huang, Y. S.; Ho, C. H.; Tiong, K. K. Composition Dependent Band Gaps of Single Crystal Cu₂ZnSn(S_xSe_{1-x})₄ Solid Solutions. *Solid State Phenom.* **2013**, *194* (May 2014), 139–143. <https://doi.org/10.4028/www.scientific.net/SSP.194.139>.
- (78) Andrade-Arvizu, J.; Izquierdo-Roca, V.; Becerril-Romero, I.; Vidal-Fuentes, P.; Fonoll-Rubio, R.; Sánchez, Y.; Placidi, M.; Calvo-Barrio, L.; Vigil-Galán, O.; Saucedo, E. Is It Possible to Develop Complex S-Se Graded Band Gap Profiles in Kesterite-Based Solar Cells? *ACS Appl. Mater. Interfaces* **2019**, *11* (36). <https://doi.org/10.1021/acsami.9b09813>.
- (79) SEOL, J.; LEE, S.; LEE, J.; NAM, H.; KIM, K. Electrical and Optical Properties of CuZnSnS Thin Films Prepared by Rf Magnetron Sputtering Process. *Sol. Energy Mater. Sol. Cells* **2003**, *75* (1–2), 155–162. [https://doi.org/10.1016/S0927-0248\(02\)00127-7](https://doi.org/10.1016/S0927-0248(02)00127-7).
- (80) Repins, I.; Mansfield, L.; Kanevce, A.; Jensen, S. A.; Kuciauskas, D.; Glynn, S.; Barnes, T.; Metzger, W.; Burst, J.; Jiang, C.-S.; Dippo, P.; Harvey, S.; Teeter, G.; Perkins, C.; Egaas, B.; Zakutayev, A.; Alsmeier, J.-H.; Lusk, T.; Korte, L.; Wilks, R. G.; Bar, M.; Yan, Y.; Lany, S.; Zawadzki, P.; Park, J.-S.; Wei, S. Wild Band Edges: The Role of Bandgap Grading and Band-Edge Fluctuations in High-Efficiency Chalcogenide Devices. In *2016 IEEE 43rd Photovoltaic Specialists Conference (PVSC)*; IEEE, **2016**; Vol. 2016-Novem, pp 0309–0314. <https://doi.org/10.1109/PVSC.2016.7749600>.

- (81) Schorr, S.; Gurieva, G.; Guc, M.; Dimitrievska, M.; Pérez-Rodríguez, A.; Izquierdo-Roca, V.; Schnohr, C. S.; Kim, J.; Jo, W.; Merino, J. M. Point Defects, Compositional Fluctuations, and Secondary Phases in Non-Stoichiometric Kesterites. *J. Phys. Energy* **2019**, 2 (1), 012002. <https://doi.org/10.1088/2515-7655/ab4a25>.
- (82) Kumar, M.; Dubey, A.; Adhikari, N.; Venkatesan, S.; Qiao, Q. Strategic Review of Secondary Phases, Defects and Defect-Complexes in Kesterite CZTS–Se Solar Cells. *Energy Environ. Sci.* **2015**, 8 (11), 3134–3159. <https://doi.org/10.1039/C5EE02153G>.
- (83) Kim, S.-Y.; Son, D.; Kim, Y.-I.; Kim, S.-H.; Kim, S.; Ahn, K.; Sung, S.; Hwang, D.; Yang, K.; Kang, J.; Kim, D. Void and Secondary Phase Formation Mechanisms of CZTSSe Using Sn/Cu/Zn/Mo Stacked Elemental Precursors. *Nano Energy* **2019**, 59 (December 2018), 399–411. <https://doi.org/10.1016/j.nanoen.2019.02.063>.
- (84) Fonoll-Rubio, R.; Andrade-Arvizu, J.; Blanco-Portals, J.; Becerril-Romero, I.; Guc, M.; Saucedo, E.; Peiró, F.; Calvo-Barrio, L.; Ritzer, M.; Schnohr, C. S.; Placidi, M.; Estradé, S.; Izquierdo-Roca, V.; Pérez-Rodríguez, A. Insights into Interface and Bulk Defects in a High Efficiency Kesterite-Based Device. *Energy Environ. Sci.* **2021**, 14 (1), 507–523. <https://doi.org/10.1039/D0EE02004D>.
- (85) Saucedo, S. E. As Featured in : Energy & Environmental Science Pathways and Crystallization of Kesterites. **2018**. <https://doi.org/10.1039/C7EE02318A>.
- (86) Dimitrievska, M.; Oliva, F.; Guc, M.; Giraldo, S.; Saucedo, E.; Pérez-Rodríguez, A.; Izquierdo-Roca, V. Defect Characterisation in Cu₂ZnSnSe₄ Kesterites via Resonance Raman Spectroscopy and the Impact on Optoelectronic Solar Cell Properties. *J. Mater. Chem. A* **2019**, 7 (21), 13293–13304. <https://doi.org/10.1039/C9TA03625C>.
- (87) Dimitrievska, M.; Gurieva, G.; Xie, H.; Carrete, A.; Cabot, A.; Saucedo, E.; Pérez-Rodríguez, A.; Schorr, S.; Izquierdo-Roca, V. Raman Scattering Quantitative Analysis of the Anion Chemical Composition in Kesterite Cu₂ZnSn(S_xSe_{1-x})₄ Solid Solutions. *J.*

- Alloys Compd.* **2015**, 628, 464–470.
<https://doi.org/10.1016/j.jallcom.2014.12.175>.
- (88) Son, D.-H.; Kim, S.-H.; Kim, S.-Y.; Kim, Y.-I.; Sim, J.-H.; Park, S.-N.; Jeon, D.-H.; Hwang, D.-K.; Sung, S.-J.; Kang, J.-K.; Yang, K.-J.; Kim, D.-H. Effect of Solid-H₂S Gas Reactions on CZTSSe Thin Film Growth and Photovoltaic Properties of a 12.62% Efficiency Device. *J. Mater. Chem. A* **2019**, 7 (44), 25279–25289.
<https://doi.org/10.1039/C9TA08310C>.
- (89) Giraldo, S.; Jehl, Z.; Placidi, M.; Izquierdo-Roca, V.; Pérez-Rodríguez, A.; Saucedo, E. Progress and Perspectives of Thin Film Kesterite Photovoltaic Technology: A Critical Review. *Adv. Mater.* **2019**, 31 (16), 1806692.
<https://doi.org/10.1002/adma.201806692>.
- (90) Green, M.; Dunlop, E.; Hohl-Ebinger, J.; Yoshita, M.; Kopidakis, N.; Hao, X. Solar Cell Efficiency Tables (Version 57). *Prog. Photovoltaics Res. Appl.* **2021**, 29 (1), 3–15.
<https://doi.org/10.1002/pip.3371>.
- (91) NREL. <https://www.nrel.gov/pv/cell-efficiency.html>. 2020, p 1.
- (92) Sugimoto, H. High Efficiency and Large Volume Production of CIS-Based Modules. In *2014 IEEE 40th Photovoltaic Specialist Conference (PVSC)*; IEEE, **2014**; pp 2767–2770.
<https://doi.org/10.1109/PVSC.2014.6925503>.
- (93) Cashmore, J. S.; Apolloni, M.; Braga, A.; Caglar, O.; Cervetto, V.; Fenner, Y.; Goldbach-Aschemann, S.; Goury, C.; Hötzel, J. E.; Iwahashi, T.; Kalas, J.; Kitamura, M.; Klindworth, M.; Kupich, M.; Leu, G.-F.; Lin, J.; Lindic, M.-H.; Losio, P. A.; Mates, T.; Matsunaga, D.; Mereu, B.; Nguyen, X.-V.; Psimoulis, I.; Ristau, S.; Roschek, T.; Salabas, A.; Salabas, E. L.; Sinicco, I. Improved Conversion Efficiencies of Thin-Film Silicon Tandem (MICROMORPHTM) Photovoltaic Modules. *Sol. Energy Mater. Sol. Cells* **2016**, 144, 84–95.
<https://doi.org/10.1016/j.solmat.2015.08.022>.
- (94) Zhou, Y.; Leng, M.; Xia, Z.; Zhong, J.; Song, H.; Liu, X.; Yang, B.; Zhang, J.; Chen, J.; Zhou, K.; Han, J.; Cheng, Y.; Tang, J. Solution-Processed Antimony Selenide Heterojunction Solar Cells.

- Adv. Energy Mater.* **2014**, *4* (8), 1301846.
<https://doi.org/10.1002/aenm.201301846>.
- (95) Froehlicher, G.; Lorchat, E.; Zill, O.; Romeo, M.; Berciaud, S. Rigid-Layer Raman-Active Modes in N-Layer Transition Metal Dichalcogenides: Interlayer Force Constants and Hyperspectral Raman Imaging. *J. Raman Spectrosc.* **2018**, *49* (1), 91–99.
<https://doi.org/10.1002/jrs.5236>.
- (96) Bhattacharya, R. N.; Pramanik, P. A Photoelectrochemical Cell Based on Chemically Deposited Sb₂Se₃ Thin Film Electrode and Dependence of Deposition on Various Parameters. *Sol. Energy Mater.* **1982**, *6* (3), 317–322. [https://doi.org/10.1016/0165-1633\(82\)90037-5](https://doi.org/10.1016/0165-1633(82)90037-5).
- (97) Choi, Y. C.; Mandal, T. N.; Yang, W. S.; Lee, Y. H.; Im, S. H.; Noh, J. H.; Seok, S. Il. Sb₂Se₃-Sensitized Inorganic-Organic Heterojunction Solar Cells Fabricated Using a Single-Source Precursor. *Angew. Chemie* **2014**, *126* (5), 1353–1357.
<https://doi.org/10.1002/ange.201308331>.
- (98) Liu, D.; Tang, R.; Ma, Y.; Jiang, C.; Lian, W.; Li, G.; Han, W.; Zhu, C.; Chen, T. Direct Hydrothermal Deposition of Antimony Triselenide Films for Efficient Planar Heterojunction Solar Cells. *ACS Appl. Mater. Interfaces* **2021**, *13* (16), 18856–18864.
<https://doi.org/10.1021/acsami.1c02393>.
- (99) Li, Z.; Liang, X.; Li, G.; Liu, H.; Zhang, H.; Guo, J.; Chen, J.; Shen, K.; San, X.; Yu, W.; Schropp, R. E. I.; Mai, Y. 9.2%-Efficient Core-Shell Structured Antimony Selenide Nanorod Array Solar Cells. *Nat. Commun.* **2019**, *10* (1), 125.
<https://doi.org/10.1038/s41467-018-07903-6>.
- (100) Mavlonov, A.; Razykov, T.; Raziq, F.; Gan, J.; Chantana, J.; Kawano, Y.; Nishimura, T.; Wei, H.; Zakutayev, A.; Minemoto, T.; Zu, X.; Li, S.; Qiao, L. A Review of Sb₂Se₃ Photovoltaic Absorber Materials and Thin-Film Solar Cells. *Sol. Energy* **2020**, *201* (February), 227–246.
<https://doi.org/10.1016/j.solener.2020.03.009>.
- (101) Wang, X.; Tang, R.; Jiang, C.; Lian, W.; Ju, H.; Jiang, G.; Li, Z.; Zhu, C.; Chen, T. Manipulating the Electrical Properties of Sb₂(S,Se)₃ Film for High-Efficiency Solar Cell. *Adv. Energy Mater.*

- 2020**, *10* (40), 2002341. <https://doi.org/10.1002/aenm.202002341>.
- (102) Tang, R.; Wang, X.; Lian, W.; Huang, J.; Wei, Q.; Huang, M.; Yin, Y.; Jiang, C.; Yang, S.; Xing, G.; Chen, S.; Zhu, C.; Hao, X.; Green, M. A.; Chen, T. Hydrothermal Deposition of Antimony Selenosulfide Thin Films Enables Solar Cells with 10% Efficiency. *Nat. Energy* **2020**. <https://doi.org/10.1038/s41560-020-0652-3>.
- (103) Han, W.; Gao, D.; Tang, R.; Ma, Y.; Jiang, C.; Li, G.; Chen, T.; Zhu, C. Efficient Sb₂(S,Se)₃ Solar Modules Enabled by Hydrothermal Deposition. *Sol. RRL* **2021**, *2*, 2000750. <https://doi.org/10.1002/solr.202000750>.
- (104) Liu, X.; Chen, J.; Luo, M.; Leng, M.; Xia, Z.; Zhou, Y.; Qin, S.; Xue, D.-J.; Lv, L.; Huang, H.; Niu, D.; Tang, J. Thermal Evaporation and Characterization of Sb₂Se₃ Thin Film for Substrate Sb₂Se₃/CdS Solar Cells. *ACS Appl. Mater. Interfaces* **2014**, *6* (13), 10687–10695. <https://doi.org/10.1021/am502427s>.
- (105) Ghosh, G.; Olesinski, R. W.; Abbaschian, G. J.; Diagrams, A. P. Sb (Antimony) Binary Alloy Phase Diagrams. In *Alloy Phase Diagrams*; ASM International, 2016; Vol. 6, pp 585–590. <https://doi.org/10.31399/asm.hb.v03.a0006202>.
- (106) Vidal-Fuentes, P.; Placidi, M.; Sánchez, Y.; Becerril-Romero, I.; Andrade-Arvizu, J.; Jehl, Z.; Pérez-Rodríguez, A.; Izquierdo-Roca, V.; Saucedo, E. Efficient Se-Rich Sb₂Se₃/CdS Planar Heterojunction Solar Cells by Sequential Processing: Control and Influence of Se Content. *Sol. RRL* **2020**, *4* (7), 1–11. <https://doi.org/10.1002/solr.202000141>.
- (107) Vidal-Fuentes, P.; Guc, M.; Alcobe, X.; Jawhari, T.; Placidi, M.; Pérez-Rodríguez, A.; Saucedo, E.; Roca, V. I. Multiwavelength Excitation Raman Scattering Study of Sb₂Se₃ Compound: Fundamental Vibrational Properties and Secondary Phases Detection. *2D Mater.* **2019**, *6* (4), 045054. <https://doi.org/10.1088/2053-1583/ab4029>.
- (108) Chen, C.; Li, W.; Zhou, Y.; Chen, C.; Luo, M.; Liu, X.; Zeng, K.; Yang, B.; Zhang, C.; Han, J.; Tang, J. Optical Properties of Amorphous and Polycrystalline Sb₂Se₃ Thin Films Prepared by Thermal Evaporation. *Appl. Phys. Lett.* **2015**, *107* (4), 043905.

<https://doi.org/10.1063/1.4927741>.

- (109) Vadapoo, R.; Krishnan, S.; Yilmaz, H.; Marin, C. Electronic Structure of Antimony Selenide (Sb₂Se₃) from GW Calculations. *Phys. status solidi* **2011**, *248* (3), 700–705. <https://doi.org/10.1002/pssb.201046225>.
- (110) Maghraoui-Meherzi, H.; Ben Nasr, T.; Dachraoui, M. Synthesis, Structure and Optical Properties of Sb₂Se₃. *Mater. Sci. Semicond. Process.* **2013**, *16* (1), 179–184. <https://doi.org/10.1016/j.mssp.2012.04.019>.
- (111) Yuan, C.; Jin, X.; Jiang, G.; Liu, W.; Zhu, C. Sb₂Se₃ Solar Cells Prepared with Selenized Dc-Sputtered Metallic Precursors. *J. Mater. Sci. Mater. Electron.* **2016**, *27* (9), 8906–8910. <https://doi.org/10.1007/s10854-016-4917-3>.
- (112) Filip, M. R.; Patrick, C. E.; Giustino, F. GW Quasiparticle Band Structures of Stibnite, Antimonelite, Bismuthinite, and Guanajuatite. *Phys. Rev. B* **2013**, *87* (20), 205125. <https://doi.org/10.1103/PhysRevB.87.205125>.
- (113) Chen, C.; Bobela, D. C.; Yang, Y.; Lu, S.; Zeng, K.; Ge, C.; Yang, B.; Gao, L.; Zhao, Y.; Beard, M. C.; Tang, J. Characterization of Basic Physical Properties of Sb₂Se₃ and Its Relevance for Photovoltaics. *Front. Optoelectron.* **2017**, *10* (1), 18–30. <https://doi.org/10.1007/s12200-017-0702-z>.
- (114) Zeng, K.; Xue, D.-J.; Tang, J. Antimony Selenide Thin-Film Solar Cells. *Semicond. Sci. Technol.* **2016**, *31* (6), 063001. <https://doi.org/10.1088/0268-1242/31/6/063001>.
- (115) Novoselov, K. S. Electric Field Effect in Atomically Thin Carbon Films. *Science (80-.)*. **2004**, *306* (5696), 666–669. <https://doi.org/10.1126/science.1102896>.
- (116) Lin, Y.-C.; Lu, N.; Perea-Lopez, N.; Li, J.; Lin, Z.; Peng, X.; Lee, C. H.; Sun, C.; Calderin, L.; Browning, P. N.; Bresnehan, M. S.; Kim, M. J.; Mayer, T. S.; Terrones, M.; Robinson, J. A. Direct Synthesis of van Der Waals Solids. *ACS Nano* **2014**, *8* (4), 3715–3723. <https://doi.org/10.1021/nn5003858>.
- (117) Placidi, M.; Dimitrievska, M.; Izquierdo-Roca, V.; Fontané, X.; Castellanos-Gomez, A.; Pérez-Tomás, A.; Mestres, N.; Espindola-

- Rodriguez, M.; López-Marino, S.; Neuschitzer, M.; Bermudez, V.; Yaremko, A.; Pérez-Rodríguez, A. Multiwavelength Excitation Raman Scattering Analysis of Bulk and Two-Dimensional MoS₂: Vibrational Properties of Atomically Thin MoS₂ Layers. *2D Mater.* **2015**, *2* (3). <https://doi.org/10.1088/2053-1583/2/3/035006>.
- (118) Das, S.; Robinson, J. A.; Dubey, M.; Terrones, H.; Terrones, M. Beyond Graphene: Progress in Novel Two-Dimensional Materials and van Der Waals Solids. *Annu. Rev. Mater. Res.* **2015**, *45* (1), 1–27. <https://doi.org/10.1146/annurev-matsci-070214-021034>.
- (119) Zhou, Y.; Wang, L.; Chen, S.; Qin, S.; Liu, X.; Chen, J.; Xue, D.-J.; Luo, M.; Cao, Y.; Cheng, Y.; Sargent, E. H.; Tang, J. Thin-Film Sb₂Se₃ Photovoltaics with Oriented One-Dimensional Ribbons and Benign Grain Boundaries. *Nat. Photonics* **2015**, *9* (6), 409–415. <https://doi.org/10.1038/nphoton.2015.78>.
- (120) Li, K.; Chen, C.; Lu, S.; Wang, C.; Wang, S.; Lu, Y.; Tang, J. Orientation Engineering in Low-Dimensional Crystal-Structural Materials via Seed Screening. *Adv. Mater.* **2019**, *1903914*, 1903914. <https://doi.org/10.1002/adma.201903914>.
- (121) Kodalle, T.; Heinemann, M. D.; Greiner, D.; Yetkin, H. A.; Klupsch, M.; Li, C.; van Aken, P. A.; Lauermaun, I.; Schlattmann, R.; Kaufmann, C. A. Elucidating the Mechanism of an RbF Post Deposition Treatment in CIGS Thin Film Solar Cells. *Sol. RRL* **2018**, *2* (9), 1800156. <https://doi.org/10.1002/solr.201800156>.
- (122) Deringer, V. L.; Stoffel, R. P.; Wuttig, M.; Dronskowski, R. Vibrational Properties and Bonding Nature of Sb₂Se₃ and Their Implications for Chalcogenide Materials. *Chem. Sci.* **2015**, *6* (9), 5255–5262. <https://doi.org/10.1039/C5SC00825E>.
- (123) Huang, M.; Xu, P.; Han, D.; Tang, J.; Chen, S. Complicated and Unconventional Defect Properties of the Quasi-One-Dimensional Photovoltaic Semiconductor Sb₂Se₃. *ACS Appl. Mater. Interfaces* **2019**, *11* (17), 15564–15572. <https://doi.org/10.1021/acsami.9b01220>.
- (124) Stolaroff, A.; Lecomte, A.; Rubel, O.; Jobic, S.; Zhang, X.; Latouche, C.; Rocquefelte, X. Deciphering the Role of Key Defects in Sb₂Se₃, a Promising Candidate for Chalcogenide-Based Solar Cells. *ACS Appl. Energy Mater.* **2020**, *3* (3), 2496–

2509. <https://doi.org/10.1021/acsaem.9b02192>.
- (125) Li, Z.; Chen, X.; Zhu, H.; Chen, J.; Guo, Y.; Zhang, C.; Zhang, W.; Niu, X.; Mai, Y. Sb₂Se₃ Thin Film Solar Cells in Substrate Configuration and the Back Contact Selenization. *Sol. Energy Mater. Sol. Cells* **2017**, *161* (July 2016), 190–196. <https://doi.org/10.1016/j.solmat.2016.11.033>.
- (126) Chen, C.; Wang, L.; Gao, L.; Nam, D.; Li, D.; Li, K.; Zhao, Y.; Ge, C.; Cheong, H.; Liu, H.; Song, H.; Tang, J. 6.5% Certified Efficiency Sb₂Se₃ Solar Cells Using PbS Colloidal Quantum Dot Film as Hole-Transporting Layer. *ACS Energy Lett.* **2017**, *2* (9), 2125–2132. <https://doi.org/10.1021/acseenergylett.7b00648>.
- (127) Yuan, C.; Zhang, L.; Liu, W.; Zhu, C. Rapid Thermal Process to Fabricate Sb₂Se₃ Thin Film for Solar Cell Application. *Sol. Energy* **2016**, *137*, 256–260. <https://doi.org/10.1016/j.solener.2016.08.020>.
- (128) Li, D.-B.; Yin, X.; Grice, C. R.; Guan, L.; Song, Z.; Wang, C.; Chen, C.; Li, K.; Cimaroli, A. J.; Awani, R. A.; Zhao, D.; Song, H.; Tang, W.; Yan, Y.; Tang, J. Stable and Efficient CdS/Sb₂Se₃ Solar Cells Prepared by Scalable Close Space Sublimation. *Nano Energy* **2018**, *49*, 346–353. <https://doi.org/10.1016/j.nanoen.2018.04.044>.
- (129) Wen, X.; Chen, C.; Lu, S.; Li, K.; Kondrotas, R.; Zhao, Y.; Chen, W.; Gao, L.; Wang, C.; Zhang, J.; Niu, G.; Tang, J. Vapor Transport Deposition of Antimony Selenide Thin Film Solar Cells with 7.6% Efficiency. *Nat. Commun.* **2018**, *9* (1), 2179. <https://doi.org/10.1038/s41467-018-04634-6>.
- (130) Yuan, S.; Deng, H.; Yang, X.; Hu, C.; Khan, J.; Ye, W.; Tang, J.; Song, H. Postsurface Selenization for High Performance Sb₂S₃ Planar Thin Film Solar Cells. *ACS Photonics* **2017**, *4* (11), 2862–2870. <https://doi.org/10.1021/acsp Photonics.7b00858>.
- (131) Ma, Y.; Tang, B.; Lian, W.; Wu, C.; Wang, X.; Ju, H.; Zhu, C.; Fan, F.; Chen, T. Efficient Defect Passivation of Sb₂Se₃ Film by Tellurium Doping for High Performance Solar Cells. *J. Mater. Chem. A* **2020**, *8* (14), 6510–6516. <https://doi.org/10.1039/D0TA00443J>.

- (132) Hu, X.; Tao, J.; Weng, G.; Jiang, J.; Chen, S.; Zhu, Z.; Chu, J. Investigation of Electrically-Active Defects in Sb₂Se₃ Thin-Film Solar Cells with up to 5.91% Efficiency via Admittance Spectroscopy. *Sol. Energy Mater. Sol. Cells* **2018**, *186* (May), 324–329. <https://doi.org/10.1016/j.solmat.2018.07.004>.
- (133) Hu, X.; Tao, J.; Chen, S.; Xue, J.; Weng, G.; Kaijiang; Hu, Z.; Jiang, J.; Chen, S.; Zhu, Z.; Chu, J. Improving the Efficiency of Sb₂Se₃ Thin-Film Solar Cells by Post Annealing Treatment in Vacuum Condition. *Sol. Energy Mater. Sol. Cells* **2018**, *187* (August), 170–175. <https://doi.org/10.1016/j.solmat.2018.08.006>.
- (134) Hu, X.; Tao, J.; Wang, Y.; Xue, J.; Weng, G.; Zhang, C.; Chen, S.; Zhu, Z.; Chu, J. 5.91%-Efficient Sb₂Se₃ Solar Cells with a Radio-Frequency Magnetron-Sputtered CdS Buffer Layer. *Appl. Mater. Today* **2019**, *16*, 367–374. <https://doi.org/10.1016/j.apmt.2019.06.001>.
- (135) Tao, J.; Hu, X.; Guo, Y.; Hong, J.; Li, K.; Jiang, J.; Chen, S.; Jing, C.; Yue, F.; Yang, P.; Zhang, C.; Wu, Z.; Tang, J.; Chu, J. Solution-Processed SnO₂ Interfacial Layer for Highly Efficient Sb₂Se₃ Thin Film Solar Cells. *Nano Energy* **2019**, *60*, 802–809. <https://doi.org/10.1016/j.nanoen.2019.04.019>.
- (136) Ren, D.; Chen, S.; Cathelinaud, M.; Liang, G.; Ma, H.; Zhang, X. Fundamental Physical Characterization of Sb₂Se₃-Based Quasi-Homojunction Thin Film Solar Cells. *ACS Appl. Mater. Interfaces* **2020**, *12* (27), 30572–30583. <https://doi.org/10.1021/acsami.0c08180>.
- (137) McKenna, K. P. Self-Healing of Broken Bonds and Deep Gap States in Sb₂Se₃ and Sb₂S₃. *Adv. Electron. Mater.* **2021**, *2000908*, 2000908. <https://doi.org/10.1002/aelm.202000908>.
- (138) Williams, R. E.; Ramasse, Q. M.; McKenna, K. P.; Phillips, L. J.; Yates, P. J.; Hutter, O. S.; Durose, K.; Major, J. D.; Mendis, B. G. Evidence for Self-Healing Benign Grain Boundaries and a Highly Defective Sb₂Se₃–CdS Interfacial Layer in Sb₂Se₃ Thin-Film Photovoltaics. *ACS Appl. Mater. Interfaces* **2020**, *12* (19), 21730–21738. <https://doi.org/10.1021/acsami.0c03690>.
- (139) Chen, C.; Tang, J. Open-Circuit Voltage Loss of Antimony Chalcogenide Solar Cells: Status, Origin, and Possible Solutions.

- ACS Energy Lett.* **2020**, *5* (7), 2294–2304.
<https://doi.org/10.1021/acsenergylett.0c00940>.
- (140) Chen, C.; Bobela, D. C.; Yang, Y.; Lu, S.; Zeng, K.; Ge, C.; Yang, B.; Gao, L.; Zhao, Y.; Beard, M. C.; Tang, J. Characterization of Basic Physical Properties of Sb₂Se₃ and Its Relevance for Photovoltaics. *Front. Optoelectron.* **2017**, *10* (1), 18–30.
<https://doi.org/10.1007/s12200-017-0702-z>.
- (141) Wang, K.; Chen, C.; Liao, H.; Wang, S.; Tang, J.; Beard, M. C.; Yang, Y. Both Free and Trapped Carriers Contribute to Photocurrent of Sb₂Se₃ Solar Cells. *J. Phys. Chem. Lett.* **2019**, *10* (17), 4881–4887. <https://doi.org/10.1021/acs.jpcclett.9b01817>.
- (142) Yang, W.; Lee, S.; Kwon, H.-C.; Tan, J.; Lee, H.; Park, J.; Oh, Y.; Choi, H.; Moon, J. Time-Resolved Observations of Photo-Generated Charge-Carrier Dynamics in Sb₂Se₃ Photocathodes for Photoelectrochemical Water Splitting. *ACS Nano* **2018**, *12* (11), 11088–11097. <https://doi.org/10.1021/acsnano.8b05446>.
- (143) Phys, J. A.; Kim, S.; Shibata, H.; Niki, S. Improvement of Minority Carrier Lifetime and Conversion Efficiency by Na Incorporation in Cu₂ZnSnSe₄ Solar Cells. **2017**, *023106* (June).
<https://doi.org/10.1063/1.4993288>.
- (144) Gharibshahian, I.; Orouji, A. A.; Sharbati, S. Alternative Buffer Layers in Sb₂Se₃ Thin-film Solar Cells to Reduce Open-circuit Voltage Offset. *Sol. Energy* **2020**, *202* (April), 294–303.
<https://doi.org/10.1016/j.solener.2020.03.115>.
- (145) Chen, Z.; Guo, X.; Guo, H.; Ma, C.; Qiu, J.; Yuan, N.; Ding, J. Fabrication of a Semi-Transparent Thin-Film Sb₂Se₃ Solar Cell. *Mater. Lett.* **2019**, *236* (October), 503–505.
<https://doi.org/10.1016/j.matlet.2018.10.173>.
- (146) Wen, X.; He, Y.; Chen, C.; Liu, X.; Wang, L.; Yang, B.; Leng, M.; Song, H.; Zeng, K.; Li, D.; Li, K.; Gao, L.; Tang, J. Magnetron Sputtered ZnO Buffer Layer for Sb₂Se₃ Thin Film Solar Cells. *Sol. Energy Mater. Sol. Cells* **2017**, *172* (July), 74–81.
<https://doi.org/10.1016/j.solmat.2017.07.014>.
- (147) Phillips, L. J.; Savory, C. N.; Hutter, O. S.; Yates, P. J.; Shiel, H.; Mariotti, S.; Bowen, L.; Birkett, M.; Durose, K.; Scanlon, D. O.;

- Major, J. D. Current Enhancement via a TiO₂ Window Layer for CSS Sb₂Se₃ Solar Cells: Performance Limits and High V_{oc}. *IEEE J. Photovoltaics* **2019**, *9* (2), 544–551.
<https://doi.org/10.1109/JPHOTOV.2018.2885836>.
- (148) Wang, X.; Tang, R.; Yin, Y.; Ju, H.; Li, S.; Zhu, C.; Chen, T. Interfacial Engineering for High Efficiency Solution Processed Sb₂Se₃ Solar Cells. *Sol. Energy Mater. Sol. Cells* **2019**, *189* (August 2018), 5–10.
<https://doi.org/10.1016/j.solmat.2018.09.020>.
- (149) Li, G.; Li, Z.; Liang, X.; Guo, C.; Shen, K.; Mai, Y. Improvement in Sb₂Se₃ Solar Cell Efficiency through Band Alignment Engineering at the Buffer/Absorber Interface. *ACS Appl. Mater. Interfaces* **2019**, *11* (1), 828–834.
<https://doi.org/10.1021/acsami.8b17611>.
- (150) Wang, C.; Lu, S.; Li, S.; Wang, S.; Lin, X.; Zhang, J.; Kondrotas, R.; Li, K.; Chen, C.; Tang, J. Efficiency Improvement of Flexible Sb₂Se₃ Solar Cells with Non-Toxic Buffer Layer via Interface Engineering. *Nano Energy* **2020**, 104577.
<https://doi.org/10.1016/j.nanoen.2020.104577>.
- (151) Li, Z.-Q.; Ni, M.; Feng, X.-D. Simulation of the Sb₂Se₃ Solar Cell with a Hole Transport Layer. *Mater. Res. Express* **2020**, *7* (1), 016416. <https://doi.org/10.1088/2053-1591/ab5fa7>.
- (152) Shen, K.; Zhang, Y.; Wang, X.; Ou, C.; Guo, F.; Zhu, H.; Liu, C.; Gao, Y.; Schropp, R. E. I.; Li, Z.; Liu, X.; Mai, Y. Efficient and Stable Planar n–i–p Sb₂Se₃ Solar Cells Enabled by Oriented 1D Trigonal Selenium Structures. *Adv. Sci.* **2020**, *2001013*, 2001013.
<https://doi.org/10.1002/advs.202001013>.
- (153) Li, K.; Wang, S.; Chen, C.; Kondrotas, R.; Hu, M.; Lu, S.; Wang, C.; Chen, W.; Tang, J. 7.5% n–i–p Sb₂Se₃ Solar Cells with CuSCN as a Hole-Transport Layer. *J. Mater. Chem. A* **2019**, *7* (16), 9665–9672. <https://doi.org/10.1039/C9TA01773A>.
- (154) Zhang, J.; Kondrotas, R.; Lu, S.; Wang, C.; Chen, C.; Tang, J. Alternative Back Contacts for Sb₂Se₃ Solar Cells. *Sol. Energy* **2019**, *182* (January), 96–101.
<https://doi.org/10.1016/j.solener.2019.02.050>.

- (155) Liang, X.; Guo, C.; Liu, T.; Liu, Y.; Yang, L.; Song, D.; Shen, K.; Schropp, R. E. I.; Li, Z.; Mai, Y. Crystallographic Orientation Control of 1D Sb₂Se₃ Nanorod Arrays for Photovoltaic Application by In Situ Back-Contact Engineering. *Sol. RRL* **2020**, *2000294*, 2000294. <https://doi.org/10.1002/solr.202000294>.
- (156) Würfel, P. *Physics of Solar Cells: From Principles to New Concepts*; WILEY-VCH Verlag GmbH & Co. KGaA, Weinheim, **2015**.
- (157) Scheer, R.; Schock, H. *Chalcogenide Photovoltaics*; Wiley-VCH Verlag GmbH & Co. KGaA: Weinheim, Germany, **2011**. <https://doi.org/10.1002/9783527633708>.
- (158) Smets, A.; Jäger, K.; Isabella, O.; Swaaij, R. Van; Zeman, M. *Solar Energy - The Physics and Engineering of Photovoltaic Conversion Technologies and Systems*; Routledge, **2014**; Vol. 273. <https://doi.org/10.4324/9781315751191-5>.
- (159) Kittel, C. *Introduction to Solid State Physics, 8th Edition*; John Wiley & Sons Ltd, **2004**.
- (160) Peter Y. Yu Manuel Cardona. Fundamentals of Semiconductors. In *Problems in Solid State Physics with Solutions*; WORLD SCIENTIFIC, **2011**; pp 315–332. https://doi.org/10.1142/9789814365031_0020.
- (161) Liang, G.-X.; Luo, Y.-D.; Chen, S.; Tang, R.; Zheng, Z.-H.; Li, X.-J.; Liu, X.-S.; Liu, Y.-K.; Li, Y.-F.; Chen, X.-Y.; Su, Z.-H.; Zhang, X.-H.; Ma, H.-L.; Fan, P. Sputtered and Selenized Sb₂Se₃ Thin-Film Solar Cells with Open-Circuit Voltage Exceeding 500 MV. *Nano Energy* **2020**, *73* (April), 104806. <https://doi.org/10.1016/j.nanoen.2020.104806>.
- (162) Shockley, W.; Queisser, H. J. Detailed Balance Limit of Efficiency of P-n Junction Solar Cells. *J. Appl. Phys.* **1961**, *32* (3), 510–519. <https://doi.org/10.1063/1.1736034>.
- (163) van Roosbroeck, W.; Shockley, W. Photon-Radiative Recombination of Electrons and Holes in Germanium. *Phys. Rev.* **1954**, *94* (6), 1558–1560. <https://doi.org/10.1103/PhysRev.94.1558>.
- (164) De Vos, A.; Landsberg, P. T.; Baruch, P.; Parrott, J. E. Entropy

- Fluxes, Endoreversibility, and Solar Energy Conversion. *J. Appl. Phys.* **1993**, *74* (6), 3631–3637. <https://doi.org/10.1063/1.354503>.
- (165) Hirst, L. C.; Ekins-Daukes, N. J. Fundamental Losses in Solar Cells. *Prog. Photovoltaics Res. Appl.* **2011**, *19* (3), 286–293. <https://doi.org/10.1002/pip.1024>.
- (166) Landsberg, P. T.; Markvart, T. The Carnot Factor in Solar-Cell Theory. *Solid. State. Electron.* **1998**, *42* (4), 657–659. [https://doi.org/10.1016/S0038-1101\(97\)00253-0](https://doi.org/10.1016/S0038-1101(97)00253-0).
- (167) SITES, J. Quantification of Losses in Thin-Film Polycrystalline Solar Cells. *Sol. Energy Mater. Sol. Cells* **2003**, *75* (1–2), 243–251. [https://doi.org/10.1016/S0927-0248\(02\)00166-6](https://doi.org/10.1016/S0927-0248(02)00166-6).
- (168) Shockley, W.; Read, W. T. Statistics of the Recombinations of Holes and Electrons. *Phys. Rev.* **1952**, *87* (5), 835–842. <https://doi.org/10.1103/PhysRev.87.835>.
- (169) Hall, R. N. Electron-Hole Recombination in Germanium. *Phys. Rev.* **1952**, *87* (2), 387–387. <https://doi.org/10.1103/PhysRev.87.387>.
- (170) Rietveld, H. M. A Profile Refinement Method for Nuclear and Magnetic Structures. *J. Appl. Crystallogr.* **1969**, *2* (2), 65–71. <https://doi.org/10.1107/S0021889869006558>.
- (171) Coelho, A. A.; Evans, J.; Evans, I.; Kern, A.; Parsons, S. The TOPAS Symbolic Computation System. *Powder Diffr.* **2011**, *26* (S1), S22–S25. <https://doi.org/10.1154/1.3661087>.
- (172) Balzar, D.; Audebrand, N.; Daymond, M. R.; Fitch, A.; Hewat, A.; Langford, J. I.; Le Bail, A.; Louër, D.; Masson, O.; McCowan, C. N.; Popa, N. C.; Stephens, P. W.; Toby, B. H. Size–Strain Line-Broadening Analysis of the Ceria Round-Robin Sample. *J. Appl. Crystallogr.* **2004**, *37* (6), 911–924. <https://doi.org/10.1107/S0021889804022551>.
- (173) Whitfield, P. S. Spherical Harmonics Preferential Orientation Corrections and Structure Solution from Powder Diffraction Data – a Possible Avenue of Last Resort. *J. Appl. Crystallogr.* **2009**, *42* (1), 134–136. <https://doi.org/10.1107/S0021889808041149>.
- (174) Cheary, R. W.; Coelho, A. A.; Cline, J. P. Fundamental

- Parameters Line Profile Fitting in Laboratory Diffractometers. *J. Res. Natl. Inst. Stand. Technol.* **2007**, *109* (1), 1–25.
<https://doi.org/10.6028/jres.002>.
- (175) Shongalova, A.; Correia, M. R.; Vermang, B.; Cunha, J. M. V.; Salomé, P. M. P.; Fernandes, P. A. On the Identification of Sb₂Se₃ Using Raman Scattering. *MRS Commun.* **2018**, *8* (03), 865–870.
<https://doi.org/10.1557/mrc.2018.94>.
- (176) Fleck, N.; Hobson, T. D. C.; Savory, C. N.; Buckeridge, J.; Veal, T. D.; Correia, M. R.; Scanlon, D. O.; Durose, K.; Jäckel, F. Identifying Raman Modes of Sb₂Se₃ and Their Symmetries Using Angle-Resolved Polarised Raman Spectra. *J. Mater. Chem. A* **2020**, *8* (17), 8337–8344. <https://doi.org/10.1039/d0ta01783c>.
- (177) Lin, L. yan; Jiang, L. qin; Qiu, Y.; Fan, B. dian. Analysis of Sb₂Se₃/CdS Based Photovoltaic Cell: A Numerical Simulation Approach. *J. Phys. Chem. Solids* **2018**, *122* (March), 19–24.
<https://doi.org/10.1016/j.jpcs.2018.05.045>.
- (178) Huang, M.; Cai, Z.; Wang, S.; Gong, X.; Wei, S.; Chen, S. More Se Vacancies in Sb₂Se₃ under Se-Rich Conditions: An Abnormal Behavior Induced by Defect-Correlation in Compensated Compound Semiconductors. *Small* **2021**, *2102429*, 2102429.
<https://doi.org/10.1002/sml.202102429>.
- (179) Shin, B.; Zhu, Y.; Bojarczuk, N. A.; Jay Chey, S.; Guha, S. Control of an Interfacial MoSe₂ Layer in Cu₂ZnSnSe₄ Thin Film Solar Cells: 8.9% Power Conversion Efficiency with a TiN Diffusion Barrier. *Appl. Phys. Lett.* **2012**, *101* (5), 053903.
<https://doi.org/10.1063/1.4740276>.
- (180) Giraldo, S.; Kim, S.; Andrade-Arvizu, J. A.; Alcobé, X.; Malerba, C.; Valentini, M.; Tampo, H.; Shibata, H.; Izquierdo-Roca, V.; Pérez-Rodríguez, A.; Saucedo, E. Study and Optimization of Alternative MBE-deposited Metallic Precursors for Highly Efficient Kesterite CZTSe:Ge Solar Cells. *Prog. Photovoltaics Res. Appl.* **2019**, *27* (9), 779–788.
<https://doi.org/10.1002/pip.3147>.
- (181) Ould Salem, M.; Fonoll, R.; Giraldo, S.; Sanchez, Y.; Placidi, M.; Izquierdo-Roca, V.; Malerba, C.; Valentini, M.; Sylla, D.; Thomere, A.; Ahmedou, D. O.; Saucedo, E.; Pérez-Rodríguez, A.;

- Jehl Li-Kao, Z. Over 10% Efficient Wide Bandgap CIGSe Solar Cells on Transparent Substrate with Na Predeposition Treatment. *Sol. RRL* **2020**, *4* (11), 2000284.
<https://doi.org/10.1002/solr.202000284>.
- (182) Kohara, N.; Nishiwaki, S.; Hashimoto, Y.; Negami, T.; Wada, T. Electrical Properties of the Cu(In,Ga)Se₂/MoSe₂/Mo Structure. *Sol. Energy Mater. Sol. Cells* **2001**, *67* (1–4), 209–215.
[https://doi.org/10.1016/S0927-0248\(00\)00283-X](https://doi.org/10.1016/S0927-0248(00)00283-X).
- (183) Lopez-Marino, S.; Espíndola-Rodríguez, M.; Sánchez, Y.; Alcobé, X.; Oliva, F.; Xie, H.; Neuschitzer, M.; Giraldo, S.; Placidi, M.; Caballero, R.; Izquierdo-Roca, V.; Pérez-Rodríguez, A.; Saucedo, E. The Importance of Back Contact Modification in Cu₂ZnSnSe₄ Solar Cells: The Role of a Thin MoO₂ Layer. *Nano Energy* **2016**, *26* (June), 708–721. <https://doi.org/10.1016/j.nanoen.2016.06.034>.
- (184) Abou-Ras, D.; Kostorz, G.; Bremaud, D.; Kälin, M.; Kurdesau, F. V.; Tiwari, A. N.; Döbeli, M. Formation and Characterisation of MoSe₂ for Cu(In,Ga)Se₂ Based Solar Cells. *Thin Solid Films* **2005**, *480–481*, 433–438.
<https://doi.org/10.1016/j.tsf.2004.11.098>.
- (185) Contreras, M. A.; Egaas, B.; Dippo, P.; Webb, J.; Granata, J.; Ramanathan, K.; Asher, S.; Swartzlander, A.; Noufi, R. On the Role of Na and Modifications to Cu(In,Ga)Se₂ Absorber Materials Using Thin-MF (M = Na, K, Cs) Precursor Layers. *Conf. Rec. IEEE Photovolt. Spec. Conf.* **1997**, *96*, 359–362.
- (186) Sekkina, M. M. A. Novel Investigations on Thermogravimetric and Differential Thermal Analyses of Elemental, Compound and Mixed Semiconductors. *J. Therm. Anal.* **1988**, *34*, 749–759.
- (187) Rau, U.; Braunger, D.; Herberholz, R.; Schock, H. W.; Guillemoles, J.-F.; Kronik, L.; Cahen, D. Oxygenation and Air-Annealing Effects on the Electronic Properties of Cu(In,Ga)Se₂ Films and Devices. *J. Appl. Phys.* **1999**, *86* (1), 497–505.
<https://doi.org/10.1063/1.370758>.
- (188) Repins, I.; Contreras, M. A.; Egaas, B.; DeHart, C.; Scharf, J.; Perkins, C. L.; To, B.; Noufi, R. 19.9%-Efficient ZnO/CdS/CuInGaSe₂ Solar Cell with 81.2% Fill Factor. *Prog. Photovoltaics Res. Appl.* **2008**, *16* (3), 235–239.

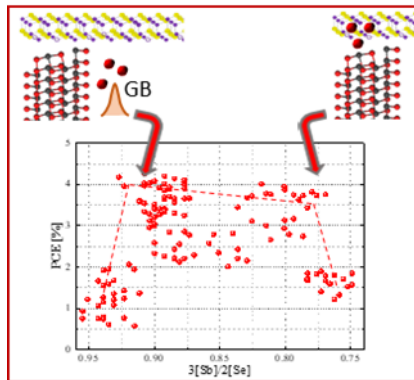
<https://doi.org/10.1002/pip.822>.

- (189) Choubey, R. K.; Desai, D.; Kale, S. N.; Kumar, S. Effect of Annealing Treatment and Deposition Temperature on CdS Thin Films for CIGS Solar Cells Applications. *J. Mater. Sci. Mater. Electron.* **2016**, *27* (8), 7890–7898. <https://doi.org/10.1007/s10854-016-4780-2>.
- (190) Xie, H.; López-Marino, S.; Olar, T.; Sánchez, Y.; Neuschitzer, M.; Oliva, F.; Giraldo, S.; Izquierdo-Roca, V.; Lauermann, I.; Pérez-Rodríguez, A.; Saucedo, E. Impact of Na Dynamics at the Cu₂ZnSn(S,Se)₄/CdS Interface during Post Low Temperature Treatment of Absorbers. *ACS Appl. Mater. Interfaces* **2016**, *8* (7), 5017–5024. <https://doi.org/10.1021/acsami.5b12243>.

Appendix

Efficient Se-rich $\text{Sb}_2\text{Se}_3/\text{CdS}$ planar-heterojunction solar cells by sequential processing: control and influence of Se content

P. Vidal-Fuentes, M. Placidi, Y. Sánchez, I. Becerril-Romero, J. Andrade-Arvizu, Z. Jehl, A. Pérez-Rodríguez, V. Izquierdo-Roca, E. Saucedo*



www.solar-rrl.com

ISSN 2367-198X · Sol. RRL · 4 · No. 7 (2020)

7/2020



Solar RRL

Rapid Research Letters
Full Papers · Reviews



34 3d¹⁰4s²4p⁴
Se
Selenium
78.96

Efficient Se-Rich Sb₂Se₃/CdS Planar Heterojunction Solar Cells by Sequential Processing: Control and Influence of Se Content

Pedro Vidal-Fuentes, Marcel Placidi, Yudania Sánchez, Ignacio Becerril-Romero, Jacob Andrade-Arvizu, Zacharie Jehl, Alejandro Pérez-Rodríguez, Víctor Izquierdo-Roca, and Edgardo Saucedo

WILEY-VCH